UNIVERSITY OF CALIFORNIA
SANTA CRUZ

PALEORECORDS OF ANTARCTIC ICE MOTION, SUBGLACIAL HYDROLOGY, AND CHEMICAL WEATHERING

A dissertation submitted in partial satisfaction of the
requirements for the degree of

DOCTOR OF PHILOSOPHY

in

EARTH SCIENCES

by

Gavin Gerard Piccione

September 2023

The Dissertation of Gavin G. Piccione is approved:

Professor Terrence Blackburn, chair

Professor Slawek Tulaczyk

Professor Mathis Hain

Peter Biehl
Vice Provost and Dean of Graduate Studies

TABLE OF CONTENTS

List of Figures

List of Tables

ABSTRACT

Paleorecords of Antarctic ice motion, subglacial hydrology, and chemical weathering

by

Gavin Gerard Piccione

With more than 70m of sea level equivalent ice stored in the polar ice sheets, sea level forecasting is heavily reliant on projections of ice sheet response to changes in global climate. One way that Earth scientists have approached this problem is to look back at past warm periods to determine how terrestrial ice mass changed in during previous climatic events. In Antarctic, however, there is an added complexity that 97.6% of the modern continent is covered by ice, which restricts access to the geologic record. Without terrestrial archives of Antarctic ice sheet evolution, it is challenging to parameterize the dominant processes that govern ice sheet sensitivity to climate and the environmental effects of ice loss. In this dissertation, I applied geochronologic, isotopic, elemental, and spectroscopic analyses to Antarctic subglacial chemical precipitates – a novel terrestrial record of basal conditions – to investigate the processes that link climate change, Antarctic ice motion, and the hydrologic system at the ice-bed interface. Collectively, this work expands our understanding of Antarctic evolution on centennial to millennial timescales and establishes Antarctic subglacial precipitates as climate archives analogous to speleothems.

The first two chapters investigate the physical processes associated with subglacial hydrology and ice motion. By applying geochronologic and geochemical analyses to a

group of precipitates that formed over tens-of-thousands of years during the Late Pleistocene, we showed that the continent-wide Antarctic subglacial hydrologic system responds rapidly (within 60 yrs.) to millennial-scale climate events, with more intense subglacial flushing during warm periods and diminished basal meltwater flow during cold periods. This close coupling between climate and subglacial hydrologic activity requires changes to Antarctic ice surface slope caused by hundreds of meters of thinning at the ice sheet margins. These studies provide evidence that the Antarctic gains and loses ice during millennial-scale climate cycles and indicate that subglacial meltwater flushing drive higher ice velocities that promote ice thinning and grounding line retreat.

The latter chapters focus on the mechanisms that control the chemical composition of subglacial waters, to help discern the environmental effects of Antarctic ice loss on geologic timescales. The third chapter uses stable isotope measurements (carbon and oxygen) on a suite of 49 subglacial precipitates to show that microbial activity mobilizes fossil carbon stored in rocks and sediment throughout the Antarctic continent. This respired CO_2 drives a continent-wide silicate weathering cycle that mobilizes elements from the subglacial bedrock, which may play an important role in fertilizing the Southern Ocean ecosystem. Chapter 4 established 10 kyr record of trace metal cycling beneath the East Antarctic Ice Sheet (EAIS) measured in a subglacial precipitate that formed across glacial termination III. This record implies that climate modulated changes in subglacial flushing intensity regulate the mobilization of redox sensitive trace metals on geologic timescales.

To my parents, Victoria and John, for the love and support that led me to pursue my dream of becoming a geologist.

To Graham, and the early morning coffees and discussions that always remind me of the joy of doing science.

Acknowledgments

My fondest memories of graduate school were the ones spent chewing on juicy science questions with colleagues at reading group, dialing in methods with labmates, or hanging out with friends around Santa Cruz. The kindness, guidance, and generosity of this community not only supported me through my doctoral work, but also helped me grow as a person during my graduate school years. Though I cannot adequately express my gratitude to the long list of people who have been there for me before and during my PhD, I am happy to take this opportunity to thank a small group who have played a particularly impactful role in my life and in my graduate studies.

Thank you to my advisor Terry Blackburn, for the years of support and mentorship. Through the ups and downs of graduate school, I always appreciated you being there to push me to become a better scientist, and to offer guidance and confidence when I needed it. From the beginning I always felt that you put the success of your students first, and that support gave me strong foundation for my graduate work. I will always look back fondly on the days working with you at UCSC and look forward to all of our future collaborations. Thank you to be Slawek Tulaczyk for spending countless hours sharing your knowledge of glaciology, and expertise in navigating academia. I learned a great deal from your scientific approach and your healthy skepticism, which I will carry with me throughout my scientific career. Thank you to Mathis Hain for guiding me through the carbon cycle, and the fundamentals of geochemical modeling.

I am extremely grateful to my labmate, colleague, and best friend Graham Edwards. The early morning coffees, the times when I would swivel in my chair to get your

opinion on a new science idea, working at the museum, and all of the G's boondoggles were the true highlights of graduate school for me. Cheers to the Santa Cruz days, and all of the days ahead!

Thank you to Amanda Donaldson for your love and kindness through the years. I've learned so much from you, both personally and scientifically, and I am so grateful to have spent this chapter with you.

Thank you to my parents, Victoria and John, for filling my life with love and encouraging me to pursue my passion for geology since I was a little boy. Your unwavering support has always guided me and paved my way. To my big brother, Dillon, for all of the adventures growing up and for always being my role model. Thank you to my step-mother, Hope Ryan, for opening so many doors and always sharing your wisdom.

I am endlessly grateful for my Santa Cruz family, Eleanor and George Balassone, for all of the fun times at 1038 Escalona. You have both taught me the most important lessons in graduate school: countless pro-tips on keeping a clean household, the best strategies for throwing the perfect party, the wonders of Costco, the recipe for Lbow's famous marinara sauce, and that enjoying life should always come first.

Thank you to all of my friends in Santa Cruz for all of the wonderful memories. A special shoutout to Adam Price and Seth Burgess: AP, thanks for all of the great times in the office, at the Boulder Creek house, in the gym, and everywhere in between; Seth, thanks for the basketball games, showing me around the ranch, and all the dance lessons.

Thank you to all of my colleagues and labmates at UCSC. To Jessica Gagliardi, I've had a blast working with you in the lab for the past two years. Thanks for sharing your love for Billy Joel, bagels, and rocks! Thank you to all of my undergraduate labmates through the years. Special thanks to Dylan Tasker, for being there in my early years at UCSC and sharing your insights in the chemistry lab. Stefani Himes, your dedication to our work, perseverance through the trials and tribulation of research, and profound understanding of the most important aspects of life were always inspiring to me. I count you as one of my most important colleagues in graduate school and am extremely proud of the work we did. Thank you to Sophia Pinter, Chloe Tinglof, and Noah Brigham, for the years of Antarctic research and for inspiring me with your excitement for isotope geochemistry.

Finally, thank you to everyone who has been there for me before and during graduate school whose name I have not mentioned. You know who you are and please know how grateful I am for having spent time with you and for your support.

Introduction

Antarctic climate sensitivity is of broad scientific and societal importance because the Antarctic ice sheet is the largest and most uncertain potential contributor to sea level[1]. Modern observations describe dramatic increases in ice loss from the West Antarctic Ice Sheet (WAIS) driven by climate forcing[2], and indicate the potential for heightened mass loss from the East Antarctic Ice Sheet (EAIS) in the near future[3,4]. Despite this growing body of evidence, model projections for Antarctic response to future climate warming are highly uncertain, with unknown parameters associated with the feedbacks between ice sheet, atmospheric, and ocean forcings[5]. One of the principal reasons for these knowledge gaps is limited access to the Antarctic geologic record due to almost complete ice cover. While Southern Ocean sediment cores provide some constraints on ice sheet mass balance through time, archives from the Antarctic continent are crucial to link changing ice mass to the glacial mechanisms that govern ice sheet climate sensitivity and the environmental effects of ice loss.

Beneath the Antarctic ice sheet there is an active, continent-wide hydrologic system that may play a central role in ice sheet-climate feedbacks[6]. Remote sensing observations of the ice-bed interface indicate that subglacial water flushing causes punctuated (<1 yr.) ice flow acceleration[7] and could trigger the onset of ice streams[8]. Model simulations describe a possible connection between these modern observations and long-term climate forcing[9], whereby subglacial meltwater reduces affective pressure at the ice sheet bed and drives faster ice velocities, which allows for rapid ice

response to climate warming. Whether subglacial meltwater causes sustained ice motion during centennial to millennial climate cycles is uncertain, however, due to a lack of data describing subglacial hydrologic activity on these timescales.

Antarctic meltwater discharge can also influence the biogeochemistry, and most importantly carbon fluxes, in the Southern Ocean by releasing limiting nutrients[10]. Missions to characterize basal waters beneath the modern ice sheet via ice drilling have identified diverse and abundant microbial communities in basal fluids[11]. Interactions between microbes and comminuted glacial sediment beneath ice sheets drive elevated biochemical weathering rates relative to global riverine values[12]. The flow of these waters can potentially fertilize the SO by delivering limiting nutrients like organic carbon[13] and iron[14]. Though the spatial and temporal extent of subglacial biogeochemical weathering and the effect Antarctic meltwater discharge over geologic timescales is unknown.

This dissertation applies geochronologic, isotopic, elemental, and spectroscopic analyses to Antarctic subglacial chemical precipitates – a novel terrestrial record of basal conditions – to investigate the processes that link climate change, Antarctic ice motion, and the hydrologic system at the ice-bed interface. These samples, made primarily of carbonate and opal, form in subglacial water and are transported to the ice sheet surface within upward-flowing sections of basal ice[15]. In each chapter, I apply geochemical measurements to characterize precipitate parent water compositions and provenance, and pair these data with geochronologic constraints to investigate the temporal evolution of the basal environment.

In Chapter 1, we studied two opal-calcite precipitates from the EAIS side of the Ross Sea Embayment to discern how the ice sheet responded to millennial-scale climate change during the Late Pleistocene. Combined isotopic (C, O, and Sr) and elemental (Rare Earth Elements) analyses showed that opal and calcite layers resulted from cycles of meltwater freezing beneath the ice sheet periphery, followed by flushing of subglacial water from the ice sheet interior. By pairing geochemical data with U-series depositional age models, we found that these freeze-flush cycles closely follow Southern Hemisphere millennial-scale climate, with freezing during cold periods and flushing during warm periods. Based on models of ice sheet thermodynamics, the most likely mechanism linking climate with subglacial hydrology is ocean thermal forcing, which must drive hundreds-of-meters of ice thinning along the Antarctic margins during millennial warm periods to elicit the subglacial flushing response observed in our precipitate records. This study, published in the journal *Nature Communications*, provides evidence for high sensitivity of Antarctic ice to ocean thermal forcing, suggesting that ice at the Antarctic margins responds dynamically when a threshold in ocean forcing is reached.

In Chapter 2, we studied two subglacial precipitates from Reckling Moraine, Antarctica, which provide a high-resolution, ~10 kyr record of subglacial meltwater flushing during the Late Pleistocene. These precipitates consist of calcite matrix with episodic siliciclastic-rich layers produced by unidirectional subglacial water currents. To discern changes in subglacial hydrologic activity, we measured sand layer frequency, grain size (both proxies for subglacial water velocity), and isotopic and

elemental compositions of calcite (proxies for water provenance) in each sample. U-Th geochronology was added to establish temporal constraints on the observed changes in the basal flushing intensity. Comparison between these timeseries data and Southern Hemisphere climate records reveals that both basal flushing velocity and the delivery of interior meltwaters to the ice sheet margins increased during millennial-scale warm periods, with only a <60-yr lag between the onset of climate change and the subglacial hydrologic response. The most likely driver of this rapid coupling is steepened ice sheet surface slope driven by Southern Hemisphere warming and increased ocean temperatures. Enhanced subglacial flushing throughout the millennial warm period provides evidence for a feedback between ice sheet acceleration and basal hydrology, whereby increased flushing rate drive higher ice velocities that may also promote further ice thinning and grounding line retreat.

Chapters 3 and 4 shift in scope from the physical processes associated with subglacial hydrology and ice motion, towards the mechanisms that control the chemical composition of subglacial waters. In Chapter 3, we report a large stable oxygen and carbon isotope dataset from 49 subglacial precipitates that offers a continent-wide view of the biogeochemical conditions in subglacial water over the past 6.7 million years. By combining precipitate ages, carbon isotope data, and oxygen isotope data, we show that microbes live throughout the continent and have produced CO_2 through respiration of fossil organic matter since the Miocene. Adding Sr isotope data and element proxies for parent water alkalinity, we show that microbially produced CO_2 drives chemical weathering of silicate bedrock, the degree to which depends on the bedrock type (e.g.

basalt versus granite). This dataset suggests that Antarctica subglacial silicate weathering is a potentially large source of nutrients to the Southern Ocean, while refuting a large methane flux from the Antarctic basal environment.

In Chapter 4, we present a 25 kyr record of hydrogeochemical conditions and trace metal cycling beneath the East Antarctic Ice Sheet (EAIS) measured in a subglacial precipitate that formed across glacial termination III. Variations in precipitate texture and deposition rate record a subglacial hydrologic response across the termination, where increased meltwater flushing before the termination gives way to diminished subglacial hydrologic activity in the cold climate period following the termination. The isotopic composition (O, C, Sr, and U) of calcite tracks this apparent hydrologic change, with a higher fraction of meltwaters flushed from the ice sheet interior before and during the termination, and a shift towards the development of an isolated brine along the ice sheet margin after the termination. Elemental and spectroscopic data indicate that this post-termination hydrologic isolation led to the development of manganous/ferruginous conditions in precipitate parent waters that dissolved redox sensitive elements (Fe, Mn, Mo, Cu) from the bedrock substrate. These data support a connection between hydrologic activity and trace metal flux beneath the Antarctic ice sheet, where oxygen supplied through meltwater flushing prevents the dissolution of redox sensitive elements, while hydrologic isolation results in suboxic conditions that support biogeochemical weathering of metal-rich phases.

Chapter 1

Subglacial precipitates record Antarctic ice sheet response to late Pleistocene millennial climate cycles

Reprinted from:

Piccione, G., Blackburn, T., Tulaczyk, S. et al. Subglacial precipitates record Antarctic ice sheet response to late Pleistocene millennial climate cycles. Nat Commun 13, 5428 (2022). https://doi.org/10.1038/s41467-022-33009-1

1.1 Abstract

Ice cores and offshore sedimentary records demonstrate enhanced ice loss along Antarctic coastal margins during millennial-scale warm intervals within the last glacial termination. However, the distal location and short temporal coverage of these records leads to uncertainty in both the spatial footprint of ice loss, and whether millennial-scale ice response occurs outside of glacial terminations. Here we present a >100kyr archive of periodic transitions in subglacial precipitate mineralogy that are synchronous with Late Pleistocene millennial-scale climate cycles. Geochemical and geochronologic data provide evidence for opal formation during cold periods via cryoconcentration of subglacial brine, and calcite formation during warm periods through the addition of subglacial meltwater originating from the ice sheet interior. These freeze-flush cycles represent cyclic changes in subglacial hydrologic-connectivity driven by ice sheet velocity fluctuations. Our findings imply that oscillating Southern Ocean temperatures drive a dynamic response in the Antarctic ice sheet on millennial timescales, regardless of the background climate state.

1.2 Introduction

One of the persistent challenges involved in both reconstructions and projections global mean sea level is determining what sectors of the Antarctic Ice Sheet (AIS) are vulnerable to significant retreat, the timescales of such retreat, and the conditions that trigger ice loss events[16]. Modern observations[17,18] of retreating ice near marine-terminating ice sheet margins demonstrate the potential for rapid AIS mass fluctuations brought on by changing Southern Ocean temperature[19] (hereafter referred to as ocean

thermal forcing). The key link between this ocean thermal forcing and ice sheet mass lies in the delivery of heat to the ice sheet margins, which affect ice shelves and grounding lines. Ice sheet stability is regulated by ice shelves[20] and grounding line positions[21], which are vulnerable to thinning and retreat when contacted by warm ocean waters. Ice sheet models suggest that ice shelf decay can result in enhanced flow of grounded ice up to 1000 km upstream of the grounding lines of large outlet glaciers and ice streams[22]. On millennial timescales this feedback could cause substantial velocity changes in these fast-flowing ice drainage pathways[23], ultimately affecting continent-wide ice sheet mass balance[24].

Millennial-scale Southern Ocean temperature oscillations are driven by a feedback between ocean-atmosphere teleconnections that is modulated by Atlantic Meridional Overturn Circulation (AMOC)[25]: the mean state ocean circulation responsible for cross-equatorial heat transport from the Southern Hemisphere to the Northern Hemisphere. Changes to the intensity of AMOC result in out-of-phase polar temperature cycles[26] recorded by isotopic climate proxies in ice cores, identified as Dansgaard-Oeschger cycles in the Greenland ice core records and Antarctic Isotope Maxima (AIM) events in Antarctic ice core records. This oceanic teleconnection, called the bipolar seesaw, also affects atmospheric circulation by regulating the temperature gradient between the middle and high latitudes[27], which shifts the intertropical convergence zone intertropical convergence north when AMOC rate is high (Northern Hemisphere/Southern Hemisphere warm/cold periods) and south when AMOC rate is decreased (Northern Hemisphere/ Southern Hemisphere cold/warm periods)[28]. As the

intertropical convergence zone migrates southwards during AIM events, Southern Hemisphere westerly winds experience parallel latitudinal shifts and strengthening[29], causing upwelling of relatively warm circumpolar deep waters onto the Antarctic continental shelf[30]. Antarctic marginal ice is effected by these upwelling cycles, which deliver circumpolar deep waters to the base of ice shelves and grounding lines, triggering enhanced basal melting and retreat during Southern Hemisphere millennial warm periods[19].

Although ice sheet models[24] and modern observations[17,18] indicate that the AIS is susceptible to ice loss through ocean thermal forcing, regional differences in ice bed topography, drainage geometry, and ice thickness[31] in peripheral sectors of Antarctica may lead to geographic differences in grounding line vulnerability, adding spatiotemporal complexity to ice sheet response. Millennial-scale climate oscillations also vary in intensity depending on the background climate state, where large continental ice sheets during glacial periods[32] and enhanced atmospheric CO_2 concentrations during full interglacial conditions[33,34] dampen the amplitude of millennial-scale climate variability. In contrast, intermediate climate states are characterized by more frequent, larger magnitude changes in polar temperature[35]. Therefore, geologic evidence of AIS evolution across a wide geographic range and diverse climate states is necessary to support simulations of suborbital changes in ice mass. However, existing geologic records documenting millennial-scale AIS mass loss[36–38] are limited to bipolar seesaw events during the last two glacial terminations, are constrained by low-resolution age models, and are restricted spatially to ice shelf

systems and offshore sediments. This leaves the regional extent and magnitude of AIS response to suborbital climate change unconstrained.

Here, we present observations from an archive of subglacial hydrologic evolution recorded by chemical precipitates that formed >900 km apart beneath the East Antarctic Ice Sheet (EAIS), over a combined >100 kyr period during the Late Pleistocene. This dataset provides a sequence of high-resolution U-series age constraints of ice sheet evolution in response to millennial-scale climate change. Mineralogic and geochemical variations in subglacial precipitates provide evidence for periodic changes in subglacial hydrologic connectivity between the AIS interior and margin that occur contemporaneously with bipolar seesaw-related Southern Hemisphere climate cycles. Combining precipitate data with a reduced-complexity model of ice sheet thermodynamics, we demonstrate a link between subglacial hydrologic conditions and millennial-scale changes in ice sheet velocity.

1.3 Results

1.3.1 Changes in Subglacial Precipitate Mineralogy Correlated with Millennial Climate Cycles

In this study, we report geochronological and geochemical results collected from two subglacial precipitates that formed over tens of thousands of years in subglacial aqueous systems on the EAIS side of the Transantarctic Mountains (TAM) (Fig. 1). Sample MA113 comes from Mount Achernar Moraine (henceforth MAM; 84.2°S, 161°E), a nearly motionless body of blue ice on the side of Law Glacier[39] (Fig. 2), The moraine is located ca. 20 km downstream of the polar plateau, with debris derived

locally from Beacon Supergroup and the Ferrar Group[15]. Sample PRR50489 was found at Elephant Moraine (henceforth EM; 76.3°S, 157.3°E), a supraglacial moraine in a blue ice area of Transantarctic Mountains, where ~100 ka of ice sublimation has released debris from basal ice of the East Antarctic ice sheet[40,41] (Fig. 1), which also consists predominantly of rocks from Beacon and Ferrar[42]. Precipitates form in subglacial water, and are transported to the ice surface within upward-flowing sections of glacier ice before being exposed on the surface as the surrounding ice sublimates[15]. The exhumation of precipitates within basal ice sections makes it difficult to precisely locate their formation site. However, constraints on ice velocities and sublimation rates can be used to place their most likely formation area within ca. 10 km of where they were collected. For example, the length of time for the emergence of basal debris to MAM is estimated to be at least 35 ka[15]. Considering the youngest radiometric U-series age obtained for sample MA113 (25.44 ka), there was little time for the precipitate to travel over horizontal distances, supporting a formation area proximal to the MAM. A similar emergence time of ca. 40-50 ka can be estimated for PRR50489, but a greater minimum formation time (147 Ka) allows the possibility of a longer horizontal distance traveled. However, if we assume a basal transport velocity scaled similarly to other EAIS basal ice[39], PRR50489 could have traveled only 10 km of horizontal distance in 100 kyr. Hence, we interpret that both samples MA113 and PRR50489 likely formed in basal overdeepenings found within several kilometers upstream of EM and MAM[31], which offer suitable settings for precipitate formation because they would allow subglacial water bodies to persist over long time periods (Supplementary note 1).

Samples PRR50489 and MA113 are 3 and 9cm thick respectively, with alternating layers of calcite and opal-A (Fig.2a, b; Fig. 3a) implying cyclic changes in the subglacial environment. Unlike subglacial precipitates forming in alpine settings[43,44] and beneath the Laurentide ice sheet[45], PRR50489 and MA113 do not display characteristics indicative of formation by regelation or in a basal film, and instead require cm-scale or deeper subglacial cavities that remain open on >10 kyr timescales. Textures within each of these samples indicate that opal and calcite form via two different mechanisms. Calcite layers nucleate on the substrate and form acicular (MA113; Fig. 2a) or bladed (PRR50489; Fig. 3a, b) crystals in botryoidal shapes. Opals fill void space between calcite crystals and form distinct layers with flat tops, implying formation from nucleation in the water column followed by particle settling. While diagenetic transformation in these samples cannot be completely ruled out, petrographic analyses of calcite layers show no evidence for calcite dissolution or reprecipitation (Supplementary Fig. 1; Supplementary Fig. 2), and X-ray diffraction data from opal suggest that they are present in the opal-A form (Supplementary Fig. 3; Supplementary note 4).

We measured ^{234}U-^{230}Th ages on eleven opal layers from PRR50489 that constrain the timeframe of precipitation from 230 to 147 ka (Fig. 2), and ten opal and calcite layers from MA113 ranging in age from 55 to 42 ka (Fig. 3). We construct a stratigraphic age model for each sample using a Bayesian Markov chain Monte Carlo model in which the principal of superposition is imposed on each dated layer to refine age estimates based on stratigraphic order[46] (Supplementary Fig. 4). Depth profiles of

Si and Ca concentration collected using Energy Dispersive X-ray Spectroscopy provide a continuous representation of sample mineralogy: with high Ca areas representative of calcite and low Ca areas representative of opal. We pair stratigraphic age models with Ca concentration spectra to create timeseries describing the oscillations of precipitate mineralogy (Fig. 2d; Fig. 3c). These mineralogic timeseries reveal a temporal cyclicity in opal deposition, with opal layers in PRR50489 precipitated every 8-10 kyr between marine isotope stages 7 and 6, and opal layers in MA113 precipitated every 2-4 kyr during marine isotope stage 3. To investigate a possible link between cycles of precipitate mineralogy and climate, we compare timeseries for each precipitate with climate proxies in both Antarctic (Fig. 2e; Fig. 3d,e,g) and Greenland (Fig. 3f) ice cores. Visual comparison between Ca-spectra and Antarctic temperature proxies reveals a consistent, linear relationship between climate cycles and precipitate mineralogy, with calcite formation (high Ca wt%) during warm AIM peaks, and opal formation (low Ca wt%) during Antarctic cold periods (Fig. 2 and 3). Yet this visual comparison does not consider that climate forcing is a continuum, while precipitate mineralogy is binary. As such, there exists for each sample a threshold in climate forcing (Fig 2b; 3d: horizontal bar) above/below which precipitate mineralogy is predominantly calcite/opal. The apparent linear synchrony between precipitate mineralogy and Southern Hemisphere temperature indicates that bipolar-seesaw-driven climate change triggers variability in EAIS subglacial environments. A more quantitative comparison between the sample mineralogy and climate records that

considers a threshold response requires additional discussion of the glaciologic processes controlling this relationship and is presented in a later section.

1.3.2 Millennial-Scale Cycles in Subglacial Hydrologic Connectivity

To understand the link between ocean-atmosphere-cryosphere teleconnections and the mineralogy of subglacial precipitates, we first utilize geochemical and isotopic measurements to characterize the precipitate source fluids. The carbon ($\delta^{13}C_{VPDB}$) and oxygen ($\delta^{18}O_{VSMOW}$) isotopic compositions of opal and calcite-forming waters are distinct for both PRR50489 (Fig. 4a) and MA113 (Fig. 4b), with calcites forming from waters with low $\delta^{18}O$ values, and opals forming from waters with $\delta^{18}O$ values up to 7‰ higher. The low $\delta^{18}O$ compositions of the calcite endmember suggest origination of meltwaters generated beneath the EAIS interior[47,48], likely in conjunction to the modest additional ^{18}O-depletion occurring as meltwaters experience freezing in transit to the ice sheet margin[49]. The heaviest $\delta^{18}O$ compositions of the opal endmember fluid (-46.15‰ for PRR50489 and -52.10‰ for MA113) are similar to the $\delta^{18}O$ of ice proximal to the region where samples were exhumed[48,50], suggesting that these waters originate as basal meltwater formed closer to the ice sheet margin. Another distinguishing characteristic of opal and calcite-forming waters are their cerium anomalies (Ce*), a proxy for redox conditions[51] (Fig. 4; Fig. 5c). In both samples, Ce* correlates with sample mineralogy, with calcite Ce* values indicating precipitation from oxidizing waters (Ce*<1), while the most ^{18}O-enriched opals exhibit Ce* values indicating precipitation from intermediate to reduced waters (Ce*>1) (Fig. 4; Fig. 5c).

In most cases, $\delta^{18}O$ values of opal scale with Ce*, pointing to variable mixing ratios between an oxidizing and a more reducing water during the formation of both minerals (Fig. 4a,b). The $\delta^{13}C_{CaCO3}$ composition of calcite from both samples are ^{13}C-depleted (-23‰ for PRR50489 and -18‰ for MA113) suggesting that carbon is sourced from similarly ^{13}C-depleted subglacial organic matter (~ -26‰ in PRR50489) that is oxidized during microbial respiration. Similarly ^{13}C-depleted carbon is observed in other EAIS basal aqueous systems[52,53]. For water closed off from the atmosphere, microbial respiration can function as the only significant source of CO_2. This CO_2 undergoes hydrolysis to H_2CO_3 and is utilized in the chemical weathering of the substrate. In an area with bedrock dominated by silicate materials, most or all of the HCO_3^- in the system will result from silicate weathering reactions, which would result in $\delta^{13}C_{DIC}$ within 3‰ of $\delta^{13}C_{ORG}$[54,55]. The ~5‰ offset between $\delta^{13}C_{CaCO3}$ of PRR50489 and MA113 can be caused either by a slightly different organic source or contact with bedrock that contains more DIC derived from carbonate weathering.

Calcite layers in both samples exhibit trends in $\delta^{13}C$ and $\delta^{18}O$ compositional space that suggest mixing between two isotopically distinct fluids with different solute concentrations (Fig. 5). To match the trends in the calcite data for PRR50489 and MA113, a ^{13}C- and ^{18}O-depleted, calcite-forming endmember water must have 40-fold and 5-fold higher total carbon concentration respectively, relative to a low-carbon, opal-forming endmember water. Though $\delta^{13}C$ of the opal-forming water cannot be directly measured, for the mixing curve to fit calcite compositions and opal $\delta^{18}O$ values, the opal-forming endmember waters must have higher $\delta^{13}C$ values ($\delta^{13}C$ >-5 ‰): a

composition comparable to that of sub-AIS brines[56]. Similar mixing relationships are observed between the $^{87}Sr/^{86}Sr$ and $\delta^{18}O$ composition of opals and calcite (Fig. 3c,d), requiring endmember waters to be distinct in both Sr concentration and isotopic composition. In both samples, the opal-forming waters have more radiogenic (higher) $^{87}Sr/^{86}Sr$ and higher $\delta^{18}O$ than the calcite-forming waters. Mixing between strontium and oxygen show that 20- to 50-fold of the total Sr in the system originates in the opal-forming endmember (Fig. 4c, d). Due to their similar geochemical behavior, strontium and calcium concentrations in saline waters scale proportionally[57]. On this basis, the two endmember fluids must have distinctive Ca concentrations, with the opal-forming endmember accounting for >95% of Ca in the system. This mixing relationship affirms the prevalence of two endmember waters with divergent concentrations: a highly Ca-rich, C-poor opal-forming brine that dominates the aqueous cation budget, and a relatively Ca-dilute, C-rich calcite-forming meltwater that adds oxygen and carbon to the system.

Together, redox and isotopic data permit the identification of suitable analogs for both endmember waters. The opal endmember is characterized by low carbon and high calcium concentrations, a ^{13}C-enriched $\delta^{13}C$ composition, a $\delta^{18}O$ composition that matches ice proximal to the TAM, and a Ce* value indicative of intermediate to reducing fluids, supporting the idea that opal precipitated from a subglacial brine with limited oxygen. A potential analog matching these criteria are $CaCl_2$ brines that emanate from beneath the modern EAIS in the McMurdo Dry Valleys (MDV)[58]. In addition to the aforementioned similarities between the opal endmember and MDV

brines, $\delta^{234}U_o$ and bulk rare earth element compositions of MDV brines[59] (Supplementary Fig. 5) match that of the precipitate opals. In comparison, the calcite endmember water has high carbon and low calcium concentrations, low $\delta^{13}C$ and $\delta^{18}O$ compositions, and a Ce* signature indicative of oxidizing fluids. Combined, these geochemical signatures support a water composition analogous to glacial meltwater originating beneath the interior domes of East Antarctica, which would form from waters with highly ^{18}O-depleted, oxygen-rich meltwater from dome-ice, can have high concentrations of ^{13}C-depleted carbon from microbial respiration[11,52], and would be much more dilute than marginal brines. One analog for this glacial meltwater endmember is C-rich, low salinity jökulhlaup water measured at Casey Station[60] that flushed from subglacial lakes beneath Law Dome, and resulted in subglacial aragonite precipitation during an AIM warm period[61].

To test if water mixing is a plausible mechanism for the observed opal and calcite layers, we use the frezchem database[58] within the geochemical program PHREEQC[62] to simulate mixing of the two endmember waters identified in the above-mentioned geochemical analyses (see Methods for full description of PHREEQC models). Monomineralic opal layers represent periods of amorphous Si saturation, which can occur in subglacial environments through cryoconcentration[63]. Supplementary figure 6 shows a set of PHREEQC simulations that demonstrate opal saturation during freezing of a $CaCl_2$ brine, where, unlike the result predicted from any other surface waters, the deficiency of carbon in the brine precludes calcite precipitation. Since geochemical data suggest calcite precipitation from an oxidized, carbon-rich, and isotopically

distinct glacial meltwater, we explore conditions under which calcite saturates upon mixing with plausible compositions of EAIS basal meltwater with $CaCl_2$ brine. Mixing the Casey Station jökulhlaup water with opal-forming brines, we identify a strong supersaturation in calcite over a broad range of mixing proportions (Supplementary Fig. 7), and a cessation of opal precipitation consistent with discrete calcite pulses during mixing. While we have explored alternative formation mechanisms in supplementary note 2, our preferred interpretation of the combined geochemical, isotopic, and modeling results is that freeze-flush cycles in sub-EAIS drainage system drive the alternating opal-calcite precipitation at the base of the ice sheet.

1.3.3 Millennial-Scale Ice Sheet Variability

The key finding from our subglacial precipitate archive is that millennial-scale ocean-atmosphere-cryosphere teleconnections trigger geochemical and hydrologic responses beneath the EAIS, where AIM warm phases drive enhanced delivery of interior subglacial meltwaters to the ice sheet margin. Subsequent millennial cold phases promote upstream expansion of basal freezing along the margins, decreasing the hydrologic connectivity and enabling cryoconcentration within remnant subglacial liquids to the point of opal precipitation. We illustrate how millennial climate cycles may lead to shifts in subglacial hydrologic connectivity using a Reduced Complexity Model of Ice Sheet Thermodynamics (RCMIST; Supplementary note 3). Switches between subglacial melting and freezing are controlled by the basal thermal energy balance, which is comprised of two heat sources: geothermal heat and shear heating,

and one sink: conductive heat loss. Therefore, one of these three parameters must change on millennial timescales to elicit the observed hydrologic response. There is no physical reason for geothermal heat flow to vary on millennial timescales, hence we treat it as invariable. Variation in surface temperature accompanying AIM cycles could affect conductive heat loss, but the ~1500 m of ice in the sample source areas[64] would severely dampen these signals and cause a significant time lag for their transfer to the ice sheet bed (Supplementary note 3). Thus, we infer that shear heating is the most promising mechanism for driving millennial-scale freeze-flush cycles.

Following the simplifying assumption that shear heating can be attributed to ice motion at or near the basal interface[65], we identify two glaciologic variables – ice surface slope and ice thickness – that both drive shear heating and can change on millennial timescales. Changes in ice surface accumulation can drive ice thickening and basal melting during millennial warm phases, and ice thinning and basal freezing during millennial cold phases. However, ice cores proximal to our sample collection sites show a minimal change in accumulation rate above their noise floor of ~0.01m/yr during AIM cycles[66–69], and detailed records from ice proximal to EM show no change in accumulation during AIM events at the end of the last glacial period[70]. The only millennial-scale variations in accumulation rates clearly resolved in ice core records occur in WDC[71], which is influenced by maritime climate and is not representative of our two sample collection sites located at the edge of the EAIS polar plateau. Therefore, we discount the accumulation-driven model as an unsatisfactory explanation for our observation and favor the ice-dynamical mechanism to explain the observed millennial-

scale subglacial hydrologic response (Supplementary note 3). Ice sheet models[24] show that the tendency for the ice sheet to thicken during warm periods with higher accumulation rates (e.g., interglacials) is overcome by an increase in the dynamic ice thinning associated with grounding line retreat in response to Southern Ocean warming. The dynamic effect driving ice sheet evolution in response to ocean thermal forcing on grounding lines is incorporated into our simplified model of shear heating through the ice surface slope, which steepens when the ice in the Ross Embayment thins during grounding line retreat (AIM warm phases) and becomes shallower when ice sheet thickness in the Ross Embayment increases during grounding line advances (millennial cold phases). Our model framework assumes that ice thickness at the foothills of the TAM, which is by itself driven by the position of the grounding line in the Ross Embayment, is a linear function of the isotopic records of climate from either WDC (MA113) or EDC (PRR50489) ice cores (Fig. 2d; Fig. 3d). Changes in this ice thickness feed into variations in ice surface slope, basal shear stress, ice velocity, and basal shear heating, which affect the basal heat budget in the TAM.

Calculated basal freezing/melting rates in the two inferred regions of sample formation provide a satisfactory visual match to the radiometrically dated records of calcite and opal precipitation from PRR50489 and MA113 (Fig. 2; Fig. 3). This result is consistent with linear sensitivity of ice thickness in the Ross Embayment to the climatic variations reflected in isotope proxies in AIS ice core records, which are dominated by variability in ocean conditions with additional impacts of atmospheric temperature changes[72]. Scaling laws for ice sheet volumes[73] indicate a high sensitivity

of ice volume to ice thickness changes, implying that the volume of AIS exhibited non-linear sensitivity to the millennial-scale climate forcing recorded in Antarctic ice cores. Collectively, our paired ice sheet thermodynamic simulations and precipitate records demonstrates that the ice on the EAIS side of the Ross Sea experiences significant thickness and volume fluctuations not only in response to large climate warming events during glacial terminations, but also in response to climate cycles that are both smaller in amplitude and shorter in duration than major terminations, such as AIM events. Ice thickness changes forced by orbital variations in global temperature[74] may amplify this subglacial hydrologic response beyond what is observed from our subglacial precipitate record, which does not include a glacial termination.

To produce basal freeze-melt cycles that are temporally correlated with precipitate opal-calcite transitions (Fig. 2; Fig. 3), the RCMIST requires changes to ice thickness of a few hundred meters at the foothills of TAMs (e.g., near the mouth of the valley containing David Glacier for PRR50489) (Supplementary Fig. 1; Supplementary Fig. 2), a small fraction of the ~1 km of post-LGM ice drawdown in the TAMS[75,76]. This forcing propagates through outlet glaciers on a timescale of 1 kyr, causing ice thickness changes of dozens of meters in precipitate source area at the edge of the EAIS plateau (Supplementary note 3). Ice sheet model runs simulating AIS response to millennial-scale ocean-thermal forcing support the possibility of thickness change on this scale throughout the Late Pleistocene[24]. Our results imply that ice around the Ross Embayment exhibits a high sensitivity to millennial-scale ocean thermal forcing during both glacial and interglacial background climate states. On this basis, ice drawdown of

a magnitude ca. 10-20% of the total LGM to modern thinning[75,77] are possible during AIM events throughout the Late Pleistocene. While dating uncertainties in AIS precipitates prevent us from assessing leads or lags in ice response to climate forcing, the agreement between opal-calcite transitions and Southern Hemisphere millennial climate cycles implies synchroneity (within dating uncertainties between 1-3 kyr) between millennial climate cycles and ice sheet thickness changes.

Results from our RCMIST indicate that opal-calcite transitions are triggered by ice velocity changes generated by ocean-atmosphere teleconnections. Rather than a linear response to smooth climate forcing, the precipitate record describes millennial-scale ice sheet motion governed by thresholds in ocean and atmospheric temperature, corroborating numerical models for ice sheet behavior in AIS embayments[78]. Although many unconstrained physical parameters of the ice sheet system make direct quantification of climate thresholds beyond the scope of this manuscript, we can compare opal-calcite timeseries data with ice core records to place approximate bounds on the climate state required to elicit a millennial-scale ice sheet response. Our RCMIST simulations describe a minimum ice sheet thickness change –which corresponds with a value in ice core isotopic records– needed to generate a millennial-scale subglacial hydrologic response (Supplementary Eq. 4; Supplementary Fig. 9; Supplementary Fig. 10). We test the viability of this approximate climate threshold value (Fig. 2c and Fig. 3d), by calculating the probability of calcite precipitation above it and opal precipitation below it. For a record completely unrelated to climate threshold forcing, there will be an equal probability of calcite or opal above or below the climate

threshold, resulting in a 50% success rate. Samples MA113 and PRR50489 return 97% and 85% match respectively, between calcite above the climate threshold and opal below it. This consistent relationship corroborates the idea that climate forcing is responsible for opal-calcite transitions, and points to a dynamic ice sheet response to threshold climate forcing as the triggering mechanism of ice sheet velocity and volume changes.

1.4 Discussion

The results presented here indicate that two rock samples each consisting of opal and calcite layers, separated by ~900km, and deposited tens of thousands of years apart, formed because of cyclic subglacial hydrologic processes that match the patterns of Southern Ocean and Antarctic climate changes recorded in ice cores, implying a link between AIS basal conditions and Southern Hemisphere climate. More specifically, the sites of precipitate formation oscillated between the freezing of local brines sourced from the proximity of the TAM during cold periods, and the influx of far field EAIS meltwaters during warm periods. Predictions of modern subglacial thermal conditions[79,80] indicate that large portions of the EAIS are at, or near the pressure melting point, with widespread melting in the ice sheet interior and freezing along the ice sheet periphery (Fig. 1a). Comparisons between simulations of modern basal melt rate[80] and precipitate collection sites (Fig. 1b, c) indicate that both PRR50489 and MA113 are found within 10 km of the regional boundary between basal freezing and melting predicted by an ice sheet model with 5-km horizontal resolution[80]. Given the

evidence suggesting that the depositional area of the precipitates was within 10 km of their collection sites, PRR50489 and MA113 likely formed close to this subglacial freeze-melt boundary. We therefore propose that the cycles of basal melting and freezing indicated by opal-calcite precipitates are the result of migrations of the basal thermal and hydrologic boundary, causing changes in the connectivity between waters from the interior and edge of the ice sheet following millennial-scale climate cycles (Fig. 6). This finding suggests that the subglacial hydrologic response to climate forcing propagates from near ice sheet margins to the ice sheet interior during climate change events.

Based on our RCMIST, the most parsimonious explanation for changes in subglacial hydrologic connectivity is acceleration of ice flow during AIM phases. The driving mechanism for ice sheet acceleration on these timescales is generally regarded to be grounding line migration stemming from ocean thermal forcing on ice shelves and grounding lines[81]. During millennial cold periods, grounded ice advances towards the continental shelf edge. As the bipolar seesaw takes effect, the ocean-atmosphere teleconnection between slowing AMOC and strengthening Southern Hemisphere westerly winds drives upwelling of relatively warm circumpolar intermediate waters[72], which contact ice shelves and grounding lines. Ice shelf thinning reduces back stress and increases ice discharge across the grounding lines[19], leading to gradual catchment-scale ice flow acceleration[22]. Corresponding ice thinning starts near grounding lines and propagates upstream, leading to steepening of surface slopes and increased driving and basal shear stress. Higher ice flow rates and basal stress increase basal shear

heating, which triggers enhanced basal melting and subglacial hydrologic connectivity. Proxy records for Southern Ocean sea surface temperature[82] and upwelling[83] provide evidence for millennial scale variations in-phase with the bipolar seesaw. This finding suggests that Antarctic ice volume is sensitive to ocean forcing on millennial timescales during all background climate states, providing a conceptual framework for assessing future ice mass loss and for interpretating distal evidence for sea-level high stands during Quaternary warm climate periods[84].

The basal thermal regime of AIS outlet glaciers is highly complex, with models demonstrating along-flow transitions between frozen and unfrozen basal conditions resulting from variations in bed topography, ice thickness, and flow rate along the ice flowlines[85]. While we acknowledge that localized basal temperature change could affect precipitate mineralogy, the collective geochronological and geochemical dataset presented here strongly favors hydrologic cycles driven by regional, rather than local, ice response. The consistent relationship between subglacial transitions from freezing to melting recorded at two distant locations over a combined timeframe of over 100 kyr requires a highly regular triggering mechanism that is linked to the broader climate system. On both a glacier and regional scale, temporal fluctuations between basal freezing and melting in the regions immediately upstream of these sample locations necessitate a change in ice sheet dynamics, as atmospheric temperature change could not propagate to the ice sheet base on millennial timescales (Supplementary note 3) and millennial-scale variations in surface accumulation are either nil[66–69] or temporally inconsistent[71]. This requisite dynamic ice sheet response implicates grounding line

migration and ocean forcing as the preferred mechanism for the observed millennial-scale subglacial hydrologic changes regardless of spatial extent. Based on the locations of the two chemical precipitates studied here, an ocean-cryosphere teleconnection must operate in two ice catchments that are separated by ~900 km and are not part of the same ice drainage basin, pointing to an embayment-wide ice mass and grounding line fluctuation on millennial timescales. Geochemical evidence for millennial-scale flushing of dome-like meltwaters to marginal locations (Fig. 4) suggests that ice sheet acceleration in response to ice shelf perturbation enhances hydrologic connectivity between subglacial waters separated by hundreds of kilometers. Given these spatiotemporal constraints, we conclude that opal-calcite transitions in subglacial precipitates result from millennial-scale migration of the regional freeze-melt boundary beneath grounded ice around the Ross Embayment.

The strength of AMOC is modulated by Northern Hemisphere ice volume and global CO_2, such that millennial climate cycles achieve maximum magnitude and frequency during intermediate climate conditions, and are weak during peak glacial or interglacial periods[35]. Current records of AIS mass loss on millennial timescales[36–38] are interpreted to result from Southern Ocean forcing. Yet, these records are confined to glacial terminations leaving it unclear whether ocean temperature drives AIS mass loss outside of orbitally driven warm periods, and whether lower magnitude interglacial ocean forcing can elicit an AIS response. The subglacial precipitate record and modeling efforts presented here suggest that subglacial hydrologic changes, and ice mass variation are triggered by grounding line migration and ice thickness changes at

the mouth of TAM outlet glaciers in the Ross Embayment. This dynamic ice response requires a high sensitivity of the AIS to ocean thermal forcing regardless of the background climate state, suggesting that ice at the Antarctic margins responds dynamically when a threshold in ocean forcing is reached. Archives of Southern Ocean upwelling rate demonstrate changes in upwelling intensity during both millennial and orbital cycles[83], driving contemporaneous ocean temperature cycles[82]. Our results, when combined with models for AIS loss during glacial terminations[21], demonstrate that resulting ocean thermal forcing drives ice loss that trumps any increases in accumulation rates, exerting dominant control of over ice dynamics and mass balance on both millennial and orbital timescales.

1.5 Methods

1.5.1 Subglacial precipitate opal-calcite timeseries

Time series describing mineralogic shifts between opal and calcite in two subglacial precipitates are derived from ^{234}U-^{230}Th ages combined with elemental characterization (Supplementary methods). Accuracy of the uranium method is evaluated using Uranium standard NBS4321 (Supplementary Fig. 8). To construct the stratigraphic age model for each sample, we input sample height and ^{234}U-^{230}Th dating dates into a Bayesian Markov chain Monte Carlo model that considers the age of each layer and its stratigraphic position within the sample to refine the uncertainty of each date using a prior distribution based on the principal of superposition[46]. Elemental maps showing calcium and silicon concentration (Fig.2a; Fig. 3a, b) were produced using Energy

Dispersive X-ray Spectroscopy (EDS) measured on the Thermoscientific Apreo Scanning Electron Microscope (SEM) housed at UCSC. EDS data were generated using an Oxford Instruments UltimMax detector and were reduced using AZtecLive software. To quantify the opal-calcite transitions in the samples, Si and Ca concentration data were produced from line scans across precipitate layers (Fig. 2a; Fig. 3a,b). For sample MA113, detritus within two calcite layers results in Si peaks that do not correspond to opal. These areas are identified by high aluminum concentrations and are corrected to reflect a calcite composition. Timeseries in figure 1a and 1d were then generated by plotting the Bayesian stratigraphic age model, against Ca concentration spectra. The linear relationship between the opal-calcite timeseries and ice core climate proxies implies synchroneity between precipitate mineralogic changes and Southern Hemisphere millennial climate. However, dating uncertainties in our U-series ages are on the order of 1kyr and in the ice core record are ~0.5kyr [86], thus we are not able to quantify sub-millennial leads or lags between the AIS response and climate cycles. Nonetheless, stratigraphic consistency between dated layers, the regular frequency of mean ages, and the significant correlation between our mineralogic timeseries and climate proxy records supports our conclusion of a link between climate teleconnections and subglacial hydrology. Furthermore, as was previously mentioned, calcite layers form rapidly upon introduction of carbon-rich, alkaline waters from the EAIS interior to the marginal system, and the system then slowly transitions back to opal precipitation after hydrologic connectivity is shut off and the waters freeze. Therefore, it is possible that there is missing time between calcite layers that is not

accounted for in stratigraphic age models. However, based on the regularity of opal depositional cycles, and the similarity between precipitate opal-calcite cycles and climate proxies, these unconformities do not represent enough time to disrupt the millennial-scale cyclicity of the precipitate mineralogy.

Correlation between opal-calcite timeseries from both samples and ice core climate records is assessed both visually, and by testing the probability that opal-calcite transitions respond to the crossing of a climate threshold. Although the link between subglacial hydrologic events and Southern Hemisphere climate cycles is the result of a complex ocean-atmosphere-cryosphere feedback, stacked records reveal a clear overlap between the mineral transitions in precipitates and ice core climate proxies on a millennial timescale (Fig. 2b, c; Fig. 3c, d). We test the relationship between climate forcing and subglacial precipitate mineralogic transitions by setting a climate threshold based on the minimum ice thickness change required to elicit a millennial-scale response in the subglacial environment as described by our RCMIST (Supplementary Eq. 4). We then calculate the probability that calcite is precipitated at temperatures above this threshold and opal is precipitates at temperatures below it. As a first step in this threshold calculation, we use a Monte Carlo simulation to randomly create 10,000 possible sample accumulation histories within the uncertainty bounds defined by our age models. We identify a best fit precipitate timeseries based on which accumulation model results in the best match of calcite above and opal below the defined temperature threshold.

1.5.2 Stable Isotopic Analyses

Carbonate isotope ratios ($\delta^{13}C_{CO3}$ and $\delta^{18}O_{CO3}$) were measured by UCSC Stable Isotope Laboratory using a Themo Scientific Kiel IV carbonate device and MAT 253 isotope ratio mass spectrometer. Referencing $\delta^{13}C_{CO3}$ and $\delta^{18}O_{CO3}$ to Vienna PeeDee Belemnite (VPDB) is calculated by two-point correction to externally calibrated Carrara Marble 'CM12' and carbonatite NBS-18[87]. Externally calibrated coral 'Atlantis II'[88] was measured for independent quality control. Typical reproducibility of replicates was significantly better than 0.05 ‰ for $\delta^{13}C_{CO3}$ and 0.1 ‰ for $\delta^{18}O_{CO3}$.

To measure organic carbon isotope ratios ($\delta^{13}C_{org}$), inorganic carbon (IC) was extracted with 1M buffered acetic acid (pH 4.5), followed by repeated water rinses to completely remove the buffered acetic acid and residual cations from the sample IC. These IC-extracted sample residues were then freeze-dried, weighed, encapsulated in tin, and analyzed for carbon (C) stable isotope ratios and concentrations by the University of California Santa Cruz Stable Isotope Laboratory using a CE Instruments NC2500 elemental analyzer coupled to a Thermo Scientific DELTAplus XP isotope ratio mass spectrometer via a Thermo-Scientific Conflo III. Measurements are corrected to VPDB for $\delta^{13}C$. Measurements are corrected for size effects, blank-mixing effects, and drift effects. Typical reproducibility is significantly better than 0.1 ‰ for $\delta^{13}C_{org}$.

Opal layers were analyzed at the Stanford University Stable Isotope Biogeochemistry Laboratory for $\delta^{18}O_{SIO2}$ by conventional BrF_5 fluorination (e.g. refs. [89,90]) and measured with O_2 gas as the analyte on a Thermo Scientific MAT 253+ dual-inlet isotope ratio mass spectrometer (IRMS)[91,92]. Briefly, 2-3 mg opal samples were

loaded into nickel reaction tubes and heated for 2 hours at 250 ºC at high vacuum. Samples were then repeatedly pre-fluorinated at room temperature with 30 mbar aliquots of BrF_5 until <1 mbar of non-condensable gas was present. A 30x stoichiometric excess of BrF_5 was added to the nickel tubes and sealed. The nickel tubes were then heated at 600 ºC for 16 hours to quantitatively produce O_2. The generated O_2 gas is then sequentially released into the cleanup line, cryogenically cleaned and frozen onto a 5Å mole sieve trap immersed in liquid nitrogen, equilibrated at room temperature with the IRMS dual-inlet sample-side bellows and measured for $\delta^{18}O$ against a reference tank of known $\delta^{18}O$ composition (24.3‰). Opal $\delta^{18}O$ is reported based on daily corrections made to four primary silicate standards (NBS-28, UWG-2, SCO and L1/UNM_Q, which are quartz, garnet, olivine and quartz, respectively), spanning ~13‰, and have been recently calibrated to the VSMOW2-SLAP2 scale[90,93]. Three secondary standards (BX-88 (Stanford Laboratory internal standard), UCD-DFS (obtained from H. Spero, UC Davis; values reported in ref. [94]) and PS1772-8 (obtained from J. Dodd, Northern Illinois University; measured at U. of New Mexico and reported in ref [95], which are quartz, opal-CT and opal-A, respectively) were also analyzed over the course of the analyses. Replicate measurements of standards demonstrate reproducibility of <0.3‰ for all secondary and primary standards except the PS1772-8 standard, though heterogeneity in this standard is suspected with laboratory averages reported in the literature[95] ranging from 40.2 to 43.6‰ (average value of 41.5‰ in this study).

Carbonate isotope ratios ($\delta^{13}C_{CO3}$ and $\delta^{18}O_{CO3}$) were measured by UCSC Stable Isotope Laboratory using a Themo Scientific Kiel IV carbonate device and MAT 253 isotope ratio mass spectrometer. Referencing $\delta^{13}C_{CO3}$ and $\delta^{18}O_{CO3}$ to Vienna PeeDee Belemnite (VPDB) is calculated by two-point correction to externally calibrated Carrara Marble 'CM12' and carbonatite NBS-18[87]. Externally calibrated coral 'Atlantis II'[88] was measured for independent quality control. Typical reproducibility of replicates was significantly better than 0.05 ‰ for $\delta^{13}C_{CO3}$ and 0.1 ‰ for $\delta^{18}O_{CO3}$.

To measure organic carbon isotope ratios ($\delta^{13}C_{org}$), inorganic carbon (IC) was extracted with 1M buffered acetic acid (pH 4.5), followed by repeated water rinses to completely remove the buffered acetic acid and residual cations from the sample IC. These IC-extracted sample residues were then freeze-dried, weighed, encapsulated in tin, and analyzed for carbon (C) stable isotope ratios and concentrations by the University of California Santa Cruz Stable Isotope Laboratory using a CE Instruments NC2500 elemental analyzer coupled to a Thermo Scientific DELTAplus XP isotope ratio mass spectrometer via a Thermo-Scientific Conflo III. Measurements are corrected to VPDB for $\delta^{13}C$. Measurements are corrected for size effects, blank-mixing effects, and drift effects. Typical reproducibility is significantly better than 0.1 ‰ for $\delta^{13}C_{org}$.

Opal layers were analyzed at the Stanford University Stable Isotope Biogeochemistry Laboratory for $\delta^{18}O_{SIO2}$ by conventional BrF_5 fluorination (e.g. refs. [89,90]) and measured with O_2 gas as the analyte on a Thermo Scientific MAT 253+ dual-inlet isotope ratio mass spectrometer (IRMS)[91,92]. Briefly, 2-3 mg opal samples were

loaded into nickel reaction tubes and heated for 2 hours at 250 ºC at high vacuum. Samples were then repeatedly pre-fluorinated at room temperature with 30 mbar aliquots of BrF_5 until <1 mbar of non-condensable gas was present. A 30x stoichiometric excess of BrF_5 was added to the nickel tubes and sealed. The nickel tubes were then heated at 600 ºC for 16 hours to quantitatively produce O_2. The generated O_2 gas is then sequentially released into the cleanup line, cryogenically cleaned and frozen onto a 5Å mole sieve trap immersed in liquid nitrogen, equilibrated at room temperature with the IRMS dual-inlet sample-side bellows and measured for $\delta^{18}O$ against a reference tank of known $\delta^{18}O$ composition (24.3‰). Opal $\delta^{18}O$ is reported based on daily corrections made to four primary silicate standards (NBS-28, UWG-2, SCO and L1/UNM_Q, which are quartz, garnet, olivine and quartz, respectively), spanning ~13‰, and have been recently calibrated to the VSMOW2-SLAP2 scale[90,93]. Three secondary standards (BX-88 (Stanford Laboratory internal standard), UCD-DFS (obtained from H. Spero, UC Davis; values reported in ref. [94]) and PS1772-8 (obtained from J. Dodd, Northern Illinois University; measured at U. of New Mexico and reported in ref [95], which are quartz, opal-CT and opal-A, respectively) were also analyzed over the course of the analyses. Replicate measurements of standards demonstrate reproducibility of <0.3‰ for all secondary and primary standards except the PS1772-8 standard, though heterogeneity in this standard is suspected with laboratory averages reported in the literature[95] ranging from 40.2 to 43.6‰ (average value of 41.5‰ in this study).

1.5.3 Sr Isotopic Analysis

Sr isotopic measurements were made at the UCSC Keck Isotope Laboratory. Sr compositions are measured on a TIMS in a one sequence static measurement: ^{88}Sr is measured on the Axial Faraday cup, while ^{87}Sr, ^{86}Sr, ^{85}Rb, and ^{84}Sr are measured on the low cups. Accuracy of the $^{87}Sr/^{86}Sr$ measurements is evaluated using Sr standard SRM987 compared to a long-term laboratory average value of 0.71024, with a typical reproducibility of ±0.00004.

1.5.4 LA ICP-MS Methods

Laser ablation inductively coupled plasma–mass spectrometry (LA ICP-MS) analyses were conducted at the Facility for Isotope Research and Student Training (FIRST) at Stony Brook University. Analyses were made using a 213 UV New Wave laser system coupled to an Agilent 7500cx quadrupole ICP-MS. The National Institute of Standards and Technology (NIST) 612 standard was used for approximate element concentrations using signal intensity ratios. Laser data were reduced in iolite[96]; element concentrations were processed with the trace-element data reduction schemes (DRS) in semiquantitative mode, which subtracts baselines and corrects for drift in signal.

1.5.5 Geochemical models of mineralogic cyclicity in subglacial precipitates

To understand the conditions under which discrete pulses of opal and calcite are precipitated following cold and warm Antarctic climate periods respectively, we integrate geochemical and isotopic characterization of the precipitates to inform simulations run using the aqueous geochemical modeling program PHREEQC[62]. The

high ion concentrations of subglacial fluids necessitates the use of the Pitzer specific ion interaction approach, which allows PHREEQC to model the aqueous speciation and the mineral saturation index of brines, and has been shown to yield results[58] consistent with the subzero database FREZCHEM[97]. Our modeling approach to simulating opal-calcite transitions can be describe in three parts: 1) Identify the water composition and conditions under which opal will precipitate and calcite will not; 2) Identify the composition and volume of water required to mix with opal-forming fluids to produce calcite; 3) Utilize the $\delta^{18}O$ and $\delta^{13}C$ isotopic composition of calcite and opal, along with the known or inferred composition of mixing waters (Fig. 4) to constrain the relative volumes of brine and meltwater, thereby testing the validity of the mixing model. While the exact ionic strength of subglacial fluids and temperature of the subglacial aqueous system is unknown, we outline a plausible scenario for discrete layers of opal and calcite that fit modeled conditions at the base of the ice sheet[79], and the geochemical constraints measured in precipitates.

Opal precipitation occurs when a solution is saturated with respect to amorphous silica. Opal solubility is both temperature and pH dependent[98], with lower pH favoring precipitation. The silicon concentrations of subglacial waters[12] and mature brines that emanate from ice sheets[99] are typically tens of ppm, —values similar to other surface waters[100]— and Si concentration does not scale with total dissolved solids[101]. At these relatively low Si concentrations, saturation of amorphous silica cannot be achieved without a mechanism to concentrate Si in solution. For aqueous systems beneath an ice sheet, this mechanism is very likely cryoconcentration via subglacial freezing, which

extracts water from the cavity at the base of the ice sheet, concentrating solutes and raising mineral saturation[43,102,103]. Yet, most surface waters upon reaching saturation of amorphous silica will also be at saturation for calcite[43,103], thus not matching the discrete opal layers observed in our precipitates. This suggests that the opals form from a mature brine[101] that is relatively free of HCO_3^-. We describe mixing relationships between Sr, C, O, and U isotopic compositions, along with Ce* values, that match subglacial fluids observed beneath the EAIS. A candidate fluid that fits our compositional criteria are $CaCl_2$ brines, which occur in the McMurdo Dry Valleys (MDV) as shallow subsurface waters[104–107], deep groundwaters[58,106,108], and surface waters[109–111], most notably feeding Lake Vanda[99,112] and Don Juan Pond(DJP)[108,113,114]. Ca-Cl-rich brines also occupy regions that were previously covered by the North American[101] and Fennoscandian ice sheet[115], implying that they are a natural product of fluid isolation beneath ice sheets. Therefore, $CaCl_2$ brines are a plausible composition for brine beneath the EAIS. The most geochemically well characterized MDV brines are those that feed DJP, therefore, we explore opal precipitation by equilibrating DJP brine with ice, calcite, and opal at a range of temperatures between -5˚C to 5˚C. At full concentration, DJP brine causes melting of the overlying ice due to its exceptionally high ionic strength, resulting in significant dilution of the original solution, which inhibits opal precipitation (Supplementary Fig. 6a). Subsequent simulations of 10x and 50x diluted DJP brine over the same range of temperatures result in a gradual increase of opal saturation due to the incremental removal of water via cryoconcentration (Supplementary Fig. 6b, c). In these modeled iterations, opal

precipitation is controlled by the amount of water removed from the solution by freezing, which itself is controlled by ionic strength. At 10x concentrated, the solution does not freeze enough to drive opal precipitation, while opal is precipitated from the 50x diluted solution between -3˚C and -4˚C. A fourth PHREEQC model was run equilibrating DJP brine with ice, calcite, and opal over this temperature range, indicating that opal precipitation is reached once ~75% of the water in the original solution is lost via freezing, which occurs at -3.5˚C (Supplementary Fig. 6d).

Simulation of calcite precipitation during AIM warm periods assumes that 'meltwaters' are mixed with the concentrated 'glacial brines' from part 1. The decision to model calcite precipitation using the admixture of new waters, rather than to reverse subglacial freezing, is based on the disparity in geochemistry between calcite and opal-forming waters (Fig. 4; Fig. 5). Based on the hypothesis that calcite layers form when waters from the EAIS interior are flushed to the ice sheet edge, meltwaters driving calcite precipitation are likely to have become higher in alkalinity and dissolved ions through water-rock interaction and chemical weathering of silicate minerals in the substrate during long-term storage beneath the EAIS. Calcite and opal data in $^{87}Sr/^{86}Sr$ vs $\delta^{18}O$ space provide further evidence that the two endmember waters —brine and subglacial meltwater— dissolve silicates with different provenance. Figure 4c and 4d show $^{87}Sr/^{86}Sr$ vs $\delta^{18}O$ mixing curve between opals and calcite, which indicate that the brine provides 98% of Sr to the system from a source with an $^{87}Sr/^{86}Sr$ of 0.7135, while the meltwater endmember has a far lower concentration of Sr (2 %) derived from a reservoir with an $^{87}Sr/^{86}Sr$ of 0.71. These data are consistent with a brine that weathers

silicate minerals over long periods, and a meltwater that drives silicate weathering with a very different provenance over a relatively short time duration. The $\delta^{13}C$ of the calcite (-23 ‰) (Fig. 4; Fig. 5) also provides evidence for the chemical composition of meltwaters, implying that they accumulated carbon through microbial respiration, which does not fractionate during the transition from aqueous CO_2 to HCO_3^- if 100% of the carbon undergoes this conversion. Given, the similarity between $\delta^{13}C$ composition of calcite and that of respired carbon, it is unlikely that dissolution of sedimentary carbonates took place in the meltwater, which would have added a significantly less ^{13}C-depleted source of carbon to the reservoir. This framework suggests that candidate compositions for calcite endmember fluids are waters with a similar history of subglacial exposure to glaciated sediments. The EAIS waters that best fit this description are jökulhlaup waters[60] observed near Casey Station, Antarctica. Using PHREEQC, we explore mixing of brine from part 1 with jökulhlaup waters from Casey Station[60], by simulating a range of possible mixing ratios between brine and meltwater. We infer, based on the Ca:Sr ratios from other surface water systems that contain $CaCl_2$ brine, that the ratio of Ca concentration between the brine and meltwater matches the ratio of Sr concentration between the two fluids (brine:meltwater = 98:2). Results show that without at least 30% meltwater the mixture too diluted with respect to Ca and HCO_3^- to precipitate calcite. PHREEQC mixing models successfully produced discrete pulses of calcite with mixtures between 30% and 80% meltwater; conditions under which the admixture is undersaturated with respect to opal because the solution is too dilute with respect to Si and is supersaturated with respect to calcite

leading to precipitation (Supplementary Fig. 7). Therefore, the addition of carbon-rich, alkaline meltwaters to opal precipitating, Ca-Cl-rich brines can trigger calcite supersaturation driving rapid calcite growth, consistent with our geochronologic outputs and calcite morphology. Collectively this modeling effort, along with the timescale data presented in figures 2 and 3, and the fibrous crystal textures, suggests that calcite forms rapidly after meltwaters are added to the subglacial aqueous system. However, the relative volume of meltwater added is unclear from these results alone and requires further isotopic constraints outlined below.

For both the calcite and opal oxygen isotope data, the formation water $\delta^{18}O$ (Fig. 4; Fig. 5) is calculated using the appropriate equilibrium water-mineral fractionation factors assuming a temperature (T) of 0˚C (273.15K). For calcite we use the empirical $1000\ln\alpha$ versus $1/T$ relationship of[116] and for opal the $1000\ln\alpha$ versus $1/T^2$ relationship of[117] for T in kelvin. The $1000\ln\alpha$ values for calcite and opal are 33.6‰ and 44.2‰, respectively, and we calculate the formation waters avoiding the non-linearity associated with delta notation far from the standard of choice (in this case VSMOW). As such, we calculate the formation waters composition as: $\alpha = (1000+\delta^{18}O_{mineral})/(1000+\delta^{18}O_{water})$.

Calcite data, in $\delta^{13}C$ vs $\delta^{18}O$ space, define a trend that suggests they form through admixture with an ^{13}C- and ^{18}O-depleted water. The carbon concentration dependent mixing curve that best fits that calcite data alone requires that the isotopically depleted endmember, what we'll refer to here as the meltwater endmember carries a higher DIC than the isotopically heavier water, which we'll now refer to as the brine endmember.

In figure 4, we assume that isotopically heaviest opals record the $\delta^{18}O$ composition of the brine endmember and that the $\delta^{13}C$ composition matches marine carbon derived from the substrate (-0 ‰), the latter of which is recorded by sodic carbonates suspected of forming from brines in the Lewis Cliff area[118]. Under such assumptions the carbon ratio between meltwater and brine is 97:3 for PRR50489 (Fig. 4a) and 80:20 in MA113 (Fig. 4b), a result that is consistent with the calcite precipitation model presented above, whereby the addition of a carbon rich, oxidized meltwater, to a reduced or intermediate $CaCl_2$ brine, triggers calcite precipitation. As shown in supplementary figure 6, the calcite data imply formation when there is >30% of meltwater in the mixture. The array of calcite data can also be fit by a mixing model that assumes an isotopically more ^{13}C-depleted carbon composition ($\delta^{13}C$ = -15 ‰). While feasible, this is a less appealing solution, as a $\delta^{13}C$ of -15 ‰ does not match the composition of any specific carbon source and would require a mixture of waters. The data presented here suggests that over the ~100ka of aggregate sample precipitation, there are two consistent endmember waters: an intermediate to reduced brine that is locally derived (star in second quadrant, Fig. 4), and an oxidized meltwater that is from the polar plateau (star in third quadrant, Fig. 4).

Acknowledgements

We thank G. Faure for his sample collection at the Elephant Moraine and A. Grunow and the Byrd Polar Rock Repository for providing sample PRR50489. We also thank Warren Sharp for a helpful pre-submission review of a previous version of this work, and G. H. Edwards and S. Hemming for insightful input. This research was

funded by the NSF graduate research fellowship, NSF 2042495, NSF 2045611, and NSF 0944578.

1.6 Figures and Tables

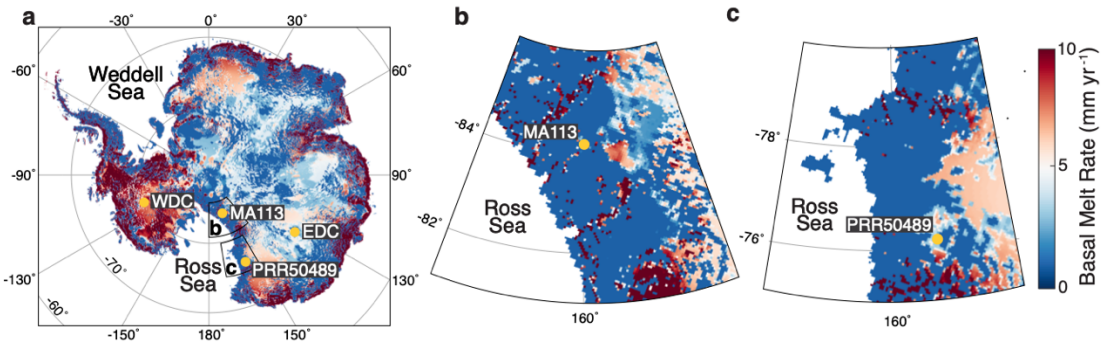

Figure 1.1: Antarctic Mean Basal Melt Rate. a. Map of estimated modern mean basal melt rate[80] truncated at 10mm yr^{-1}. **b.** Map zoomed in to show basal melt rate near location of MA113. **c.** Map zoomed in to show basal melt rate near location of PRR50489. Data sourced from: "Van Liefferinge, B. and Pattyn, F.: Using ice-flow models to evaluate potential sites of million year-old ice in Antarctica, Clim. Past, 9, 2335–2345, https://doi.org/10.5194/cp-9-2335-2013, 2013." Data licensed under: https://creativecommons.org/licenses/by/3.0/.

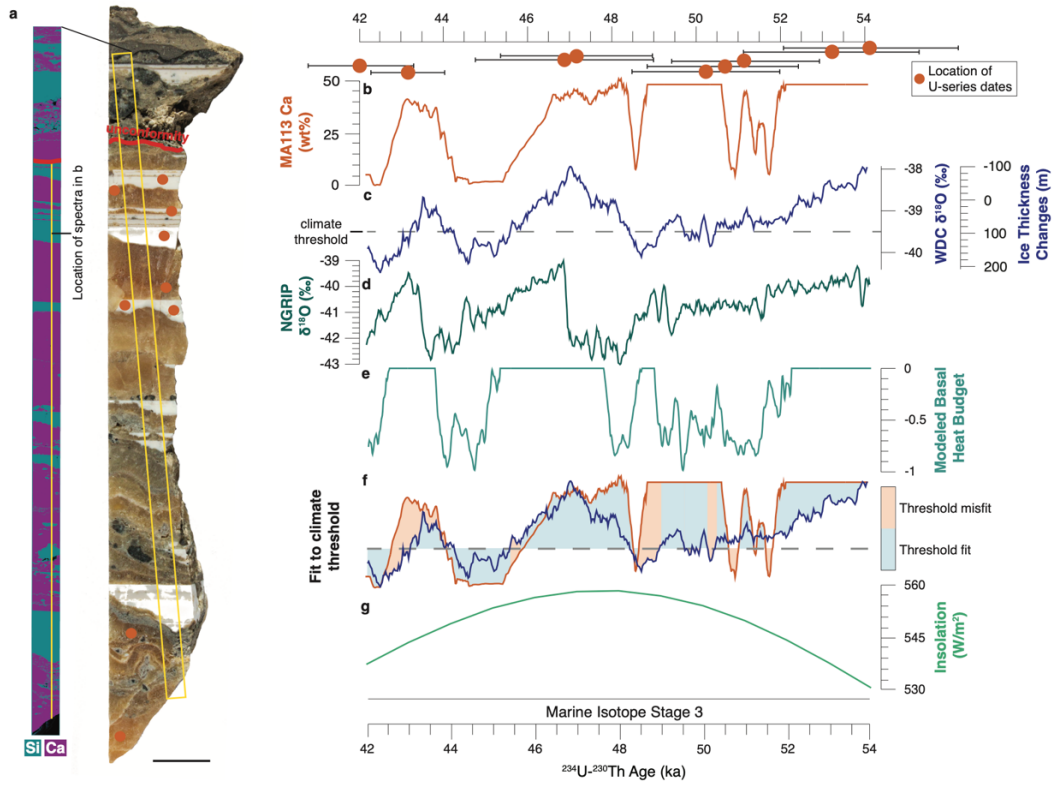

Figure 1.2: Sample MA113 SEM-EDS image and comparison to climate records. **a.** slab and SEM-EDS image of sample MA113. Scale bar is 1 cm. **b.** Ca concentration of subglacial precipitate sample MA113. High values represent calcite precipitation; low values represent opal precipitation. U-series dates include 2σ uncertainties bars. **c.** $\delta^{18}O$ measured in West Antarctic Divide Ice Core (WDC)[119]. Grey dashed line delineates threshold value for magnitude of ice thickness change necessary to elicit subglacial hydrologic response. **d**. $\delta^{18}O$ measured in Northern Greenland Ice Core Project (NGRIP)[120]. **e.** RCMIST output of basal heat budget over the formation time frame of sample MA113 in units of mm/year of equivalent basal freezing rate. Negative values indicate freezing. Positive values correspond to basal melting and are truncated at 0 mm/yr. Forcing for RCMIST is provided by ice thickness changes at the foothills of the Transantarctic Mountains, which are parameterized as a linear function of the ice core isotopic record. The magnitude and scale of these thickness changes is shown on the y-axis. **f.** Binary measure of fit between mineral cyclicity in b and climate threshold on WDC data in c. A fit is defined as points where both WDC values fall above the climate threshold and calcite is precipitated, or WDC values fall below the threshold and opal is precipitates. Otherwise, the point is considered misfit. **g.** Southern Hemisphere summer insolation (75˚S) over the period of MA113 formation**.** The record in d is synchronized to AICC2012 chronology; the record in b is synchronized WD2014 chronology. Isotope ratios are on the VSMOW (Vienna Standard Mean Ocean Water) scale.

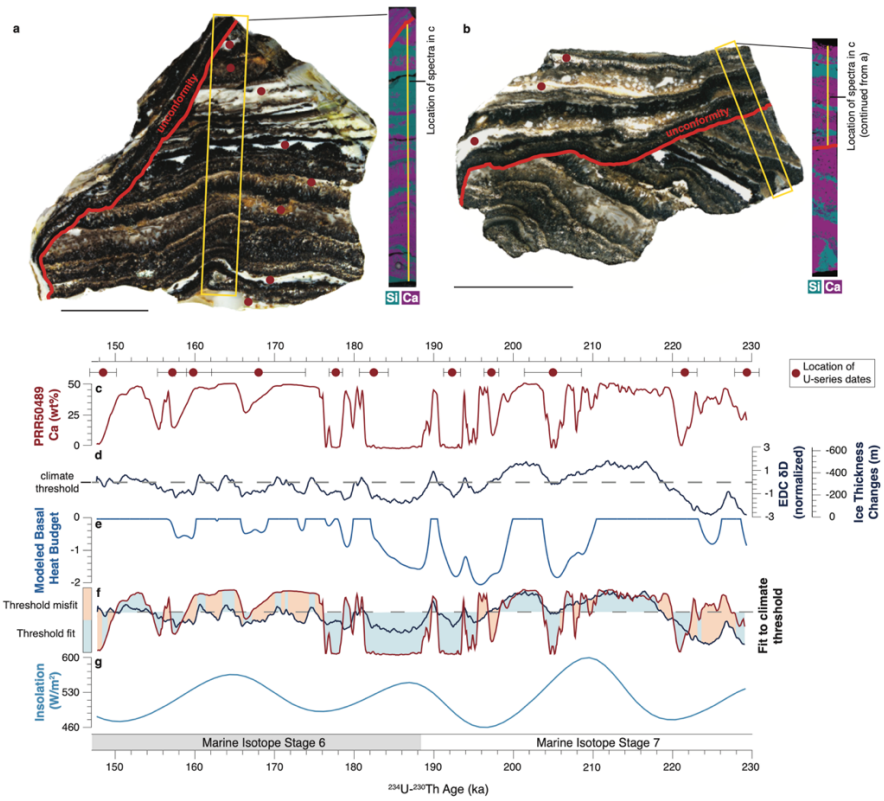

Figure 1.3: Sample PRR50489 SEM-EDS image and comparison to climate records. **a.** Slab and SEM-EDS image of sample PRR50489. **b.** Slab and SEM-EDS image of second piece of sample PRR50489. This piece of sample includes material above angular unconformity. Scale bars are 1 cm **c.** Ca concentration of subglacial precipitate sample PRR50489. High values represent calcite precipitation; low values represent opal precipitation. U-series dates include 2σ uncertainties bars. **d.** δD measured in EPICA Dome C Ice Core (EDC)[121,122]. EDC record is detrended and converted to a z-score by zero-mean normalization to eliminate orbital trends. Grey dashed line delineates threshold value for magnitude of ice thickness change necessary to elicit subglacial hydrologic response. **e.** RCMIST output of basal heat budget over the formation period of sample PRR50489 in units of mm/year of equivalent basal freezing rate. Negative values indicate freezing. Positive values correspond to basal melting and are truncated at 0 mm/yr. Forcing for RCMIST is provided by ice thickness changes at the foothills of the Transantarctic Mountains, which are parameterized as a linear function of the ice core isotopic record. The magnitude and scale of these thickness changes is shown on the y-axis. **f.** Binary measure of fit between mineral cyclicity in c and climate threshold on EDC data in d. A fit is defined as points where both EDC values fall above the climate threshold and calcite is precipitated, or EDC values fall below the threshold and opal is precipitates. Otherwise, the point is considered misfit. **g.** Southern Hemisphere summer insolation (75˚S) over the period of PRR50489 formation. Record in **d is** synchronized to AICC2012 chronology.

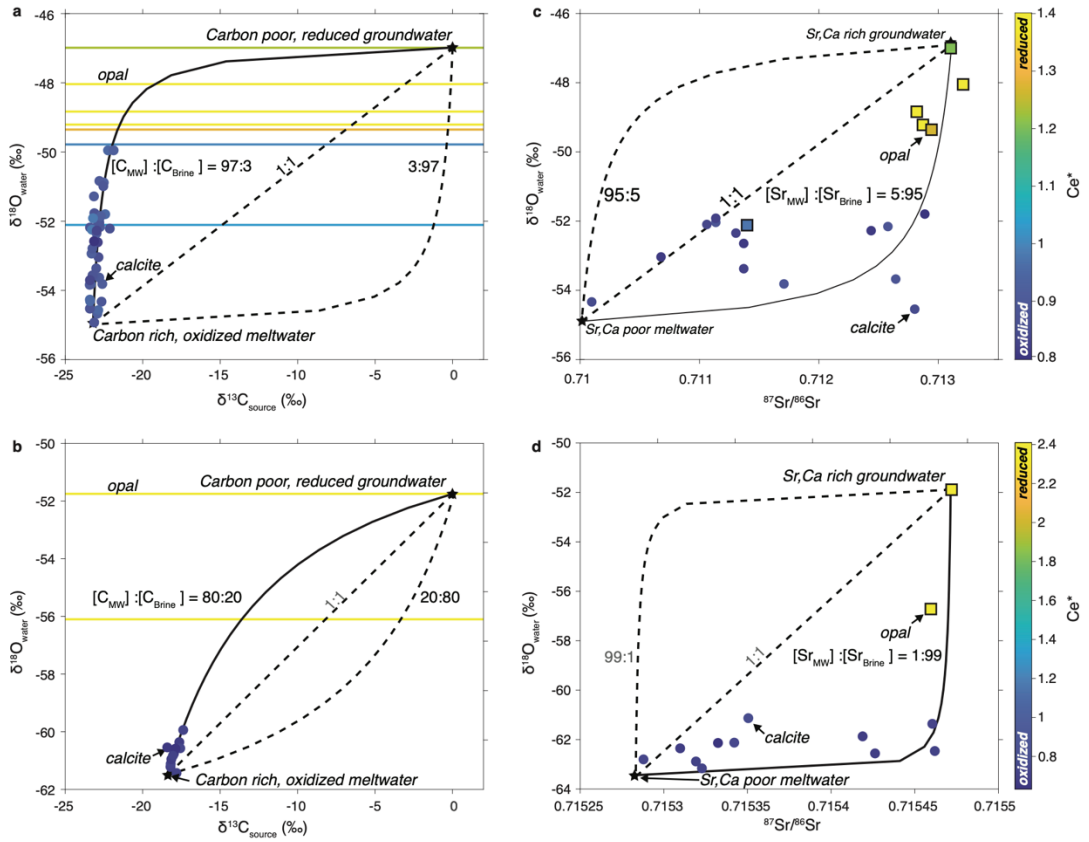

Figure 1.4: Stable isotope mixing models for precipitates PRR50489 and MA113. **a.** $\delta^{18}O$ of the precipitating fluid versus $\delta^{13}C$ composition of the C source, plotted for PRR50489 calcite and opal. Endmembers (stars) include an opal precipitating fluid that is a carbon poor, brine with lower oxygen contents; and a calcite precipitating fluid that is a carbon rich, oxidizing meltwater. Solid curved line represents mixing model between the two endmembers[123]. To fit calcite data, mixing model requires meltwater to have a total carbon concentration 40-fold higher than brine. **b.** As in **a**, but data are from sample MA113. To fit calcite data, mixing model requires meltwater to have a total carbon concentration 5-fold higher than brine. **c.** $\delta^{18}O$ of the precipitating fluid versus $^{87}Sr/^{86}Sr$ composition of the Sr source, plotted for PRR50489 calcite (circles) and opal (squares). To fit data, mixing model requires meltwater to have a total strontium concentration 20-fold lower than brine **d.** As is c, but data are from MA113. To fit data, mixing model requires meltwater to have a total strontium concentration 50-fold lower than brine. Dashed lines represent mixing models with different C or Sr ratios. All data are color coded by Ce* value, with blue being the lowest, most oxidizing values, and yellow being the highest, most reducing values. Oxygen isotopic compositions corrected to water compositions assuming equilibrium fractionation during calcite formation and a formation of 0˚C.

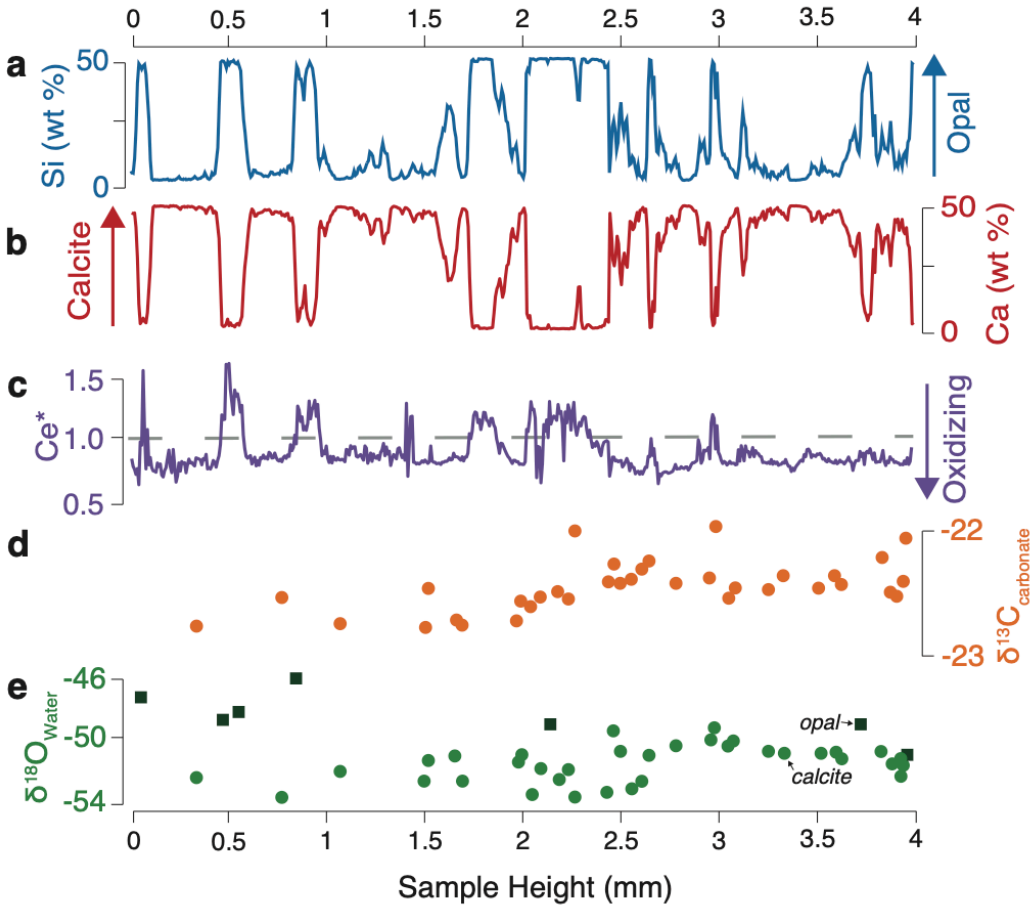

1.5: Geochemical Data from PRR50489. a. LA ICP-MS Si concentration curve **b.** LA ICP-MS Ca concentration curve **c**. LA ICP-MS Ce* curve **d**. $\delta^{13}C$ data from calcite layers **e**. $\delta^{18}O$ data from calcite and opal layers. Opal layers are represented by areas with high Si and low Ca concentrations; calcite layers have high Ca concentration and low Si concentration.

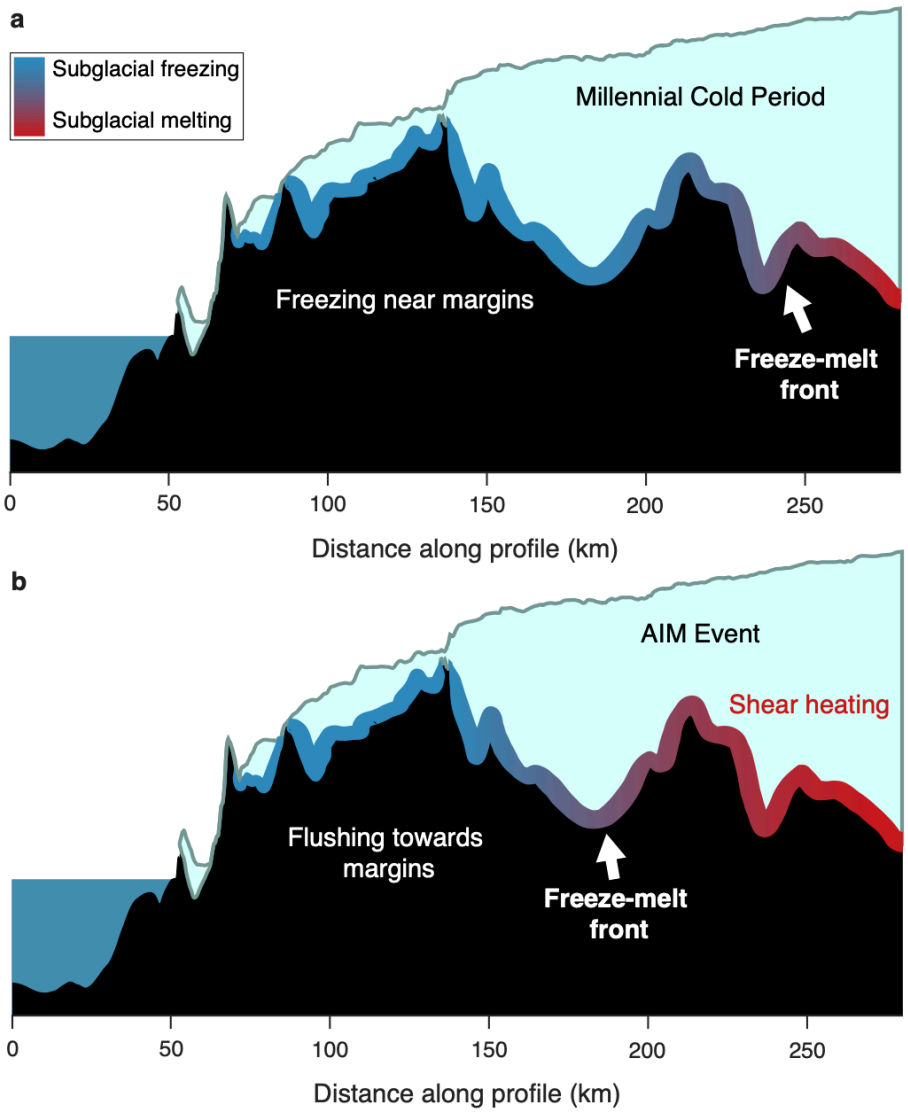

Figure 1.6: Schematic of subglacial hydrologic change during millennial climate cycles. **a.** Schematic of subglacial hydrologic systems during a millennial-scale cold period. During this time marginal aqueous systems are frozen and isolated from interior meltwater inputs. **b.** Schematic of subglacial hydrologic systems during a millennial-scale warm period (AIM). During these events accelerated ice drives basal shear heating, which allows the basal freeze-melt front to migrate towards the ice sheet margin. This process allows subglacial meltwater from the ice sheet interior to flush towards the margin. Total distance of horizontal migration of the freeze-melt front is unknown but must be >10 km based on precipitate collection location and inferred location of formation.

Table 1.1: Sr isotope compositions from samples MA113 and PRR50489

Sample Identifier	**87Sr/86Sr**	**STD err% (1 sigma)**
Opal		
MA113_Op2	7.1571E-01	1.03E-03
MA113_Op4	7.1680E-01	1.07E-03
MA113_Op5	7.1547E-01	7.01E-04
MA113_Op7	7.1562E-01	7.04E-04
PRR 50489-OpA	7.1148E-01	6.80E-04
PRR 50489-OpB	7.1365E-01	6.58E-04
PRR 50489-OpBC	7.1148E-01	6.43E-04
PRR 50489-OpC	7.1313E-01	1.35E-03
PRR 50489-OpD	7.1189E-01	6.48E-04
PRR 50489-OpF	7.1268E-01	1.74E-03
Calcite		
MA113c_0B	7.1543E-01	8.43E-04
MA113 C_0C	7.1536E-01	9.80E-04
MA113 C_0C	7.1532E-01	9.77E-04
MA113 C_0D	7.1533E-01	1.03E-03
MA113 C_0F	7.1535E-01	6.28E-04
MA113 C_1A	7.1534E-01	7.61E-04
MA113 C_1C	7.1533E-01	7.35E-04
MA113c_5B	7.1529E-01	7.21E-04
MA113c_7A	7.1544E-01	6.10E-04
MA113c_7B	7.1548E-01	6.70E-04
MA113c_8A	7.1547E-01	6.51E-04
G1_PRR50489_6	7.1145E-01	6.08E-04
G1_PRR50489_7	7.1120E-01	6.69E-04
G1_PRR5089_16	7.1274E-01	6.14E-04
G1_PRR5089_17	7.1181E-01	6.68E-04
G2_PRR5089_8	0.70897875	6.07E-04
G2_PRR5089_10	7.1009E-01	8.21E-04
G2_PRR5089_11	7.1307E-01	2.83E-03
G2_PRR5089_12	7.1071E-01	7.13E-04
G2_PRR5089_13	7.1281E-01	1.44E-03
G2_PRR5089_14	7.1112E-01	5.85E-04
G3_PRR5089_1	7.1145E-01	7.19E-04
G3_PRR5089_2	7.1120E-01	6.69E-04
G3_PRR5089_5	7.1259E-01	7.10E-04
G3_PRR5089_6	7.1181E-01	5.72E-04
G3_PRR5089_8	7.1138E-01	6.68E-04
G3_PRR5089_9	7.1298E-01	6.40E-04

Table 1.2: C and O isotope compositions from calcite layers in MA113 and PRR50489

Sample identifier	δ13C Total Carbon (‰ VPDB)	δ18O (‰ VPDB)	Yield µmol CO2	Equivalent µg CaCO3	Initial mV44	δ18O (‰ SMOW, WATER @ 273.15 K)
MA113_ 0A	-18.27	-57.59	0.79	79	17461	-60.55
MA113_ 0B	-17.63	-57.40	0.75	75	17034	-60.36
MA113_ 1B	-18.00	-56.79	0.67	67	12942	-59.75
MA113_ 2A	-17.98	-57.80	0.75	75	16944	-60.76
MA113_ 2B	-17.81	-58.47	0.85	85	18195	-61.43
MA113_ 3	-17.71	-57.61	0.82	82	17944	-60.57
MA113_ 4A	-17.92	-57.62	0.42	42	6317	-60.58
MA113_ 4B	-18.20	-58.24	0.90	90	23062	-61.20
MA113_ 4C	-18.19	-58.17	0.74	74	14123	-61.13
MA113_ 4D	-18.13	-57.97	0.70	70	12884	-60.93
MA113_ 4E	-18.06	-57.89	0.65	65	11599	-60.85
MA113_ 5	-17.38	-56.98	0.66	66	12053	-59.94
G1_PRR5089_6	-22.99	-50.39	0.81	81	17759	-53.37
G1_PRR5089_7	-22.79	-49.02	1.26	126	49045	-52.01
G1_PRR5089_8	-22.91	-48.94	1.28	128	49055	-51.93
G1_PRR5089_9	-23.00	-48.79	1.17	117	49051	-51.78
G1_PRR5089_10	-23.14	-48.30	1.28	128	49051	-51.29
G1_PRR5089_13	-23.09	-51.91	1.16	116	49058	-54.89
G1_PRR5089_14	-22.95	-51.74	1.07	107	45605	-54.72
G1_PRR5089_16	-23.18	-49.16	1.26	126	49054	-52.15
G1_PRR5089_17	-23.26	-50.82	1.24	124	49049	-53.80
G2_PRR5089_2	-22.75	-49.15	0.54	54	9590	-52.14
G2_PRR5089_3	-22.53	-48.81	0.95	95	29666	-51.80
G2_PRR5089_4	-22.82	-48.97	0.96	96	29158	-51.96
G2_PRR5089_5	-22.55	-47.91	0.53	53	9093	-50.90
G2_PRR5089_6	-22.74	-47.88	1.27	127	49085	-50.87
G2_PRR5089_7	-22.57	-47.98	1.02	102	36039	-50.97
G2_PRR5089_8	-22.78	-49.07	0.51	51	8285	-52.06
G2_PRR5089_9	-22.60	-50.84	0.36	36	5278	-53.82
G2_PRR5089_10	-22.65	-51.35	0.34	34	4792	-54.33
G2_PRR5089_12	-22.92	-50.05	0.85	85	21596	-53.03
G2_PRR5089_13	-22.90	-50.69	0.87	87	22231	-53.67
G2_PRR5089_14	-22.84	-49.10	0.38	38	5469	-52.09
G2_PRR5089_11	-22.97	-48.80	0.57	57	10472	-51.79
G2_PRR5089_1	-22.33	-49.18	0.63	63	10821	-52.17
G2_PRR5089_8	-22.23	-46.97	0.64	64	10722	-49.96

G2_PRR5089_1b	-21.87	-46.97	0.47	47	7077	-49.96
G3_PRR5089_1	-22.95	-49.66	0.62	62	7365	-52.64
G3_PRR5089_2	-22.72	-48.94	0.59	59	6887	-51.93
G3_PRR5089_3	-22.95	-51.59	0.61	61	7211	-54.57
G3_PRR5089_4	-23.22	-49.98	0.45	45	5103	-52.96
G3_PRR5089_5	-23.22	-49.28	0.63	63	7520	-52.27
G3_PRR5089_6	-23.31	-50.83	0.75	75	9192	-53.81
G3_PRR5089_7	-23.05	-48.98	0.57	57	6615	-51.97
G3_PRR5089_8	-23.02	-49.35	0.7	70	8423	-52.34
G3_PRR5089_9	-23.31	-51.56	0.69	69	8332	-54.54
G3_PRR5089_10	-23.18	-49.78	1.11	111	15746	-52.76
G4_PRR5089_1	-22.89	-49.22	1.07	107	14906	-52.21
G4_PRR5089_2	-23.11	-49.64	0.92	92	11937	-52.62
G4_PRR5089_3	-23.23	-50.59	0.71	71	8668	-53.57
G4_PRR5089_4	-23.3	-50.74	0.96	96	12725	-53.72
G4_PRR5089_5	-23.4	-51.3	1.05	105	14415	-54.28

Table 1.3: C and O isotope compositions from opal layers in MA113, PRR50489, and EMA-2.

sample + aliquot	δ18O (VSMOW)	δ18O (‰ SMOW, WATER @ T based on mixing ratio)
MA-113_Op7	-9.25	-51.75
MA-113_Op5	-14.15	-56.10
PRR 50489-A	-8.48	-52.11
PRR 50489-BBC	-5.96	-49.79
PRR 50489-C	-5.45	-49.35
PRR 50489-E	-3.04	-46.99
PRR 50489-F	-5.07	-48.83
PRR 50489-F	-5.36	-49.21
PRR 50489-G	-4.12	-48.04
EMA-2	2.86	-40.50

Table 1.4: U-series data from samples MA113 and PRR50489.

Sample ID	Analysis ID	mineral	Dist. (µm)	Th (ppm)	U (ppm)	[232Th/238U] a	2σ unc	[230Th/232Th] (measured) a	2σ unc	[234U/238U] a	2σ unc	[230Th/238U] a	2σ unc	Date (uncorrected) (ka)	2σ unc	Date (corrected) (ka) b	2σ unc b	[234/238] initial (corrected) b,c	2σ unc b
MA113	'MA113c_1A_UTH'	calcite	70140	0.02	0.31	0.018568	0.000109	48.03	0.46	2.19	0.012	0.89	0.01	54.13	0.84	53.43	0.91	2.39	0.01
MA113	'MA113_1C_UTH'	calcite	63730	0.03	0.53	0.016113	0.000025	57.02	2.90	2.20	0.003	0.92	0.05	55.81	3.54	55.22	3.56	2.41	0.01
MA113	'MA113c_4A_2_UTh'	calcite	40500	0.07	0.23	0.092957	0.000273	9.57	0.13	2.23	0.010	0.89	0.01	52.76	0.95	49.27	1.98	2.43	0.01
MA113	'MA113_Op5_UTH'	opal	36210	0.01	0.16	0.010666	0.000025	78.54	2.78	2.22	0.030	0.84	0.03	49.46	2.28	49.06	2.29	2.40	0.03
MA113	'MA113_opal_5_2'	opal	30150	0.02	0.42	0.014372	0.000134	58.95	3.85	2.26	0.011	0.85	0.06	48.95	3.91	48.43	3.92	2.45	0.02
MA113	'MA113_C5_1'	calcite	25200	0.16	0.62	0.082016	0.001209	10.16	0.17	2.28	0.012	0.83	0.02	47.46	1.32	44.43	2.01	2.46	0.01
MA113	'MA113_c5_2_UTH'	calcite	24180	0.39	1.34	0.094571	0.000117	8.64	0.11	2.23	0.006	0.82	0.01	47.61	0.72	44.02	1.92	2.41	0.01
MA113	'MA113_Op6_UTH'	opal	20120	0.02	0.23	0.023886	0.000094	33.31	1.00	2.25	0.012	0.80	0.02	45.69	1.68	44.80	1.74	2.42	0.01
MA113	'MA113c_7A_UTH'	calcite	19720	0.07	0.25	0.093237	0.000315	8.35	0.10	2.20	0.009	0.78	0.01	45.58	0.71	41.99	1.92	2.37	0.01
MA113	'MA113_Op7_UTH'	opal	16970	0.03	0.22	0.044423	0.000122	16.40	0.67	2.19	0.016	0.73	0.03	42.46	2.08	40.75	2.25	2.34	0.02
MA113	'MA113_TC_1_UTH'	calcite	150	0.00	0.71	0.000141	0.000000	3298.45	12.99	2.19	0.003	0.46	0.00	25.44	0.10	25.44	0.04	2.28	0.00
PRR50489	PRR50489_OpA	opal	2320	0.43	14.20	0.031325	0.000051	182.75	0.78	1.85	0.002	1.82	0.01	229.57	3.68	229.22	1.59	2.63	0.02
PRR50489	PRR50489_OpB	opal	6436	1.29	11.99	0.110017	0.000161	55.15	0.18	1.99	0.003	1.93	0.01	216.23	2.06	215.11	1.59	2.82	0.01
PRR50489	PRR50489_OpBBC1	opal	14563	0.24	2.94	0.084287	0.000174	73.26	1.54	2.06	0.002	1.96	0.04	205.50	7.73	204.61	3.68	2.89	0.05
PRR50489	PRR50489_OpBBC2	opal	17038	0.25	6.94	0.037265	0.000039	164.00	0.59	2.07	0.002	1.94	0.01	197.07	1.69	196.70	0.96	2.87	0.01
PRR50489	PRR50489_OpBC	opal	19081	0.11	11.94	0.009287	0.000015	667.20	3.84	2.11	0.002	1.97	0.01	194.25	2.30	194.15	1.09	2.92	0.02
PRR50489	PRR50489_C	opal	21827	0.49	6.64	0.074985	0.000368	81.94	0.63	2.10	0.003	1.95	0.02	192.64	3.00	191.89	1.87	2.90	0.02
PRR50489	PRR50489_OpCD	opal	30892	0.46	1.58	0.300760	0.001098	20.34	0.50	2.14	0.016	1.95	0.05	183.37	9.01	180.29	6.02	2.91	0.07
PRR50489	PRR50489_OpD	opal	32714	0.41	11.57	0.036599	0.000029	176.42	0.52	2.34	0.032	2.05	0.01	167.14	5.00	166.75	3.49	3.15	0.08
PRR50489	PRR50489_E	opal	34612	0.16	35.68	0.004614	0.000003	1326.04	4.22	2.30	0.002	1.95	0.01	157.42	1.00	157.37	0.75	3.02	0.01
PRR50489	PRR50489_F	opal	36547	0.21	16.24	0.013396	0.000053	456.54	4.68	2.30	0.002	1.95	0.02	157.07	3.09	156.94	1.72	3.02	0.03
PRR50489	PRR50489_G	opal	39090	0.05	15.62	0.003510	0.000010	1638.63	5.62	2.23	0.002	1.83	0.01	148.16	1.46	148.12	0.86	2.87	0.02

All calculations use the decay constants of Jaffet et al., 1971 (238U), Cheng et al., 2013 (234U and 230Th) and , Le Roux and Glendeni

Square brackets denote activity ratio

a All ratios measured with mixed 229Th-236U tracer calibrated agai

b corrected for detrital Th assuming an initial (230Th/232

c [234/238] initial is corrected for radiogenic ingrowth and decay based on the detrital-corected date

Chapter 2

Accelerated Antarctic ice loss through ocean forced changes in subglacial hydrology

2.1 Abstract

Recent changes in Southern Ocean temperature have been linked with catchment-wide Antarctic ice acceleration and loss. The ice sheet models producing future sea level projections, however, rely on controversial mechanisms to match this rapid response, possibly due to the omission of feedbacks between subglacial water pressure and ice velocity. While modern remote sensing data tie increased subglacial water pressure to punctuated (<1 yr.) ice acceleration events, it is unclear whether this feedback promotes prolonged ice acceleration, influencing ice mass balance over centennial to millennial climate events. Here we present a ten-thousand-year record of subglacial water dynamics and chemistry from ~110 ka East Antarctic calcite and sediment-bearing subglacial precipitates. Time series of sediment frequency and grain size indicate that subglacial meltwater flushing cycles correlate with Southern Ocean temperature. Similarly, shifts in calcite geochemical composition record climate-driven changes in subglacial water provenance. The synchronized and sustained (~1 ka) changes in Antarctic basal hydrology with climate support subglacial water drainage systems as having a key role in transferring the climate forcing acting on ice sheet

margins, deep into the ice sheet interior. The demonstrated coupling between subglacial water and climate clarifies the current rapid ice response to climate change in Antarctica and underscores a need and means to heighten the sensitivity of ice sheet models.

2.2 Introduction

Resolving the timescales over which ice sheets respond to climate change is a fundamental issue in current efforts to forecast the contribution of Antarctica to global sea level rise under various warming scenarios[5,124]. Pioneering work on advective, and diffusive glaciological response mechanisms indicated that within a polar ice sheet, climate-driven perturbations propagate several times faster than the ice flow velocity[125]. Given that the bulk of the Antarctic ice sheet (AIS) moves slowly[126], early numerical ice sheet models suggested that it may take up to several centuries for future climate warming to result in a significant contribution to sea level rise from Antarctica[127]. However, rapid changes observed within the AIS in the recent decades[18] do not appear to be consistent with such slow ice sheet response timescales, suggesting that some other glaciological mechanisms, such as the subglacial hydrologic system, may accelerate the response of ice sheets to climate change[128].

Remote sensing of the AIS has revealed a widespread subglacial hydrologic system consisting of saline groundwaters[129], lakes[130], and channels[131] connecting subglacial water bodies over hundreds of kilometers[132]. Drainage of Antarctic subglacial water has been mapped using satellite altimetry, which demonstrates episodic flushing over periods of months to years[133–135]. The timing and magnitude of this flushing is

controlled by the basal hydraulic potential[136], which is set mainly by the ice surface slope[136], but can also respond to changes in ice thickness and meltwater input[130]. Shallow ice-surface gradients, thick ice, and low ice flow velocities in AIS plateau result in numerous lakes that are stable over decades to millennia. Whereas beneath the AIS periphery, steeper surface slopes, thinner ice, and enhanced meltwater production via frictional melting trigger lake filling and flushing cycles over months to years[130]. One example of satellite observations at Crane Glacier along the Antarctic Peninsula describes subglacial lake discharge within years of ice-surface steepening that followed the retreat of the ice front off of a topographic ridge 6km downstream[137]. This result supports a rapid connection between basal water flushing rates and ice motion, which may provide link between climate-related ice dynamics and long-term reorganization of the subglacial hydrologic system.

On decadal[138] to millennial[139] timescales, climate forcing causes Antarctic grounding line retreat that may alter the subglacial hydrologic system by steeping the ice-surface slope, which drives ice acceleration and increases basal water supply through frictional melting[130]. Enhanced subglacial meltwater flushing following the initiation of ice motion can trigger further ice acceleration by decreasing basal traction[140] – a relationship supported by satellite altimetry data that provide several examples of ice flow acceleration induced by floods emanating from subglacial lake basins[7,141]. Additionally, discharge of buoyant subglacial meltwaters at grounding lines may enhance submarine ice melting and promote further ice retreat[142,143]. These modern observations leave open the possibility that the inclusion of realistic subglacial

water dynamics can make ice sheet response to climate change significantly faster than suggested by analytical or numerical ice sheet models that disregard it[125,127]. However, there are currently no geological records that describe the subglacial hydrologic and ice motion response to ice motion response to longer climate change, hindering evaluations of how subglacial hydrology influences Antarctic ice mass balance.

Here we present a ~10kyr archive of subglacial hydrologic changes recorded in finely laminated subglacial calcite precipitates that formed within the David Glacier system during the later stages of Marine Isotope Stage 5. High-resolution U-series age constraints paired with spectral analyses of sedimentary laminae and geochemical characterization of subglacial waters demonstrate that the periodicity of subglacial flushing events, the size of abundance of siliciclastic grains and the composition of waters all correlate with climate records that track the temperatures of the Southern Ocean. We interpret the changes in subglacial water velocity and provenance as a response to climate-driven grounding line migration. Our records support a model[9] in which the feedback between grounding-line retreat, ice acceleration and subglacial hydrologic dynamics represents an important mechanism for rapid and enhanced response of the ice sheet to climate forcing.

2.3 Results

A 10kyr archive of subglacial flushing, water dynamics and compositional change is recorded by two finely laminated accumulations of detrital silicate grains and calcite, which formed within a subglacial cavity beneath the AIS. Both samples were collected from Reckling Moraine (RM), East Antarctica, a sublimating section of exhumed basal

ice that has entrained mostly rocks from the Transantarctic Mountains, the Wilkes subglacial basin, and a small percentage of chemical precipitates formed in subglacial environments[42]. Reckling moraine is located along the ice divide separating the David Glacier catchment and an adjacent catchment that includes Mawson Glacier (Fig. 1b). Rocks deposited at RM are transported from upstream locations in horizontally flowing ice, before being exhumed as the ice flows up against the Transantarctic Mountains. Based on ice velocities and exhumation timescales of basal ice exhumation in this area of the TAM, our two subglacial precipitates likely formed within 10 km upstream of RM[139], placing their probable formation locations within the hydrologic network draining the David glacial catchment (Extended Data Fig. 1). This hydrologic system draining David glacier extends from Dome C to the Southern Ocean, and contains numerous mapped subglacial lakes of varying size[144] (Fig. 1b).

The focus of this study is on two subglacial precipitates, which consist predominantly of micron-scale laminations of clay-rich calcite that alternate with clean, columnar calcite (Fig. 2a-c; Methods). Superimposed on these recurrent laminations are layers of concentrated microcrystalline calcite containing silt to sand-sized (<250 μm) silicate grains often clustering at the base of the clay-rich calcite layers (Fig. 2d,e; Methods). The sand grains within these layers are well sorted and rounded, both hallmarks of fluvial transport and unlike the textures observed in ice deposits (Fig. 2e). These clastic layers are observed to pinch-out laterally, fining in transition, indicating unidirectional water flow (Fig. 2f). Similarly, unidirectional flow produces the observed oblique foliation in the distribution of microcrystalline calcite[145] (Fig. 2h).

Laminated couplets from RM record a hydrologic sequence similar to those recorded in cave deposits[146]: a high flow event can erode the previously deposited calcite, rounding euhedral crystals, which can be capped by layers of sand to silt sized particles within a microcrystalline calcite matrix (Fig. 2g). Assuming a water depth of 1m, the suspension of the largest particles (100-200 μm) places the high flow velocity at >1 cm s^{-1}, while the absence of any larger sand limits this flow velocity to <10 cm s^{-1}. A return to low flow produces columnar calcite that transitions from clay-rich to clean calcite (Fig. 2g). The absence of sand grains in this layer limits the water velocity of this low flow regime to < 1 cm s^{-1}. Each sedimentary layer is interpreted to represent a discrete flushing event, where water and sediment are delivered unidirectionally into the sample forming water body and is followed by a period of low water flow. The more frequent micron-scale layering of clay-rich to clean calcite represent smaller, more frequent flushing events, while the sand layers represent less frequent, higher energy flushing events. A sediment core recovered via drilling at Subglacial Lake Mercer contains similar laminations containing clay and silt couplets, which have been also interpretated to represent fill-drain events in the lake[147].

To determine the timing over which these changes in sediment delivery or subglacial water chemistry occurred, we produced ^{234}U-^{230}Th dates on the calcite from 10 and 12 horizons in each sample respectively (Methods and Extended Data Table 1). These calcite precipitation dates place the formation of each sample to 107.5 to 115.2 ka and 106.7 to 114.2ka (during MIS5e). The ^{234}U-^{230}Th date and the stratigraphic position of each dated horizon is used to produce a stratigraphic age model for each

sample using a Markov-Chain Monte Carlo approach[46] (Extended Data Fig. 2; Methods). This stratigraphic age model provides the basis with which to construct a time series of 1) the periodicity of sediment delivery (Fig. 3), 2) the abundance of sand grains (Fig. 4f) and 3) chemical or isotopic changes in calcite composition (Fig. 4c,d,e).

To construct a time series of the periodicity in sediment delivery for each sample we utilized an evolutionary FFT technique (Methods) which revealed two dominant, though time-variant frequencies that can be correlated to physical aspects of the samples (Fig. 3 and Extended Data Fig. 3). The micron-scale laminations of clay-rich and clean calcite are associated with a centennial-scale frequency (Fig. 3 and Extended Data Fig. 4). This high frequency change in sediment volume is present throughout the entire ~10 ka record of both samples, however, a consistent, high-power periodicity is only identified at two discrete time intervals: 108.5-109 ka and 112-113 ka (Fig. 3a; Fig. 4g; and Extended Data Fig. 4). The next significant frequency parsed by the FFT is 500–1000-year periodicity (Fig. 3a,e and Extended Data Fig. 4). This frequency is physically associated with a ~cm-thick cycles in the total volume of siliciclastic delivered to the water body the samples formed in (Fig. 3c,e; Extended Data Fig. 3; and Extended Data Fig. 4). In addition to changes in frequency, we measured the abundance of sand sized grains (Methods). A time series of sand abundance (Fig. 4f) also displays two prominent peaks at 108.5-109 ka and 112-113 ka. Recalling from above, that each sedimentary layer represents a discrete flushing event, we interpret this periodic record of sediment delivery as resulting from the cyclic

flushing of subglacial lakes upstream, and thus a record of lake flushing within the David Glacier catchment. These periodic, centennial-scale cycles of Antarctic subglacial water flushing are consist with drainage events previously identified in grounding line landforms on the Ross Sea continental shelf30. These apparent changes in depositional energy, including variations in frequency of delivery (Fig. 3a and 4g), changes in sediment volume (Fig. 3c) and grainsize (Fig 4f) are attributed to changes in the water velocity from the flushing of upstream lakes with different volumes. For example, the micron-scale cycles in silicate and microcrystalline calcite content are interpreted to represent relatively low energy flushing events, while an increase in siliciclastic volume and grain size indicates an increase in flushing energy. Collectively, these physical data identify two isolated time periods, at 108.5-109 ka and 112-113 ka of increased water velocity.

Chemical precipitates that form in aqueous environments under the AIS reflect the chemistry of waters from which they precipitate[43,139,148]. To characterize the precipitate parent waters, we report calcite isotopic composition ($^{87}Sr/^{86}Sr$, $^{234}U/^{238}U_i$, $\delta^{18}O$, $\delta^{13}C$) (Fig. 4c,d and Extended Data Table 2) and elemental concentrations ([U]) (Fig 4e) over the ~10ka formation interval. The isotopic composition and secular changes in chemistry are the same for each sample (PRR52588 and PRR53557), suggesting that both samples form in the same body of water, despite the apparent differences in sand volumes and precipitation rates. Beginning with the compositional absolute values, the $\delta^{18}O_{SMOW}$ (-54 to -55 ‰, assuming T= 0 °C; Extended Data Table 2; Methods) of calcite precipitate parent waters are highly depleted in ^{18}O, with $\delta^{18}O$ values between

9.4 and 14 ‰ lower than the ice measured at the nearby Taylor Dome ice core[149] and ca. 10 ‰ lower than modern precipitation near Reckling moraine[150]. Yet, because the local ice velocities place precipitate formation locations within 10km of RM, these ^{18}O compositions require that waters have flowed ~100km from the headwaters of the David glacier catchment into lakes more proximal to RM (Fig. 1). As all subglacial waters were initially basal meltwaters, we utilize a comparison between the geochemical measurements from the precipitates with Antarctic meteoric ice values as a metric for the relative age of the subglacial water and interpret changes in precipitate chemistry through time as evidence for changes in the subglacial hydrologic system. For example, the radiogenic $^{87}Sr/^{86}Sr$ compositions (>0.71) depart from meteoric glacial ice (~0.709) [151,152], indicating that these waters have chemically weathered silicate rocks during rock-water contact[153] (Fig. 4c). Similarly, the ($^{234}U/^{238}U$) (>2.6) activity ratio of subglacial waters, show that these waters are enriched in ^{234}U beyond melted glacial ice (~1.14 [154]) (Fig. 4d), which occurs through the alpha-injection of ^{234}U sourced from ^{238}U in silicate rock, also indicating long term physical contact between subglacial waters and silicate rocks[155]. Finally, calcite U concentration can be controlled by the U concentration of the water[145] and thus the degree of rock-water interaction. Therefore, elevated [U] up to ca. 40ppm are likely indicate parent waters that have experienced long-term storage in the subglacial environment.

The elemental and isotopic composition of the calcite-forming subglacial waters change over the ~10 ka time interval. Long term trends include a decrease in $^{87}Sr/^{86}Sr$, U concentrations and [$^{234}U/^{238}U$]. Superimposed on this long-term record geochemical

trend are two peaks, particularly well resolved by the higher fidelity $^{87}Sr/^{86}Sr$ and [U] time series at 108.5-109 ka and 112-113 ka (Fig. 4). During these time intervals, the calcite forming waters exhibit both higher values in $^{87}Sr/^{86}Sr$, ($^{234}U/^{238}U$) and [U] as well as the highest variability in these values. The peaks in $^{87}Sr/^{86}Sr$, ($^{234}U/^{238}U$) composition suggests an increase in the proportion of waters that have experienced longer periods rock-water contact. The higher variability in compositions across these two time periods indicates more active mixing between waters of variable compositions: likely evolved waters and fresher meltwaters. Outside of these time intervals, the compositions are both less variable, and exhibit lower values of $^{87}Sr/^{86}Sr$, [$^{234}U/^{238}U$], and [U] (Fig.4).

2.4 Discussion

The sedimentary and geochemical time series collected from the RM samples show that the dynamics and provenance of subglacial waters varied in concert with two short but prominent Antarctic warm periods at 108.5-109 ka and 112-113. To examine the relationship between millennial-scale climate variations and the response of subglacial hydrology recorded in precipitate samples we compare the sample time series with the δD at EPICA Dome C (Fig. 4a), a paleotemperature proxy that is positively correlated with the temperature of Southern Ocean waters abutting Antarctica[82]. The two peaks resolved in the sediment and geochemical data mimic the EDC climate record, aligning with millennial-scale Southern Hemisphere warm periods known as Antarctic Isotopic Maximum or AIMs (Fig. 4). These short lived, AIM warm periods are driven by combined suppression of northward heat transport by Atlantic Meridional Overturning

Circulation[25] (AMOC) and the upwelling of warm Southern Ocean deep waters induced from southward shifts in Southern Hemisphere westerlies[29]. During MIS 5d, the strong and stable nature of AMOC[35] leads to relatively small millennial scale temperature changes (yellow dashed line, Fig 4a). However, the AIMS are readily identified by: 1) their temporal association with two Dansgaard-Oeschger (D-O) events (at ~109 and ~113 ka) in Greenland temperature records (purple, Fig. 4b) which consistently occur throughout the late Pleistocene within 300 years of peak AIM warming[119]; and 2) a decomposed record of AIM events in reference to the LR04 marine record[156] (solid yellow line, Fig. 4b).

The sedimentological and geochemical data proxies for subglacial water dynamics and provenance collected from RM samples show a hydrologic response that aligns with the climatically warm AIM periods. For example, both the abundance of sand and an increase in the frequency of subglacial flooding occur during these warm periods, implying that a greater volume of water contributes to a higher water energy and more frequent filling and flushing of subglacial lakes (Fig. 4f, g). In parallel, the calcite forming waters exhibit both the highest values in $^{87}Sr/^{86}Sr$, ($^{234}U/^{238}U$), and [U], and the highest variability in compositions during AIM periods. Off-AIMs, the precipitate chemical compositions are both less variable, and exhibit lower values of $^{87}Sr/^{86}Sr$, ($^{234}U/^{238}U$), [U]. This covariation in water compositions suggests that calcites form from a mixture between two waters, and that the relative contribution from each water in the sample catchment changes in response to centennial to millennial climate events. The high $^{87}Sr/^{86}Sr$ and ($^{234}U/^{238}U$) during AIM periods indicates contribution from an

endmember water that experienced prolonged rock water contact, consistent with waters residing for long durations in a subglacial lake upstream from Reckling moraine (Fig. 1, inset). The lower $^{87}Sr/^{86}Sr$, ($^{234}U/^{238}U$), and [U] values off-AIMS, and the gradual shift to lower values over the ~10 ka sampling period, are indicative of fresher meteoric meltwater or a marine carbonate bedrock source ($^{87}Sr/^{86}Sr$ ~0.709, [$^{234}U/^{238}U$] 1.14 and $\partial^{13}C$ ~0). Mixing models fit to all measured calcite isotopic data ($\delta^{18}O$, $\delta^{13}C$, $^{87}Sr/^{86}Sr$, $^{234}U/^{238}U$) define parabolic mixing curves between these endmembers (Extended Data Fig. 5), which require the distal water to have nearly 10 times the amount of Sr, U and C —again consistent with long-term rock-water contact—while the of proximal glacial meltwater is relatively dilute with respect to C, Sr and U. Based on $\delta^{18}O$ and $\delta^{13}C$ values of this more dilute endmember, these waters could be a sourced from melting of glacial ice generated more proximal to RM by an active outlet glacier where, as suggested by ref[157], freshly comminuted sediment can contain easily dissolved marine carbonates. In summary, during the climatically warm AIM periods, calcite-forming water compositions are dominated by the presence of distal lake water that has experienced prolonged rock-water interaction. As the climate cools over the 10kyr period of sample formation, and during millennial-scale cold events water compositions shift towards fresh glacial meltwater sourced proximal to RM. We interpret this shift to more geochemically evolved waters during warm AIM periods as resulting from a regional increase in subglacial hydrological connectivity, which enables addition of more interior subglacial waters (e.g., from Wilkes subglacial lakes[144]) that flush >100km downglacier through the hydrologic system draining the

David glacier catchment. Though radar-detected lakes in the ice sheet interior have been stable through the entire multi-decadal period of Antarctic remote sensing observation[6], geologic evidence for increased delivery of subglacial water from the ice sheet interior to marginal environments during millennial-scale warm periods is observed in ref. [139].

The temporal coincidence between variations in subglacial water dynamics and provenance with millennial-scale changes in climate supports the conceptual model for a key role of subglacial hydrology in enhancing climate sensitivity of marine-terminating Antarctic outlet glaciers[9]. Within the framework of this model, as illustrated in figure 5, the warming of ocean waters abutting the AIS during a warm period leads to submarine ice melting and the retreat of grounding lines. This grounding line movement leads to a steepening of ice surface slopes, causing ice velocities to accelerate and the volume of subglacial waters to increase due to basal shear heating. This increase in water dynamics results in shortening of the fill-drain cycles of subglacial lakes and in the regional increase of subglacial water fluxes, which is expected to increase subglacial water pressures and trigger faster ice flow. When increased subglacial water fluxes reach the grounding lines they can promote their continued retreat because they represent a significant buoyance flux that promotes vertical seawater mixing, enhanced vertical heat and salt transfer, and increased melting at the ice-ocean interface[9].

Estimates of the lag time between the sample data (constrained by the highest probability age model) and climate records place the peaks in hydrologic response to

within 60 years of peak AIM warming (Extended Data Fig. 6). This result indicates that ocean forcing drives a subglacial hydrologic response that propagates >100km upstream of the grounding line within decades of the initial change in Southern hemisphere climate. The ≤60-year lag period between climate warming and the subglacial hydrologic response likely represents the propagation time for ocean warming to trigger grounding line retreat, ice sheet steepening, and ultimately, a subglacial hydrologic response. Marine archives for ice dynamic response to ocean forcing provide supporting evidence for ice sheet retreat within a decade of a climate warming event[36,138]. Compared to the flushing observed over days to months by satellite altimetry beneath fast moving areas of the modern ice sheet[130], the decade to millennial events observed in our subglacial precipitates represent a larger reordering of the subglacial hydrologic system on a catchment-scale linked to climate-forced ice motion.

While ocean thermal forcing is invoked to explain grounding line retreat and ice acceleration in modern ice systems[18,19], the RM precipitate present a ten-thousand year, high-resolution record of how warm ocean waters can drive changes in water pressure, and presumably with it ice acceleration, propagating deep into the ice sheet interior where large glacial and chemically mature waters reside[8] (e.g. Wilkes lake district, Fig. 1). In total, the analyzed subglacial archive supports the existence of rapidly responding positive feedback whereby Southern Ocean warming increases ice velocity, subglacial water supply, connectivity, and pressure, all of which feed back into higher ice velocities and may also promote further grounding line retreat due to the enhanced

buoyancy fluxes and ice melting at the grounding line (Fig. 5c). The demonstrated connection between subglacial water and climate suggests that the feedbacks outlined here play a fundamental role in how ice sheets respond rapidly to climate change, both in the modern and the past, and underscores how the inclusion of these processes can improve the predictive power of ice sheet models.

2.5 Methods

2.5.1 Subglacial Precipitate U-series age models

Geochronologic analyses were made on ~1 mm thick sections of each subglacial precipitate sampled parallel to calcite layers (Extended Data Fig. 1). U-series measurements were made at the W.M. Keck Isotope laboratory at UCSC following the methods described in ref. [148]. To construct the stratigraphic age model for each sample, we input sample height and ^{234}U-^{230}Th dates into a Bayesian Markov chain Monte Carlo model that considers the age of each layer and its stratigraphic position within the sample to refine the uncertainty of each date using a prior distribution based on the principal of superposition[46]. Sample PRR53557 produced a more precise age-depth model than sample PRR52588, due to higher precipitation rates per unit time. Therefore, we use the age parameters from sample PRR53557 to produce a revised age-depth model for sample PRR52588 using a Monte Carlo simulation that finds the optimal time constraints, within dating uncertainties from PRR52588, to match the precipitate mineral line spectra from the two samples. This Monte Carlo simulation assumes, based on visual analyses of the mineral line spectra from the samples, that these two precipitates formed over the same time periods and that their calcite spectra should match through time. We choose tie points between the two samples where z-positions in PRR52588 match time constraints from PRR53557. We then run simulations for 10,000 age-depth models, within the 2σ uncertainty

of the PRR52588 age constraints, and choose the age model that produces the most optimal match in line spectra between the two samples.

2.5.2 Precipitate Sedimentological Characterization

Our sedimentological characteristics of the two subglacial precipitates from RM were made based on analysis of images captured with a Scanning Electron Microscope-Energy Dispersive X-ray Spectroscopy (SEM-EDS) on a Thermoscientific Apreo SEM with an Oxford Instruments UltimMax detector housed at UCSC. The two precipitate samples are made entirely of calcite with intermixed silicate detritus. Therefore, elemental maps showing silicon concentration allow for the characterization of the size and distribution of detrital grains throughout the samples. EDS silicon maps were imaged across the sample layers (Fig. 2). These maps show alternating, micron-scale layers of pure and detritus-rich calcite through the entire sample. The silicate grains in the detritus-rich calcite are uniformly distributed and are consistently smaller than the 2μm pixel size in the images; were refer to these <2μm grains as clay-sized particles. Discrete layers with larger silicate grains are interspersed throughout the sample. We measure the size of these grains using the analyze particles function in ImageJ software, which describes a grain size distribution between 6 and 90μm or between silt to fine sand (Extended Data Fig. 7).

In addition to elemental maps of the two precipitates, we used thin sections to characterize sedimentary textures from both samples. In thin section, fibrous and bladed calcite crystals are clearly visible. Both pure to clay-rich calcite laminations, and layers of silt to sand-sized particles are also apparent. In some areas below sand-

rich layers, rounded and smoothed calcite crystals indicate erosion. Several thin section textures, including pinched out detritus layers and oblique foliation of calcite crystals, indicate laminar water flow.

2.5.3 Spectral Analyses

To explore the timing and cyclicity of sample layers, we produced timeseries describing the amount of silicate detritus across each layer within the two subglacial precipitates. Spectra were produced by imaging the samples; converting the images to grey-scale to increase contrast of detritus; and using the image processing software, Fiji, to produce spectral outputs from box scans of grey-scale image transects (Fig. 3b,d). Spectral output for sand-sized grains was produced in Fiji by filtering silicon EDS maps to include only silicate grains larger than the 2μm pixel size. We used box scans across sample layers to account for slight lateral variation of detritus. Timeseries were produced by plotting these spectra versus age-depth models. We analyzed these timeseries for dominant frequency using the Fast Fourier Transform method of the Evolutionary Spectral Analysis feature in the program Acycle[158] (Fig. 2a). FFT measurements were determined using sliding windows with a width ~1.5x the size of the largest observed frequency in our spectra. Dominant frequencies were visualized as deconstructed spectra using the Signal Multiresolution Analyzer application in Matlab (Fig. 3e).

2.5.4 Isotopic and Elemental Analyses

Sr isotopic measurements were made at the UCSC Keck Isotope Laboratory following protocols outlined in ref. [148]. The absolute standard error for the precipitate Sr isotope measurements reported here are between 2.8e-5 and 4.8e-6 (Extended Data Table 3), which are smaller than the markers in figure 3.

Carbonate isotope ratios ($\delta^{13}C_{CO3}$ and $\delta^{18}O_{CO3}$) were measured by UCSC Stable Isotope Laboratory using a Themo Scientific Kiel IV carbonate device and MAT 253 isotope ratio mass spectrometer. Referencing $\delta^{13}C_{CO3}$ and $\delta^{18}O_{CO3}$ to Vienna PeeDee Belemnite (VPDB) is calculated by two-point correction to externally calibrated Carrara Marble 'CM12' and carbonatite NBS-18[87]. Externally calibrated coral 'Atlantis II'[88] was measured for independent quality control. Typical reproducibility of replicates was significantly better than 0.05 ‰ for $\delta^{13}C_{CO3}$ and 0.1 ‰ for $\delta^{18}O_{CO3}$. The reported $\delta^{18}O$ values are corrected for the fractionation between the solid calcite and liquid parent water, in order to represent the oxygen isotope composition of the subglacial parent water. This $\delta^{18}O$ fractionation is calculated using the appropriate equilibrium water $\delta^{18}O$ water-mineral fractionation factors assuming a temperature (T) of 0 °C (273.15 K). We use the empirical $1000\ln\alpha$ versus $1/T^2$ relationship reported in ref. [116]. The $1000\ln\alpha$ value for calcite is 33.6‰, and we calculate the formation waters avoiding the non-linearity associated with delta notation far from the standard of choice (in this case VSMOW). As such, we calculate the formation water composition as: $\alpha = (1000 + \delta^{18}O_{mineral}) / (1000 + \delta^{18}O_{water})$. Since we do not have independent constraints on the parent water temperatures, uncertainties of $\delta^{18}O_{water}$ values must consider deviation from the 0˚C assumed formation temperature. If we set a conservative range in subglacial meltwater temperatures between -10˚C and 10˚C, temperature affect could result in a $\delta^{18}O_{water}$ of ±3‰ from the reported values. Given that the range in measured $\delta^{18}O_{water}$ values from the two precipitates between -54.2‰ and -55.2‰, the highest possible parent water $\delta^{18}O$ values is -51.2‰. This value is approximately 7‰ lower than any $\delta^{18}O$ measured in the nearby Taylor Dome ice core, supporting precipitate formation in waters delivered from upstream in the David glacier catchment. Further, given the uncertainty imparted by parent water temperature on the

precipitate $\delta^{18}O$ values, it is not possible to interpret oxygen isotopes compositional changes resulting from increased flushing during warm climate periods.

Laser ablation inductively coupled plasma–mass spectrometry (LA ICP-MS) analyses were conducted at the Facility for Isotope Research and Student Training (FIRST) at Stony Brook University, following protocols outlined in ref. [139].

Acknowledgements

This chapter reflects a manuscript in preparation with the following coauthors: Sophia Pinter, Terrence Blackburn, Slawek Tulaczyk, and Troy Rasbury. We thank Hilde Schwartz for helpful discussion about sedimentary structures within the Reckling precipitates. This research was funded by the NSF graduate research fellowship, NSF 2042495, and NSF 2045611.

2.6 Figures and Tables

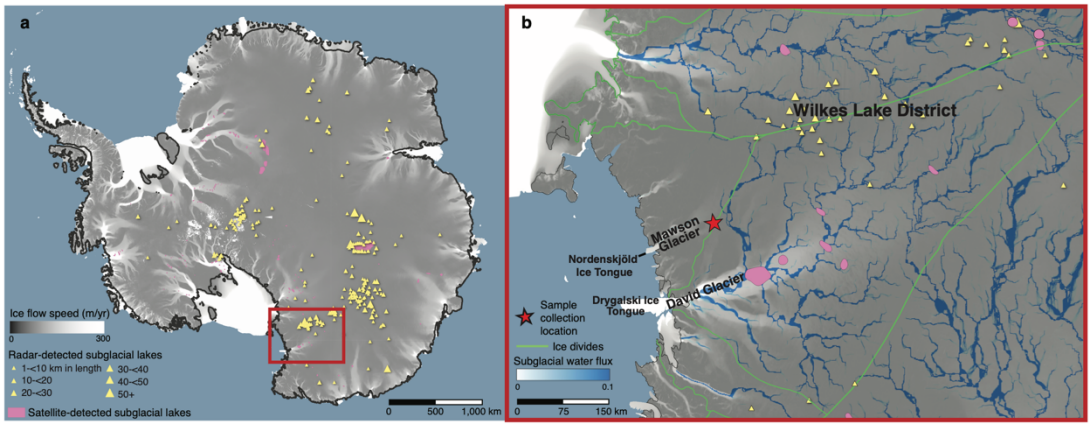

Figure 2.1: Map of Antarctic Subglacial Lakes. a. Map of the Antarctica ice velocity (black-white gradient) showing radar (yellow) and satellite detected (pink) subglacial lakes[144]. The boxed area of the East Antarctic Ice Sheet (EAIS) is shown in panel (b). **b.** Map from inset in panel (a) of modeled subglacial drainage patterns[159] (blue) and glacial catchments boundaries[160] (green). Subglacial lakes from the Wilkes lakes region (yellow diamonds) are located upstream of where samples were collected from Reckling Moraine (red star) and are possible lakes contributing to the fill and flush cycles recorded by precipitate samples.

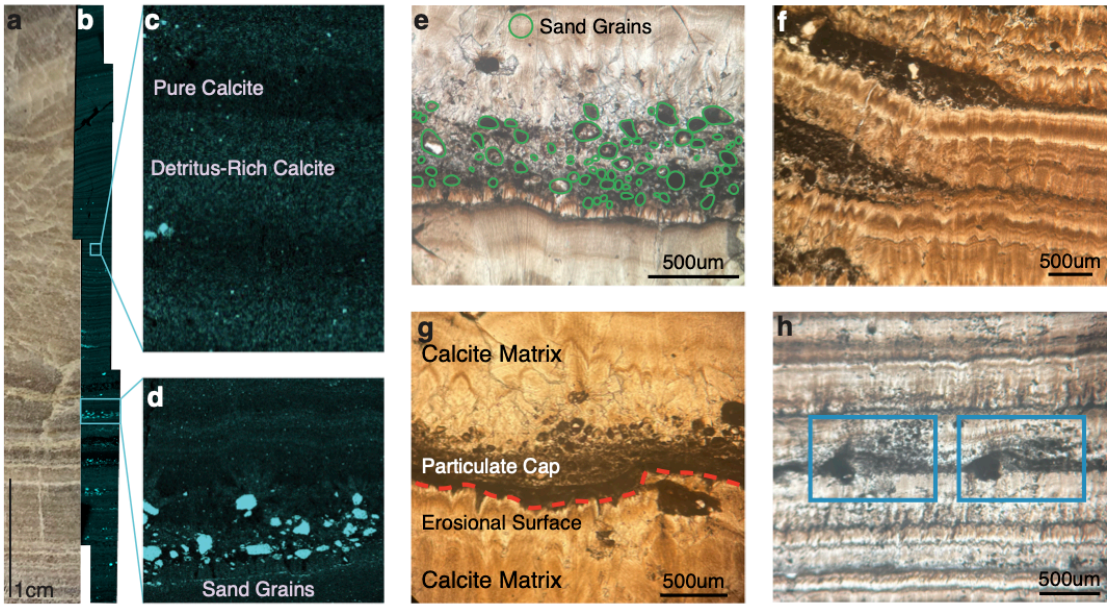

Figure 2.2: Sedimentary textures in Reckling Moraine subglacial precipitates. a. Plain light image of sample PRR53557, which consists of alternation, micron-scale laminations of clay-rich, and clean calcite. **b**. SEM EDS elemental colored by silica concentration. **c**. Primary sample structure consisting of packages of pure calcite and detritus rich calcite distinguished by silica concentration **d.** Layer with sand grains. **e-h.** Thin section images of sedimentary textures. **e.** Layer of rounded sand-sized grains within calcite laminae. **f.** Clastic layers (dark brown on left) that pinch out laterally along calcite layer surfaces. **g**. Erosional surface capped and filled in with silt-sized particles in the microcrystalline calcite matrix. **h.** Oblique foliation (blue boxes) on the right of two larger sand grains.

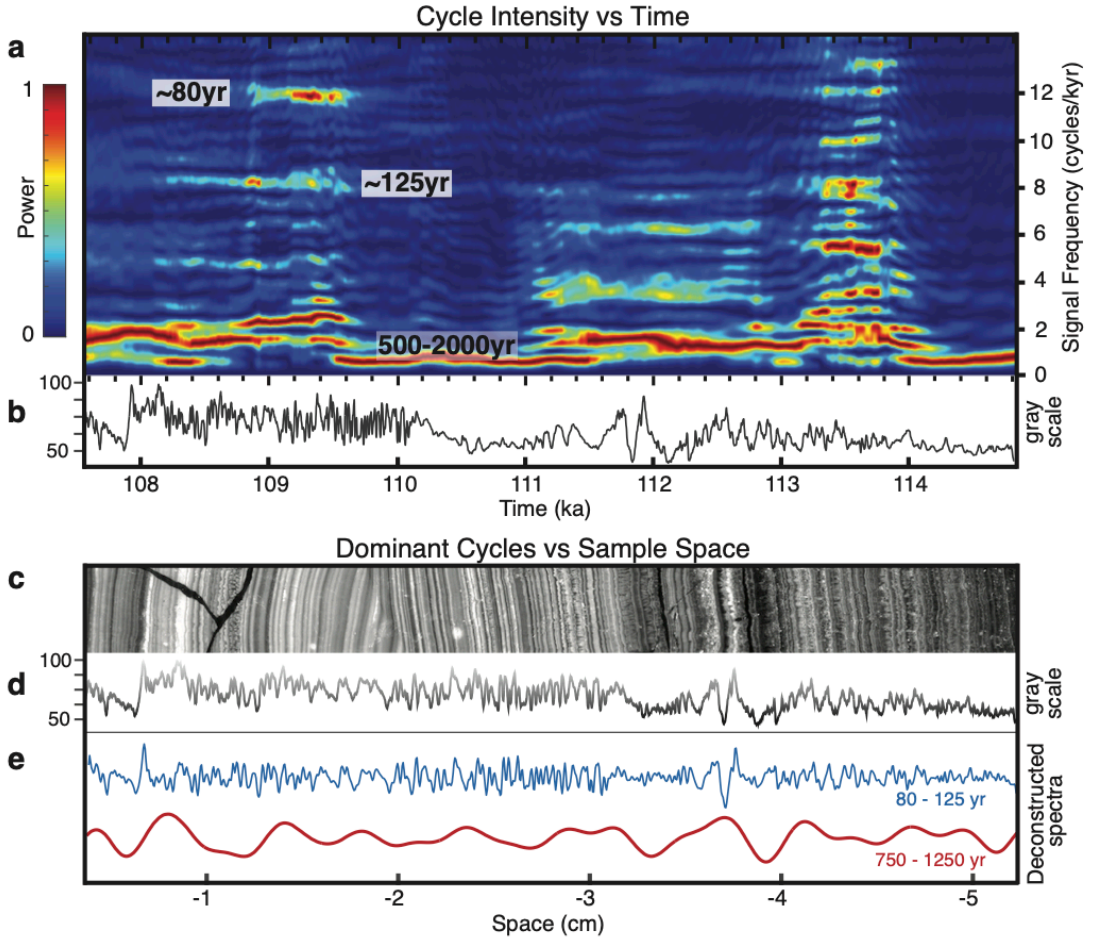

Figure 2.3: Spectral Analyses of sample PRR53557. a. Evolutionary FFT analysis of detrital silicate concentration showing cycle power over time. **b.** Spectral data derived from calcite opacity of sample thin section plotted in the time domain. **c.** grey scale image of sample. **d.** Spectral data in space domain. **e.** deconstructed spectra for centennial scale (blue) and millennial scale (red) cyclicity in sediment (Methods). A complementary figure for sample PRR52588 is included in the extended data (Extended Data Fig. 4).

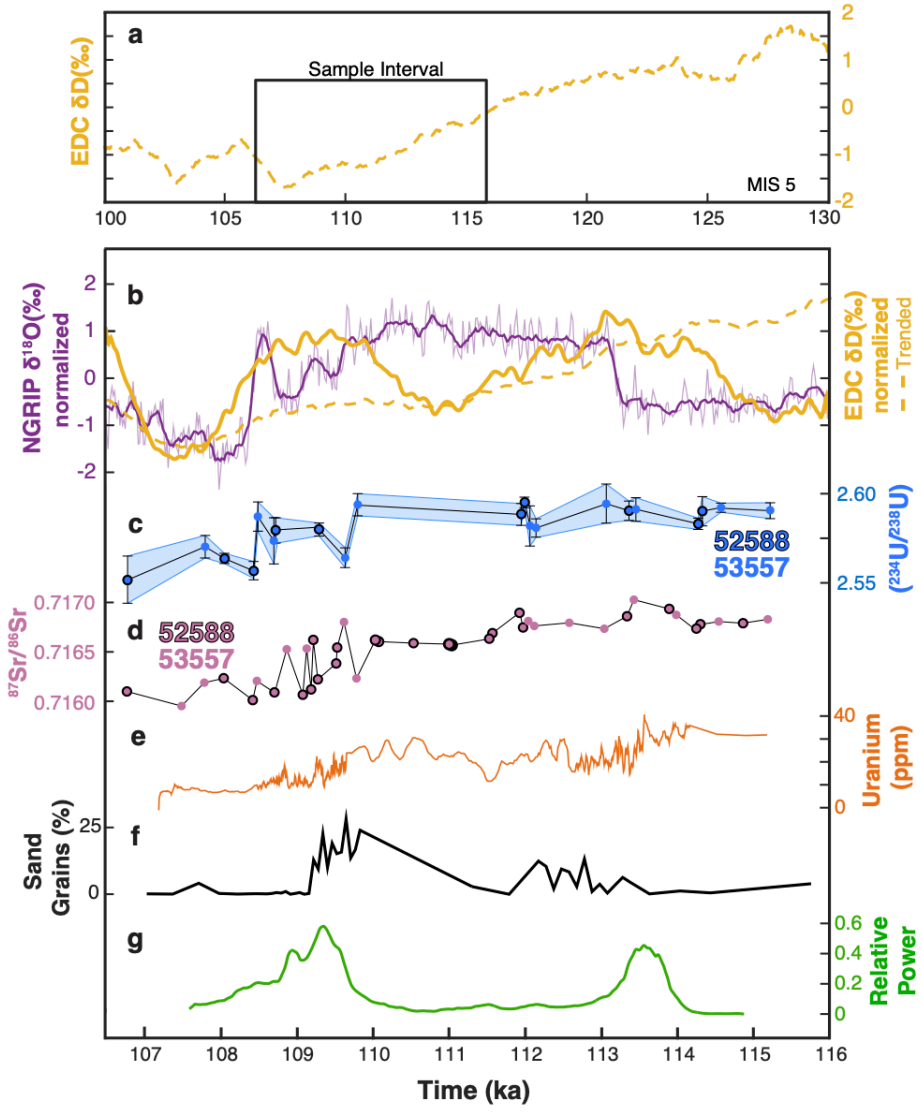

Figure 2.4: Comparison between sample PRR53557 and climate records. **a.** δD (‰) a proxy for Antarctic surface temperature at EPICA Dome C (EDC), on the AICC2012 timescale, over the last interglacial. **b.** (Dashed yellow) EDC δD (‰) over sample interval (box inset from panel a). (Purple) Northern Greenland Ice Core Project δ^{18}O (‰) record, a proxy for temperature in Greenland showing polar seesaw related Dansgaard-Oeschger (D-O) events at ~109 and 113 ka. (Solid yellow) decomposed AIMs from EDC by removal of the LR04 marine isotope record[161] following[156]. b-e) Measured geochemical data from subglacial precipitates. Blue envelope in (c) describes 2σ uncertainties in $^{234}U/^{238}U$ data. Uncertainties (2σ) in Sr isotope compositions are smaller than pink markers in (d). f) abundance sand grains (measured in percent of total sample area). g) spectral power through time of periodicities from 80 – 130 yr.

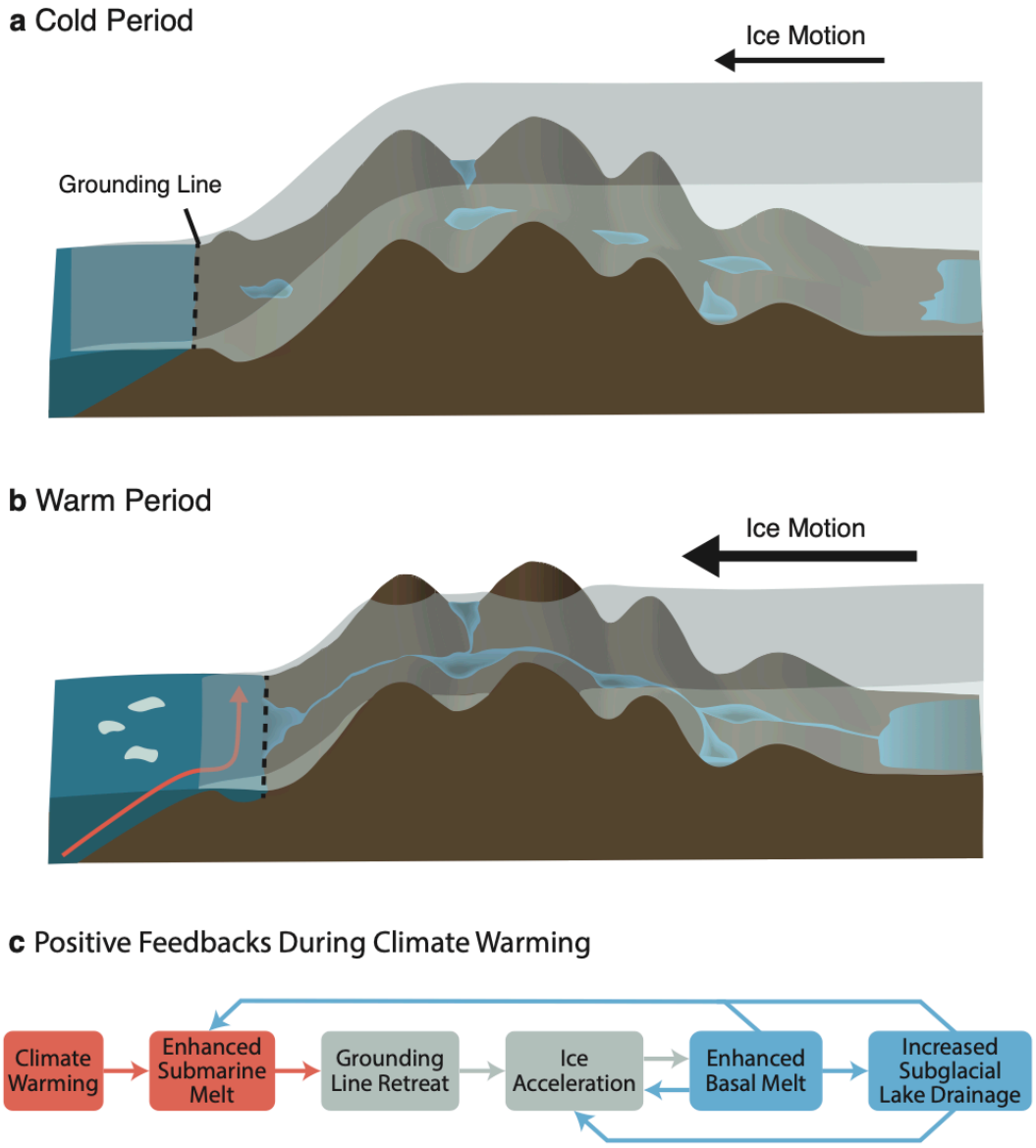

Figure 2.5: Schematic illustration of the EAIS differing under Southern Ocean temperature conditions. a. Cold period conditions result in an advanced grounding line, thicker ice shelf, and subglacial hydrologic system isolated by regions of basal freezing. **b.** Warmer ocean conditions cause grounding line retreat, ice acceleration and thinning, and a response from the hydrologic system that includes increased water volumes and connectivity to interior lakes with longer rock-water interaction times. **c.** Proposed positive feedback between climate, subglacial hydrology and ice loss. Red boxes pertain to climate forcing, gray to the ice response and blue to subglacial hydrology.

Table 2.1: Sr isotope compositions from Reckling Moraine precipitates

Sample Identifier	87Sr/86Sr	Absolute STD err (1σ)
PRR52588-1 Sr	0.716860	1.50007E-05
PRR52588-2 Sr	0.716751	9.24818E-06
PRR52588-3 Sr	0.716766	6.82118E-06
PRR52588-4 Sr	0.716442	7.41895E-06
PRR52588-7 Sr	0.716621	8.65675E-06
PRR52588-8 Sr	0.716417	6.62274E-06
PRR52588-9 Sr	0.716087	6.26831E-06
PRR52588-10 Sr	0.716099	6.51201E-06
PRR52588_B	0.716790	1.48701E-05
PRR52588_3_2	0.716776	7.69737E-06
PRR52588_3_4	0.716935	8.37347E-06
PRR52588_3_5	0.716747	7.79672E-06
PRR52588_3_6	0.716632	6.69936E-06
PRR52588_3_7	0.716568	2.61244E-05
PRR52588_3_8	0.716588	5.63066E-06
PRR52588_3_9	0.716620	7.07065E-06
PRR52588_3_10	0.716544	9.96051E-06
PRR52588_3_11	0.716221	7.79846E-06
PRR52588_3_12	0.716120	4.82953E-06
PRR52588_3_13	0.716012	7.46494E-06
PRR52588_3_14	0.716232	7.25493E-06
PRR53557_3_2 Sr	0.715952	1.11265E-05
PRR53557_3_3 Sr	0.716188	1.03734E-05
PRR53557_3_6 Sr	0.716206	9.10550E-06
PRR53557_3_8 Sr	0.716533	5.47293E-06
PRR53557_3_10 Sr	0.716802	6.01658E-06
PRR53557_3_12 Sr	0.716232	1.96353E-05
PRR53557_3_14 Sr	0.716762	7.15415E-06
PRR53557_3_15 Sr	0.716794	6.26975E-06
PRR53557_3_17 Sr	0.716734	2.85004E-05
PRR53557_3_19 Sr	0.716812	1.23885E-05
PRR53557_3_21 Sr	0.717028	6.57286E-06
PRR53557_3_23 Sr	0.716874	1.79410E-05
PRR53557_2_3 Sr	0.716807	6.80403E-06
PRR53557_2_2 Sr	0.716829	6.55612E-06
PRR53557_3_T1 Sr	0.716836	5.57893E-06

Table 2.2: C and O isotope compositions from Reckling Moraine precipitates.

Sample identifier	δ13C (‰ VPDB)	δ18O (‰ VPDB)	Yield µmol CO2	Equivalent µg CaCO3	Initial mV44	δ18O (‰ SMOW, WATER @ 273.15 K)
PRR_52588_ 1	-18.18	-51.83	0.7	70	12528.29	-54.8423
PRR_52588_ 2	-18.35	-52.27	0.59	59	9595.31	-55.2809
PRR_52588_ 3	-18.14	-51.7	0.5	50	7507.89	-54.7127
PRR_52588_ 5	-18.28	-51.96	0.71	71	12543.4	-54.9719
PRR_52588_ 6	-18.13	-51.99	0.73	73	13098.89	-55.0018
PRR_52588_ 7	-18.14	-51.79	0.25	25	3309.78	-54.8025
PRR_52588_ 8	-18.01	-51.91	0.76	76	14051.93	-54.9221
PRR_52588_ 9	-17.88	-51.9	0.42	42	5823.18	-54.9121
PRR_52588_ 10	-17.95	-51.91	0.46	46	6546.88	-54.9221
PRR53557_3_2	-17.77	-51.2	0.97	97	1.02	-54.2143
PRR53557_3_6	-17.99	-51.62	1.04	104	1.04	-54.6330
PRR53557_3_8	-18	-51.67	0.8	80	1.02	-54.6828
PRR53557_3_10	-18.11	-51.6	0.71	71	1.01	-54.6131
PRR53557_3_12	-18.21	-51.33	0.75	75	1.02	-54.3439
PRR53557_3_14	-17.92	-51.21	0.85	85	1	-54.2243
PRR53557_3_15	-18.11	-51.67	0.88	88	1	-54.6828
PRR53557_3_17	-18.03	-51.63	0.85	85	1	-54.6430
PRR53577_3_19	-18.09	-52.09	0.89	89	1	-55.1015
PRR53557_3_21	-18.03	-51.86	0.87	87	1	-54.8722
PRR53557_3_23	-18.03	-51.79	1.03	103	1.02	-54.8025
PRR53557_2_2	-18.1	-51.87	0.81	81	1	-54.8822
PRR53557_2_3	-17.9	-51.46	0.77	77	1	-54.4735
PRR53557_T1	-17.95	-51.87	1.06	106	1.04	-54.8822

Table 2.3: U-series data from Reckling Moraine precipitates.

Sample Name	Th (ppm)	U (ppm)	[232Th/238U]	2σ unc	[230Th/232Th]	2σ unc	[234U/238U]	2σ unc	[230Th/238U]	2σ unc	U-Th age (ka)	Th-corrected age(ka)	2σ unc	[234U / 238U]i	2σ unc
PRR52588_3_1	0.48	27.79	0.017551	0.08	270.29	0.30	2.1508	0.10	1.50865	0.31	114.48	114.28	0.60	2.590	0.0032
PRR52588_3_2	0.21	19.05	0.011281	0.16	421.56	0.94	2.1560	0.12	1.51239	0.96	114.46	114.34	1.76	2.597	0.0083
PRR52588_1_	0.22	17.48	0.012889	0.11	367.62	0.36	2.1593	0.22	1.50692	0.38	113.52	113.37	0.80	2.597	0.0055
PRR52588_3_5	0.11	17.26	0.006638	0.08	710.86	0.28	2.1674	0.09	1.50074	0.29	112.08	112.00	0.54	2.602	0.0030
PRR52588_2_	0.18	18.19	0.010044	0.12	468.69	0.40	2.1627	0.24	1.49717	0.42	112.07	111.96	0.87	2.595	0.0062
PRR52588_3_1	0.38	19.01	0.020372	0.26	227.94	0.34	2.1647	0.09	1.47680	0.43	109.52	109.30	0.75	2.587	0.0037
PRR52588_9_	0.48	16.76	0.029296	0.26	158.16	0.57	2.1660	0.25	1.47355	0.63	109.05	108.73	1.16	2.586	0.0072
PRR52588_3_1	0.83	20.83	0.041027	0.22	111.93	0.39	2.1496	0.19	1.46045	0.44	108.90	108.44	0.85	2.563	0.0052
PRR52588_3_1	1.25	18.88	0.067817	0.18	67.86	0.28	2.1550	0.07	1.46360	0.33	108.81	108.06	0.68	2.570	0.0029
PRR52588_10_	1.02	19.78	0.052668	0.25	86.44	1.67	2.1508	0.26	1.44792	1.69	107.37	106.78	2.85	2.558	0.0134
PRR53557_3_3	0.26	17.22	0.015462	0.06	297.26	0.30	2.1627	0.28	1.46175	0.31	107.97	107.80	0.71	2.577	0.0064
PRR53557_3_4	0.03	16.89	0.001762	0.20	2620.29	0.51	2.1627	0.58	1.46830	0.55	108.72	108.70	1.39	2.580	0.0131
PRR53557_3_6	0.03	13.42	0.001928	0.23	2403.95	0.87	2.1733	0.22	1.47416	0.90	108.52	108.49	1.56	2.594	0.0083
PRR53557_3_1	0.06	14.90	0.004375	0.15	1043.89	0.40	2.1610	0.22	1.45259	0.42	107.06	107.02	0.79	2.571	0.0056
PRR53557_3_1	0.08	15.18	0.005517	0.04	847.14	0.21	2.1738	0.28	1.48633	0.21	109.87	109.81	0.63	2.600	0.0063
PRR53557_3_1	0.22	23.99	0.009330	0.19	503.59	0.52	2.1564	0.13	1.49418	0.56	112.25	112.15	1.02	2.587	0.0052
PRR53557_3_1	0.11	17.05	0.006872	0.33	689.51	1.29	2.1633	0.14	1.50681	1.33	113.15	113.07	2.39	2.601	0.0111
PRR53557_3_1	0.07	18.43	0.003797	0.11	1237.02	1.43	2.1577	0.08	1.49387	1.43	112.12	112.07	2.52	2.589	0.0114
PRR53557_3_2	0.09	19.89	0.004487	0.09	1056.35	0.25	2.1599	0.30	1.50732	0.26	113.51	113.46	0.74	2.598	0.0067
PRR53557c_2_	0.05	18.07	0.002647	0.12	1798.85	0.18	2.1570	0.09	1.51438	0.21	114.61	114.58	0.43	2.599	0.0026
PRR53557c_2_	0.02	6.03	0.003859	0.27	1236.52	0.41	2.1537	0.10	1.51744	0.49	115.23	115.23	0.91	2.597	0.0045

Chapter 3

Microbes drive subglacial CO2 production and silicate weathering throughout Antarctica

3.1 Abstract

Biogeochemical reactions in water beneath the Antarctic ice sheet produce greenhouse gasses that may influence the global carbon cycle by weathering bedrock or leaking to the atmosphere. Yet basal waters have been accessed in only three locations along the modern West Antarctic margins, limiting measurements of the subglacial carbon cycle in both space and time. Here, we present $\delta^{13}C$ values from carbonate precipitates deposited over 6.7 million years in basal waters throughout Antarctica, which point to persistent and widespread cycling of fossil organic carbon to CO_2 through microbial respiration. Correlation between $\delta^{13}C$ values, parent water alkalinity, and bedrock type demonstrate that respired CO_2 is neutralized through silicate weathering, indicating that microbially-mediated silicate weathering beneath Antarctica has persisted throughout the continent since the Miocene.

3.2 Introduction

Melting at the base of the Antarctic Ice Sheet (AIS) supplies a continent-wide subglacial hydrologic system [79], where water flows through channels from the thickest portions of the ice sheet interior, outwards towards the thinner edges [162]. Discovery of

abundant microbial populations [11] in these waters has motivated modeling studies suggesting that anoxic conditions beneath the AIS interior can support the degradation of continent-wide reserves of legacy organic carbon by methanogenic archaea, producing methane that can leak to the atmosphere and add to the greenhouse gas budget [163]. However, in the few areas along the Antarctic periphery where basal water has been sampled [164–167], oxygen supplied from basal ice drives near-complete oxidation of methane when it reaches the ice-bed interface [168]. In these suboxic waters, microbes instead produce CO_2 via respiration, leading to biogeochemical weathering reactions that generate solute fluxes in excess of global riverine values [12]. High silicate weathering rates beneath the AIS can have the opposite effect as methane release on the global carbon cycle: where methane release would contribute to greenhouse gases, the discharge of nutrient-rich basal waters can fertilize the Southern Ocean and cause atmospheric CO_2 drawdown [14]. Whether the few measurements of subglacial water from the Antarctic periphery represent conditions beneath the broader ice sheet is uncertain, because physical erosion, basal meltwater flushing rates, and the geologic composition of the substrate – three of the main physical parameters controlling silicate weathering and methanogenesis [169,170] – are sensitive to local glaciologic and environmental conditions [130,171]. Therefore, subglacial microbial greenhouse gas production and weathering may be highly variable throughout the continent, while ice dynamic response to climate cycles [5] may also change these biogeochemical processes through time.

The cold, dark, and isolated aqueous system below polar ice sheets may represent an important analog for both habitable zones on icy celestial bodies in the solar system [172], or the subglacial environment beneath the Neoproterozoic snowball Earth ice sheets [173]. However it's the inaccessible interior of Antarctica, where waters can remain isolated for tens of thousands of years beneath kilometers of ice, that may prove to be the most similarly extreme environment. In the areas along the Antarctic margins where subglacial water has been sampled, fine grained rock powder and organic matter supplied from the bedrock substrate sustain microbial activity that drives biogeochemical weathering [174]. Atmosphere derived oxygen is delivered to the subglacial environment through melting of meteoric ice at the ice sheet base. This oxygen facilitates microbially mediated oxidation of these materials, releasing nutrients and greenhouse gasses (CO_2 and CH_4), and providing a source of acid that drives subglacial chemical weathering. Due to the protracted residence time of Antarctic subglacial waters, oxygen can be partially or fully consumed by chemolithoautotrophic microorganisms that use other electron acceptors like nitrogen [11], iron [166], and sulfur [175] as energy sources [176]. Suboxic to anoxic conditions driven by microbial oxygen consumption leads to increased solubility of metals like Fe and Mn that are the most important limiting nutrients to Southern Ocean organisms. However, since subglacial erosion rates and fluid residence times vary between central and peripheral regions of Antarctica, the availability of redox pairs and nutrients in the ice sheet interior is uncertain, precluding continent-scale estimates for microbial activity, subglacial silicate weathering rates, and greenhouse gas production. Given the low levels of

oxygen and organic matter in subglacial environments beneath snowball Earth and the absence of these beneath extraterrestrial ice sheets, the supply of redox pairs and nutrients to the Antarctic subglacial environment likely determines whether it is a true analog for these settings.

3.3 Results and Discussion

3.3.1 Continent-Wide Record of Subglacial Chemistry Since the Miocene

Here, we present geochemical and geochronologic data from 49 carbonate precipitates that formed from water at the base of the Antarctic Ice Sheet. These samples are found at the ice sheet surface throughout the continent, either in exhumed sections of basal ice bordering the Transantarctic Mountains (TAM) or at formerly glaciated sectors along the ice sheet margins (Fig. 1). Previous research focusing on subglacial precipitates from the TAM demonstrated that they can be dated and used to characterize the geochemical compositions of their parent waters, making them effective Antarctic paleoclimate archives [139,148]. We expand on these earlier studies by providing age constraints on a large suite of precipitates that formed between 16 and 6770 ka (Fig. 2; fig. S1) [177]. This ca. 6.7 Ma record of geochemical conditions in subglacial water across Antarctica provides: i) insight into the degree of biogeochemical weathering in diverse regions throughout the ice sheet, and ii) a test of the sensitivity of these subglacial conditions to global climate events.

We report $\delta^{18}O_{CaCO3}$ from each subglacial precipitate and use these data to calculate the oxygen isotope composition of their parent waters ($\delta^{18}O_{water}$) [177]. Measured $\delta^{18}O_{water}$ values in all but two precipitates are ~10‰ lower than local snow and ice [150] (Fig. 1a), indicating that these samples form in parent waters sourced primarily from beneath the ice sheet interior that flush towards the margins. These water provenance data are consistent with thermodynamic models of the ice-bed interface [79] that suggest that the highest subglacial melting rates occur in the central regions of the AIS, and most waters present in the relatively colder basal environments along the ice sheet margins originate 10s to 100s of kilometers upstream in the ice sheet interior. Based on the sample collection locations and modeled AIS subglacial drainage patterns [159], the suite of subglacial precipitates measured here form in waters sourced from several distinct subglacial hydrologic catchments (Fig. 1b). Therefore, the composition of this sample collection represents that of subglacial waters throughout the continent.

Despite the large continent-scale range over which precipitate parent waters originate, $\delta^{13}C_{CaCO3}$ values cluster in two main groups based on sample location: precipitates collected along the TAM exhibit only a small range of $\delta^{13}C_{CaCO3}$ values between -23.5 and -16‰, while samples from peripheral areas around the ice sheet are comparatively ^{13}C-rich, with $\delta^{13}C_{CaCO3}$ values between -10.2 and 0.2‰ (Fig. 1c). This geographic dichotomy in $\delta^{13}C_{CaCO3}$ between TAM and peripheral samples implies that waters in the interior of the ice sheet have a distinct carbon source relative to waters that form along the ice sheet edges (Fig. 1b). Comparison between $\delta^{13}C_{CaCO3}$ and $\delta^{18}O_{water}$ from individual TAM precipitates can be fit by a parabolic mixing curve (fig.

S2), implying that samples form in a two-component mixture of subglacial fluids with distinct carbon and oxygen isotope compositions: one ^{13}C-poor endmember with low $\delta^{18}O$ values indicative a water source from the ice sheet interior, and one comparatively ^{13}C-rich endmember with $\delta^{18}O$ values matching water sourced from local ice. Of these two endmembers, mixing curves imply that the relatively ^{13}C- and ^{18}O-poor interior water contributes >90% of the total carbon in the precipitates (supplementary material). Similar mixing relationships from TAM subglacial precipitates have been interpreted as mixing of interior water with peripheral water as they flush towards the ice sheet margins: a process that plays a key role in triggering calcite precipitation [139]. Therefore, the parabolic distribution of $\delta^{13}C_{CaCO3}$ and $\delta^{18}O_{water}$ values of individual TAM precipitates confirms the distinct carbon sources in the ice sheet interior and edges respectively, where TAM subglacial precipitates form from dissolved carbon that accumulates in subglacial waters as they travel over hundreds of kilometers from the ice sheet interior. Conversely, precipitates forming near the ice sheet margins have $\delta^{13}C_{CaCO3}$ values consistent with the ^{13}C-rich endmember from the TAM samples (~0‰), suggesting that they likely source carbon locally (Fig. 1c).

3.3.2 Microbial Respiration of Subglacial Fossil Carbon

The $\delta^{13}C_{CaCO3}$ value of Antarctic subglacial precipitates is controlled by the carbon source and the pH of the parent solution. Thick ice cover and lack of moulins in Antarctica [157] prevents atmospheric carbon from entering the subglacial environment except in rare areas along the ice sheet edges [178], so possible carbon sources to the basal environment include carbonate bedrock and organic matter from buried soils and

sediments. These two source reservoirs have distinct $\delta^{13}C$ values, where carbonate bedrock has a marine value of 0±5‰, and organic matter along the substrate defines a range between -10‰ and -80‰ (Fig. 1c). The $\delta^{13}C$ of organic matter is further differentiated depending on the type of organic material, with C4 plants ranging from -10 to -16‰, bacteria and algae from -15 to -35‰, C3 plants from -24 to -30‰, and methane from -30 to -80‰ (Fig. 1c) [179,180]. For an environment that is closed off from atmospheric gas exchange (hereafter referred to as a closed system) CO_2 can neither enter nor leave the system, and the $\delta^{13}C_{CaCO3}$ can only deviate by up to 12 ‰ from the isotope composition of source carbon depending on the pH of the parent solution [54]. Therefore, the tight range of $\delta^{13}C_{CaCO3}$ values in TAM precipitates (-23.5 ‰ to -16 ‰) is consistent with a subglacial carbon source dominated by C3 plant matter, bacteria, and algae (Fig. 1c), with the possibility for a relatively small methane source (<5% of total dissolved inorganic carbon (DIC); supplementary materials). Precipitates collected along the ice sheet edges, on the other hand, have higher $\delta^{13}C_{CaCO3}$ values (-10.2 ‰ to 0.2 ‰) that are similar to subglacial precipitates measured beneath smaller mountain glaciers worldwide and in areas previously covered by the Laurentide ice sheet [45,181–189] (Fig. 1c). The higher $\delta^{13}C_{CaCO3}$ values alone do not refute an atmospheric carbon source, but in the absence of evidence for atmospheric connection to the Antarctic ice-rock interface [157], these higher $\delta^{13}C_{CaCO3}$ values likely reflect carbon from carbonate bedrock.

To further characterize the source of carbon in subglacial precipitates, we measured the carbon isotope composition ($\delta^{13}C_{OM}$) and the ratio of carbon to nitrogen (C:N) from organic matter isolated from each precipitate. Measured $\delta^{13}C_{OM}$ values (-34.5‰ to -

19.4‰) and C:N ratios (0.2 to 92.5) are consistent with bacteria, marine and freshwater particulate organic carbon, plant matter, and coal (fig. S3; fig. S4). The $\delta^{13}C_{CaCO3}$ values of TAM subglacial precipitates are, on average, only 5‰ lower than their $\delta^{13}C_{OM}$ values (fig. S5), indicating that the DIC beneath the EAIS interior is sourced almost entirely from organic material. The predominance of organic carbon indicates that little carbonate bedrock is present in the EAIS interior, pointing to a terrane that is dominated by silicate bedrock similar to the interior regions of the Greenland ice sheet or the site of the Laurentide ice sheet, where sedimentary cover has been stripped off after millions of years of glaciation [190]. Discussed in detail in the following section, the offset between $\delta^{13}C_{CaCO3}$ and $\delta^{13}C_{OM}$ reflects the pH-controlled proportion of carbonate species of the parent waters.

Since oxidation of organic matter is an extremely slow process unless biologically mediated [157], the subglacial precipitate carbon isotope data require that organic matter is mobilized by microbial respiration in subglacial water throughout the EAIS, which leads to widespread CO_2 production. Evidence for microbial respiration beneath the EAIS interior is consistent with observations from subglacial waters along the ice sheet margins [11,166,191], as well as high CO_2 concentrations, nearly complete oxygen consumption, high cell count, and low $\delta^{13}C$ values in basal ice from interior regions [52,53]. Widespread CO_2 production in EAIS interior regions refutes high concentrations of methane in subglacial waters at the ice-bed interface and suggests that any methane that seeps out from deep pore waters would be oxidized in the basal environment before it can reach the atmosphere. The uniform $\delta^{13}C_{CaCO3}$ values measured over the ~6.5 Ma

period of precipitate formation indicate that the subglacial conditions beneath the Antarctic ice sheet favor CO_2 production via microbial respiration of legacy organic matter across a range of background climate states.

3.3.3 Subglacial CO_2 Production Drives Silicate Weathering

The subglacial precipitate record presented here demonstrates that organic carbon sequestered in rocks and sediment in the basal environment throughout the interior of the EAIS is oxidized to CO_2 by microbial respiration. In a closed subglacial system, the CO_2 produced through the oxidation of organic matter is dissolved and forms carbonic acid that can weather subglacial silicate bedrock. This silicate weathering, in turn, produces bicarbonate with $\delta^{13}C$ value that depends on the pH of the solution. If carbonic acid production exceeds the rate of silicate weathering, CO_2 remains in solution and may eventually be emitted to the atmosphere [157]. If silicate dissolution is favored, any carbonic acid created from legacy carbon beneath the ice sheet would be neutralized through chemical weathering reactions, producing alkalinity and mobilizing elements from the lithosphere.

In a closed subglacial system where organic matter is the dominant source of carbon, the $\delta^{13}C_{OM}$ represents the carbon isotope composition of the DIC ($\delta^{13}C_{DIC}$), and any difference between the $\delta^{13}C_{OM}$ and $\delta^{13}C_{CaCO3}$ (hereafter referred to as $\Delta\delta^{13}C$) results from pH-controlled proportion of carbonate species (H_2CO_3, HCO_3, CO_3) in the precipitate parent waters [54] (supplementary materials). In a low pH water (pH <6), for example, carbonic acid (H_2CO_3) is the most abundant carbonate species. Because the $\delta^{13}C$ of H_2CO_3 at 0°C is lower than the $\delta^{13}C$ of carbonate alkalinity by up to 12‰, any

resulting calcite will have a proportionally higher $\delta^{13}C_{CaCO3}$ value than the $\delta^{13}C_{DIC}$. With increasing pH and decreasing fraction of H_2CO_3, the offset between the $\delta^{13}C_{CaCO3}$ and $\delta^{13}C_{DIC}$ ($\Delta\delta^{13}C$) will decrease (Fig. 3a inset). This relationship between the concentration of carbonate species and pH permits estimation of the pH of parent waters based on the $\Delta\delta^{13}C$ in each precipitate (supplementary materials). The $\Delta\delta^{13}C$ values of TAM precipitates translates to pH values of 5.5 and 7.5, suggesting a range in the degree to which respired carbonic acid is converted to alkalinity by silicate weathering (fig. S6).

To empirically test for the link between precipitate $\delta^{13}C_{CaCO3}$ values and parent water pH we compare $\Delta\delta^{13}C$ values of each precipitate to their P/Ca ratio: a proxy for the ratio of alkalinity to calcium of the parent waters (hereafter referred to as alkalinity-to-Ca ratio) [192]. The observed, and empirically calibrated relationship between high P/Ca waters and alkalinity-to-Ca ratio stems from the propensity for higher pH, alkaline waters to saturate with respect to calcite rather than the phosphate mineral apatite. Carbonate with a P/Ca value above a threshold of 0.5 mmol/mol are produced from parent waters with a high alkalinity-to-Ca ratio, while carbonates with P/Ca values <0.5 mmol/mol form in parent water with a low alkalinity-to-Ca ratio [192]. Antarctic subglacial precipitates have a range of P/Ca between 0.03 and 4.91 mmol/mol, implying basal waters with variable alkalinities (Fig. 3a). Precipitate P/Ca values are indirectly correlated with their $\Delta\delta^{13}C$, where waters with the highest alkalinity-to-Ca ratio have the lowest $\Delta\delta^{13}C$ (Fig. 3a). These data provide evidence that the $\delta^{13}C_{CaCO3}$ of TAM precipitates is controlled by the pH of the parent water, and that the range in

P/Ca and $\delta^{13}C_{CaCO3}$ values tracks the degree to which carbonic acid is consumed by silicate weathering. Based on this range in $\delta^{13}C_{CaCO3}$ values, CO_2 is completely neutralized by silicate weathering in half of the observed subglacial waters, while the other half have CO_2 in solution that can be neutralized by later silicate weathering or discharged from the basal environment.

The degree to which silicate weathering in the Antarctic subglacial environment consumes carbon acidity is controlled by the efficiency of silicate weathering, which will between catchments based on rock type and presence of fresh mineral surfaces. We can utilize both geologic maps of exposed bedrock surfaces [193] as well as the Sr isotopic composition of the precipitates to determine the rock type that was weathered by past subglacial waters. Sr isotopic composition of subglacial precipitates range from 0.711 to 0.738 and cluster based on precipitate formation area (Fig. 4), suggesting that the bedrock in AIS hydrologic catchments are the primary sources of major elements to subglacial precipitates. Figure 4 shows demonstrates a direct correlation between the $^{87}Sr/^{86}Sr$ and $\Delta\delta^{13}C$, suggesting that rock type exerts strong control on subglacial silicate weathering intensity, where samples forming on bedrock with radiogenic $^{87}Sr/^{86}Sr$ values, like Paleozoic granites (.712-0.758) along the TAM [193], undergo less efficient silicate weathering, which allows carbonic acid production to dominate over silicate weathering thus favoring higher $\Delta\delta^{13}C$ values. Whereas samples forming on bedrock with less radiogenic $^{87}Sr/^{86}Sr$ values, like Mesozoic basalts (.709-0.716) [42], undergo more efficient silicate weathering, resulting in higher alkalinity subglacial waters that neutralize carbonic acid and favor lower $\Delta\delta^{13}C$ values. Precipitate $^{87}Sr/^{86}Sr$

versus $\Delta\delta^{13}C$ values group by formation location, pointing to bedrock type of individual glacial catchments as a first-order control on whether CO_2 escape to the atmosphere (Fig. 4). Therefore, subglacial waters in catchments with bedrock that is susceptible to chemical weathering (e.g. basalt terranes) efficiently mobilize elements from the basal environment, whereas waters in catchments with less reactive bedrock (e.g. granite terranes) keep CO_2 in solution for longer periods, which may eventually escape to the atmosphere.

The subglacial precipitate geochemical dataset presented here provides a continent-scale view of the biogeochemical conditions beneath the Antarctic ice sheet. Our results extend observations of abundant microbial life in the Antarctic subglacial environment [11]. Prior observations were limited to the three peripheral locations of West Antarctica accessed by drilling operations. The data presented here expands this biologic footprint outwards to the vast interior regions of the East over the past 6.7Ma. Throughout the AIS, subglacial water hosts microbes that metabolize subglacial organic carbon through respiration fueled by oxygen released from melting the overlying ice, or by other electron acceptors like nitrogen, iron, and sulfate. Carbonic acid produced during respiration fuels silicate weathering, while the implicit oxygen consumption drives subglacial water towards anoxia, increasing the solubility of trace metals. Our result also requires that methane production is confined to sediment pore waters as it does not contribute significantly to subglacial DIC and is unlikely to escape the subglacial environment. Instead CO_2 production drives silicate weathering reactions in subglacial waters, which flush hundreds of miles from the ice sheet interior to the edges and

provide a potentially important nutrient flux to the Southern Ocean ecosystem. Evidence for widespread microbial utilization of both fossil carbon and oxygen from meltwater indicates that life below the Antarctic ice sheet is reliant a legacy biomass produced from past photosynthesis and trapped oxygen in ice once in contact with an oxygenated atmosphere, suggesting that different conditions are required to host life beneath the ice cover on extraterrestrial icy bodies. Similar conditions, however, may occur beneath ice sheets throughout Earth history, including during snowball Earth glaciations [194]. As such, abundant microbial populations beneath these ice sheets may provide a globally significant silicate weathering source.

3.4 Materials and Methods

3.4.1 U-Series and U-Pb dating of subglacial carbonate precipitates

^{234}U-^{230}Th dates were produced for 25 carbonate precipitates at the University of California Santa Cruz (UCSC) Keck Isotope Laboratory following methods described in Blackburn et al., 2020 [148]. Carbonate samples were drilled, spiked with a mixed ^{229}Th-^{236}U tracer, and digested in 3mL 7N HNO_3. U and Th separates were purified using ion chromatography with 1mL columns of 200-400 mesh, AG1-X8 anion resin, and Sr was collected in the wash steps for later purification. Total procedural blanks were <10pg for U and <25pg for Th, which are minor relative to sample concentrations. Both U and Th isotopic measurements were conducted using the IsotopX X62 Thermal Ionization Mass Spectrometer (TIMS) housed at UCSC. U and Th samples are loaded onto 99.99% purity Re ribbon. Uranium measurements were performed as a two sequence "Fara-Daly" routine: in the first sequence, ^{234}U (mass 266) is collected on the

Daly, while ^{235}U (mass 267) and ^{238}U (mass 270) is collected on the high Faraday cups equipped with $1e^{12}$ Ω resistors. The second sequence placed ^{235}U (mass 267) on the Daly and ^{236}U (mass 268) and ^{238}U (mass 270) on the high Faraday cups. The 266(Daly)/270(Faraday) composition was corrected using the Fara-Daly gain: (267Faraday/270Faraday) / (267Daly/270Faraday). Thorium isotope measurements were also done on the TIMS at UCSC. Thorium is loaded in a graphite emitter and measured as a metal. Each mass of Th is measured using a peak hopping routine on the Daly. Thorium fractionation and deadtime were estimated by running NBS U-500 as a metal. Accuracy of ^{234}U-^{230}Th dates were tested using MIS 5e coral and compared to dates in ref [195], as well as a previously dated carbonate precipitate[196]. U-Th ages are calculated using codes designed at UCSC. All ages are corrected for initial [^{230}Th/ ^{232}Th] assuming a composition of 4.4±2.2e-6. As the exact [^{230}Th/ ^{232}Th]$_i$ is unknown, we assume this ratio from the expected composition of the silicate upper crust in secular equilibrium, allowing for a departure from this composition of 50%, and propagating this uncertainty through to the final age. Decay constants for all data and models were from ref. [197]. All uncertainties are reported at 2σ, unless otherwise specified.

Five other precipitates from Elephant Moraine had apparent ages >600ka, but measured $^{234}U/^{238}U$ above secular equilibrium, suggesting formation between 600 ka and 1.5 Ma. Since 600ka is beyond 6 half-lives of ^{230}Th, these samples cannot dated using ^{234}U-^{230}Th measurements. However, this time frame is <6 half-lives of ^{234}U, so model dates for these precipitates can be derived from the measured $^{234}U/^{238}U$ ratios. Because we cannot precisely determine the initial $^{234}U/^{238}U$ of their parent waters, we

assumed a range of values between the minimum and maximum compositions of Pleistocene subglacial precipitates from Elephant moraine: 2.42 to 3.15. We calculated $^{234}U/^{238}U$ dates using the mean value of this range in initial uranium isotope composition (2.85), and propagated this uncertainty, along with the measurement uncertainty, into the final value.

Four additional samples from Elephant Moraine had both ^{230}Th and ^{234}U in secular equilibrium, suggesting formation before 1.5Ma; we calculate dates of these samples using U-Pb measurements on opal layers. We isolate the whitest opal aliquots for U-Pb measurements, as these yield the highest measured $^{206}Pb/^{204}Pb$ ratios, suggesting that white opal is the most pristine. Opal layers are first crushed to approximately sand-sized particles and leached in 7N nitric acid to remove residual calcite. Approximately 5mg of opal is digested in HF at ~150˚C for >5 hours. Samples are then converted to HCl, and U and Pb is purified using ion exchange chemistry described by Krogh [198]. Reported U and Pb isotope data are measured with Isotope Dilution-Thermal Ionization Mass Spectrometry (ID-TIMS) conducted on the UCSC IsotopX X62 Thermal Ionization Mass Spectrometer. U and Pb separates were loaded onto Re ribbon with a Si gel-0.035 M H3PO4 activator. Pb was measured with a peak jumping method on a single collector Daly-photomultiplier ion counting system, and U was measured using a static collection on Faraday cup detectors connected to 1012 Ω resistance amplifier cards. Model U-Pb dates were calculated using U-Pb Redux [199] (fig. S1). To correct for high amounts of common Pb in opals (13 – 1600 pg), we measure assign each sample an initial Pb composition based on values measured in calcite layers. This follows the

assumption that Elephant Moraine opal and calcite precipitates form mixtures of the same two waters, but opals have much higher U concentrations that results in high amounts of radiogenic Pb. Whereas, calcites have very low U concentrations, so their Pb compositions represent the background common Pb in the subglacial environment in their precipitation site. The fact that measured U-Pb compositions fall on or close to Concordia (fig. S1) demonstrates the efficacy of this method for correcting for initial Pb.

3.4.2 Stable Isotope Measurements

Carbon and oxygen isotope ratios were measured by UCSC Stable Isotope Laboratory using a Themo Scientific Kiel IV carbonate device and MAT 253 isotope ratio mass spectrometer. Referencing $\delta^{13}C_{CO3}$ and $\delta^{18}O_{CO3}$ to Vienna PeeDee Belemnite (VPDB) is calculated by two-point correction to externally calibrated Carrara Marble 'CM12' and carbonatite NBS-18[87]. Externally calibrated coral 'Atlantis II'[88] was measured for independent quality control. Typical reproducibility of replicates was significantly better than 0.05 ‰ for $\delta^{13}C_{CO3}$ and 0.1 ‰ for $\delta^{18}O_{CO3}$.

To measure organic carbon isotope ratios, inorganic carbon (IC) was extracted with 1M buffered acetic acid (pH 4.5), followed by repeated water rinses to completely remove the buffered acetic acid and residual cations from the sample IC. These IC-extracted sample residues were then freeze-dried, weighed, encapsulated in tin, and analyzed for carbon stable isotope ratios and carbon and nitrogen amounts by the University of California Santa Cruz Stable Isotope Laboratory using a CE Instruments NC2500 elemental analyzer coupled to a Thermo Scientific DELTAplus XP isotope

ratio mass spectrometer via a Thermo-Scientific Conflo III. Measurements are corrected to VPDB for $\delta^{13}C$. Measurements are corrected for size effects, blank-mixing effects, and drift effects. Typical reproducibility is significantly better than 0.1 ‰ for $\delta^{13}C_{OM}$.

3.4.3 P/Ca Measurements

Approximately 10mg of each carbonate sample was dissolved in acetic acid buffered to a pH of 4.5 for P/Ca analyses. A weak acid was used to avoid dissolution of organic phosphorus and phosphate minerals [192]. P and Ca concentrations were measured on an Element XR ICP-MS. Single element P and Ca isotope standards were used to construct calibration curves between 5 and 100ppb P, and between 5 and 75ppm Ca. Accuracy of P/Ca calculations was tested using a marine coral.

3.4.4 XRF and S K-Edge XANES

X-Ray Florescence (XRF) maps and sulfur X-ray absorption near-edge structure (XANES) spectroscopy measurements were made at the TES Beamline 8-BM [200] at NSLS-II at Brookhaven National Laboratory. Microbeam spot size was 4x4 um for spot 1, 7x4 um for spot 2, and 12x6 um for spot 3, to optimize signal for each particle's size. Replicate scans (30, 20 and 15 for spots 1, 2 and 3) were measured by continuous (on-the-fly) scanning of incident beam energy (1.75 minutes per scan). Peak-fitting analysis of sulfur speciation was carried out using a procedure modified from Einsiedl et al. [201] and using the corrections for absorption cross-section reported by Xia et al. [202]. Results were compared to those reported by Huffman et al. [203] for a variety of coal samples.

Acknowledgements

This chapter reflects a manuscript in preparation with the following coauthors: Terrence Blackburn, Mathis Hain, Slawek Tulaczyk, Colin Carney, and Jessica Gagliardi. We thank Pratigya Polisar, James Zachos, Graham Edwards, and Daniel Ibarra for helpful discussion during the preparation of the manuscript. This research was funded by the NSF graduate research fellowship, NSF 2042495, and NSF 2045611.

3.5 Figures and Tables

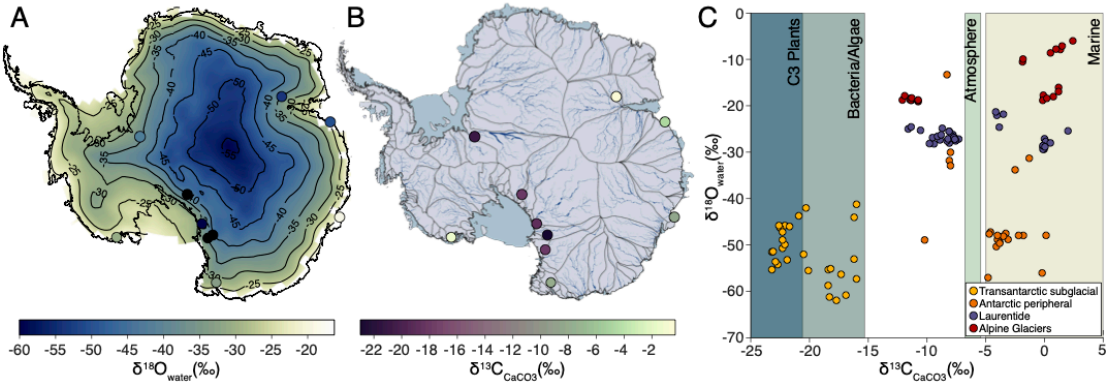

Figure 3.1: Subglacial carbonate precipitates provenance and isotope compositions. (A) Contour (black lines) and colormap of oxygen isotope composition of modern Antarctic ice [150]. Markers indicate location of subglacial precipitate measurements and are colored by $\delta^{18}O_{water}$. **(B)** Map of modeled [159] subglacial water drainage patterns beneath grounded ice sheet (blue) and glacial catchments (black) [160]. Markers indicate location of subglacial precipitate measurements and are colored by $\delta^{13}C_{CaCO3}$. **(C)** Carbon and Oxygen isotope compositions of subglacial precipitates and subglacial carbon sources. Markers indicate carbon and oxygen isotope compositions in subglacial precipitates. Rectangles are range of $\delta^{13}C$ values in potential subglacial carbon sources. Laurentide and Alpine data compiled from [45,181–189].

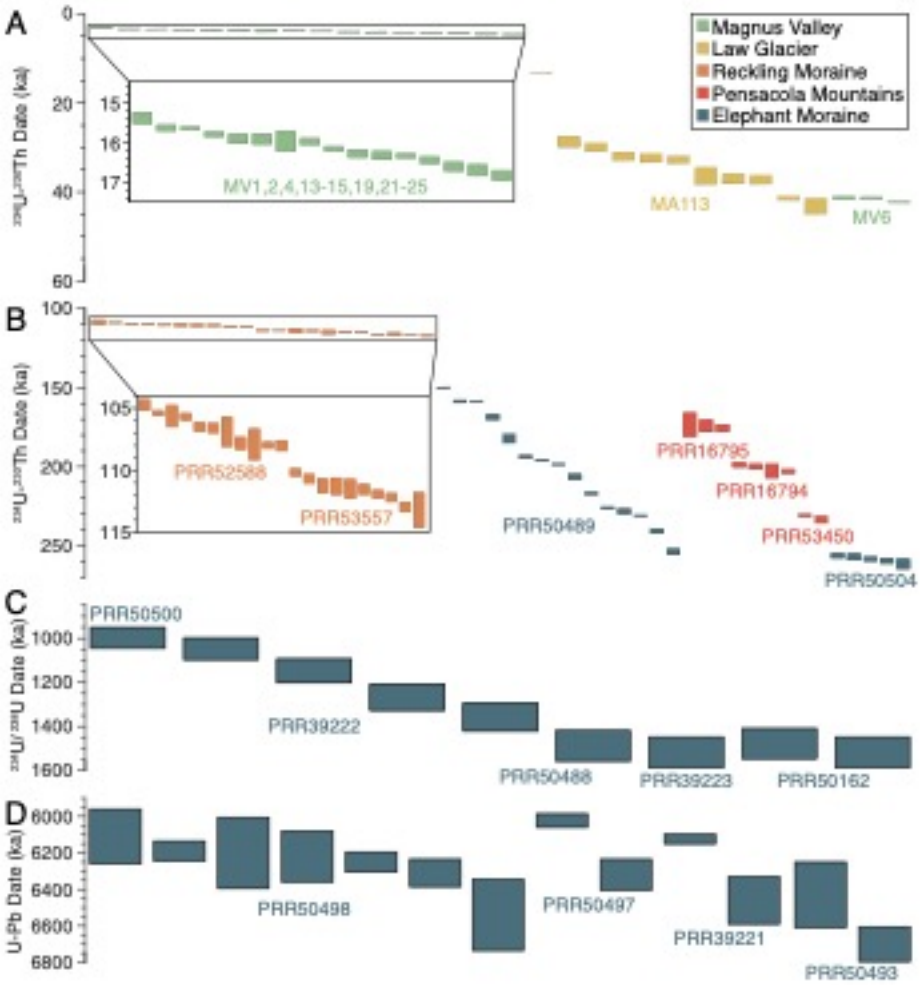

Figure 3.2: Subglacial precipitate formation ages. (A,B) ^{234}U-^{230}Th dates from subglacial precipitates formed during the Pleistocene. **(C)** $^{234}U/^{238}U$ dates from subglacial precipitates formed during the Pliocene. **(D)** ^{238}U-^{206}Pb dates from subglacial precipitates formed during the Miocene. Colored vertical bars represent dates for individual subglacial precipitate analyses with ±2σ uncertainties; they are color coded by sample collection area (legend).

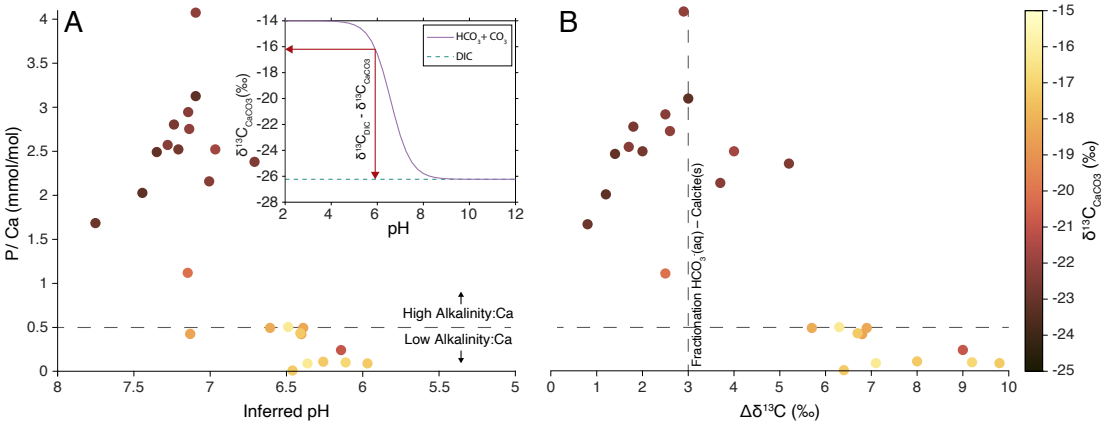

Figure 3.3: P/Ca versus the inferred pH and $\Delta\delta^{13}C$ in Antarctic subglacial precipitates. P/Ca values above 0.5 denote high alkalinity-to-Ca ratios [192]. Inset in **A.** shows the relationship between $\delta^{13}C_{CaCO3}$ and pH, with the $\delta^{13}C$ value of calcite denoted by the purple curve. This relationship allows for inference of parent water pH based on $\delta^{13}C_{OM}$ - $\delta^{13}C_{CaCO3}$.Vertical dashed line in **B.** denotes the amount of fractionation, in ‰, between HCO_3 and calcite. Markers are colored by $\delta^{13}C_{CaCO3}$.

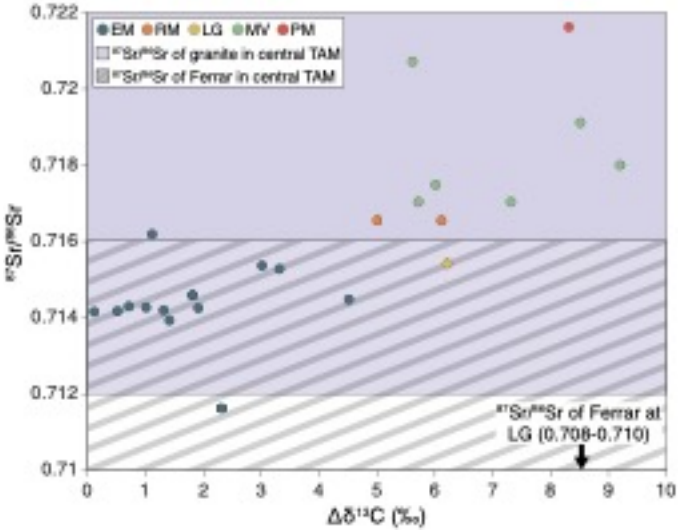

Figure 3.4: $\Delta\delta^{13}C$ versus $^{87}Sr/^{86}Sr$ of Antarctic subglacial precipitates from the Transantarctic Mountains. Markers colored by collection area (legend), which including Law Glacier (LG), the Pensacola Mountains (PM), Magnus Valley (MV), Reckling Moraine (RM), and Elephant Moraine (EM). Blue shaded area highlights the range of $^{87}Sr/^{86}Sr$ (.712-0.758) of Paleozoic granites from the central Transantarctic Mountains [193]; grey hatched region highlights the range of $^{87}Sr/^{86}Sr$ (.709-0.716) of Ferrar basalt and dolerite from the central Transantarctic Mountains [42].

Table 3.1: Sr isotope composition of Antarctic subglacial precipitates

Sample ID	87Sr/86Sr	ABS STD err (1σ)
19ACAG8a	0.728805	6.8832E-06
19ACJS01	0.747379	6.6694E-06
19CS01	0.727004	6.1737E-06
19CS02	0.709175	5.7708E-06
PRR7130	0.713622	6.2938E-06
PRR13801	0.714122	7.4674E-06
PRR16794	0.721604	6.1397E-06
PRR16795	0.722262	6.6383E-06
PRR16801B	0.721208	6.5747E-06
PRR23247	0.713891	6.6700E-06
PRR39221	0.715040	5.8741E-06
PRR39222	0.714132	7.0073E-06
PRR39223	0.714218	6.9926E-06
PRR50162	0.714121	3.2553E-05
PRR50488	0.714233	2.7690E-05
PRR50493	0.714444	7.5738E-06
PRR50498	0.716153	6.3637E-06
PRR50499	0.715244	6.4616E-06
PRR50500	0.714267	9.2031E-06
PRR50504	0.714298	6.2949E-06
PRR53450	0.721614	6.5860E-06
MV1	0.716246	2.5404E-05
MV2	0.717814	6.0380E-06
MV3	0.720361	1.0462E-05
MV4	0.719078	6.7474E-06
MV5	0.717450	8.9053E-06
MV6	0.720682	8.5932E-06
MV13	0.717322	8.2061E-06
MV14	0.717495	6.3426E-06
MV15	0.717432	6.7568E-06
MV19	0.717380	6.0775E-06
MV21	0.717360	6.3839E-06
MV22	0.717782	2.9247E-05

Table 3.2: C and O isotope composition of Antarctic subglacial carbonate precipitates.

Sample identifier	δ13C Total Carbon (‰ VPDB)	δ18O (‰ VPDB)	δ18O (‰ SMOW, WATER @ 273.15 K)
19ACJS01-1	-0.24	-51.94	-54.95
19ACJS01-2	-0.16	-53.11	-56.12
19ACJS01-3	-0.22	-53.39	-56.40
19ACJS01-4	-0.35	-53.15	-56.16
19ACJS01_5	-0.19	-47.50	-55.84
19ACJS01_6	-0.07	-52.83	-50.53
19ACAG8a_1	-7.88	-30.15	-33.23
19ACAG8a_2	-7.86	-30.08	-33.16
19ACAG8a_3	-8.09	-29.97	-33.05
19ACAG8a_4	-8.10	-29.96	-33.05
19ACAG8a_5	-7.82	-30.24	-33.32
19ACAG8a_6	-8.03	-30.09	-33.17
19ACAG8a_7	-8.08	-30.10	-33.18
19ACAG8a_8	-8.05	-29.95	-33.03
19CS01_1	-1.00	-27.94	-31.03
19CS01_2	-1.17	-28.17	-31.26
19CS01_3	-1.05	-27.97	-31.06
19CS01_4	-1.31	-28.23	-31.32
19CS02_1	-2.51	-30.64	-33.72
19CS02_2	-2.52	-30.70	-33.78
19CS02_3	-2.43	-30.08	-33.16
MM2_1	-4.02	-54.84	-57.84
MM2_2	-4.39	-53.92	-56.93
MM2_3	-4.41	-54.76	-57.76
MM2_4	-4.29	-54.50	-57.50
MM3_1	-4.66	-56.73	-59.73
MM3_2	-4.56	-55.10	-58.10
MM3_3	-4.86	-55.88	-58.88
MM3_4	-4.66	-55.84	-58.84
PRR7130_1	-20.06	-47.70	-50.73
PRR7130_2	-20.32	-48.73	-51.75
PRR7130_3	-19.53	-45.21	-48.24
PRR7130_4	-19.98	-47.19	-50.22
PRR7130_5	-20.02	-47.97	-50.99
PRR7130_6	-20.48	-48.36	-51.38
PRR13081_1	-22.38	-49.76	-52.78
PRR13081_2	-22.23	-49.71	-52.73
PRR13081_3	-22.96	-48.01	-51.03
PRR13081_4	-22.48	-49.50	-52.52

PRR13081_5	-22.51	-50.20	-53.22
PRR13081_6	-22.47	-50.26	-53.28
PRR13081_7	-22.67	-51.05	-54.06
PRR13081_8	-22.50	-49.68	-52.70
PRR13081_9	-22.43	-50.45	-53.47
PRR13081_10	-22.84	-50.15	-53.17
PRR13081_11	-22.52	-50.61	-53.63
PRR13081_12	-22.27	-50.45	-53.47
PRR16794_1	-21.20	-38.70	-41.75
PRR16794_2	-21.35	-38.88	-41.93
PRR16794_3	-21.01	-39.70	-42.75
PRR16794_4	-20.52	-39.36	-42.42
PRR16794_5	-21.34	-38.87	-41.93
PRR16794_6	-20.99	-39.59	-42.64
PRR16794_7	-20.55	-39.41	-42.46
PRR16794_8	-20.37	-38.87	-41.92
PRR16794_9	-20.89	-38.79	-41.84
PRR16794_10	-21.17	-38.17	-41.23
PRR16794_11	-21.72	-40.60	-43.65
PRR16794_12	-20.56	-39.31	-42.37
PRR16794_13	-20.77	-39.41	-42.46
PRR16794_14	-20.75	-38.84	-41.89
PRR16794_15	-20.85	-38.58	-41.64
PRR16794_16	-21.01	-38.44	-41.49
PRR16794_17	-20.93	-38.23	-41.28
PRR16794_18	-21.10	-38.35	-41.41
PRR16795_1	-20.27	-38.02	-41.07
PRR16795_2	-19.64	-37.58	-40.63
PRR16795_3	-19.62	-37.60	-40.66
PRR16795_4	-20.23	-37.69	-40.75
PRR16795_5	-20.30	-37.56	-40.62
PRR16795_6	-20.53	-37.89	-40.95
PRR16801B_1	-16.04	-40.87	-43.91
PRR16801B_2	-16.11	-41.39	-44.43
PRR16801B_3	-15.85	-41.28	-44.33
PRR16801B_4	-15.85	-41.40	-44.45
PRR23247_1	-21.46	-48.61	-51.63
PRR23247_2	-22.54	-50.07	-53.09
PRR23247_3	-21.80	-49.03	-52.05
PRR23247_4	-21.77	-49.83	-52.85
PRR23247_5	-21.80	-50.05	-53.07
PRR23247_6	-21.89	-49.76	-52.78
PRR23247_7	-21.21	-49.72	-52.74
PRR39221_1	-22.38	-42.68	-45.72
PRR39221_2	-22.40	-42.70	-45.75
PRR39221_3	-22.39	-42.68	-45.72
PRR39221_4	-22.37	-42.53	-45.57

PRR39221_5	-22.54	-42.86	-45.91
PRR39222_1	-23.17	-48.44	-51.46
PRR39222_2	-22.30	-48.13	-51.15
PRR39222_3	-22.73	-48.90	-51.92
PRR39222_4	-22.74	-48.98	-52.00
PRR39222_5	-22.74	-49.01	-52.03
PRR39222_6	-22.77	-48.91	-51.93
PRR39223_1	-22.36	-49.23	-52.25
PRR39223_2	-22.68	-50.20	-53.22
PRR39223_3	-21.79	-49.88	-52.90
PRR39223_4	-21.45	-50.39	-53.41
PRR50162_1	-22.75	-48.57	-51.59
PRR50162_2	-22.81	-49.49	-52.51
PRR50162_3	-22.84	-50.24	-53.26
PRR50162_4	-22.46	-48.35	-51.37
PRR50162_5	-22.28	-48.13	-51.15
PRR50162_6	-22.81	-50.36	-53.38
PRR50162_7	-22.88	-50.15	-53.17
PRR50162_8	-22.89	-49.91	-52.93
PRR50162_9	-22.85	-49.74	-52.76
PRR50162_10	-23.14	-50.28	-53.30
PRR50488_1	-23.20	-45.15	-48.18
PRR50488_2	-22.71	-42.64	-45.68
PRR50488_3	-22.33	-44.00	-47.04
PRR50488_4	-22.72	-43.23	-46.27
PRR50488_5	-21.98	-42.10	-45.14
PRR50490_1	-22.25	-42.03	-45.07
PRR50490_2	-21.78	-42.87	-45.91
PRR50490_3	-22.00	-42.83	-45.87
PRR50490_4	-22.30	-43.14	-46.18
PRR50490_5	-22.23	-42.92	-45.96
PRR50490_6	-22.18	-42.71	-45.75
PRR50493_1	-22.73	-42.67	-45.71
PRR50493_2	-22.75	-42.68	-45.72
PRR50493_3	-22.49	-43.28	-46.32
PRR50493_4	-22.57	-42.79	-45.83
PRR50493_5	-22.61	-42.69	-45.73
PRR50493_6	-22.43	-42.84	-45.88
PRR50497_1	-22.08	-43.57	-46.61
PRR50497_2	-22.26	-44.12	-47.16
PRR50497_3	-21.91	-43.13	-46.17
PRR50497_4	-22.21	-43.88	-46.92
PRR50498_1	-22.43	-42.05	-45.09
PRR50498_2	-22.64	-42.75	-45.79
PRR50498_3	-22.44	-44.22	-47.26
PRR50498_4	-22.48	-43.12	-46.16
PRR50498_5	-22.50	-44.29	-47.33

PRR50499_1	-21.64	-42.55	-45.59
PRR50499_2	-21.60	-42.33	-45.37
PRR50499_3	-21.77	-42.49	-45.53
PRR50499_4	-21.67	-42.78	-45.82
PRR50499_5	-21.46	-42.21	-45.25
PRR50499_6	-21.48	-42.03	-45.07
PRR50499_7	-21.75	-42.43	-45.47
PRR50500_1	-23.08	-48.35	-51.37
PRR50500_2	-23.16	-49.05	-52.07
PRR50500_3	-23.23	-49.17	-52.19
PRR50500_4	-23.19	-49.04	-52.06
PRR50500_5	-23.16	-49.08	-52.10
PRR50504_1	-19.64	-51.31	-54.32
PRR50504_2	-20.55	-52.92	-55.92
PRR50504_3	-20.35	-52.67	-55.68
PRR50504_4	-20.33	-53.08	-56.09
PRR50504_5	-20.54	-53.23	-56.24
PRR50504_6	-20.38	-53.23	-56.23
PRR50504_7	-20.36	-53.22	-56.22
PRR50504_8	-20.55	-53.33	-56.34
PRR50504_9	-20.18	-52.06	-55.07
PRR50504_10	-20.24	-52.27	-55.28
PRR50504_11	-20.32	-53.97	-56.98
PRR50504_12	-20.48	-53.77	-56.78
PRR50504_13	-20.50	-54.01	-57.02
PRR50504_14	-20.36	-53.82	-56.83
PRR50504_15	-20.63	-54.07	-57.08
PRR50504_16	-20.56	-53.75	-56.76
PRR50504_17	-20.77	-53.88	-56.89
PRR50504_18	-20.83	-53.88	-56.89
PRR50504_19	-20.19	-53.01	-56.02
PRR50504_20	-18.61	-47.93	-50.95
PRR50504_21	-19.63	-50.49	-53.51
PRR53450_1	-15.75	-39.01	-42.06
PRR53450_2	-16.16	-39.11	-42.16
PRR53450_3	-12.97	-40.95	-44.00
MV1_1	-17.96	-57.02	-60.02
MV1_2	-18.62	-56.70	-59.70
MV1_3	-18.36	-56.73	-59.73
MV1_4	-18.02	-56.82	-59.82
MV1_5	-17.51	-56.66	-59.66
MV2_1	-18.42	-56.79	-59.79
MV2_2	-19.13	-56.04	-59.04
MV2_3	-18.45	-56.71	-59.71
MV2_4	-18.70	-56.81	-59.81
MV3_1	-15.97	-54.07	-57.08
MV3_2	-15.85	-54.00	-57.01

MV3_3	-15.66	-54.35	-57.35
MV4_1	-17.05	-57.58	-60.57
MV4_2	-17.08	-57.94	-60.93
MV4_3	-17.00	-57.69	-60.68
MV4_4	-16.90	-57.85	-60.84
MV4_5	-16.85	-57.82	-60.81
MV5_1	-19.31	-54.14	-57.14
MV5_2	-19.24	-55.04	-58.04
MV5_3	-19.19	-54.59	-57.59
MV5_4	-19.46	-53.57	-56.58
MV5_5	-19.41	-53.53	-56.54
MV6_1	-16.72	-51.95	-54.96
MV6_2	-17.04	-52.45	-55.46
MV6_3	-16.72	-52.75	-55.76
MV6_4	-16.97	-52.22	-55.23
MV6_5	-16.82	-52.68	-55.69
MV6_6	-16.88	-52.56	-55.57
MV11_1	-18.57	-56.54	-59.54
MV11_2	-18.61	-56.79	-59.79
MV11_3	-18.50	-56.36	-59.36
MV11_4	-18.53	-56.59	-59.59
MV12_1	-18.58	-56.17	-59.17
MV12_2	-18.60	-56.47	-59.47
MV12_3	-18.55	-56.34	-59.34
MV12_4	-18.56	-56.30	-59.30
MV13_1	-18.57	-56.22	-59.22
MV13_2	-18.53	-56.12	-59.12
MV13_3	-18.68	-56.08	-59.08
MV13_4	-18.73	-55.77	-58.77
MV14_1	-18.51	-56.61	-59.61
MV14_2	-18.59	-56.16	-59.16
MV14_3	-18.69	-55.81	-58.81
MV14_4	-18.59	-56.71	-59.71
MV15_1	-18.59	-56.10	-59.10
MV15_2	-18.59	-56.04	-59.04
MV15_3	-18.60	-56.09	-59.09
MV15_4	-18.56	-56.08	-59.08
MV16_1	-18.63	-56.12	-59.12
MV16_2	-18.46	-55.82	-58.82
MV16_3	-18.67	-55.99	-58.99
MV17_1	-18.75	-56.14	-59.14
MV17_2	-18.62	-56.44	-59.44
MV17_3	-18.78	-56.35	-59.35
MV17_4	-18.74	-56.40	-59.40
MV19_1	-18.62	-56.05	-59.05
MV19_2	-18.69	-56.26	-59.26
MV19_3	-18.62	-55.97	-58.97

MV19_4	-18.70	-56.11	-59.11
MV20_1	-16.72	-50.86	-53.88
MV20_2	-18.64	-56.08	-59.08
MV20_3	-18.78	-55.85	-58.85
MV21_1	-18.53	-56.12	-59.12
MV21_2	-18.50	-55.87	-58.87
MV21_3	-18.49	-55.79	-58.79
MV21_4	-18.70	-55.86	-58.86
MV22_1	-18.69	-55.97	-58.97
MV22_2	-18.71	-56.01	-59.01
MV22_3	-18.78	-56.05	-59.05
MV22_4	-18.74	-55.84	-58.84
MV23_1	-18.73	-55.98	-58.98
MV23_2	-18.70	-56.34	-59.34
MV23_3	-18.71	-55.82	-58.82
MV23_4	-18.48	-55.71	-58.71
MV24_1	-18.45	-56.25	-59.25
MV24_2	-18.30	-55.02	-58.02
MV24_3	-18.40	-56.25	-59.25
MV24_4	-18.25	-55.30	-58.30
MV25_1	-17.40	-57.62	-60.61
MV25_2	-17.85	-59.29	-62.28
MV25_3	-17.80	-59.16	-62.15
MV25_4	-17.69	-59.76	-62.75

Table 3.3: Carbon isotope compositions of isolated organic material from Antarctic subglacial precipitates.

Sample identifier	δ13C Organic Carbon (‰ VPDB)	C/N	Yield (µg C)
19ACAG8a_1	-23.62	4.9	0.01774359
19ACJS01_1	-26.44	9.3	0.078873239
19CS01_1	-27.04	22.1	0.026467989
19CS01_2	-28.23	22.2	0.00186755
19CS02_1	-27.17	29.4	0.339655172
PRR16794_1	-29.94	8.7	0.002121135
PRR16794_2	-23.99	15	0.225059666
PRR23247_1	-24.03	92.5	0.050712531
PRR39221	-26.04	7.7	0.007440459
PRR39222	-24.38	75.6	0.033457249
PRR39223	-24.66	57.6	0.748229548
PRR50488_1	-23.96	44.5	0.017240543
PRR50488_2	-23.98	43.8	0.016409966
PRR50490_1	-24.89	1.7	0.002054795
PRR50490_2	-25.03	1.3	0.001808696
PRR50497	-24.78	36.8	0.116029989
PRR50498_1	-24.48	0.6	0.002811736
PRR50498_2	-24.85	0.6	0.00344936
PRR50500_1	-24.68	48	0.070708687
PRR50500_2	-24.51	57.1	0.11105042
PRR50162_1	-24.92	29.2	0.414153439
PRR50162_2	-24.65	41.2	0.041331169
PRR50493_1	-27.68	4.7	0.018285239
PRR50499_1	-25.65	11.9	0.008252427
PRR50504_1	-22.52	1.9	0.001388124
PRR50504_2	-22.61	2.3	0.001529224
PRR52588_1	-24.50	26.1	0.007514895
PRR52588_2	-25.17	18.2	0.003598057
PRR53450_1	-27.2	32.5	0.027000491
PRR53450_2	-23.23	4.5	0.04010989
PRR53557_1	-23.85	20.6	0.003861695
MV2_1	-21.58	18.5	0.003459565
MV2_2	-21.18	25.5	0.004514653
MV3_1	-33.86	5.5	0.002652911
MV3_2	-34.54	5.8	0.002614434
MV4_1	-26.12	2.5	0.000939017
MV4_2	-25.76	3.7	0.001598074
MV5_1	-24.03	21.7	0.005321267
MV5_2	-25.61	20.1	0.004627916

MV6_1	-22.45	37.6	0.019860094
MV6_2	-22.65	47	0.021447549
MV11	-31.28	12.7	0.02440613
MV14	-23.71	4.6	0.035157077
MV19	-25.34	6	0.025714914
MV22	-27.14	10.2	0.020218894
MV25	-30.68	12.3	0.028758542
MM2	-19.43	13.5	0.010916719
MM3	-11.09	17.7	0.004635965

Table 3.4: U-series data from Antarctic subglacial precipitates.

Sample Name	Th (ppm)	U (ppm)	[232Th/238U] a	2σ unc	[230Th/232Th] (measured) a	2σ unc	[234U/238U] a	2σ unc	[230Th/238U] a	2σ unc	Date (uncorrected) (ka)	2σ unc	Date (corrected) (ka) b	2σ unc b	[234/238] initial (corrected) b,c	2σ unc b
19CS01_1_2	0.520	21.936	0.00774	1.26E-05	50.439	0.521	1.000	0.001	0.3904	0.00408	53.9796	0.7359	53.2685	0.8135	0.9999	0.0016
19CS02_1_1	0.327	62.3592	0.00171	2.98E-06	164.961	1.128	1.030	0.002	0.2822	0.00199	34.8759	0.3048	34.7283	0.3147	1.0326	0.0026
19ACI501_1	0.400	64.7079	0.00202	3.12E-06	554.506	1.165	1.088	0.002	1.1186	0.00292	574.7615	47.0187	574.5973	46.9244	1.4465	0.0548
PRR16794_1_2	1.126	5.23885	0.07015	6.24E-05	27.820	0.101	2.056	0.006	1.9515	0.00731	203.3920	2.3990	201.1837	2.6391	2.8754	0.0098
PRR16794_1_3	0.428	1.99831	0.06993	9.61E-05	27.713	0.168	2.060	0.003	1.9380	0.01204	199.2297	2.9660	197.0225	3.1750	2.8598	0.0151
PRR16794_3_2	0.996	7.13676	0.04552	0.000195389	44.286	0.262	2.134	0.002	2.0158	0.01475	199.4950	3.3809	198.1253	3.4640	2.9909	0.0188
PRR16794_4_2	1.632	8.24965	0.06453	0.000753488	31.202	0.442	2.118	0.002	2.0133	0.03694	202.8690	8.6914	200.9000	8.7851	2.9815	0.0486
PRR16795_2_B	2.730	6.72761	0.13238	0.000345201	13.804	0.134	2.044	0.001	1.8273	0.01842	178.3524	3.7922	173.7887	4.4377	2.7274	0.0185
PRR50504_4_1	0.036	3.12127	0.00380	1.82E-06	465.431	0.813	1.818	0.002	1.7692	0.00320	224.3455	1.3167	224.2119	1.3186	2.5402	0.0047
PRR50504_3_1	0.054	2.71511	0.00647	7.85E-06	274.389	1.431	1.817	0.002	1.7751	0.00950	226.6465	3.3363	226.4106	3.3379	2.5488	0.0142
PRR50504_A1_	0.084	3.31115	0.00828	9.36E-06	221.359	0.854	1.837	0.003	1.8323	0.00737	239.2182	2.9845	238.9370	2.9891	2.6433	0.0126
PRR50504_3_4	0.007	1.64978	0.00142	1.54E-06	1228.427	4.351	1.726	0.005	1.7385	0.00644	252.0871	3.9641	252.0479	3.9682	2.4797	0.0120
PRR50504_4_4	0.008	1.74556	0.00153	1.11E-06	1129.753	4.261	1.711	0.003	1.7330	0.00665	257.7312	3.4196	257.6732	3.4108	2.4715	0.0130
PRR50504_4_3	0.010	1.93784	0.00169	2.02E-06	1009.033	3.512	1.693	0.002	1.7051	0.00627	254.4956	3.1216	254.4320	3.1225	2.4211	0.0117
PRR50504_3_1	0.007	1.39089	0.00156	1.89E-06	1103.680	5.672	1.704	0.002	1.7201	0.00908	255.2979	4.2850	255.2438	4.2910	2.4479	0.0172
PRR50504_4_2	0.010	1.37365	0.00230	1.75E-06	749.045	2.379	1.704	0.001	1.7224	0.00563	256.6491	2.7528	256.5573	2.7516	2.4523	0.0108
PRR50504_4_1	0.011	2.60186	0.00138	3.03E-06	1246.287	9.037	1.699	0.002	1.7231	0.01305	259.6935	6.3721	259.6475	6.3803	2.4547	0.0257
PRR53450_1_2	0.666	6.67892	0.03251	6.46E-05	67.311	0.332	2.218	0.002	2.1882	0.01162	219.2345	2.9672	218.3308	3.0026	3.2615	0.0185
MV1_1_1	0.083	7.10596	0.00382	1.12E-05	92.300	1.402	2.456	0.006	0.3524	0.00545	16.6467	0.2783	16.5112	0.2857	2.5255	0.0060
MV2_1_1	0.058	7.77022	0.00244	2.10E-06	141.052	0.872	2.458	0.002	0.3446	0.00215	16.2362	0.1083	16.1499	0.1163	2.5262	0.0018
MV2_2_1	0.143	7.00275	0.00665	2.06E-05	52.991	0.609	2.455	0.005	0.3526	0.00420	16.6602	0.2152	16.4239	0.2432	2.5250	0.0054
MV2_3_1	0.185	7.89041	0.00766	1.05E-05	45.668	0.306	2.454	0.005	0.3500	0.00240	16.5325	0.1256	16.2601	0.1824	2.5238	0.0051
MV4_1_2	0.479	11.8565	0.01318	1.88E-05	24.563	0.244	2.386	0.006	0.3238	0.00324	15.6835	0.1730	15.2012	0.2919	2.4492	0.0065
MV4_3_1	0.451	11.5462	0.01275	2.04E-05	26.370	0.667	2.398	0.005	0.3363	0.00852	16.2490	0.4389	15.7845	0.4953	2.4634	0.0051
MV5_3_9	0.156	7.01869	0.00724	9.19E-06	50.037	0.164	2.456	0.002	0.3624	0.00128	17.1492	0.0656	16.8925	0.1421	2.5278	0.0018
MV5_6_3	0.035	7.39354	0.00155	1.00E-06	221.269	0.823	2.463	0.006	0.3420	0.00129	16.0681	0.0751	15.9279	0.0755	2.5312	0.0057
MV6_1_2	0.045	17.3558	0.00085	1.42E-06	1322.115	9.228	2.760	0.006	1.1177	0.00802	53.3871	0.4931	53.3604	0.4948	3.0456	0.0071
MV6_2_1	0.056	16.3017	0.00113	1.59E-06	990.150	4.190	2.762	0.009	1.1194	0.00499	53.4182	0.3686	53.3851	0.3707	3.0488	0.0098
MV6_2_2	0.047	18.7677	0.00082	1.41E-06	1377.124	8.092	2.756	0.005	1.1319	0.00693	54.3102	0.4252	54.2871	0.4255	3.0464	0.0054
MV13_1_2	0.035	7.27193	0.00159	1.84E-06	216.378	2.721	2.468	0.005	0.3440	0.00434	16.1361	0.2190	16.0802	0.2206	2.5363	0.0051
MV14_1_1	0.049	7.77565	0.00207	4.55E-06	162.376	1.310	2.462	0.011	0.3362	0.00281	15.7905	0.1573	15.7176	0.1614	2.5284	0.0108
MV15_1_1	0.040	7.40054	0.00176	4.80E-06	202.464	2.802	2.469	0.003	0.3555	0.00502	16.7015	0.2521	16.6398	0.2532	2.5401	0.0036
MV19_1_1	0.037	7.27576	0.00164	9.60E-06	209.498	1.966	2.463	0.007	0.3436	0.00380	16.1488	0.1955	16.0915	0.1971	2.5315	0.0068
MV21_1_1	0.047	7.4178	0.00208	1.19E-06	163.952	0.936	2.457	0.003	0.3407	0.00195	16.0478	0.1004	15.9744	0.1066	2.5247	0.0034
MV22_1_2	0.095	6.91774	0.00449	7.84E-06	75.181	1.089	2.459	0.002	0.3378	0.00493	15.8913	0.2467	15.7319	0.2587	2.5256	0.0023
MV24_1_2	0.101	6.83783	0.00483	2.77E-05	70.810	0.810	2.491	0.004	0.3423	0.00438	15.8912	0.2175	15.7223	0.2321	2.5594	0.0038
MV24_1_3	0.097	6.40761	0.00494	1.53E-06	67.963	0.335	2.459	0.004	0.3358	0.00166	15.7846	0.0882	15.6096	0.1230	2.5257	0.0044
MV25_1_1	0.027	20.672	0.00043	7.45E-07	1036.095	4.135	3.310	0.002	0.4444	0.00193	15.4717	0.0727	15.4604	0.0723	3.4128	0.0025
MV25_1_2	0.020	18.7861	0.00035	6.49E-07	1259.708	11.322	3.311	0.006	0.4441	0.00407	15.4547	0.1533	15.4453	0.1534	3.4139	0.0064

All calculations use the decay constants of Jaffet et al., 1971 (238U), Cheng et al., 2013 (234U and 230Th) and , Le Roux and Glendenin, 1963 (232Th)

Square brackets denote activity ratios

Data from samples MA113 and PRR50489, from Law Glacier and Elephant Moraine respectively, reported in Piccione, et al 2022

Data from sample 19ACAG8a reported in Frisia, et al., 2017.

Data from samples PRR52588 and PRR53557, from Reckling Moraine, reported in Pinter, et al., 2023

a All ratios measured with mixed 229Th-236U tracer calibrated against U-Th gravim

b corrected for detrital Th assuming an initial (230Th/.

c [234/238] initial is corrected for radiogenic ingrowth and decay based on the detrital-corected date

Table 3.6: U-Pb data from Antarctic subglacial precipitates.

Compiled U-Pb data from Antarctic Subglacial Precipitates

Fraction	Dates (Ma) 206Pb/ 238U a	±2σ abs	Composition Pb* (pg) d	Pbc (pg) e	Pb*/ Pbc f	206Pb/ 204Pb h	Isotopic Ratios 206Pb/ 238U i	±2σ %	207Pb/ 235U i	±2σ %	207Pb/ 206Pb i	±2σ %
PRR39221 OpA												
OpA_1	6.337687161	0.264142213	29.3456651	217.8950542	0.134677977	32.28375786	0.000983617	4.169850472	0.007888985	44.69321399	0.05819525	44.8250408
PRR39221 OpB												
OpB_2	6.676195961	0.052955908	24.10736677	108.9005471	0.221370484	32.35157414	0.001036181	0.793615633	0.006445287	16.85625578	0.045133496	16.41159225
PRR50493 OpA												
OpA_1	6.610194355	0.10541351	2.430771747	13.98749632	0.173781761	29.70431338	0.001025932	1.595528956	0.004773266	44.70408527	0.033758985	43.44144741
PRR50493 OpB												
OpB_1	6.777050908	0.074171526	7.834100783	48.3910975	0.161891364	28.19203242	0.001051843	1.095026754	0.006582987	23.36406285	0.045411373	22.73352941
PRR50497 OpF												
OpF_1	6.098607457	0.18786058	25.30422027	102.6194776	0.246583016	36.83180129	0.000946494	3.08184217	0.004239527	53.63950475	0.032500644	52.53974901
PRR50497 OpA												
OpA_1	6.603118473	0.388583337	15.29248088	167.549971	0.091271164	28.22754392	0.001024834	5.887860221	0.00902431	57.58955633	0.063892979	57.76799599
PRR50498 OpA												
OpA_1	6.491976013	0.151096332	41.18726017	139.5764665	0.295087426	43.13609528	0.001007575	2.328604216	0.008312024	24.15971415	0.059857956	24.26270443
OpA_2	6.580074699	0.276573318	247.3389849	1640.449018	0.150775173	32.71337456	0.001021255	4.205339739	0.009807696	36.03878479	0.069682736	36.23514703
OpA_3	6.478980164	0.165659013	31.60458542	119.4120983	0.264668203	40.98104523	0.001005557	2.558153769	0.00825181	26.65739019	0.059543585	26.75571916
PRR50498 OpB												
OpB_1	6.547267029	0.107579112	60.40560008	139.3103883	0.43360442	53.53655834	0.001016161	1.643949335	0.007446549	19.20990516	0.053172263	19.26724576
OpB_2	6.693303141	0.298049446	64.73067774	198.1517204	0.326672297	45.67187795	0.001038838	4.455262205	0.007911842	25.18782106	0.055261454	24.91897308
R50498_BlackCarbonate	-	-				18.75143252					1.204958253	0.045032898

d Total mass of radiogenic Pb.
e Total mass of common Pb.
f Ratio of radiogenic Pb (including 208Pb) to common Pb.
g Th/U ratio of magma from which mineral crystallized.
h Measured ratio corrected for fractionation and spike contribution only.
i Measured ratios corrected for fractionation, tracer, blank and initial common Pb.

Chapter 4

A 25-kyr Record of Antarctic Subglacial Trace Metal Cycling

4.1 Abstract

The supply of bioavailable iron to the Southern Ocean influences climate on glacial-interglacial timescales by regulating the efficiency of the biological pump, wherein phytoplankton growth drives CO_2 fixation and burial in the deep ocean. Antarctic subglacial meltwaters are an important source of trace metals that fertilizes present day Southern Ocean ecosystems. However, the effect of Antarctic meltwater discharge on ocean productivity over orbital timescales is unknown, in part because there are no geologic records that constrain the evolution of trace metal mobilization at the Antarctic ice-bed interface. Here we present a 25kyr record of aqueous trace metal cycling beneath the East Antarctic Ice Sheet (EAIS) measured in a subglacial precipitate that formed across glacial termination III. Variations in precipitate deposition rate and oxygen isotope composition suggest that frequent subglacial meltwater flushing events leading up to the termination supplied oxygen to precipitate parent waters. Following the termination, ice motion slowed and subglacial flushing rates decreased, causing isolation of precipitate parent waters and the development of manganous/ferruginous conditions that dissolved redox sensitive elements (Fe, Mn, Mo, Cu) from the substrate. These results support a connection between climate and

trace metal flux beneath the Antarctic ice sheet, where changes in subglacial hydrologic activity during climate cycles leads regulates trace metal concentrations in basal waters.

4.2 Introduction

Southern Ocean (SO) biological productivity exerts a central influence on the concentration of CO_2 in the atmosphere by regulating the efficiency of the ocean biological pump [204]. Despite the SO comprising the largest sink of anthropogenic CO_2 [205,206], modern primary productivity in this region is limited by the availability of iron (Fe) [207] and manganese (Mn) [208,209] in surface waters, which allows excess CO_2 upwelled from the deep ocean to leak to the atmosphere. During glacial periods and millennial-scale cold events in the past, increased iron fertilization of phytoplankton supported more efficient SO organic matter burial and resulting atmospheric CO_2 drawdown [210–212]. Glaciogenic aeolian dust is considered the primary source of the amplified Fe flux during cold climates [212,213]. However, recent studies show that Antarctic subglacial meltwater [214–219] and iceberg rafted detritus [220,221] contribute up to an order of magnitude more bioavailable Fe to the modern ocean than aeolian dust [222], suggesting that subglacial trace metal sources may significantly enhance SO primary productivity on geologic timescales [14].

Elevated trace metal concentrations in Antarctic subglacial water derive from biogeochemical weathering of bedrock in the basal environment. The continent-wide hydrologic system beneath the Antarctic ice sheet hosts abundant microbial communities that use redox pairs and nutrients sourced from the overlying ice and bedrock substrate to support their metabolism [53,223]. Throughout most of the continent,

melting of basal ice is lone source of oxygen to the ice-bed interface. Accordingly, areas with high basal melting and flushing rates tend to have more oxic waters, while microbial utilization of oxygen in less hydrologically active regions can drive subglacial waters towards anoxia [130,169]. This range of redox conditions gives rise to diverse biological niches where microbial reactions facilitate both silicate weathering [168], and trace metal cycling through processes like sulfide oxidization [11] and iron reduction [166]. Biogeochemical weathering operating over the centennial to millennial residence time of Antarctic subglacial water produces elevated trace element concentrations relative to those in seawater or typical riverine systems [12], including metals that are essential micronutrients for the SO ecosystem (e.g. Fe, Co, Mn, Cu).

The export of trace elements from the Antarctic subglacial environment to the SO may be affected by increased meltwater discharge during future climate warming [222]. Over geologic timescales, flushing of Antarctic subglacial water is regulated by Southern Hemisphere climate, where ocean forcing triggers melting of marine terminating outlet glaciers during warm periods, which causes steepening of the ice sheet surface slope and enhanced subglacial flushing rates [139,224]. Greater meltwater discharge during warm climates could increase the magnitude of trace metals released from the Antarctic basal environment. However, it is unclear how fluctuations in meltwater flow influence subglacial trace metal cycling, particularly since enhanced hydrologic activity is expected to supply more oxygen to the ice-bed interface and thus limit the solubility of redox sensitive elements. The absence of centennial to millennial-scale records documenting trace element mobility beneath the Antarctic ice sheet leads

to uncertainty in the effect of Antarctic subglacial discharge on SO primary production over geologic timescales.

To evaluate how Antarctic subglacial trace metal cycling responds to climate, we present a 25 kyr record of hydrological and chemical conditions beneath the EAIS measured in a subglacial chemical precipitate that formed across glacial termination III (TIII): the rapid transition from glacial to interglacial climates at the Marine Isotope Stage (MIS) 8-7 boundary between 251ka and 243ka [122,225]. Using ^{234}U-^{230}Th carbonate dates to construct a depositional age model, we find that a prominent transition in precipitate texture occurs during TIII. Variations in isotopic compositions (Sr, U, C, and O) and accumulation rate across this boundary support a shift in the subglacial hydrologic system, where heightened meltwater flushing rates prior to TIII give way to less frequent flushing and greater isolation of interior and peripheral waters after the termination. As a consequence of prolonged isolation following the glacial termination, precipitate parent waters become manganous/ferruginous and exhibit a dramatic increase in trace metal concentrations. These data support a connection between climate cycles and subglacial trace element mobility, where reduced hydrologic activity following terminations cause subglacial waters to become enriched in redox sensitive elements.

4.3 Results and Discussion

4.3.1 Subglacial Hydrologic Response Across Glacial Termination III

We report geochronological and geochemical data from sample PRR50504: a chemical precipitate that formed in water at the base of the Antarctic Ice Sheet, was

brought to the surface in an exhumed section of basal ice, and was collected at Elephant Moraine, East Antarctica. This precipitate – a ~2 cm accumulation of opal and carbonate – consists of two distinct textures: the bottom 1.6cm of the sample is made up of ~200μm, alternating layers of white opal and tan carbonate, and the top 0.4cm consists of brown carbonate with two black opal layers (Fig. 1a). Using ^{234}U-^{230}Th carbonate dates along a transect from the top to the bottom of the sample, we constructed an age model that constrains a 25 kyr period of deposition between 259.2ka and 224.8ka (Fig. S1; Materials and Methods). The carbonate and opal layers in the bottom section were deposited from 259.2ka to 247ka during the end of MIS 8. Following a depositional hiatus, the top carbonate formed from 239.7ka to 224.8ka during MIS 7 (Fig. 1b). Based on this age model, the boundary between the top and bottom sections of the sample represents an unconformity that occurred from 247ka to 239.7ka, coinciding with TIII (Fig. 1). The change in precipitate textures across this boundary suggests that the rapid climate change during the termination led to variations in Antarctic subglacial hydrologic system.

To characterize the composition and provenance of precipitate parent waters in the pre- and post-termination sections of PRR50504, we measured Sr, C, O, and U isotopes in carbonate layers across the sample. Carbonate isotope compositions fall on two-component mixing lines in C-O, O-Sr, and U-Sr space that have similar mixing trajectories and endmember compositions to those previously reported for Antarctic subglacial opal-carbonate precipitates [139,224] (Fig. 2). Based on the endmember compositions, PRR50504 formed from the admixture of subglacial meltwater from

beneath the EAIS interior and a cryogenic brine beneath the EAIS periphery [139]. The meltwater endmember has a low $\delta^{13}C$ value (-20.6‰) and a low $\delta^{18}O$ value (-57.5‰), which are within the range of carbon and oxygen isotope compositions of subglacial waters that originate in the EAIS interior [139,223]. The brine endmember has a higher $\delta^{13}C$ value (0‰) and a higher $\delta^{18}O$ value (-46‰), both consistent with fluid that originated in the EAIS peripheral region close to the sample collection location [139,223]. The brine endmember also has a higher $^{234}U/^{238}U$ value (2.65 versus 2.45 in the meltwater endmember), and 100-fold higher Sr concentration than the meltwater endmember, suggestive of longer periods of water-rock interaction during brine formation. Isotope compositions from both above and below the unconformity fall on these two-component mixing lines, indicating that the two sections formed from the same waters (Fig. 2). However, carbonates from below the unconformity fall closer to the meltwater endmember, suggesting that there was efficient flushing of subglacial meltwater from the ice sheet interior prior to TIII. Carbonate compositions above the unconformity fall closer to the brine endmember, indicating that their parent waters consist of a larger brine component. This greater brine fraction in the upper carbonate indicates that the precipitate parent waters experienced greater isolation from interior meltwaters following TIII.

We further examine the connection between climate change across TIII and Antarctic subglacial hydrologic activity by simulating the evolution of basal meltwater production using a reduced-complexity model of ice sheet thermodynamics, which predicts temporal variations in Antarctic subglacial melting by considering how shear

heating and conductive heat loss change in response to climate fluctuations (Fig. 1e; SI Appendix, section S1). This simulated meltwater production tracks Southern Hemisphere climate, with the highest rates of basal melting during warm periods and decreased melting during cold periods, consistent with existing records of Antarctic subglacial hydrologic activity [139,224]. Across the 25kyr depositional period of PRR50504, the accumulation rate (Fig. 1d) and depositional frequency of opal-carbonate layers (Fig. S2, SI Appendix, section S2) respond to trends meltwater production rates, suggesting that climate modulated the freeze-flush cycles that led to opal and carbonate formation in PRR50504. From 258ka to 251ka, increased meltwater input (Fig. 1d) drove more frequent centennial-scale freeze-flush cycles (Fig. S2) and higher accumulation rates (Fig. 1e). At 251ka the subglacial meltwater production reached a threshold value that was large enough to dilute the precipitate parent water to the point where it was no longer saturated with respect to opal and carbonate, causing precipitation formation to stop (Fig. 1e). The cessation of precipitate formation following dilution from subglacial meltwater is consistent with results presented by Piccione et al., [139], who showed that a typical admixture of subglacial meltwater and brine dip below carbonate saturation when the solution contains >80% meltwater. Carbonate formation in the top section of the sample resumes after meltwater input decreases past this threshold value. The ~3.3ka between TIII and the resumption of carbonate precipitation may represent the period of time over which parent waters became concentrated enough to reach carbonate saturation again. The slower accumulation rates in the top of the sample are likely the result of less frequent

subglacial flushing events (Fig. S2) resulting from diminished meltwater production rates (Fig. 1e), though they may also be affected by increased concentrations of trace metals in parent waters, which have been shown to slow inhibit carbonate precipitation[226].

Ice surface slope is the most important factor controlling Antarctic subglacial hydraulic gradients [130]. Therefore, the trends in subglacial flushing rates across TIII evident in PRR50504 (Fig. 1; Fig. S2) likely result from climate-driven changes in the ice sheet geometry that modulate meltwater supply (Fig. 1e). Similar climate forced fluctuations in Antarctic subglacial hydrologic activity has been observed in records outside of terminations [139,224]. Pleistocene glacial terminations trigger peak ice motion and thinning along the EAIS periphery [74]. Consequent subglacial shear heating and steepening of the ice surface gradient caused the highest influx of meltwater to PRR50504 parent waters during TIII (Fig. 1e). Immediately following terminations ice motion slows, but ice accumulation likely take millennia to reestablish peak glacial thicknesses. This period of slow ice motion, thin ice, and low ice surface slopes along the Antarctic margins produces the lowest rates of subglacial meltwater production (Fig. 1e), and likely causes subglacial freezing and diminished meltwater flushing intensities. Our dataset establishes this connection between climate cycles and subglacial hydrology, where the reduced subglacial hydrologic activity following TIII facilitates the isolation of precipitate parent waters from interior meltwaters.

4.3.2 Antarctic Subglacial Trace Metal Mobilization Linked to Climate Cycles

The diminished Antarctic subglacial hydrologic activity following TIII not only drove slower accumulation rates in PRR50504, but also triggered a significant shift in parent water chemistry (Fig. 3). In the pre-TIII bottom section of the sample, opal and carbonate contain little to no trace metals, save for one prominent layer with high Fe concentrations (Fig. 3). Elemental maps collected using micro-X-Ray fluorescence (μ-XRF) imaging show that this iron is concentrated in a single particulate-rich layer (Fig. 3b). Measurements of X-Ray absorption near edge structure (μ-XANES) spectra on these particles indicate that they are Fe(III)-rich silicates, consistent with detrital sediments (Fig. 4b). In the portion of PRR50504 deposited after TIII, laser ablation multi-collector inductively coupled MS (LA ICP-MS) and μ-XRF analyses demonstrate enriched concentrations of redox sensitive trace elements including Fe, Mn, Cu, S, and Mo (Fig. 3b,c). In this upper section of the sample, Fe, Mn, and Cu are abundant in particles directly above the unconformity, as well as in the two black opal layers (Fig. 3b). However, the strongest enrichments of all five elements are located in the carbonate layers (Fig. 3b). Negative correlations between trace element concentrations and Si (Fig. S3), and a lack of association with Al (Fig. S4), provide further evidence that Fe, Mn, Cu, S, and Mo are concentrated in the carbonate rather than in detrital grains or clays. Incorporation of these redox sensitive elements in the carbonate and opal layers is strong indication that they were present in high concentrations in the precipitate parent water.

Mobilization of redox sensitive elements beneath ice sheets has been attributed to suboxic or anoxic fluids where chemolithotrophic organisms drive chemical weathering of trace-metal bearing phases (e.g. sulfides, Fe or Mn-oxides) [176]. In PRR50504, we measure the elemental concentrations of Fe, Mn, Cu, and Mo, paired with Fe, Mn, and S K-edge μ-XANES to explore the redox conditions in parent waters that led to the apparent trace metal cycling following TIII. Collectively, these experiments show that the subglacial waters were near the redox boundary between manganous and ferruginous conditions during the deposition of the top section of the sample. First, Mn K-edge μ-XANES show that Mn-rich areas at the top of the sample are a Mn^{2+}-carbonate (Fig. 4c), formation of which requires reducing conditions where dissolution of Mn-oxides from the bedrock substrate drive high concentrations of Mn^{2+} in solution [227]. Second, Fe and Mn concentrations are correlated (Fig. S5) and are of similar magnitude (Fig. 3c), indicating that both Fe and Mn were highly concentrated in the parent waters. Based on Fe K-edge μ-XANES, the detritus directly above the unconformity is mixed Fe^{2+} and Fe^{3+} silicates (Fig. 4b), consistent with glaciogenic sediments weathered in anoxic environments [228]. Third, S K-edge μ-XANES show that high concentrations of sulfur (Fig. 3b) are present sulfate (Fig. 4a), meaning that parent waters did not become sufficiently anoxic to drive sulfate reduction (i.e. sulfidic or euxinic conditions). Finally, elevated Mo and Cu concentrations in the top of the sample coincide with high Mn and Fe concentrations (Fig. 3b,c), consistent with Fe-Mn-oxide dissolution in a manganous or ferruginous environment [229,230].

The manganous/ferruginous, sulfate-rich conditions that develop in PRR50504 parent waters after TIII match those in the groundwater brine beneath Taylor Glacier that is discharged from Blood Falls [166,231]. Though Blood Falls brines originate primarily from cryoconcentrated marine waters [59], the evidence presented here for brine formation in the EAIS interior suggests that similar fluids can occur in a range of subglacial settings. Given the prevalence and geographic distribution of metal-rich subglacial waters emanating from beneath Antarctica [217–219] and Greenland [222,232–234], the hydrologically isolated, suboxic environments that produce these brines are likely ubiquitous beneath ice sheets. Our dataset from PRR50504 shows that isolation and oxygen depletion in subglacial water bodies can occur in response to natural and episodic cycles in hydrologic activity, which are linked to climate change through ice sheet dynamics.

Our record of Antarctic subglacial hydrochemistry across TIII suggests that ice dynamic response to rapid warming during the termination increased the intensity meltwater flushing from the ice sheet interior to the margins. As climate cooled from peak termination temperatures, reduced ice motion, shallow ice sheet surface slope, and thinner ice reduced subglacial flushing and isolated waters on the ice sheet periphery from the broader hydrologic system. The consequent reduction in oxygen supplies led to manganous/ferruginous conditions and high concentrations of trace metals in the precipitate parent water. Collectively, these data demonstrate that the mobility of trace metals beneath the Antarctic ice sheet is controlled by feedback between climate

change, ice motion, and hydrologic flushing intensity. On this basis, trace metal flux in Antarctic subglacial meltwaters likely fluctuates in response to climate cycles.

4.4 Materials and Methods

4.4.1 U-series Isotope Measurements and Age Model

^{234}U-^{230}Th dates were produced for eight carbonate layers in sample PRR50504 at the University of California Santa Cruz (UCSC) Keck Isotope Laboratory following methods described in Blackburn et al., 2020 [148]. Samples were separated into ~2mm chunks and carbonate was digested in 3mL 7N HNO_3, which dissolves carbonate but not opal layers. The liquid was separated and spiked with a mixed ^{229}Th-^{236}U tracer. U and Th separates were purified using ion chromatography with 1mL columns of 200-400 mesh, AG1-X8 anion resin, and Sr was collected in the wash steps for later purification. Total procedural blanks were <10pg for U and <25pg for Th, which are minor relative to sample concentrations. Both U and Th isotopic measurements were conducted using the IsotopX X62 Thermal Ionization Mass Spectrometer (TIMS) housed at UCSC. U and Th samples are loaded onto 99.99% purity Re ribbon. Uranium measurements were performed as a two sequence "Fara-Daly" routine: in the first sequence, ^{234}U (mass 266) is collected on the Daly, while ^{235}U (mass 267) and ^{238}U (mass 270) is collected on the high Faraday cups equipped with $1e^{12}$ **Ω** resistors. The second sequence placed ^{235}U (mass 267) on the Daly and ^{236}U (mass 268) and ^{238}U (mass 270) on the high Faraday cups. The 266(Daly)/270(Faraday) composition was corrected using the Fara-Daly gain: (267Faraday/270Faraday) / (267Daly/270Faraday). Thorium isotope measurements were also done on the TIMS at UCSC. Thorium is

loaded in a graphite emitter and measured as a metal. Each mass of Th is measured using a peak hopping routine on the Daly. Thorium fractionation and deadtime were estimated by running NBS U-500 as a metal. Accuracy of ^{234}U-^{230}Th dates were tested using MIS 5e coral and compared to dates in ref [195], as well as a previously dated carbonate precipitate[196]. U-Th ages are calculated using codes designed at UCSC. All ages are corrected for initial [$^{230}Th/^{232}Th$] assuming a composition of 4.4±2.2e-6. As the exact [$^{230}Th/^{232}Th]_i$ is unknown, we assume this ratio from the expected composition of the silicate upper crust in secular equilibrium, allowing for a departure from this composition of 50%, and propagating this uncertainty through to the final age. Decay constants for all data and models were from ref. [197]. All uncertainties are reported at 2σ, unless otherwise specified.

To construct the stratigraphic age model for each sample, we input sample height and ^{234}U-^{230}Th dating dates into a Bayesian Markov chain Monte Carlo model that considers the age of each layer and its stratigraphic position within the sample to refine the uncertainty of each date using a prior distribution based on the principal of superposition[46].

4.4.2 LA ICP-MS Analyses

Laser ablation inductively coupled plasma–mass spectrometry (LA ICP-MS) analyses were conducted at the Facility for Isotope Research and Student Training (FIRST) at Stony Brook University, following protocols outlined in ref. [139].

4.4.3 Micro X-Ray Absorption Spectroscopy (XANES) and X-Ray Fluorescence (XRF) imaging

X-Ray Florescence (XRF) maps and X-ray absorption near-edge structure (XANES) spectroscopy measurements were made at the TES Beamline 8-BM [200], and at the XFM Beamline 4-BM at NSLS-II at Brookhaven National Laboratory. Microbeam spot size was 4x4 um for spot 1, 7x4 um for spot 2, and 12x6 um for spot 3, to optimize signal for each particle's size. Replicate scans (30, 20 and 15 for spots 1, 2 and 3) were measured by continuous (on-the-fly) scanning of incident beam energy (1.75 minutes per scan). Peak-fitting analyses for XANES were done using the Athena software[235].

4.4.4 C and O Stable Isotope Analyses

Carbon and oxygen isotope ratios were measured by UCSC Stable Isotope Laboratory using a Themo Scientific Kiel IV carbonate device and MAT 253 isotope ratio mass spectrometer. Referencing $\delta^{13}C_{CO3}$ and $\delta^{18}O_{CO3}$ to Vienna PeeDee Belemnite (VPDB) is calculated by two-point correction to externally calibrated Carrara Marble 'CM12' and carbonatite NBS-18[87]. Externally calibrated coral 'Atlantis II'[88] was measured for independent quality control. Typical reproducibility of replicates was significantly better than 0.05 ‰ for $\delta^{13}C_{CO3}$ and 0.1 ‰ for $\delta^{18}O_{CO3}$.

4.4.5 Sr Isotope Analyses

Sr isotopic measurements were made at the UCSC Keck Isotope Laboratory following protocols outlined in ref. [148]. The absolute standard error for the precipitate Sr isotope measurements reported here are between 2.8e-5 and 4.8e-6

Acknowledgements

This chapter reflects a manuscript in preparation with the following coauthors: Troy Rasbury, Paul Northrup, Terrence Blackburn, and Slawek Tulaczyk. We thank Phoebe Lam and John Hawkings for helpful discussion during the preparation of the manuscript. This research was funded by the NSF graduate research fellowship, NSF 2042495, and NSF 2045611.

4.5 Figures and Tables

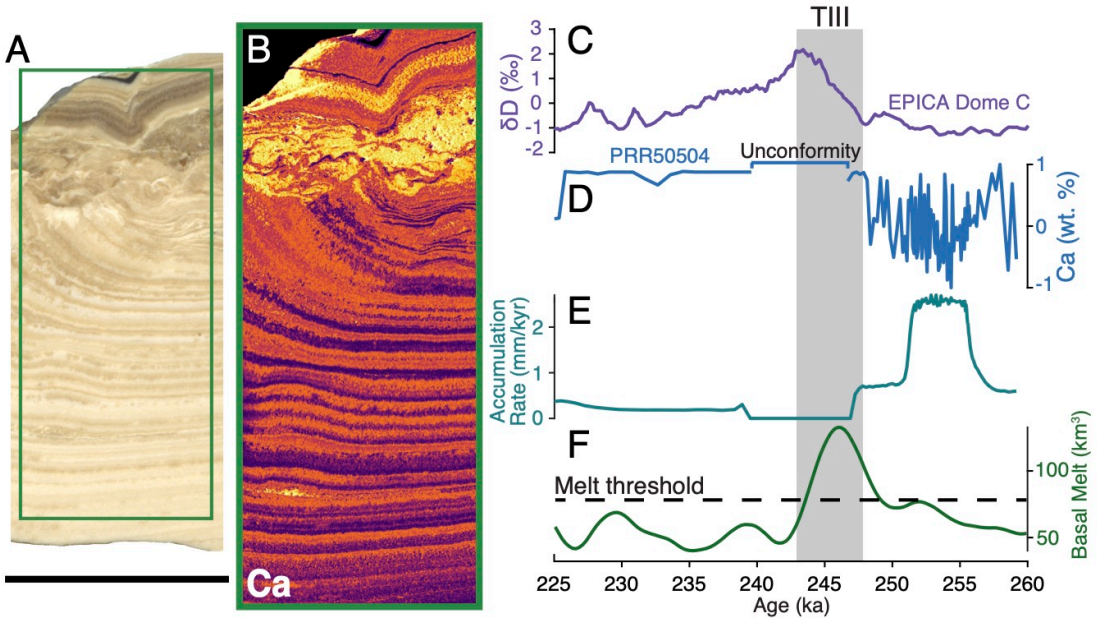

Figure 4.1: Sample PRR50504 formation timeseries versus EPICA Dome C Ice Core Record. (**A**) Plain light image of sample PRR50504. Green box delineates location of map in B. **(B)** Map of Ca measured with μ-XRF. **(C)** δD measured in the EPICA Dome C Ice Core [121,122]. **(D)** Timeseries of Ca concentration (wt%) in PRR50504. High Ca values represent carbonate layers; low Ca values represent opal layers. **(E)** Calculated accumulation rate of PRR50504. Period of time with accumulation rate of 0 corresponds to the unconformity near the top of the sample. **(F)** Modeled meltwater production rates beneath Antarctica (SI Appendix, section S1).

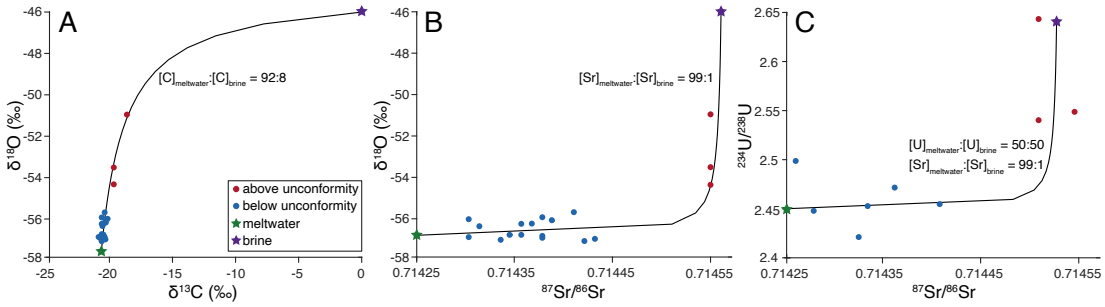

Figure 4.2: Two-component oxygen, carbon, strontium, and uranium isotope mixing models for PRR50504 carbonate layers. (A) PRR50504 carbonate data in $\delta^{18}O$ versus $\delta^{13}C$ space. Based on mixing model trajectory, meltwater endmember has a 12.5-fold higher carbon concentration than the brine endmember. (B) As in A, but in $\delta^{18}O$ versus $^{87}Sr/^{86}Sr$ space. Based on mixing model trajectory, brine endmember has a 100-fold higher Sr concentration than the brine endmember. (C) As in A and B, but in $^{234}U/^{238}U$ versus $^{87}Sr/^{86}Sr$ space. Markers represent individual carbonate measurements and are colored based on their position in the sample, where blue markers represent carbonate from the bottom section and red markers present carbonate in the top section. Stars delineate endmember compositions, with colored green for the meltwater endmember and purple for the brine endmember.

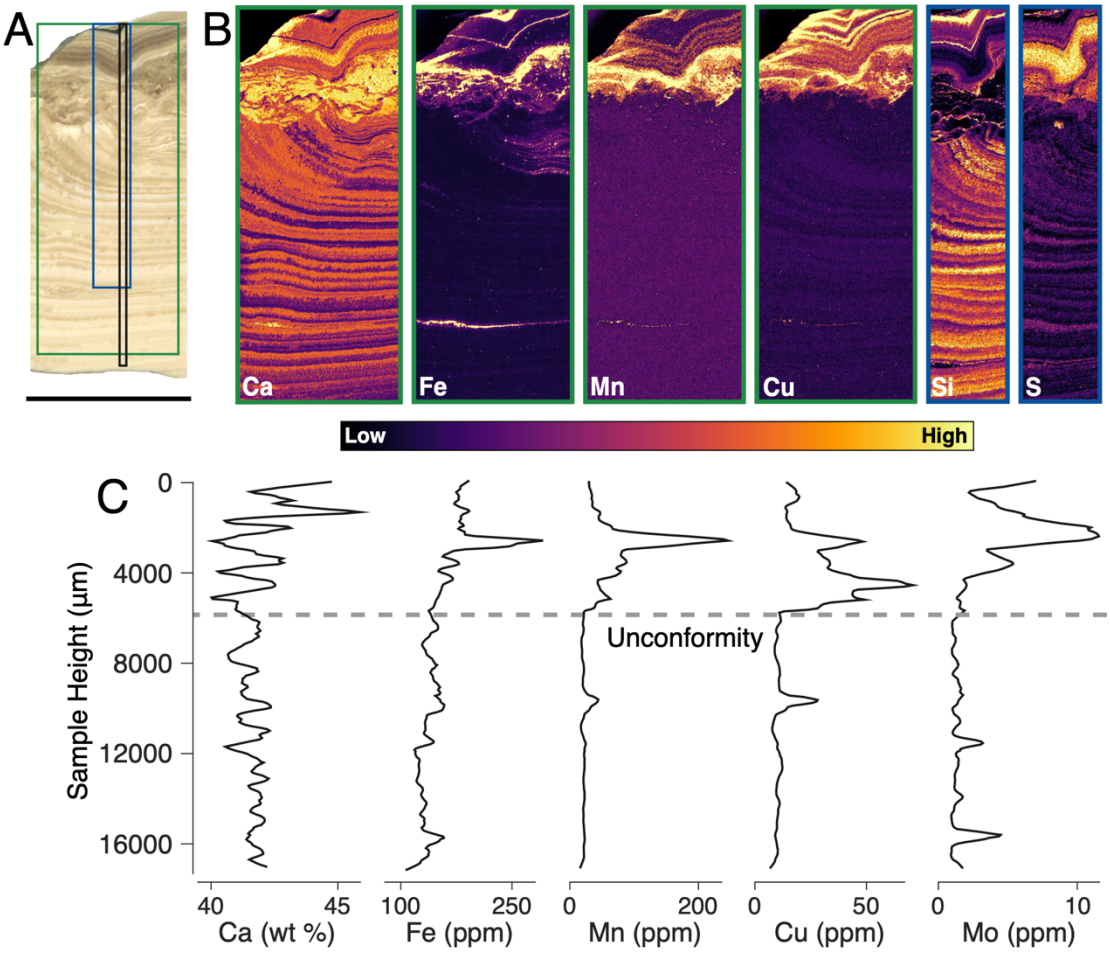

Figure 4.3: Elemental composition of sample PRR50504 measured with XRF and LA ICP-MS. (A) Plain light image of PRR50504. The green box delineates the location of Ca, Fe, Mn, and Cu µ-XRF maps in B; the blue box delineates the location of the Si and S µ-XRF maps in B; and the black box delineates the location of the LA ICP-MS analyses in C. **(B)** µ-XRF maps of Ca, Fe, Mn, Cu, Si, and S. **(C)** LA ICP-MS Ca, Fe, Mn, Cu, and Mo concentration analyses across layers in PRR50504.

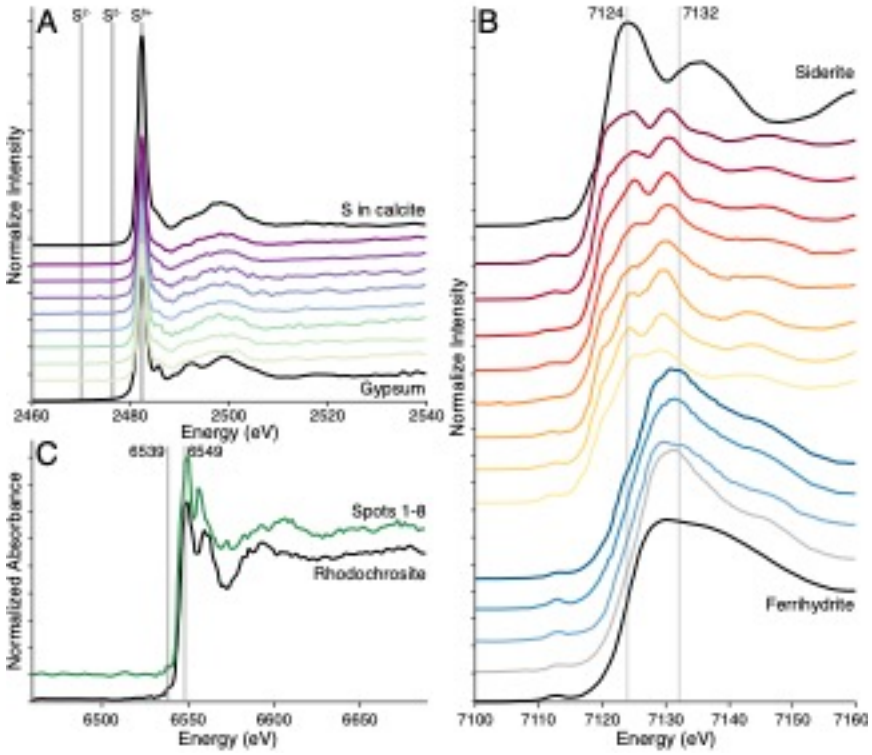

Figure 4.4: Mn, Fe, and S K-edge Micro X-Ray Absorption Near Edge Structure (μ-XANES) spectra from PRR50504. (A) Sulfur K-edge μ-XANES from eight spots in the upper section of PRR50504. All areas measured have a peak energy position that matches sulfate (S^{2+}). Black spectra are sulfur-rich carbonate (top) and gypsum (bottom) sulfate standards. **(B)** Iron K-edge μ-XANES from eleven spots in the upper section of PRR50504 (colored red to blue) and a spectrum from three spots from the lower section of PRR50504 (combined into the single grey spectrum). Black spectra are from an Fe^{2+} standard (siderite, top) and an Fe^{3+} standard (ferrihydrite, bottom). Red spectra from the upper portion of the sample have peaks at 7124 and 7132 eV that indicate mixed Fe^{2+} and Fe^{3+}. Blue and grey only have peaks at 7132eV that they consist of just Fe^{3+}. **(C)** Mn K-edge μ-XANES from eight Mn-rich spots in the upper section of PRR50504 (combined in the green spectrum) and a Mn-carbonate standard (rhodochrosite, black spectrum). Both spectra have weak pre-edge peak at 6539eV, and an edge position at 6549eV indicative of Mn^{2+} carbonate [236].

Table 4.1: Sr isotope composition of calcite and opal layers in PRR50504.

Sample Identifier	mineral	87Sr/86Sr	ABS STD err (1σ)
PRR50504_3_1	opal	0.71496418	7.27808E-06
PRR50504_3_4	opal	0.71408495	4.38131E-05
PRR50504_3_6	opal	0.71425876	5.17226E-05
PRR50504_3_6_2	opal	0.71433104	1.51415E-05
PRR50504_3_7	opal	0.71566692	2.43271E-05
PRR50504_3_8	opal	0.71513139	1.6576E-05
PRR50504_3_8_2	opal	0.71503151	1.2954E-05
PRR50504_3_9	opal	0.71417233	5.47144E-05
PRR50504_3_9_2	opal	0.71418708	0.006669169
PRR50504_3_10	opal	0.71429799	6.29488E-06
PRR50504_Bot	opal	0.71437398	1.47665E-05
PRR50504_3_1	calcite	0.71456629	1.61458E-05
PRR50504_3_1_2	calcite	0.71452919	6.39672E-06
PRR50504_3_2	calcite	0.714481	6.28602E-06
PRR50504_3_4	calcite	0.71425945	2.16571E-05
PRR50504_3_4_2	calcite	0.71425661	5.81181E-06
PRR50504_3_5	calcite	0.71425661	5.81181E-06
PRR50504_3_6	calcite	0.71442464	2.8635E-05
PRR50504_3_7	calcite	0.7146571	9.31638E-05
PRR50504_3_7_2	calcite	0.71433781	6.8886E-06
PRR50504_3_8_2	calcite	0.71432745	6.62272E-06
PRR50504_3_9	calcite	0.71437372	1.12239E-05
PRR50504_3_9_2	calcite	0.71434667	6.82119E-06
PRR50504_3_10	calcite	0.7142837	1.10271E-05
PRR50504_Bot	calcite	0.71423741	7.958E-05
PRR50504_Bot_2	calcite	0.71441927	5.64022E-06
PRR50504_4_1	calcite	0.71441793	6.14257E-06
PRR50504_4_2	calcite	0.71433784	6.23394E-06
PRR50504_4_3	calcite	0.71432638	6.49633E-06
PRR50504_4_4	calcite	0.71437365	6.64574E-06
PRR50504_4_5	calcite	0.71441002	5.90939E-06
PRR50504_4_6	calcite	0.71434851	6.82497E-06
PRR50504_4_7	calcite	0.71437016	6.39195E-06
PRR50504_4_8	calcite	0.7143045	5.9769E-06
PRR50504_4_9	calcite	0.71429538	6.83471E-06
PRR50504_4_10	calcite	0.71452829	5.70273E-06
PRR50504_4_11	calcite	0.71452505	6.49993E-06

Table 4.2: C and O isotope composition of PRR50504 calcite.

Sample identifier	δ13C Total Carbon (‰ VPDB)	δ18O (‰ VPDB)	δ18O (‰ SMOW, WATER @ 273.15 K)
PRR50504_4_11	-19.63	-50.49	-53.51
PRR50504_4_10	-18.61	-47.93	-50.95
PRR50504_4_9	-20.19	-53.01	-56.02
PRR50504_4_8	-20.83	-53.88	-56.89
PRR50504_4_7	-20.77	-53.88	-56.89
PRR50504_4_6	-20.56	-53.75	-56.76
PRR50504_4_5	-20.63	-54.07	-57.08
PRR50504_4_4	-20.36	-53.82	-56.83
PRR50504_4_3	-20.50	-54.01	-57.02
PRR50504_4_2	-20.48	-53.77	-56.78
PRR50504_4_1	-20.32	-53.97	-56.98
PRR50504_A1	-19.64	-51.72	-54.32
PRR50504_A2	-20.55	-53.34	-55.92
PRR50504_A3	-20.35	-53.09	-55.68
PRR50504_A4	-20.33	-53.51	-56.09
PRR50504_A5	-20.54	-53.65	-56.24
PRR50504_A6	-20.38	-53.65	-56.23
PRR50504_A7	-20.36	-53.64	-56.22
PRR50504_A8	-20.55	-53.76	-56.34

Table 4.3: U-series data from PRR50504 calcite.

Analysis ID	mineral	Th (ppm)	U (ppm)	[232Th/238U] a	2σ unc	[230Th/232Th] (measured) a	2σ unc	[234U/238U] a	2σ unc	[230Th/238U] a	2σ unc	Date (uncorrected) (ka)	2σ unc	Date (corrected) (ka) b	2σ unc b	[234/238] initial (corrected) b,c	2σ unc b
'PRR50504_4_11_UTh	calcite	0.0364	3.1213	0.00380	1.82E-06	465.431	0.813	1.8178	0.0020	1.7692	0.0032	224.3455	1.3167	224.2119	1.3186	2.5402	0.0047
'PRR50504_3_1_UTH_w230I'	calcite	0.0538	2.7151	0.00647	7.85E-06	274.389	1.431	1.8170	0.0020	1.7751	0.0095	226.6465	3.3363	226.4106	3.3379	2.5488	0.0142
'PRR50504_A1_1_w230I_UTH'	calcite	0.0840	3.3112	0.00828	9.36E-06	221.359	0.854	1.8366	0.0029	1.8323	0.0074	239.2182	2.9845	238.9370	2.9891	2.6433	0.0126
'PRR50504_3_4_w230I_UTH'	calcite	0.0072	1.6498	0.00142	1.54E-06	1228.427	4.351	1.7265	0.0053	1.7385	0.0064	252.0871	3.9641	252.0479	3.9682	2.4797	0.0120
'PRR50504_4_4_UTh'	calcite	0.0082	1.7456	0.00153	1.11E-06	1129.753	4.261	1.7111	0.0025	1.7330	0.0067	257.7312	3.4196	257.6732	3.4108	2.4715	0.0130
'PRR50504_4_3_UTh'	calcite	0.0100	1.9378	0.00169	2.02E-06	1009.033	3.512	1.6930	0.0021	1.7051	0.0063	254.4956	3.1216	254.4320	3.1225	2.4211	0.0117
'PRR50504_3_10_w230I_UTH'	calcite	0.0066	1.3909	0.00156	1.89E-06	1103.680	5.672	1.7045	0.0016	1.7201	0.0091	255.2979	4.2850	255.2438	4.2910	2.4479	0.0172
'PRR50504_4_2'	calcite	0.0097	1.3736	0.00230	1.75E-06	749.045	2.379	1.7039	0.0015	1.7224	0.0056	256.6491	2.7528	256.5573	2.7516	2.4523	0.0108
'PRR50504_4_1_UTh'	calcite	0.0110	2.6019	0.00138	3.03E-06	1246.287	9.037	1.6990	0.0021	1.7231	0.0131	259.6935	6.3721	259.6475	6.3803	2.4547	0.0257

All calculations use the decay constants of Jaffet et al., 1971 (238U), Cheng et al., 2013 (234U and 230Th) and , Le Roux and Glendenin, 1963 (232Th)
Square brackets denote activity ratios

a All ratios measured with mixed 229Th-236U tracer calibrated against U-Th gravimetric solution

b corrected for detrital Th assuming an initial (230Th/232Th) of 4.4±2.2e-6

c [234/238] initial is corrected for radiogenic ingrowth and decay based on the detrital-corected date

Appendix A

Supplementary Information to "Subglacial precipitates record Antarctic ice sheet response to late Pleistocene millennial climate cycles"

Reprinted from:

Piccione, G., Blackburn, T., Tulaczyk, S. et al. Subglacial precipitates record Antarctic ice sheet response to late Pleistocene millennial climate cycles. Nat Commun 13, 5428 (2022). https://doi.org/10.1038/s41467-022-33009-1

Supplementary methods

^{234}U-^{230}Th dates were produced at the University of California Santa Cruz (UCSC) Keck Isotope Laboratory. Samples were spiked with a mixed ^{229}Th-^{236}U tracer that was calibrated against a gravimetric U-Th solution for isotope dilution analyses. They were then digested in 3mL 7N HNO_3 (calcite) or concentrated 4mL HF + HNO3 (opal) via benchtop dissolution and dried down. U and Th separates were purified using ion chromatography with 1mL columns of 200-400 mesh, AG1-X8 anion resin. Samples were loaded onto the column in 1mL of 7N HNO_3 and major elements were washed off with an additional 2ml HNO_3. Loading and washing eluant was collected and saved for Sr analyses. Thorium was eluted in 2mL of 6N HCl. Uranium was then eluted in 2mL of ultra-pure water. This column procedure was then repeated to achieve U and Th purity levels necessary for analyses. Total procedural blanks were <10pg for U and <25pg for Th, which are minor relative to sample concentrations. Both U and Th isotopic measurements were conducted using the IsotopX X62 Thermal Ionization Mass Spectrometer (TIMS) housed at UCSC. U and Th samples are loaded onto 99.99% purity Re ribbon. Uranium is loaded in a Si-gel activator and measured as UO_2. Uranium compositions were corrected for oxide isobaric interferences following ref.[237]. Uranium measurements were performed as a two sequence "Fara-Daly" routine: in the first sequence, ^{234}U (mass 266) is collected on the Daly, while ^{235}U (mass 267) and ^{238}U (mass 270) is collected on the high Faraday cups equipped with $1e^{12}$ Ω resistors. The second sequence placed ^{235}U (mass 267) on the Daly and ^{236}U (mass 268) and ^{238}U (mass 270) on the high Faraday cups. The 266(Daly)/270(Faraday) composition was

corrected using the Fara-Daly gain: (267Faraday/270Faraday) / (267Daly/270Faraday). Uranium compositions were corrected for oxide isobaric interferences following ref.[237]. Mass dependent fractionation correction was applied using a linear correction with correction factor determined from long-term measurement of standards. Uranium dead times for the Daly were calibrated using NBS U-500. Accuracy of the uranium method is evaluated using Uranium standard NBS4321 (Supplementary Fig. 8). Thorium isotope measurements were also done on the TIMS at UCSC. Thorium is loaded in a graphite emitter and measured as a metal. Each mass of Th is measured using a peak hopping routine on the Daly. Thorium fractionation and deadtime were estimated by running NBS U-500 as a metal. Accuracy of ^{234}U-^{230}Th dates were tested using MIS 5e coral and compared to dates in ref [195], as well as a previously dated carbonate precipitate[196]. U-Th ages are calculated using codes designed at UCSC. All ages are corrected for initial [$^{230}Th/^{232}Th$] assuming a composition of 4.4±2.2e-6. As the exact $[^{230}Th/^{232}Th]_i$ is unknown, we assume this ratio from the expected composition of the silicate upper crust in secular equilibrium, allowing for a departure from this composition of 50%, and propagating this uncertainty through to the final age. Decay constants for all data and models were from ref. [197]. All uncertainties are reported at 2σ, unless otherwise specified.

Supplementary Note 1

In the main text, we have briefly discussed the potential source areas of the two precipitate samples: MA113 and PRR50489. Here, we provide further relevant details.

Sample MA113 is found at Mount Achernar Moraine (henceforth MAM; 84.2°S, 161°E), a nearly motionless body of blue ice on the side of Law Glacier, with average surface velocity of about 25 m a^{-1} [39]. The moraine is located ca. 20 km downstream of the polar plateau, and its debris is derived locally, with Beacon and Ferrar Group rocks dominating the sample collection area. The subglacial origin of the geologic material is supported by an abundance of striated and faceted clasts[15]. Subglacial debris is transported to the surface of MAM with upward-flowing ice from the depths of Law Glacier, and is accumulated on the surface as the surrounding ice sublimates (e.g., figure 9 in ref. [15]). Graly et al. (2018) inferred that the most plausible mechanism of subglacial entrainment of the debris is regelation in an open hydrological system and assessed that suitable conditions for this process exist 30-50 km upstream from the moraine[48]. The length of time for the emergence of basal debris to MAM is estimated to be at least 35 ka[15], which is close to the youngest radiometric U-series age obtained for sample MA113 (25.44 ± 0.59 ka). The similarity between the two timescales supports the possibility that the sample formed in a location much more proximal to MAM than 30-50 km, perhaps in one of the overdeepenings or steps in bedrock topography in Law Glacier valley that can be found within several kilometers of the moraine (e.g., Figure 7 in ref. [39]). Such a topographic depression represents suitable settings for precipitate formation because the bed geometry would allow subglacial waters to become isolated and overconcentrated to the point of opal precipitation during regional basal freezing periods and millennial cold phases. Calcite precipitation may occur as the regional basal water system reconnects to topographic depression during

the regional expansion of basal melting, which is associated with warm AIM phases in our model (Fig. 6). Whereas we cannot pinpoint the exact location from which the sample MA113 originated, we conjecture that it was formed in a subglacial topographic depression located several kilometers to a few dozens of kilometers upstream of MAM.

Sample PRR50489 comes from Elephant Moraine (henceforth EM; 76.3°S, 157.3°E), a supraglacial moraine in a blue ice area of Transantarctic Mountains, where ice sublimation persisting for estimated ~100 ka released debris from basal ice of the East Antarctic ice sheet[40,41]. The current sublimation rate in the area is ca. 0.04 m/year [238]. It is not yet proven what triggered the formation of EM, but it could have been related to a capture of the upper part of Mawson Glacier drainage by the southern tributaries of the David Glacier, which experienced vertical incision of hundreds of meters in the last 234 kyrs[77]. This switch from eastward ice flow towards the modern Mawson Glacier to northward flow towards David Glacier could have aided the emergence of basal ice layers at the EM. In the discussions below, we will assume that at the time of PRR50489 formation, which predates the formation of the EM itself, ice upstream of the moraine was flowing towards Mawson Glacier. However, none of our fundamental inferences would change significantly if, instead, we assumed that the modern ice flow pattern (i.e., ice flow from EM north towards David Glacier) prevailed then.

Rocks found on the surface of EM include material from the Beacon and Ferrar Supergroups and some Tertiary fragments with Neogene marine microfossils, interpreted to have come from the subglacial Wilkes Basin located to the west of the

mountain range[239]. We use the simple method employed in ref. [39] to estimate the time needed for our subglacially formed sample to emerge from the bed through 1.5-2.0 km of ice, which are the typical ice thicknesses upstream of EM in the Bedmap2 dataset[31,240]. To approximate the emergence timescale, we divide ice thickness by the sublimation rate and get a range of ca. 40-50 ka. To glean information about the precipitate source area from this emergence timescale, we must also account for the time that the sample may have spent laying on the surface of EM. Cosmogenic surface exposure ages of EM boulders were measured to be up to 60 ka [241], and meteorites found nearby have exposure ages up to 100s of thousands of years[242]. Given the significant uncertainties associated with the emergence timescale and the surface-residence timescale for this sample that was still precipitating in subglacial water <145 kyr ago, we conservatively assume a wide temporal range, 10-100 kyr, for the period it spent both traveling horizontally in basal ice and sitting on top of the moraine. Whereas the ice surface velocity over EM itself is very slow (<0.1 m/yr)[40], the proximal upstream part of the southern drainage area of David Glacier moves at ca. 5 m/yr [243]. Using the modern flow configuration[244,245], the longest ice flowline reaching EM from the regional ice divide separating drainage basins of David and Mulock Glaciers is ca. 150 km. In theory, our sample could have traveled from this area if its average velocity over our assumed upper bound for horizontal travel (100 kyrs), was 1.5 m/yr. However, this is likely to be too large an average basal transport velocity to assume over such an extended period, which includes cold glacial conditions with accumulation rates, and hence also balance ice velocities, that were 2-3 times lower than Holocene rates[71]. In

addition, a debris fragment embedded in basal ice travels at velocities lower than the surface ice velocity. For instance, in their analysis of basal debris transport to MAM, Kassab et al. (2019) assumed an average transport velocity of 0.5 m/yr even though ice surface velocities within Law Glacier are about 25 m/yr [39]. In the slower flowing region (surface velocity of 5 m/yr) upstream of EM this would be equivalent to basal transport velocity of 0.1 m/yr. At such speed, our sample would have traveled only 1-10 km in the assumed period of horizontal transport ranging from 10 to 100 kyrs. We conjecture that PRR50489 formed in a basal overdeepening within a relatively small range away from EM. Although the horizontal resolution of Bedmap2 bed topography is worse here than in the vicinity of MAM, it contains an indication of a broad overdeepening that starts a few kilometers upstream of EM

Supplementary Note 2

It is conceivable that the cyclicity in opal and calcite result from melting of compositionally distinct basal ice proximal to the precipitate formation location, rather than from geographically distinct water sources. For this explanation to be viable, would require that the opal forming basal ice be free of dissolved carbon, to prevent calcite formation upon freezing requisite for opal saturation. Basal ice, however, is noted to be highly enriched in carbon relative to meteoric ice[52,53,246]. A second requirement is that calcite forming basal water need have $\delta^{18}O$ compositions more ^{18}O-depleted than any known ice in Antarctica. The $\delta^{18}O$ compositions of sample MA113 (-61.2‰) is more ^{18}O-depleted than any known ice in Antarctica, likely meaning that this endmember water experienced some degree of freezing in transit to the ice margin.

A plausible scenario begins with ice melting beneath the wet based portion of the EAIS, 20km up glacier from MA, such as the -55 to -59 ‰ $\delta^{18}O$ compositions observed within the South Pole ice core[247]. Those waters, as they migrate from the thick, wet-based portion of the EAIS towards the margins, will undergo freezing, further depleting the $\delta^{18}O$ compositions of the water and forming basal ice that is *enriched* relative to the initial melt[248]. Collectively, these requirements suggest that both opal and calcite forming endmembers brought to the precipitate formation location in the aqueous phase, rather than as basal ice.

A second alternative precipitate formation mechanism was presented by Faure and others[249] to explain EM precipitates, and proposes that opal-calcite samples formed in subglacial hot springs when solute-rich hydrothermal groundwater interacted with melted basal ice. This explanation was made before the discovery of widespread subglacial water and brines at the base of the EAIS, when authors would have had to assume that hydrothermal groundwater is required for highly saline fluid to be present at the base of the ice sheet. We greatly expand on the geochemical characterization presented in ref. [249], add chronologic data to the EM precipitates, and find a similar subglacial precipitate from Law Glacier that forms via the same mechanism. These new data require two geographically distinct waters to mix on timescales matching SH millennial-scale climate cycles. In the following paragraph, we outline geochemical evidence that opposes a hydrothermal origin for these opal-calcite precipitates.

The two precipitates presented in this manuscript have isotopic compositions of carbon, oxygen, and uranium that would be highly improbable in the hydrothermal

formation scenario presented in ref. [249]. The $\delta^{13}C$ of the calcite endmember water for both samples clusters tightly at a highly negative value (ca. -23‰ for PRR50489 and ca. -18‰ for MA113). As described in the main text, this composition requires that microbes in the aqueous system selectively oxidized the most readily available carbon source (likely fossil terrestrial organic matter). Such uniform $\delta^{13}C$ values have been found in sediment-rich basal ice beneath the AIS[52,53], and have been hypothesized in subglacial aqueous environments[157,250]. If a hydrothermal water supplied carbon to the aqueous system, the $\delta^{13}C$ of that carbon would be similar to TAM soils (0.2 – 8.5‰ [251]) and therefore offset by 23 – 31‰ from the ~ -23‰ values measured in subglacial precipitates. Likewise, the $\delta^{18}O$ value of calcite-endmember water in both samples also appears too low to reflect a hydrothermal source. For sample PRR50489, the calcite-endmember $\delta^{18}O$ value (-55.3‰) is close to the most ^{18}O-depleted value observed in ice up glacier from EM (-56‰; Dome-C[252]), meaning that, if we conservatively assume that hydrothermal waters have a $\delta^{18}O$ between -10‰ and 10‰, >98% of the water in the subglacial system would have to come from fresh glacial meltwater. However, Antarctic meteoric ice is dominated by marine Sr and U isotopic compositions[154]. Thus, an influx of melted glacial ice would violate Sr and U isotopic values of the two samples, which instead require long-term water rock interaction[253]. What is more, the $\delta^{18}O$ value of the calcite endmember water from MA113 is -61.2‰, which is more depleted than any ice upstream of Law Glacier (South Pole Ice Core[247]). It is likely that this extremely low $\delta^{18}O$ value results from some portion of the calcite-endmember water experiencing freezing prior to mixing to form the calcite layer. For this $\delta^{18}O$

value to result from Faure's hydrothermal mechanism would require basal ice that is even more depleted than -61.2‰, which is highly unlikely given that it has never been observed in an Antarctic ice core. Finally, Enrichment in ^{234}U is consistent with a surface water and would be rare for a hydrothermal water. The extreme (500%) ^{234}U enrichment observed in our precipitates occurs from prolonged (>10 ka) water-rock interaction at the ice sheet-substrate interface. While hydrothermal water can achieve this composition following prolonged leaching of bedrock, mixing with melted glacial ice would dilute this signal with a $^{234}U/^{238}U$ signal of 1.14 [154]. Subglacial waters with elevated $^{234}U/^{238}U$ are not rare in Antarctica. Similar compositions are observed in Blood Falls brine[59], Don Juan Pond[254], and Antarctic Precipitates found at Lewis Cliff Glacier[118], the Pensacola Mtns.[148], Law Dome[61] and Boggs Valley[196]. Perhaps most importantly, precipitates from the Laurentide ice sheet[45] and Yosemite Valley[44], areas that are not volcanically active, also record ^{234}U enrichment. This prevalence of ^{234}U enrichment in subglacial waters across a wide range of space and time is an indication that long-term residence of water beneath ice sheets is a common occurrence.

In summary, our geochemical observations from precipitates MA113 and PRR50489 provide evidence that opal and calcite layers formed from mixing of two different fluids, glacial meltwater and brine. These fluids have compositions that match waters readily found beneath ice sheets, even in volcanically inactive areas. Uranium series dates from both samples demonstrate that mixing of these two fluids occurs contemporaneously with millennial-scale SH climate cycles. A formation mechanism

therefore calls on a glaciologic process for driving subglacial hydrologic changes throughout the Ross Embayment.

Supplementary Note 3

We use a reduced complexity model of ice sheet thermodynamics to demonstrate that there is a glaciologically plausible mechanism for explaining the two key observations derived from the precipitate samples MA113 and PRR50489: (i) cyclic opal-calcite precipitation from subglacial waters switching between oxygen- and carbon-poor brines and carbon- and oxygen-rich meltwaters, and (ii) the correlation between opal precipitation and millennial cold phases, and between calcite layers and millennial warm phases. Combined, these observations indicate that the subglacial water bodies in which these two samples formed, although separated by nearly 1000 km distance, experienced hydrologic isolation and cryoconcentration during millennial cold phases and became open to basal meltwater inputs during warm phases. Glaciologically, the most parsimonious explanation is that the cold millennial phases corresponded to basal freezing conditions, while warm phases to basal melting conditions in the two areas of sample formation.

Our modeling approach is inspired by the simplicity of the binge-purge model of Heinrich events[255]. In fact, initially we considered the binge-purge model to be a potential explanation for the millennial-scale opal-calcite couplets found in our samples due to the shared millennial-scale periodicity of both. However, the fundamental problem with this interpretation is that the binge-purge model predicts millennial-scale switches between basal freezing and melting for the Hudson Bay ice stream assuming

surface accumulation rates that are about one order of magnitude higher than the accumulation rates prevailing in our Antarctic study areas[66,255,256]. Hence, application of the binge-purge scaling (right-hand side of equation 12 in ref. [255]) with such small accumulation rates would yield unsatisfactorily long periodicity. Moreover, it would be a remarkable coincidence if a climatically unforced binge-purge oscillator, as proposed in ref. [255], would result in the observed correspondence between the periods of opal and calcite precipitation, and cold and warm phases of AIM cycles at two locations very distant from each other (Fig. 1). Reconstructions of recent internally driven ice stream cyclicity in West Antarctica yield periodicities of hundreds of years, which are in turn much shorter than the AIM-scale ice dynamic variability needed to explain our observations[257]. Given these considerations, we formulate the RCMIST to illustrate a glaciologically plausible link between millennial-scale climate forcing and subglacial precipitation of opal and calcite driven by changes in basal thermal regime. It is crucial to keep in mind that this model is used here solely for illustrative purposes. There are simply too many relevant observational uncertainties (e.g., locations of sample precipitation, geothermal flux at these locations, ice thickness and ice flow history during sample precipitation, etc.) to constrain a more complex model aimed at reconstructing in detail 'what really happened' during sample precipitation. Instead, our goal is to illustrate a plausible mechanism with a simple model.

Switches between basal melting and freezing conditions are controlled by the basal thermal energy balance, *E*. The three most fundamental controls on E are two sources

of heat (G = geothermal heat flow and S = shear heating accompanying ice motion), and one sink of heat (Q = conductive heat loss) (e.g., ref. [258]):

$$E=G+S-Q \quad \text{Eq. 1}$$

There is no physical reason for geothermal heat flow to vary on the timescale of AIMs. Hence, we treat it as a time invariable parameter with a value of 0.05 W/m^2 [259]. Changes in surface temperature and accumulation rate accompanying AIMs can impact the basal thermal energy balance through the conductive heat loss term, Q, but the ice sheet does mute this effect through[255]: (i) dampening the amplitude of temperature variations with depth, and (ii) introducing a time lag between surface climate forcing and basal thermal response. In ref. [255] authors pointed out that a under the purely conductive vertical heat transport, a periodic surface temperature forcing will decay exponentially with e-folding depth scale of 314 m. Given that the potential sample source areas have ice thicknesses of about 1500m[24,31,240], an AIM-scale surface temperature fluctuations of 1-3°C[86,260] would amount to 0.008-0.025°C change in ice temperature near the bed. Thicker ice would cause even more attenuation of the temperature signal and much thinner ice thickness (e.g., 1000m) would result in our model always predicting basal freezing, rather than switches between melting and freezing conditions at the ice base. Using equation 1 from ref. [261] we calculated that, even assuming an instantaneous thermal equilibration throughout ice thickness, the maximum difference between the conductive heat loss during cold and warm AIM phases would be about 0.001 W/m^2 (assuming ice thickness of 1500m, temperature

change of 3°C, and accumulation rate of 0.03 m/yr during the warm phase and 0.02 m/yr during the cold phase[262].) This is more than an order of magnitude less than the assumed geothermal flux. We will show later that it is also one to two orders of magnitude less than the contribution from the shear heating term, *S*.

The second fundamental problem with relying on vertical advection and diffusion of surface climate signals to the bed is the significant time lag with which such a transfer happens (e.g., ref. [255]). The timescale for purely conductive heat transfer can be estimated from the ratio of the square of ice thickness (*H*) to the thermal diffusivity of ice, which for *H* of 1500 m and diffusivity of 44 m^2/yr [255] yields ca. 50,000 years. The equivalent timescale for the purely advective vertical heat transfer can be approximated as the ratio of the ice thickness to the surface accumulation, which for reasonable assumptions of 1500m and 0.03 m/yr [262], respectively, also yields 50,000 years. The low accumulation rates assumed for the regions of interest are justified by both ice sheet modeling of ice sheet sensitivity to AIM forcing[24], and the fact that the two samples were found in locations where under modern conditions the surface mass balance is negative[39,263]. These low surface accumulation rates are also compatible with recent direct observations in the study regions[256] and with reconstructions of accumulation rates from the Taylor Dome ice core[66]. Although we have used one specific thickness, 1500 m, to calculate these hypothetical timescales, our results would not substantially change if we would consider a wider range of plausible thicknesses, e.g., 1000-2000 m, for which these timescales would also be in tens of thousands of years. Given that these diffusive and advective time scales are about an order of

magnitude longer than the millennial-scale AIM climate fluctuations, we do not favor variations in the conductive heat loss term (Q in equation 1) as an explanation for the cyclicity in subglacial hydrological conditions inferred from our samples.

By the process of elimination, we arrive at the shear heating term, S, in equation 1 as the most promising mechanism for triggering switches between basal melting and freezing conditions on millennial timescales. Given the slow ice motion at, and upstream of, sample collection locations[240], we approximate the shear heating term, *S*, as a product of the driving shear stress and deformational ice velocity, *U*, averaged over ice thickness:

$$S = \tau U = \frac{2A}{n+2}\tau^{n+1}H = \frac{2A}{n+2}(\rho g \alpha)^{n+1}H^{n+2} \qquad \text{Eq. 2}$$

where τ =gravitational driving stress ($\rho g H \alpha$), ρ = ice density, g = gravitational acceleration, H = ice thickness, α = ice surface slope, n = stress exponent in the ice flow law (assumed to be 3, ref. [264], table 3.3), A = ice viscosity parameter (the value for ice at 0°C in the table 3.4 in ref. [264]). We follow the simplifying assumption that all shear heating can be attributed to ice motion at/near the basal interface[65]. Equation 2 is based on shallow ice approximation assumption for an ice sheet moving through internal ice deformation. These assumptions are justified based on the relatively modest ice surface velocities dominating the two sample collection areas, MAM and EM, and the regions that feed ice into them from upstream[240,244].

Equation 2 contains two glaciological variables that vary with climate forcing, the ice surface slope and ice thickness. Since the latter is raised to a higher power (H^5) than the former (α^4), perhaps ice thickness is the preferred pathway through which millennial scale climate changes have influenced shear heating in the two sample formation areas? However, to match the observed precipitation patterns, ice thickness would have to increase during warm AIM phases and decrease during millennial cold phases. The only published model of Antarctic ice sheet sensitivity to AIM climate forcing[24] shows the ice sheet thickness decreasing with increasing temperature in both regions from which our samples have been collected. This suggests that the tendency for the ice sheet to thicken as accumulation rate increase under warming climates is overcome by an increase in the dynamic ice thinning associated with the grounding line retreat and ice flow acceleration during warm AIM phases[24]. This is certainly consistent with the fact that ice thicknesses decreased by close to 1000 m in Transantarctic Mountains[75,265] in response to climate warming after the last glacial maximum even though accumulation rates roughly doubled[71]. Similarly, Neuhaus et al. (2021) proposed that the grounding line in the Ross Embayment retreated when accumulation rates increased and advanced when they fell during Holocene millennial-scale climate variations[266].

The dynamic effect driving ice sheet evolution in response to ocean thermal forcing on grounding lines is incorporated into our simplified model of shear heating (Equation 2) through the ice surface slope, which steepens when the ice in the Ross Embayment thins during grounding line retreats (AIM warm phases) and becomes shallower when

ice sheet thickness in the Ross Embayment increases during grounding line advances (millennial cold phases). In our calculations of time-dependent shear heating we parametrize the evolution of regional ice surface slope along an ice drainage pathway connecting a sample origination region to the Ross Embayment:

$$\alpha(t) = [\Delta b + H(t) - H_{RE}(t)]/L_o \qquad \text{Eq. 3}$$

where $\Delta b =$ bedrock elevation difference between the region from which a sample originated and the part of the Ross Embayment into which ice from this region is draining (at the foothills of Transantarctic Mountains), $H(t) =$ ice thickness in the region of sample origin, $H_{RE}(t) =$ ice thickness at the foothills of Transantarctic Mountains (e.g., locations of the mouths of Law Glacier for the MAM sample and Mawson Glacier for the EM sample), $L_o =$ a length scale representing the distance between the sample origination region and the ice discharge area in the Ross Embayment. Consistent with the simplicity of our model we assume L_o to be ~100 km, which is approximately equal to the distance between MAM and EM locations and the mouths of Law and Mawson Glaciers. The bedrock elevation difference is estimated from existing bed elevation datasets[31,240] and our preferred locations of sample origin (see the discussion above). We have run multiple sensitivity tests assuming different values of Δb and L_o and the results presented below and in the main manuscript are not fundamentally dependent on the preferred values stated here being exact. The model

produces the desired switches between basal melting and freezing for wide ranges of Δb and L_o.

Whereas the ice thickness evolution in the region of sample origin, $H(t)$, is a variable calculated by the model from ice mass balance calculation (see Eq. 5 below), the ice thickness at the foothills of Transantarctic Mountains $H_{RE}(t)$ is used as the forcing function that is driving the temporal response of the simulated system to climate forcing. The underlying idea is that the climate forcing, which is represented here by isotopic records from ice cores, is driving changes in the position of the grounding lines in the Ross Embayment and, hence also the changes in $H_{RE}(t)$. Ice thickness forcing at the foothills of Transantarctic Mountains, $H_{RE}(t)$, is parametrized as a linear function of an ice core isotopic record of paleoclimate, $i(t)$, covering the time periods of sample precipitation:

$$H_{RE}(t) = H_o + C_i[i(t) - i_o] \qquad \text{Eq. 4}$$

where $H_o =$ is the initial thickness (taken from ice sheet model output of ref. [24]), $C_i =$ proportionality constant with units of meters per ‰, and $i_o =$ the initial isotopic value in ‰. For simulations of basal thermal conditions pertaining to the sample MA113 we use the $\delta^{18}O$ record from the WAIS Divide ice core[119] and for the older sample PRR50489 we use the δD record from the EDC ice core[121]. In our model the ice thickness in the sample formation area, $H(t)$, evolves through time following this simple mass-balance ODE:

$$\frac{\partial H(t)}{\partial t} = aL_a - UH(t) \qquad \text{Eq. 5}$$

where $t =$ time, $a =$ accumulation rate (0.02-0.03 m/year taken from the ice sheet model output of ref. [24]), and $L_a =$ accumulation length scale (i.e., taken to be 500 km as the approximate length of the accumulation zone upstream of the site where $H(t)$ is evaluated. The first term on the right-hand side represents an aggregated influx of ice from upstream while the second term is an aggregated outflux of ice in downstream direction. It is important to keep in mind that in this flowline formulation of mass balance, the left-hand side of this equation is implicitly multiplied by unit width, which resolves the apparent mismatch in units between the two sides of Eq. 5. The accumulation length scale should not be taken literally (e.g., as the distance from the sample origination site to the ice divide), given the fact that there is considerable flow conversion occurring as ice flow funnels from widespread upper drainage areas towards relatively narrow valleys of outlet glaciers crossing the Transantarctic Mountains. Rather, L_a is used in our model as a flowline representation of the upstream accumulation area. We examined the sensitivity of our results to different choices of L_a ranging from dozens of kilometers to over 1000 km and got the desired oscillations in basal thermal conditions when L_a ranges between ca. 300 and 800 km. For too short L_a there was only basal freezing and for too long L_a there was only basal melting. The accumulation rate is kept constant since our model sensitivity experiments indicated that varying it with time did not materially impact the model output.

One concern that can be raised about the applicability of the system of equations 4 and 5 is that they do not account for any lags between the climate forcing and the glaciological response at the sample origination sites. By neglecting these lags, we assume that they are smaller than the combined dating uncertainties of the ice core timescale and the U-series-dated sample precipitation chronology. In the case of MA113, the uncertainties in the sample age model, >1.5 kyr, are clearly higher than the uncertainties in the WAIS Divide ice core record, ~0.5 kyr [86]. For the older sample, PRR50489, we use the EDC ice core record, which has considerably higher uncertainties, 2-4 kyrs, over the period of sample precipitation[122]. In general, a lag in the glaciological response to the climate forcing would have to be >2 kyrs, to justify its inclusion in our reduced-complexity model. Below we argue that plausible response timescales are shorter than this. Propagation of glaciological perturbations takes place through kinematic-wave and diffusive processes[125], with the former dominating in low surface-slope areas moving through basal sliding (e.g., ice streams) and the latter in high surface-slope regions where ice motion is accommodated predominantly through internal deformation (section 11.3.3 in ref. [267]). As a conservative example, we will consider here the case of the MAM study area, which is located further towards the ice sheet interior than the EM region and, hence, should have longer glaciologic response times to ocean thermal forcing. Our sample precipitated in this region, MA113, formed entirely during the Marine Isotope Stage 3 when climatic conditions were colder than during the Holocene but not as cold as during the last glacial maximum[268]. There are no firm constraints on the position of the grounding line in the Ross Embayment during

MIS 3, so for simplicity we will assume that this grounding line was, on average, at the approximate position of the front of the modern Ross Ice Shelf, with fluctuations around this position during warm and cold millennial phases. This would put the point of discharge of Law Glacier into the Ross Embayment about 600 km away from the assumed average MIS 3 grounding line position. Fast flowing ice streams crossed the grounded ice in the Ross Embayment[269] and we will assume that they moved with speed of ca. 0.3 km/yr, which would translate into kinematic wave speed of ca. 1 km/yr [125]. In this scenario, glaciological effects of grounding line migration would take about 0.6 kyrs to arrive at the mouth of Law Glacier. The lower half of this glacier moves at present with high enough velocities, ca. 0.1-0.4 km/yr to infer that it is likely sliding. Hence, we will also use here the kinematic wave speed to estimate how long it would take for a glaciological perturbation at the mouth of the glacier to propagate half-way its length, i.e., ~50 km. With assumed average speed of ca. 0.2 km/yr, the kinematic wave speed is ca. 0.7 km/yr and the 50-km travel time is ca. 0.07 kyrs. The last ca. 50 km of the glacier towards the MAM experiences slow ice motion, 0.02-0.03 km/yr, suggesting dominance of internal ice deformation and diffusive processes for propagation of glaciological perturbations. Assuming average surface slope of 0.006, ice thickness of 1 km, and average ice velocity 0.02 km/yr [240,244], we estimate the horizontal diffusivity to be 10 km^2/yr, and a diffusional timescale of signal propagation of 0.25 kyrs over 50 km. Altogether, we estimate that it would take a grounding-line perturbation about 1 kyr to propagate from the grounding line to the MAM region. We justify the fact that our equations 4 and 5 do not make a provision for this lag by the

fact that 1 kyr is significantly shorter than the combined uncertainties in the chronology of our samples and of the isotopic ice core records used to force temporal variations in our model.

To produce the output shown in Figures 2e and 3e of the main manuscript text, we solved numerically the system of equations 1 through 5 using a forward-difference solver with time step of 10 years and a set of the necessary initial conditions. Each simulation was started 10,000 years before the beginning of the two precipitate records to provide model spin-up time for relaxation of the calculation from any artifacts associated with our choice of initial conditions. The basal thermal energy budget is expressed in terms of equivalent basal melting/freezing rate in units of mm/year using the volumetric latent heat of ice 3×10^8 Joules/m^3. The key tunable model parameter is C_i, the constant determining the sensitivity of ice thickness changes, $H_{RE}(t)$, to variations in isotopic records of paleoclimate (Equation 4). We used visual inspection of outputs from dozens of sensitivity runs to evaluate which values of C_i yield satisfactory agreement with the geochemical record obtained on the two samples. The sensitivity of our results to C_i is illustrated in Supplementary Figure 9a. For the set of control parameters used to generate Supplementary Figure 9a, the basal heat budget experiences switches between melting and freezing in the right time periods to explain changes between opal and calcite precipitation if the C_i parameter is between 10 and 23 m per ‰. A C_i value that is too low does not yield the expected melting-freezing switches in the last 15,000 years of the record (e.g., $C_i = 5$ m per ‰ in Supplementary Figure 9a). A C_i value that is too high results in output that predicts freezing period

between 180 and 200 kyrs BP that are too long (e.g., $C_i = 25$ m per ‰ in Supplementary Figure 9a). The satisfactory results, $C_i = 10$ to 23 m per ‰, are consistent with ice thickness changes in the Ross Embayment, $H_{RE}(t)$, of a few hundreds of meters on the millennial scale of AIM climate cycles. This magnitude of ice thickness variations corresponds to the cases of high sensitivity of the Antarctic ice sheet to ocean thermal forcing in numerical experiments of ref. [24]. Supplementary figure 10 shows equivalent results for the sample MA113, with $C_i = 10$, 50, and 250 in units of m per ‰ of $\delta^{18}O$ (since we are using the WAIS Divide ice core record for this sample). Generally, satisfactory results are obtained for MA113 when C_i is between ca. 50 and 200 m per ‰. A C_i value that is too low produces switches to basal freezing in the second half of the record that are too infrequent. While a C_i value that is too high misses some switches to basal melting (e.g., Supplementary Figure 10). Ice thickness changes that produce satisfactory results are in the range of a few hundred meters variation in $H_{RE}(t)$. This result is also consistent with the ice sheet model runs of ref. [24] that assume high sensitivity to the ocean thermal forcing.

Supplementary Note 4

Here we present preliminary thin section images and elemental maps of PRR50489 and MA113 to characterize opal and calcite textures. The hypothesized hydrologic freeze-flush mechanism for opal-calcite formation may impart certain textural characteristics to the precipitates, including delivery of detritus to the system during flushing events (i.e., in calcite layers), changes in calcite crystal growth patterns, and

evidence for detrital settling at the base of calcite layers. However, certain unknown physical parameters may preclude these textural characteristics from forming. Namely, the velocity of waters flushing during periods of subglacial connectivity is unknown and flushing events need not be catastrophic floods like those observed in active, marginal, subglacial hydrologic systems. Secondly, the timing of calcite formation, amount of sediment delivery, and frequency of flushing events during a given millennial-scale warm period are unknown and would affect the distribution of detritus within calcite layers. The amount of physically weathered detritus in the subglacial environments beneath the EAIS is likely lower in environments in the EAIS interior than in more marginal systems, where mechanical weathering is enhanced due to higher velocity ice flow[171167]. Finally, we do not know the depth nor horizontal extent of the subglacial basins, which pertains to sediment content in our samples because detritus delivery during hydrologic flushing events could be concentrated near the mouth of the basin but would not necessarily be basin wide. Therefore, while textural evidence for water motion within MA113 and PRR50489 could lend more confidence to our hypothesized hydrologic formation mechanism, the presence or absence of such features cannot confirm nor nullify this mechanism. Sample MA113 shows clear textural evidence of formation in a quiet water body that is periodically disrupted by higher energy flushing events. Opal layers fill in low points and voids in the underlying calcite and have very flat tops (Supplementary Fig. 1a, c, d), which is strong indication that they formed by settling out of a water column. Opal layers are also entirely devoid of visible detritus, indicative of formation in a low energy system incapable of clastic

delivery (Supplementary Fig. 1e, g). Conversely, many calcite layers have sand to silt-sized detritus formed during episodes of enhanced flushing energy (Supplementary Fig. 1a, c, d). In most cases detritus is concentrated at the bottom of the calcite layer pointing to flushing events ending the quiescent periods of opal growth and instigating calcite precipitation. These detritus-rich areas contain fine, <10μm-scale crystals, and give way to larger, detritus-free calcite growth of 100-1000μm-scale crystals above (Supplementary Fig. 1e, f).

Sample PRR50489 shows similar opal textures indicative of gravitational settling in a water column. However, detritus poor calcite suggests that the subglacial environment where this sample formed was much more sediment limited. However, at the base of many calcite layers, smaller crystals surround dark microdetritus or organic material that evinces hydrologic flushing and/or delivery of oxygen rich water (Supplementary Fig. 2b, c). At the tips of these layers, fibrous, clean calcite crystals grow and are eventually filled in with overlying opal.

Based on petrographic evidence of PRR50489 and MA113, we find no clear indication of diagenetic alteration in either of these subglacial precipitates. Aside from glaciotectonic disruption, opal-layers are relatively undisturbed and show no clear evidence for dissolution, which is borne out by XRD data showing that these layers remain a primary opal-A (Supplementary Fig. 3). Calcite layers are made of up delicate, fibrous crystals that also show no signs of dissolution or reprecipitation (Supplementary Fig. 1 and 2). We, therefore, regard diagenetic influence on our geochemical data to be insignificant.

Supplementary Figures

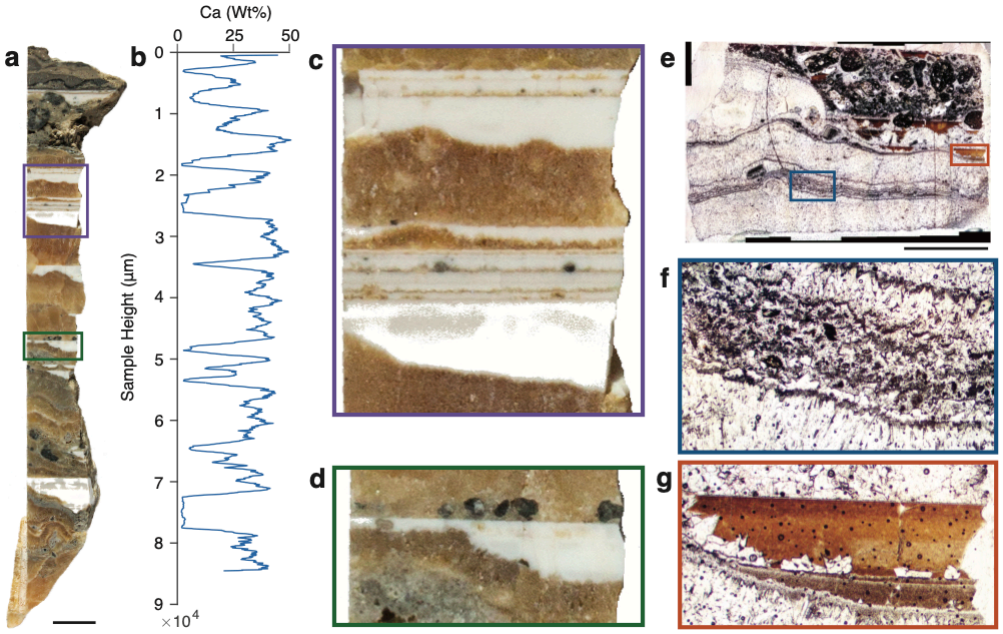

Supplementary Fig. 1 | Petrographic analysis of sample MA113. a. Plain light image of sample MA113. **b.** Slab and SEM-EDS image of second piece of sample PRR50489. Purple and green boxes outline areas highlighted in c and d respectively. **b.** Plot of Ca concentration (wt. %) in MA113 versus sample height (µm). Spectra taken from top to bottom. **c.** Zoomed in image of area in MA113. Shows clean, white opal layers that fill voids space made by underlying calcite and have flat tops, indicative of formation from gravitational settling in a water column. **d.** Zoomed in image of lower area in MA113. Detrital grains lay at the base of calcite layers above opal layers. **e.** Thin section image of upper part of MA113 in plain polarized light. Blue and orange rectangles outline areas highlighted in f and g respectively. **f.** Zoomed in image of lower portion of a calcite layer. In this area of the sample dark, detrital grains can be seen in surrounded by calcite with smaller crystals. Above this part of the layer calcite becomes detritus free and exhibits larger crystals. **g.** Zoomed in image of opal layer in MA113. Opal is devoid of detritus and drapes calcite below it. Black scale bars represent 1 cm.

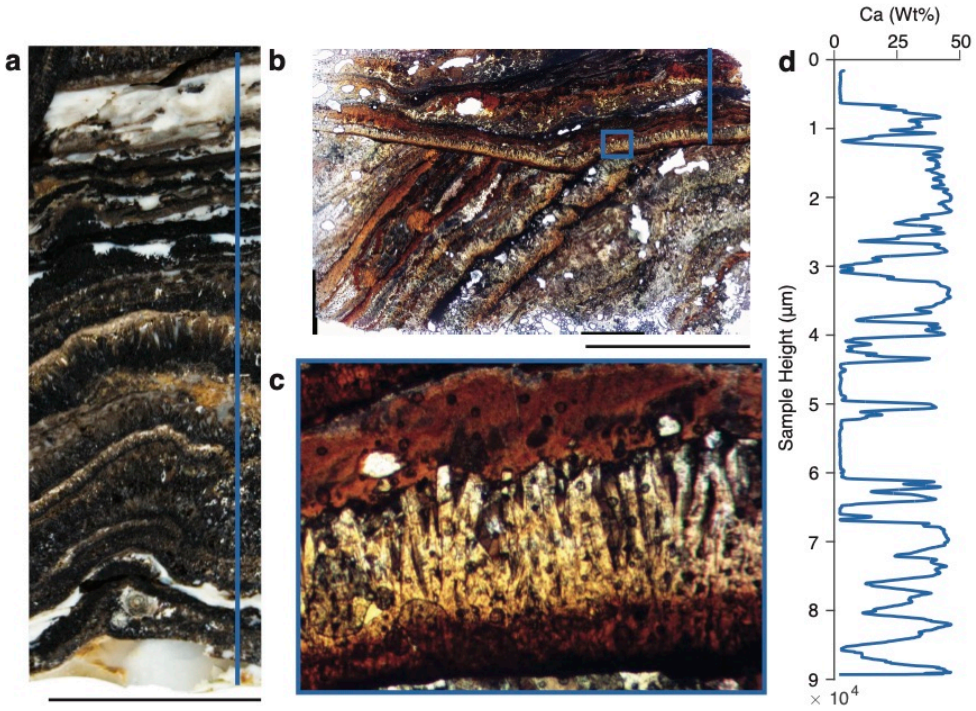

Supplementary Fig. 2 | Petrographic analysis of sample PRR50489. a. Plain light image of sample PRR50489. **b.** Thin section image of PRR50489 in plain polarized light. Blue box represents area shown in c. **c.** Zoomed in image of single calcite and opal layer. Calcite layer is bladed, with no clear indication of alteration or dissolution. Bottom of calcite layer characterized by smaller crystal size and darker color, which we interpret to be micro detritus or organic matter. Opal fills gaps in calcite crystals and drapes the calcite layer. **d.** Plot of Ca concentration (wt. %) in PRR50489 versus sample height (µm). Area where spectra were taken is represented by blue line in a and b. Spectra is taken from bottom of sample in a, and continues from bottom to top of d. Black scale bars represents 1 cm.

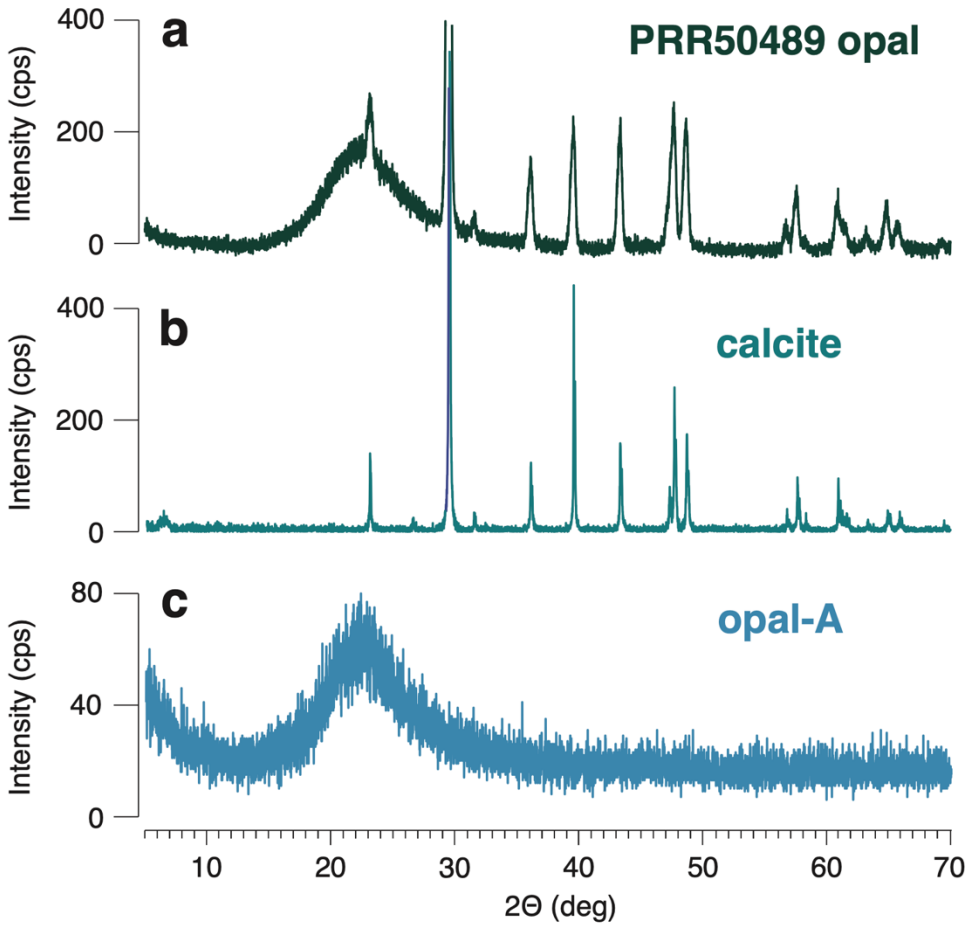

Supplementary Fig. 3 | XRD from PRR50489 opal. a. Powder XRD patterns from PRR50489 opal. This sample was not leached to remove calcite prior to sampling. So XRD patterns include both calcite and opal. **b.** Calcite XRD pattern output from Profex XRD reduction software. Peaks in calcite spectra clearly represent steepest peaks in PRR50489 spectra. **c**. Opal-A XRD pattern output from RRUF database. The largest peak at 23˚ clearly aligns with a similar peak in PRR50489 spectra.

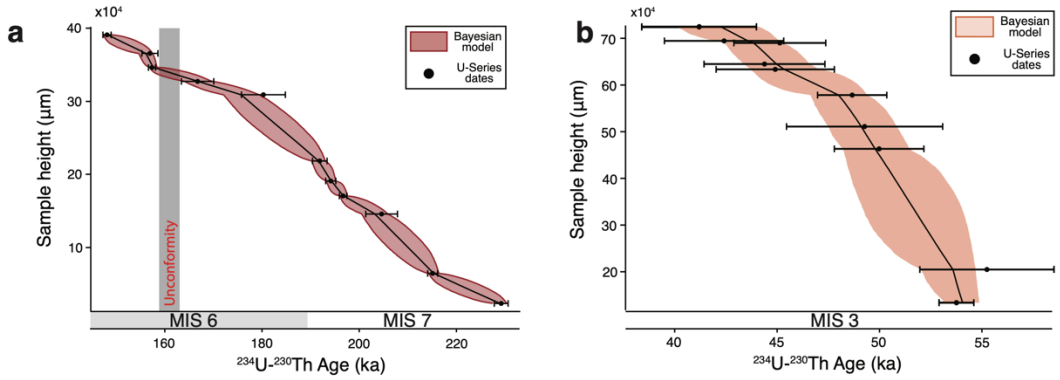

Supplementary Fig. 4 | Stratigraphic Age models. a. Height versus age curve for PRR50489. Position of angular unconformity marker in grey. **b.** Height versus age curve for MA113. Black markers are ^{234}U-^{230}Th with 2σ error bars. Red and orange envelopes are Bayesian age-depth model using stratigraphic position as a prior to refine dating uncertainties[46].

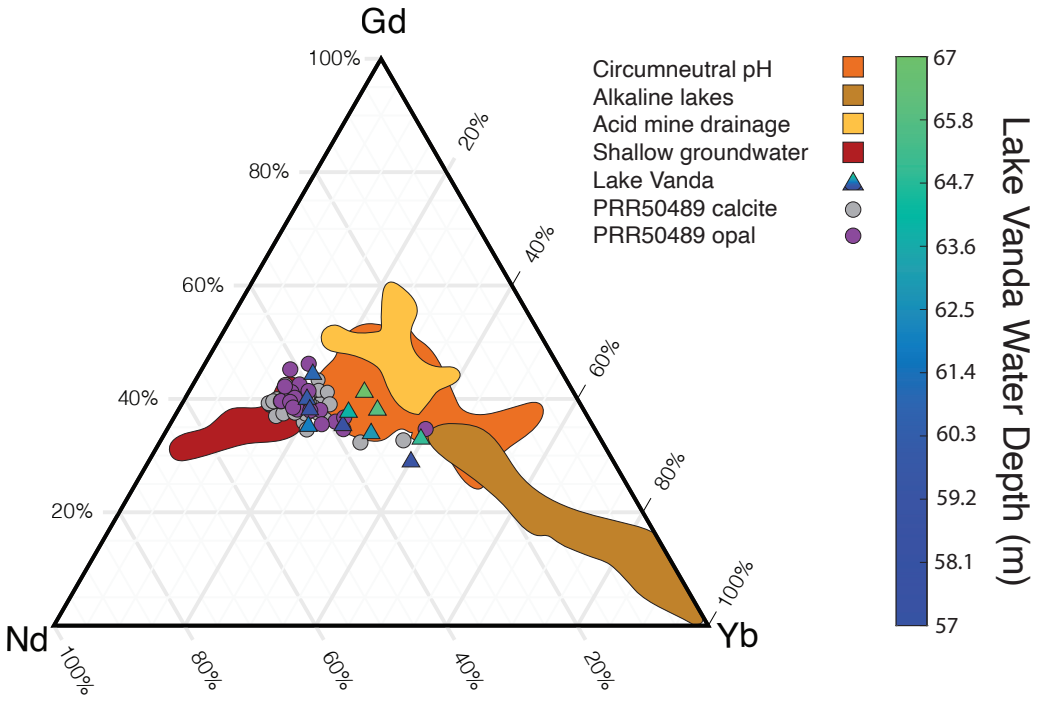

Supplementary Fig. 5 | Rare Earth Element Ternary Plot. Ternary plot with Rare Earth Elements gadolinium, neodymium, and ytterbium. Filled areas plot compositional range for different surface and groundwaters after ref.[270]. Triangles represent Lake Vanda water compositions colored based on depth from 57m to 67m depth[271]. PRR50489 calcite and opal compositions are plotted as black and blue spheres respectively. PRR50489 data were collected using LA ICP-MS.

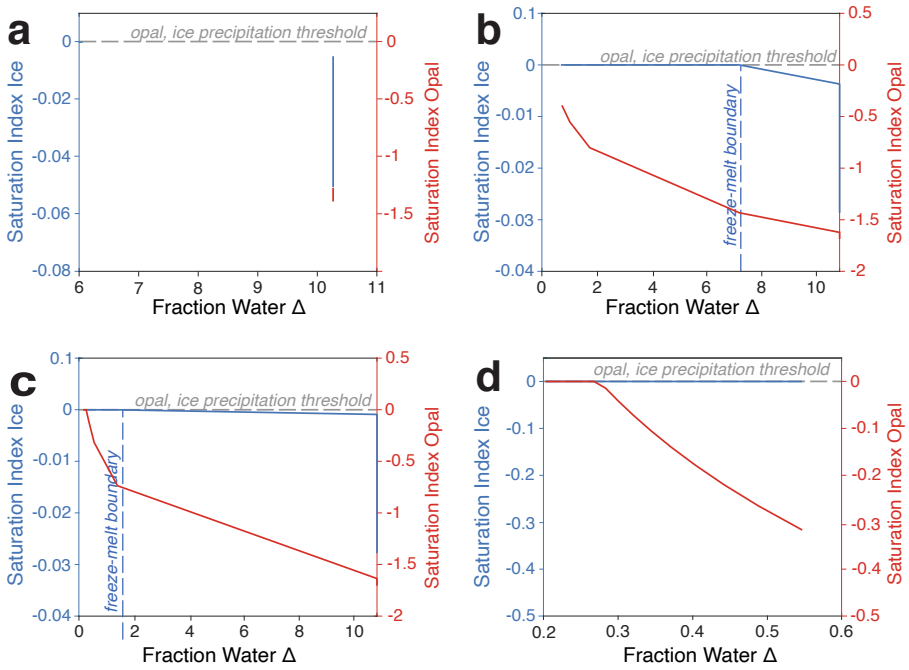

Supplementary Fig. 6 | Model simulations predicting opal formation from $CaCl_2$ brine. PHREEQC simulations of cryoconcentration of Don Juan Pond (DJP) $CaCl_2$ brine[99,108] over a range of temperatures and relative concentrations. X-axes show the relative fraction of water that enters the system (as meltwater) or leaves the system (as ice) upon equilibration of the brine with the overlying ice. Fraction water Δ values above 1 indicate meltwater addition; fraction water Δ values below indicate water loss via freezing. Plots show saturation indices (SI) — the log ratio of the ion activity product and equilibrium constant — of ice and opal. SI values greater than 0 are supersaturated with respect to that phase; values less than 0 are undersaturated. The grey, dashed lines delineate SI precipitation threshold for opal and ice. Saturation indices of calcite are not shown because the lack of carbon in DJP brine makes the solution unsaturated with respect to calcite **a.** Equilibration of concentrated DJP brine with ice and opal over a range of temperatures between -5 and 5˚C. High ionic strengths in the concentrated brine causes significant melting of overlying ice, diluting the solution with respect to opal, and inhibiting opal precipitation. **b.** Equilibration of 10x diluted DJP brine with ice and opal over a range of temperatures between -5 and 5˚C. In this case the brine starts to freeze at -2˚C, but the solution does not reach opal precipitation because the degree of freezing (i.e., cryoconcentration) of Si is suppressed by the high ionic strength of the brine. **c.** Equilibration of 50x diluted DJP brine with ice and opal over a range of temperatures between -5 and 5˚C. This solution also reaches freezing at -2˚C, but the relatively lower ionic strength allows more significant portions of cryoconcentration of Si, causing opal to precipitate near -3.5˚C **d.** Equilibration of 50x diluted DJP brine with ice and opal over a smaller range of temperatures, between -4 and -3˚C. This plot shows that opal precipitation occurs when ~75% of the water is lost via freezing, which occurs at ~ -3.5˚C.

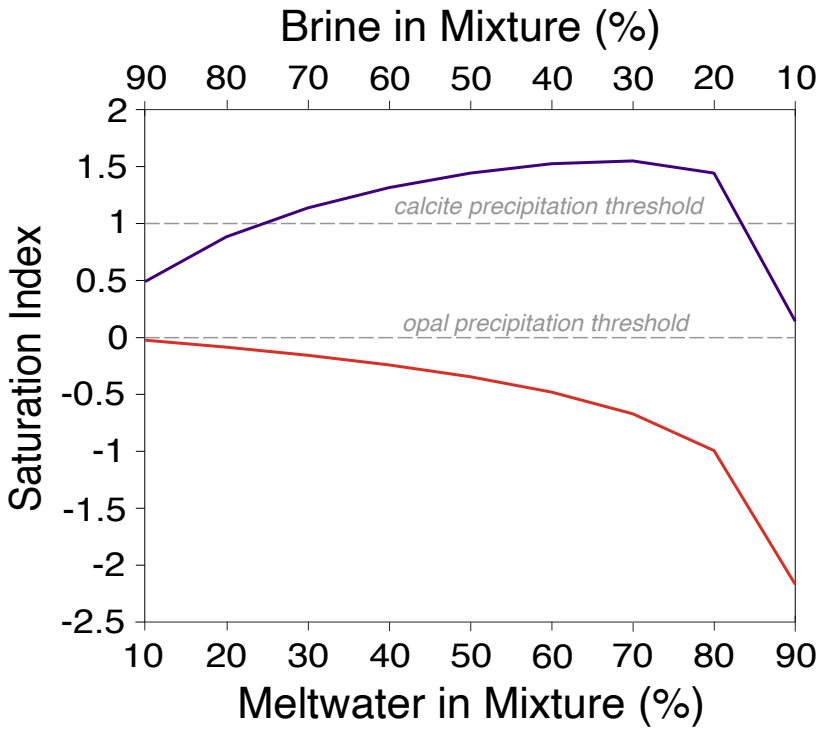

Supplementary Fig. 7 | Model simulations predicting calcite formation via mixing of meltwater and $CaCl_2$ brine. PHREEQC simulations of a range of mixing ratios between $CaCl_2$ brine and Casey Station jökulhlaup water. Brine starting temperature is set at -3.5˚C matching ideal conditions for opal precipitation shown in Extended Data figure 5; meltwater starting temperature is at -1.5˚C based on the amount of heat added to the system by shear heating in our reduced complexity ice sheet model. Calcite precipitation threshold is defined by the observation that calcite precipitation can be inhibited until strong supersaturation[272,273]. Plot shows that meltwater addition halts opal precipitation, while generating calcite precipitation in a mixing ratio between 30:70 and 80:20 meltwater to brine.

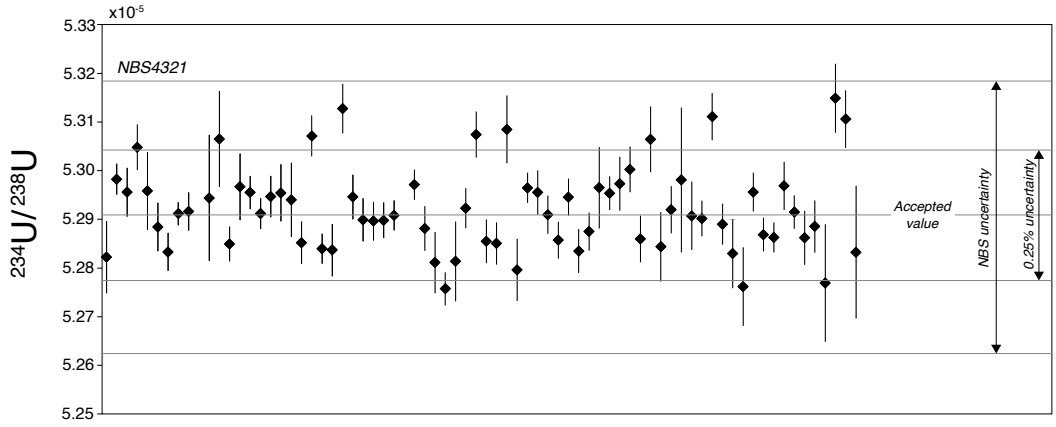

Supplementary Fig. 8 | Long-term results of measurements of NBS 4321 (5.2919 × 10^{-5}± 0.013 × 10^{-5} (0.25%)) at UCSC using an IsotopX X62, TIMS. All uncertainties are absolute 2σ.

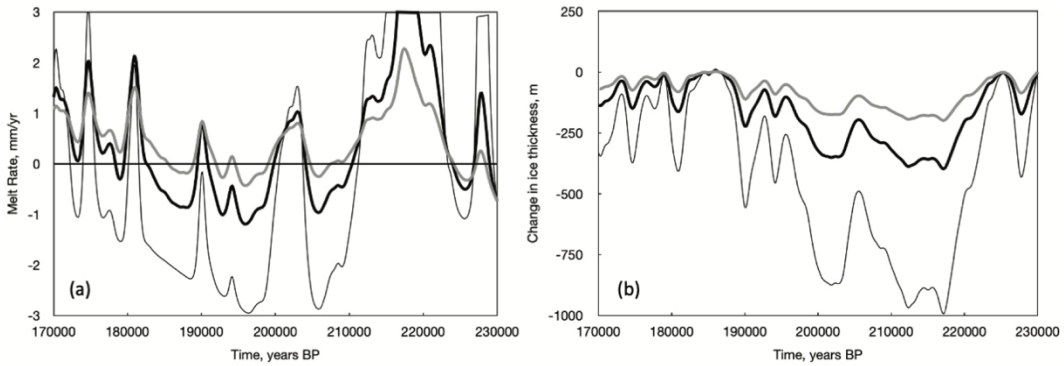

Supplementary Figure 9 | RCMIST Outputs for Sample PRR50489. a. Sensitivity of the basal thermal energy balance, expressed in terms of equivalent basal melt (+) or freeze (-) rate given in mm/year. The thick black line shows the preferred scenario for C_i = 10 m per ‰ of δD from the EDC ice core record. The thin black line gives the C_i = 25 scenario and the thick grey line is for the C_i = 5 case. **b.** Equivalent changes in ice thickness, $H_{RE}(t)$, which represent the impact of climate forcing on our model through equation 4. The same types of lines as in **a.** are used here to represent the three cases $C_i = 5$, 10 and 25 m per ‰.

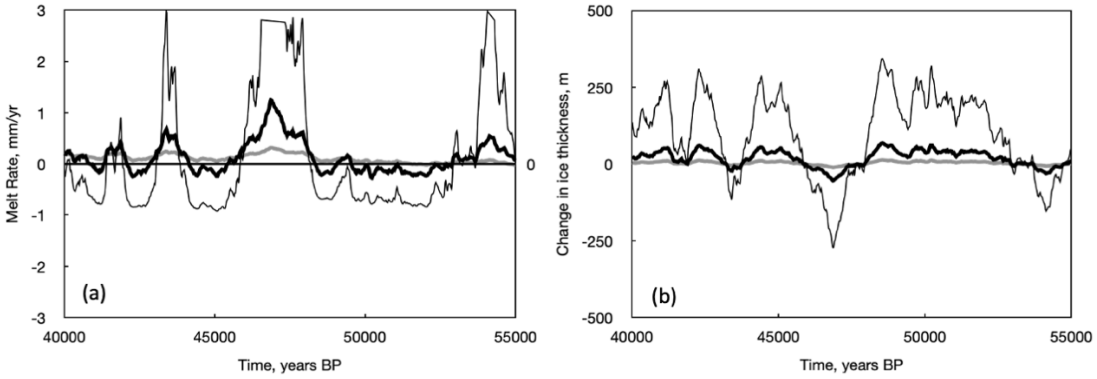

Supplementary Figure 10 | Reduced Complexity Ice Sheet Model Outputs for Sample MA113. Plots equivalent to those in Supplementary Figure 1 but for simulations pertaining to the sample MA113 and with $C_i = 10$, 50, and 250 of m per ‰ of $\delta^{18}O$, corresponding to the thick grey lines, **a.** Sensitivity of the basal thermal energy balance, expressed in terms of equivalent basal melt (+) or freeze (-) rate given in mm/year. The thick black lines show the preferred scenario for C_i = 50 m per ‰ of $d^{18}O$ from the WAIS Divide ice core record. The thin black lines give the C_i = 250 scenario and the thick grey lines are for the C_i = 10 case. **b.** Equivalent changes in ice thickness, $H_{RE}(t)$, which represent the impact of climate forcing on our model through equation 4. The same types of lines as in **a.** are used here to represent the three cases $C_i = 5$, 10 and 25 m per ‰.

Appendix B

Supplementary Information to "Accelerated Antarctic ice loss through ocean forced changes in subglacial hydrology"

Supplementary Figures

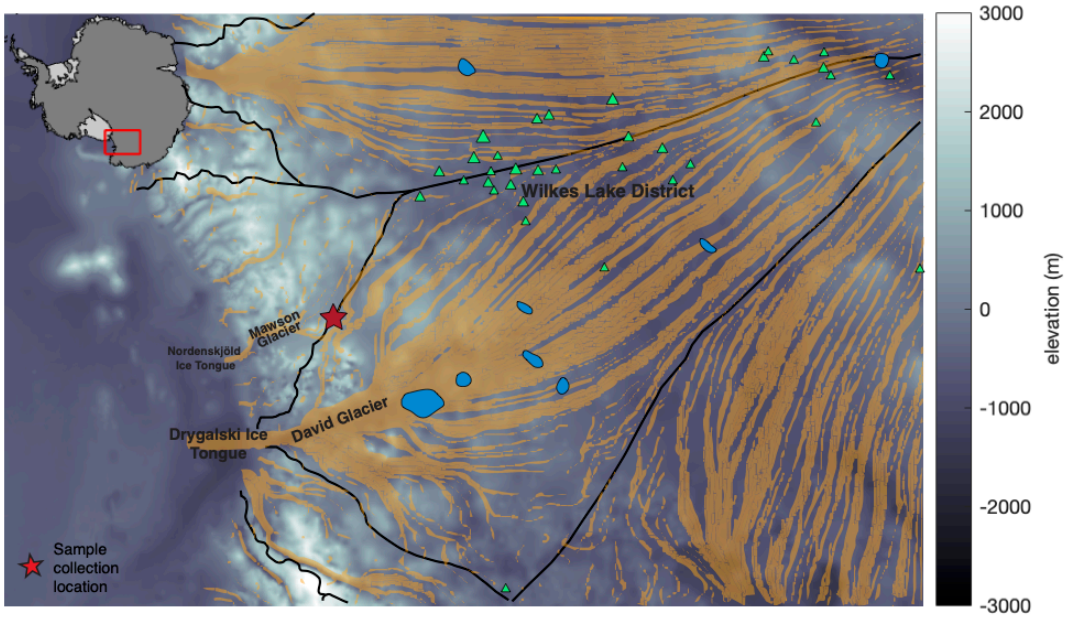

Supplementary Fig. 1 | Ice flow lines in area near Reckling moraine. Elevation map of area in East Antarctic side of the Ross Embayment[274] where Reckling moraine is located. Reckling moraine is shown as red star, satellite detected lakes shown in blue and radar detected lakes are shown in green[144], ice flowlines shown as yellow curves[160], glacial drainage boundaries are highlighted in black[245]. Reckling moraine is located on the ice boundary separating the David and Mawson glacier catchments. Ice flowlines show that the most likely formation of precipitates collected at Reckling moraine is within the David Glacial catchment in the ice flow path draining ice above the Wilkes Lake district.

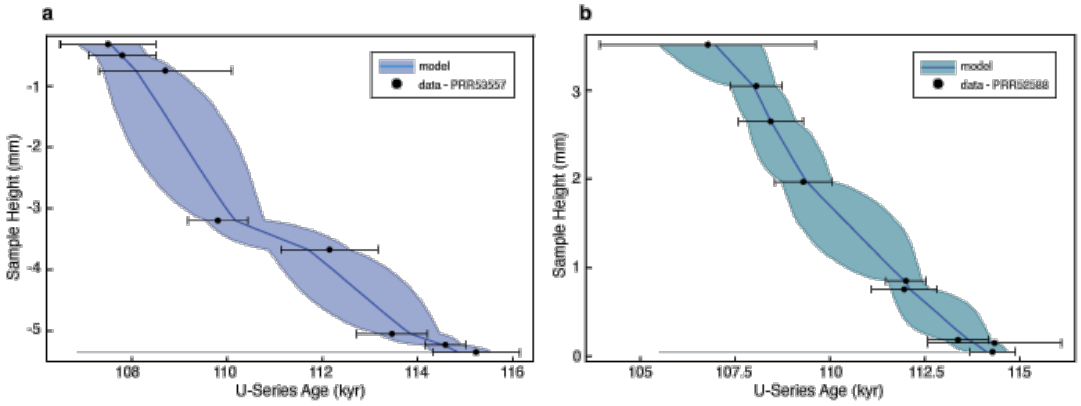

Supplementary Fig. 2 | Stratigraphic age models for each precipitate. a. PRR53557 and **b**. PRR52588. Models are produced using a Bayesian model which accounts for stratigraphic position of age data points to refine age uncertainties (Methods).

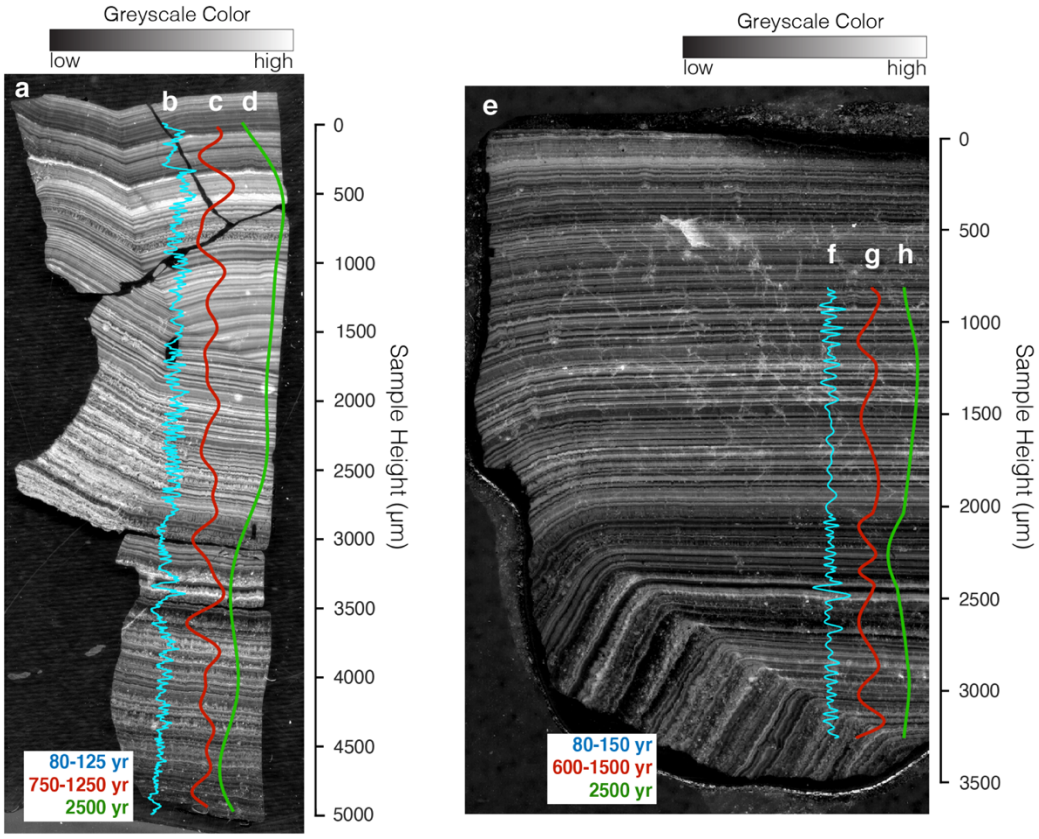

Supplementary Fig. 3 | Correlation of deconstructed spectra to precipitate layers. a. Sample PRR53557 thin section image, converted to greyscale, from which spectral data is derived. White layers indicate high sediment volume and black layers indicate low sediment volume. **b**. 80-150 year frequency of high detrital content. **c**. 750-1250 year frequency. **d**. 2500 year frequency. **e**, Sample PRR52588 thin section image. **f,g,h**. Dominant frequencies of total sediment volume in calcite layers over sample space.

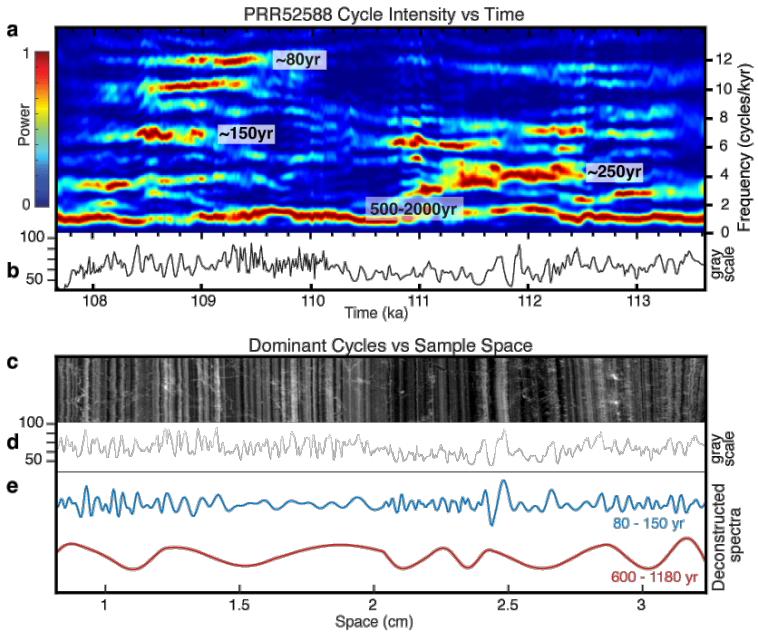

Supplementary Fig. 4 | Spectral Analyses of Samples PRR52588. a. Evolutionary FFT analysis of detritus concentration showing cycle power over time. **b**. Spectral data derived from calcite opacity in sample thin section. **c**. Thin section image from which spectral data is derived. **d**. Spectral data. **e**. Spectral data deconstructed into dominant frequencies.

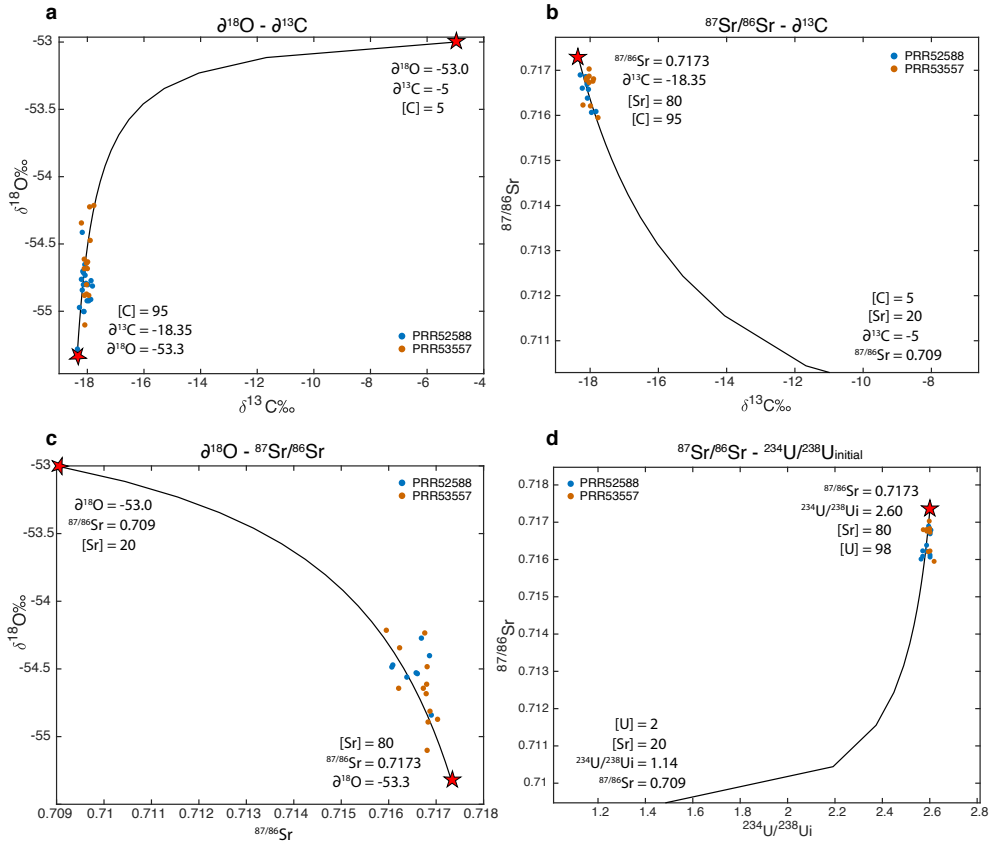

Supplementary Fig. 5 | Two end-member mixing models for calcite isotopic data. **a, b, c, d.** Parabolic mixing curves between end member fluids fit to sets of calcite isotopic data.

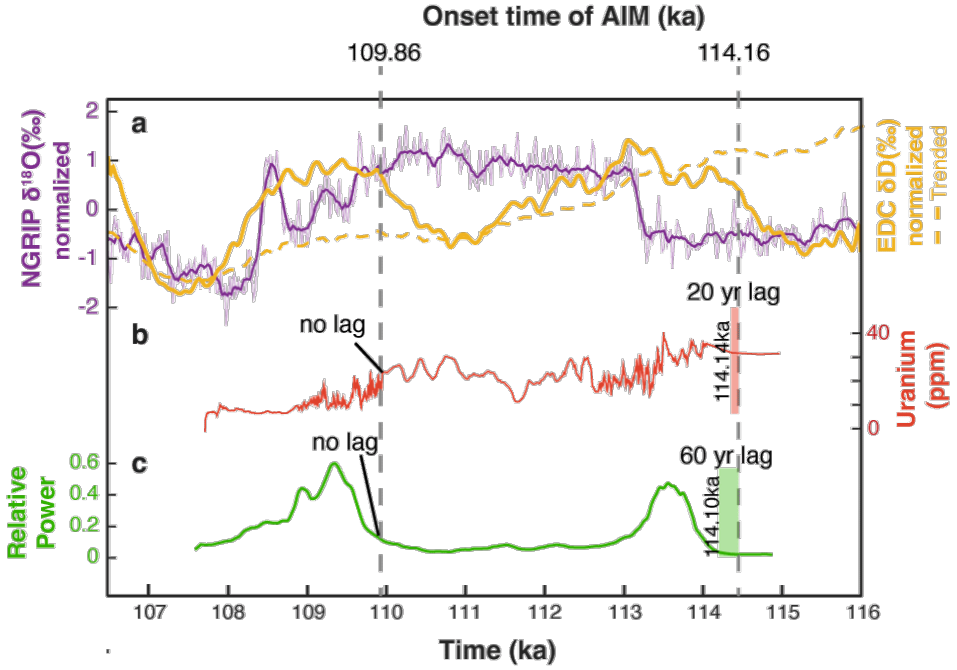

Supplementary Fig. 6 | Timing of Reckling precipitate response to climate forcing. **a.** (dashed yellow) δD (‰) at EPICA Dome C, a proxy for Antarctic surface temperature on the AICC2012 time scale. (Solid yellow) EDC δD (‰), normalized over the sample period by removing LR04 marine record. (Purple) NGRIP δ^{18}O (‰) a proxy for temperature in Greenland showing polar seesaw related Dansgaard-Oeschger (D-O) events. b. Uranium concentration (ppm) of subglacial precipitate. c. Relative spectral power through time of cycle periodicities from 80-130 yr.

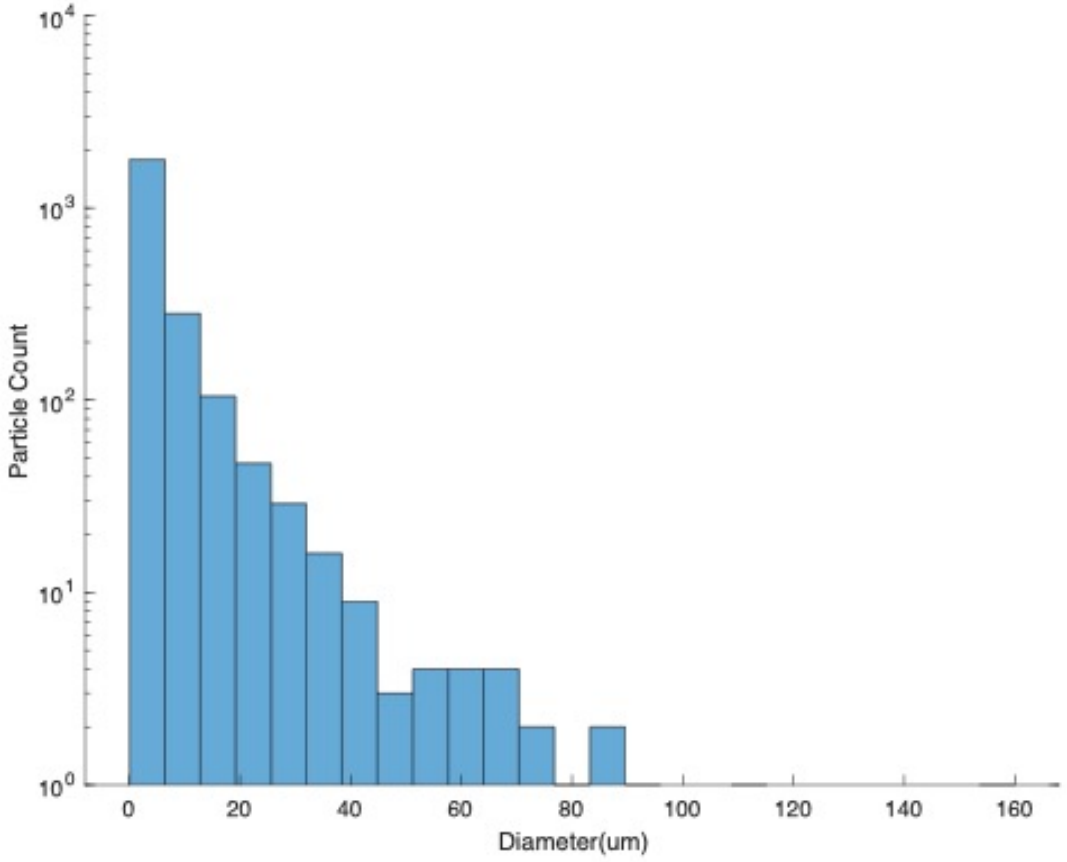

Supplementary Fig. 7 | Grain size analysis of detrital grains in Reckling moraine precipitates. Histogram shows particle size distribution of detrital grains larger than the 2μm pixel size of the SEM EDS images. Particle size analysis was made using the analyze particles function in ImageJ image processing software. These data result from image particle analyses from SEM EDS silicon elemental map of a ~2cm section of sample PRR53557. Because silicate detritus that make up the micron-scale laminations throughout the sample are <2μm (Fig. 2c), the particles analyzed here make up the discrete clay-sand rich layers superimposed on the micron-scale laminations (Fig. 2d). Histogram bins are ~7μm intervals.

Appendix C

Supplementary Information to "Microbes drive subglacial CO_2 production and silicate weathering throughout Antarctica"

Subglacial Organic Matter Source

These subglacial precipitate compositions are consistent with bacteria, marine and freshwater particulate organic carbon, plant matter, and coal (fig. S3). Widespread fossil plant matter and coal has been found in exposed sediments and sedimentary bedrock along the TAM [42], which are the likely source of precipitate organic carbon with C:N > 10. X-ray absorption near edge spectroscopy from an individual TAM precipitate helps corroborate this hypothesis by showing detrital lignite fragments, a highly bioavailable form of organic matter, incorporated in the carbonate matrix (fig. S4). Organic material with C:N values < 10 are likely sourced from legacy marine organic carbon left during marine incursions into Antarctic sedimentary basins, as well as secondary biomass built up beneath the ice sheet over time.

Mixing Relationships in Subglacial Precipitates and Carbonate Formation Mechanisms

As indicated by the $\delta^{18}O_{CaCO3}$ values, Antarctic subglacial waters can travel large horizontal distances from beneath the domes towards the ice sheet edges [162], in the process evolving in composition by mixing with other fluids and chemical weathering products [139]. Previous work on these TAM samples has identified the compositions of endmember subglacial fluids by measuring $\delta^{18}O_{water}$ and $\delta^{13}C_{CaCO3}$ from multiple stratigraphic horizons in individual subglacial precipitates [139]. We utilize the parabolic, two-component trends in C-O space to identify endmember carbon and oxygen isotope compositions for carbon rich glacial meltwaters from the ice sheet interior and fluids isolated on the ice sheet periphery [139] (fig. S2). It is the glacial meltwater endmember originating the ice sheet interior, with the lowest $\delta^{18}O_{water}$ and $\delta^{13}C_{CaCO3}$ values, that are shown in figures 1 and 3 and are the focus of this study.

Calcite formation occurs more readily in aqueous environments with a pH of 7 or higher. However approximately half of the TAM subglacial carbonates form in waters with pH between 6.5 and 7. Previous studies investigating Antarctic subglacial precipitates use isotope mixing models and PHREEQC geochemical modeling experiments to support subglacial calcite formation through mixing between carbon-rich interior waters and Ca-rich brines [139]. Based on mixing models presented in figure S2, the suite of TAM precipitates examined here are consistent with a two-component mixing formation mechanism. Importantly, the pH of precipitate parent water is calculated using the interior endmember (low $\delta^{13}C$ and $\delta^{18}O$ values), so these pH values represent interior water compositions before they reach the periphery. Calcite likely does not precipitate in these interior waters until they flush to the ice sheet edges. That

is, interior waters have higher concentrations of HCO_{3+} in solution, but the pH and ionic contentment are too low to support significant calcite precipitation. Upon mixing with peripheral brines, carbonate precipitates due to the addition of high concentrations of Ca, and possibly through additional alkalinity from silicate weathering. Though, based on the shape of mixing models the ratio of carbon concentrations in interior waters versus brines in between 99:1 and 80:20, meaning that most of the alkalinity in solution likely comes from the interior waters. Additionally, peripheral ice is thinner in most areas throughout the Antarctic ice sheet [79], which facilitates freezing in these areas. Trapping of CO_2 in overlying ice during freezing, and cryoconcentration of subglacial waters, may also facilitate subglacial calcite precipitation.

Subglacial Chemical Reactions That Control the Carbon Composition of Subglacial Precipitates

Here in we identify the series of reactions occurring beneath ice sheets operating to produce the isotopic compositions associated with the sub-EAIS environment. Here in we assume that this system begins as a fresh glacial melt of ice from beneath the polar plateau with a near neutral pH, low salinity, oxidized and only ~250 ppm CO_2. The $\delta^{18}O_{water}$ is highly depleted (<-50‰) and what little carbon there is has an atmospheric $\delta^{13}C$ signature (~ -6‰). As established in the previous section, the $\delta^{13}C_{carb}$ are consistent with a DIC that is predominantly derived from dissolved organic carbon. But the dissolution of organic carbon is, exceedingly slow and such kinetically unfavorable reactions are unlikely to account for its prevalence in the DIC. Rather, subglacial

respiration (eq.1) fueled by legacy organic matter and oxygen sourced from melting of meteoric ice, produces carbonic acid.

$$CH_2O + O_2 \rightarrow H_2CO_3 \qquad \text{Eq. 1}$$

This carbonic acid inherits the $\delta^{13}C$ composition of the oxidized organic matter (-24‰). Similarly depleted $\delta^{13}C$ values have been observed in the high CO_2 basal ice from the Allen hills, EAIS and interpreted to reflect microbial respiration. This interpretation is supported by observations in the basal ice of Taylor glacier, where similarly increased CO_2 concentrations are accompanied by decreased O_2 and increased bacterial cell counts, all three observations pointing to microbial respiration at the ice sheet base.

While this subglacial water, due to the influence of microbial activity, will have a $\delta^{13}C$ that matches the composition of TAM precipitates, calcite will not precipitate at this stage due to the lack of alkalinity. Rather, the carbonic acid ($\delta^{13}C$ <-24‰) results in the dissolution of subglacial bedrock and two possible reactions are most likely. Often considered to be the most predominant and important subglacial reaction, at least beneath alpine glaciers, is the dissolution of carbonate rocks:

$$CaCO_3 + H_2CO_3 \rightarrow Ca^{2+} + 2HCO_3^- \qquad \text{Eq. 2}$$

But the dissolution of marine carbonates with a $\delta^{13}C$ near 0‰, from carbonic acid with a $\delta^{13}C$ <-24‰, would produce bicarbonate with a $\delta^{13}C$ (-12 ‰) that does not match the

subglacial precipitate record ($\delta^{13}C$ ~23‰), suggesting this reaction is not contributing significantly to the subglacial water DIC. The dissolution of silicates, however, can contribute alkalinity to subglacial waters while preserving the isotopic signature of organic matter. The dissolution of anorthite for example,

$$CaAl_2Si_2O_8 + 2H_2CO_3 \rightarrow H_2Al_2Si_2O_8 + Ca^{2+} + 2HCO_3^- \quad \text{Eq. 3}$$

would produce bicarbonate that matches the carbonic acid. The resulting bicarbonate ($\delta^{13}C$ -24 ‰) can produce calcite either subglacially or in a marine setting (if HCO_3^- is reaches oceans) (eq. 4), however only 1 of the 2 mols of carbon freed by oxidation (eq. 1) is sequestered in calcite eq. 4).

$$Ca^{2+} + 2HCO_3^- \rightarrow CaCO_3 + H_2CO_3 \quad \text{Eq. 4}$$

In summary, the observation of depleted ($\delta^{13}C$ = -23 ‰) carbon composition in subglacial carbonates requires that there is little to no atmospheric CO_2 ($\delta^{13}C$ = -6‰) or carbonate bedrock ($\delta^{13}C$ = -6‰) contributing the subglacial dissolved inorganic carbon (DIC) (discussed further in a section below). Thus, the subglacial realm of the EAIS is a closed system, with predominantly silicate bedrock. As mentioned in the main text, the range in $\delta^{13}C$ values from precipitates tracks the evolution of carbonate species in a subglacial meltwater, which is a function of the pH of the parent waters.

We present model simulations that further describe the effect of parent water pH on precipitate $\delta^{13}C_{CaCO3}$ in the next section.

Carbon Isotope Evolution With pH

We present a model describing the evolution of the carbonate alkalinity as a function of pH for a closed system. Following Graly and others [157], this model describes the evolution of the carbonate alkalinity ($HCO_3 + CO_3$) as a function of pH for a closed system in which CO_2 is produced through microbial respiration of available oxygen. The alkalinity-pH evolution is controlled by the initial total carbon set by the model and the subsequent conversion of carbonic acid (H_2CO_3) to bicarbonate and carbonate with increasing pH (discussed in more detail below). At low pH, the total alkalinity of the closed system exceeds that of the open system due to the CO_2 converted through microbial respiration during consumption of initial oxygen in solution. The pH of the solution increases from 5.5 to 7.5 as H_2CO_3 is converted into HCO_3 and can eventually exceed 9.5 as H_2CO_3 concentrations are diminished and CO_3 concentrations increase.

The modeled change in concentration among carbonate species with changing pH provides the basis to calculate the $\delta^{13}C$ composition of each carbonate species, and importantly, the $\delta^{13}C$ composition of calcite ($\delta^{13}C_{CaCO3}$), which equals the $\delta^{13}C$ of $HCO_3 + CO_3$ (i.e. carbonate alkalinity [275]). The inset in Figure 3a shows the predicted $\delta^{13}C_{CaCO3}$ across a range of pH assuming a $\delta^{13}C_{DIC}$ value of -26‰ (approximately the carbon isotope composition of the measured organic carbon). This range of $\delta^{13}C_{CaCO3}$ is controlled by the relative abundance of each of the three aqueous carbonate species (H_2CO_3, HCO_3, CO_3), which changes depending on the pH of the subglacial fluid. In

neutral to acidic solutions, the dominant carbon species are H_2CO_3 and HCO_3^-, which undergo higher degrees of fractionation and lead to $\delta^{13}C_{CaCO3}$ values up to 12‰ higher than $\delta^{13}C_{DIC}$ (Fig. 3a inset). As a glacial meltwater interacts with silicate rock, the pH and carbonate alkalinity will increase as the silicate rock dissolves, and the dominant carbon species become HCO_3^- and CO_3^{2-}. Calcite forming in these high pH waters $\delta^{13}C_{CaCO3}$ values close to the $\delta^{13}C_{DIC}$ (Fig. 3a inset). Carbonate precipitates that have $\delta^{13}C_{CaCO3}$ within ~3‰ (fractionation factor between HCO_3^- and calcite at 0 °C) of the $\delta^{13}C_{DIC}$ formed from a neutral to high pH water where the carbonic acid is largely neutralized by silicate weathering. Whereas samples with $\delta^{13}C_{CaCO3}$ >3‰ higher than the $\delta^{13}C_{DIC}$ formed from a lower pH water where the rate carbon acidity production exceeds that of silicate weathering.

In the manuscript main text, we provide evidence that microbial respiration of organic carbon the dominant source of carbon to the TAM precipitate parent waters, thus the value of $\delta^{13}C_{DIC}$ is equal to the $\delta^{13}C_{OM}$, and the difference between precipitate $\delta^{13}C_{CaCO3}$ and $\delta^{13}C_{OM}$ ($\Delta\delta^{13}C$) represents the pH-determined relative abundance of carbonate species. Among the subglacial precipitates in the dataset presented here, $\Delta\delta^{13}C$ values range from 0.8 to 10 indicating a pH range of 5.5-7.5. The absolute $\delta^{13}C_{CaCO3}$ values reported here support widespread microbial respiration. The degree to which this carbon acidity is consumed by subglacial silicate weathering varies. The pH values inferred from carbon isotopic and proxies for alkalinity, span a pH range from relatively acidic to neutral.

Assessing The Possibility for Subglacial Methane Contribution To Precipitate Parent Water DIC

High methane concentrations have been observed in sediment pore waters beneath Subglacial Lakes Whillans and Mercer beneath the Antarctic Ice Sheet [191,276]. If this methane contributed a significant proportion of the DIC of the lake water, the extremely low $\delta^{13}C_{CH4}$ values (-75‰) [191] could strongly influence the composition of the DIC within the lake, and therefore any calcite precipitating from the lake water. Like other Antarctic waters, Subglacial Lake Whillans has a high dissolved carbon concentration (2.3 mM) [11] that far exceeds the concentrations of methane just below the sediment interface (125 uM) [191]. There is no reported $\delta^{13}C$ values for the DIC of this lake water, however, assuming that the lake water DIC is sourced from microbial respiration of oxygen and organic carbon (-23‰), the resulting DIC (-26‰) would produce carbonate with a slightly heavier carbon isotope composition (-23‰) that is consistent with the $\delta^{13}C_{CaCO3}$ we measured in TAM subglacial precipitates (Fig. 1c). In other words, calcite values reported here permit subglacial methane production at the compositions and concentrations reported at Subglacial Lake Whillans [191]. However, based on the $\delta^{13}C_{CaCO3}$ of our subglacial precipitates, contribution of methane to the subglacial DIC must be very small compared to DIC produced by microbial respiration of organic matter (≥1:20). This observation points to the subglacial environment as a setting where fresh glacial meltwaters supply oxygen to both fuel respiration and neutralize any influx of methane produced in sediment pore waters. Unlike settings in Greenland where stores of methane are released during rapid flushing during the melt season [277],

the residence time of subglacial water beneath Antarctica is likely too long for methane to escape to the atmosphere before being degraded completely by subglacial oxygen and microbial metabolism.

Despite speculation that the high pressure, low temperature, closed system conditions beneath the Antarctic ice sheet may support methanogenesis as the dominant reaction cycling subglacial carbon, our continent-wide analysis of the subglacial carbon cycle shows instead that CO_2 production via oxidation of organic matter by microbial respiration is the main carbon mobilizing reaction in the Antarctic subglacial environment. Since subglacial precipitates form at the ice-bed interface, it is possible that the parent waters for these samples are dominated by glacial meltwater, with only small supplies of sedimentary porewaters where high methane concentrations have been measured [191,276]. Indeed, three samples from Magnus Valley along the TAM have $\delta^{13}C_{OM} < -30‰$, suggesting the presence of highly depleted organic material consistent with either certain species of marine algae [180], or microbes feeding on methane [191]. Fitting a mixing model to the full group of subglacial precipitates in $\delta^{13}C_{OM}$ versus C/N space shows that organic material in several samples may comprise of a mixture between plant matter and this low $\delta^{13}C_{OM}$ material (fig. S3). If we assume that the $\delta^{13}C$ methane in subglacial lakes matches that in Subglacial Lake Whillans (-45‰), mixing models suggest that eight samples contain organic matter made up of >20% of this low $\delta^{13}C_{OM}$ material. While differentiating between ^{13}C-poor marine organic carbon and methane contributions is beyond the scope of this manuscript, previous observations of Antarctic subglacial basins suggest that methane is likely present in deep sediment pore

waters [191,276]. However, the narrow range of $\delta^{13}C_{CaCO3}$ values in our subglacial precipitate record (-23.5‰ to -16‰) suggests that this methane does not contribute significantly to the DIC of subglacial waters, and that dissolved carbon in subglacial waters is dominated by respired CO_2. Therefore, our results suggest that little methane enters the Antarctic ice-bed interface from deep sediment pore waters, and if it does it is likely completely oxidized to CO_2 before it can reach the atmosphere.

Assessing The Possibility for Carbonate Bedrock Contributing To Precipitate Parent Water DIC

An alternative explanation for the range of $\Delta\delta^{13}C$ values is that the relatively higher $\delta^{13}C_{DIC}$ values derive from incorporation of dissolved carbonate bedrock (~ 0‰). In this scenario, rocks with a higher concentration of carbon from carbonate bedrock would have heavier $\delta^{13}C_{CaCO3}$ values and higher P/Ca, because carbonate dissolution produces alkalinity. These reactions would result in a direct correlation between P/Ca values and $\Delta\delta^{13}C$, which is opposite of the trend observed in TAM precipitates (Fig. 3a). The degree of carbonate dissolution in subglacial waters can also be independently evaluated by measuring the $^{87}Sr/^{86}Sr$ value of the precipitates, as the $^{87}Sr/^{86}Sr$ of marine carbonates (<0.709) differs from that of most crustal rocks (>0.71). The $^{87}Sr/^{86}Sr$ values of TAM are too high to incorporate carbonate in large quantities, and are consistent with Sr isotope compositions measured in exposed TAM bedrock [193]. Instead, TAM precipitates describe formation from interior waters in an area of the Antarctic continent that has likely been entirely stripped of any sedimentary rock cover. This interpretation is consistent with the glaciologic history of the EAIS interior, as the ice

sheet has occupied this setting for nearly 40 million years, providing ample time to erode sedimentary cover and denude supracrustal rocks. A point of comparison is provided by the Canadian and Fennoscandia shields, where far shorter ice sheet residence histories (<3 Ma) have efficiently removed sedimentary cover.

Supplementary Figures

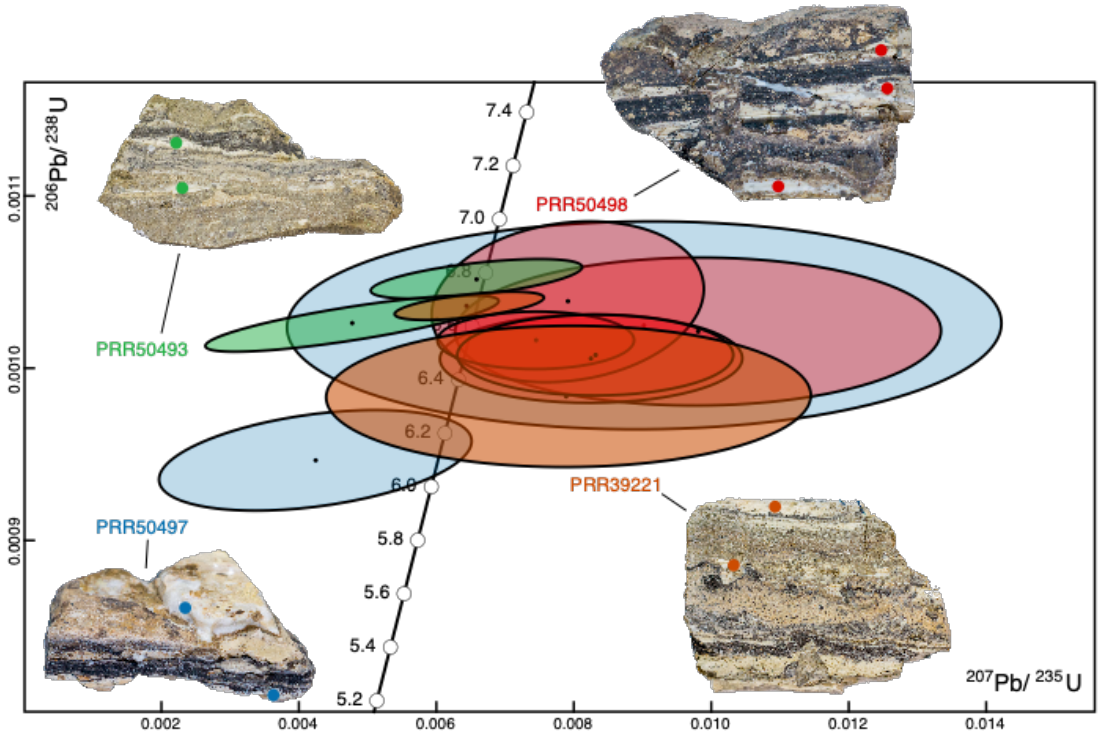

Supplementary Figure 1: Concordia diagram showing U-Pb data from Miocene Antarctic subglacial precipitates.

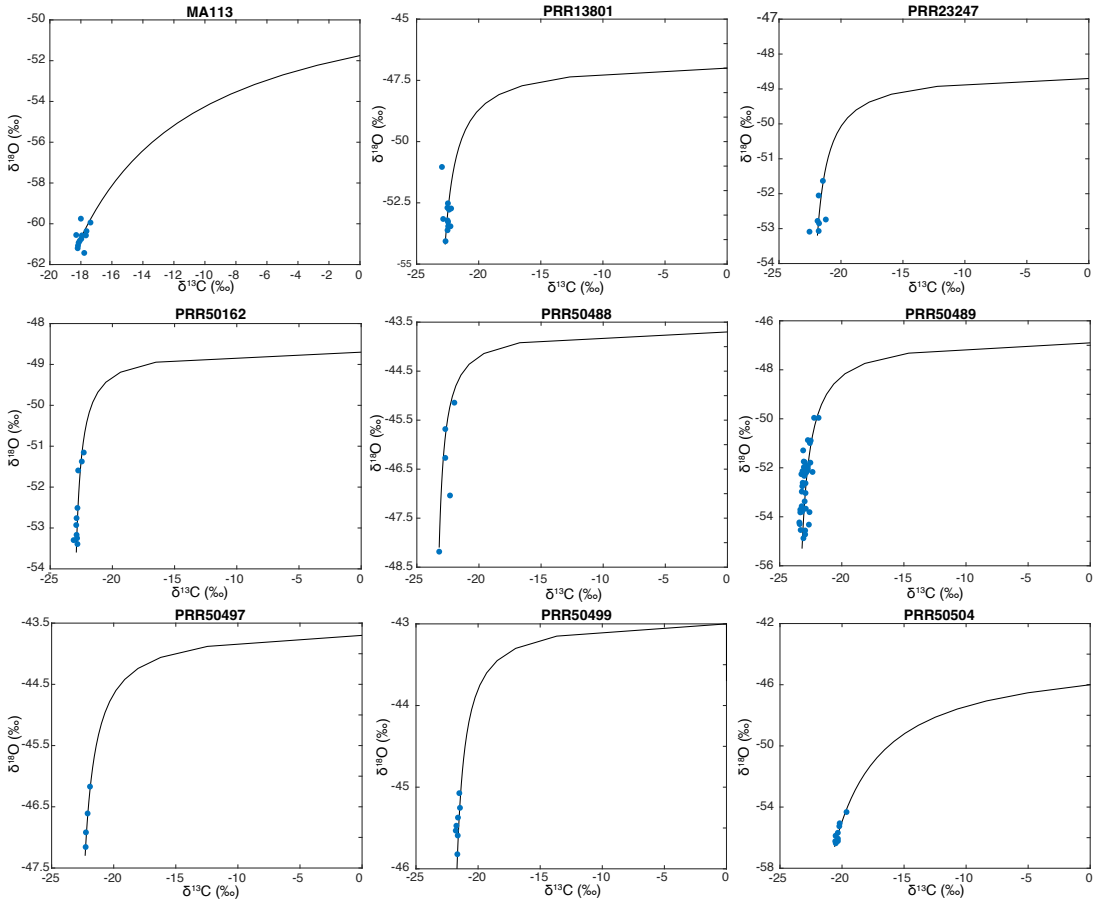

Supplementary Figure 2: Carbon versus oxygen isotope mixing models in subglacial precipitates form the Transantarctic mountains. Markers indicate carbonate measurements. Black curves are two-component mixing models that fit carbonate isotope data. Each sample is records two-waters: one carbon-rich, with ^{13}C- and ^{18}O-depleted compositions; one carbon-poor, with more ^{13}C- and ^{18}O-enriched compositions. Based on previous investigation of TAM subglacial precipitates [139], we interpret the ^{13}C- and ^{18}O-depleted fluid as meltwater sourced from the EAIS interior, and the more ^{13}C- and ^{18}O-enriched water as subglacial fluid sourced closer to the ice sheet periphery. The interior fluid contributes between 77 and 97% of the total carbon in each sample.

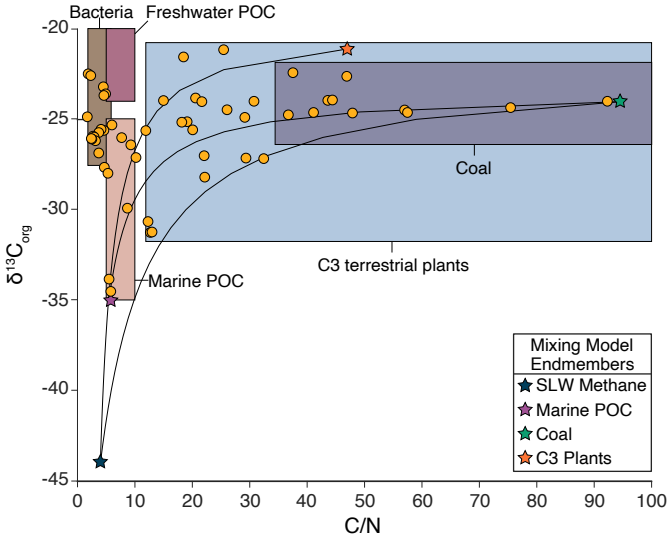

Supplementary Figure 3: C/N versus $\delta^{13}C$ of isolated organic material from subglacial precipitates. Rectangles denote values of potential source organic matter [179,180]. Black lines are models of two-component mixtures of possible end member organic material including: methane in Subglacial Lake Whillans [191], ^{13}C-poor marine particulate organic carbon (POC) [180], C3 plant matter, and coal.

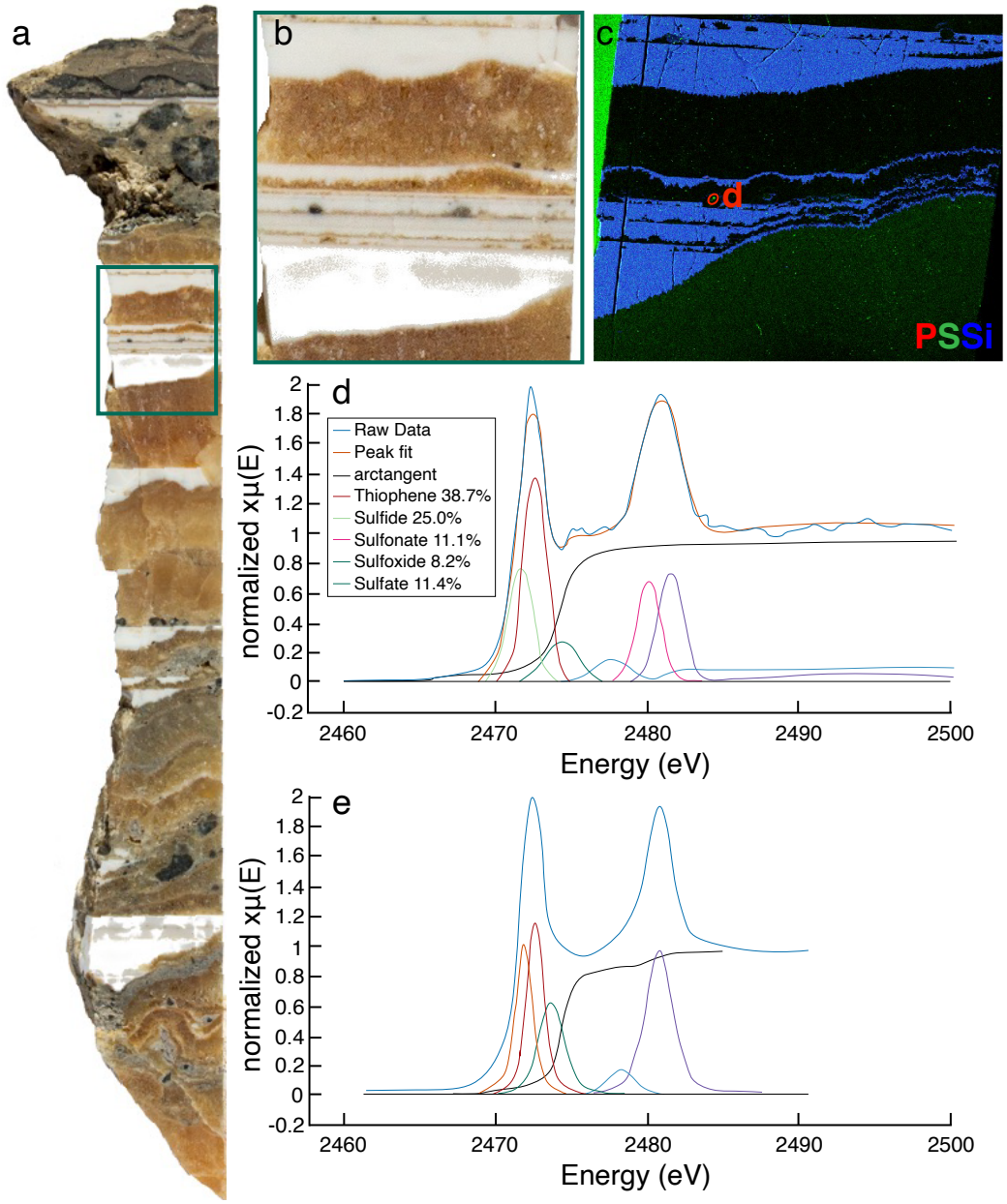

Supplementary Figure 4: XRF and XANES spectra on lignite detrital fragments from sample MA113. a. Image of sample MA113 **b.** Area in sample where XRF element map was measured. **c.** RGB X-ray Florescence element map. R = phosphorus, G = sulfur, B = silicon. **d.** Sulfur K-edge XANES from detritus in c. Peak fitting identified five sulfur bearing phases consistent with lignite coal composition, **e.** example XANES spectra from lignite [203]. Data relative to elemental sulfur.

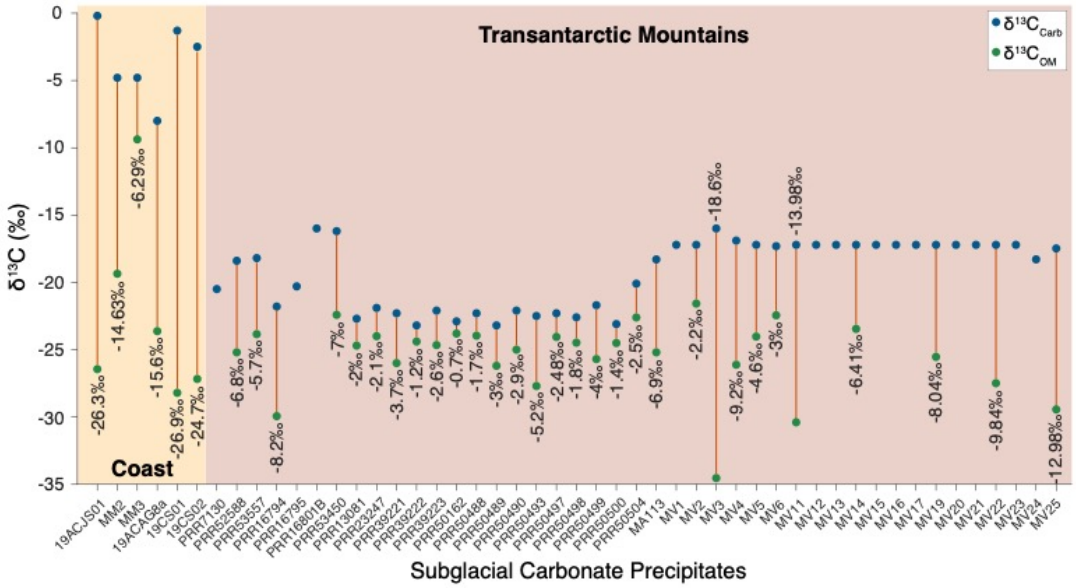

Supplementary Figure 5: Comparison between carbon isotopic composition ($\delta^{13}C_{CaCO3}$) of carbonate and isolated organic matter ($\delta^{13}C_{OM}$) in Antarctic subglacial precipitates

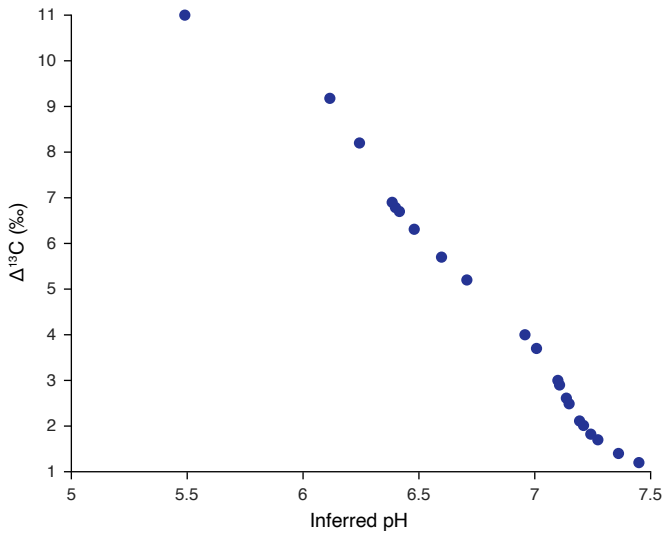

Supplementary Figure 6: $\Delta\delta^{13}C$ versus inferred pH in Antarctic subglacial precipitates from the Transantarctic Mountains.

Appendix D

Supplementary Information to "A 25-kyr Record of Antarctic Subglacial Trace Metal Cycling"

Supplemental Figures

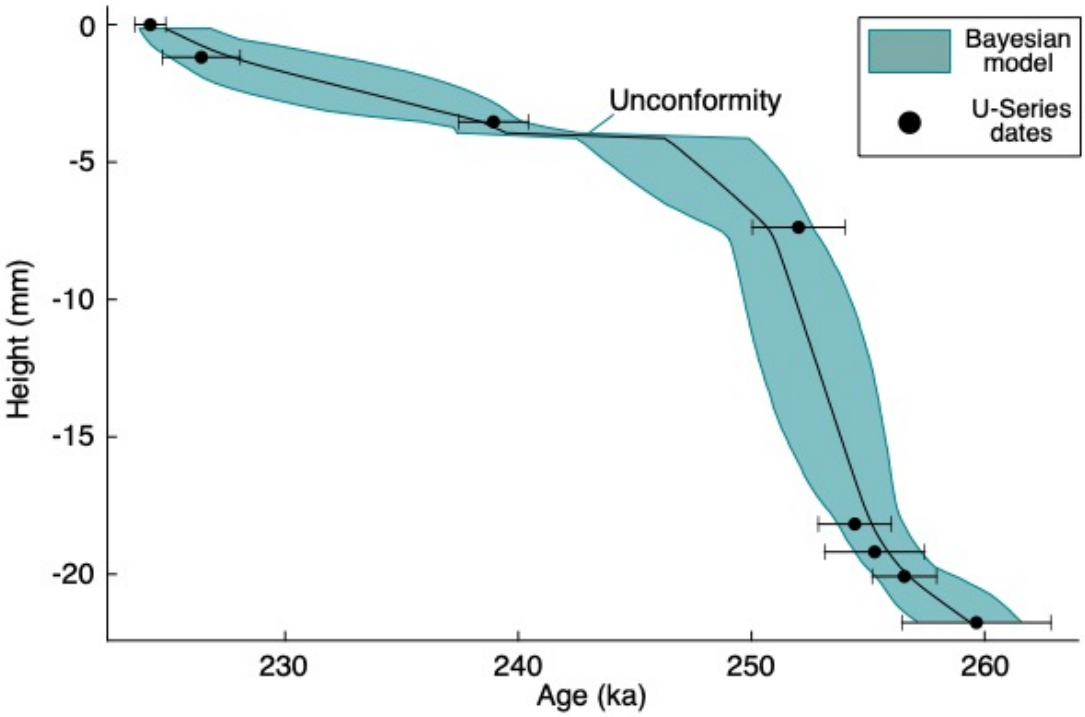

Fig. S1. Bayesian Deposition Age Model for PRR50504. Black markers are ^{234}U-^{230}Th with 2σ error bars. Blue envelope is Bayesian age-depth model using stratigraphic position as a prior to refine dating uncertainties[46].

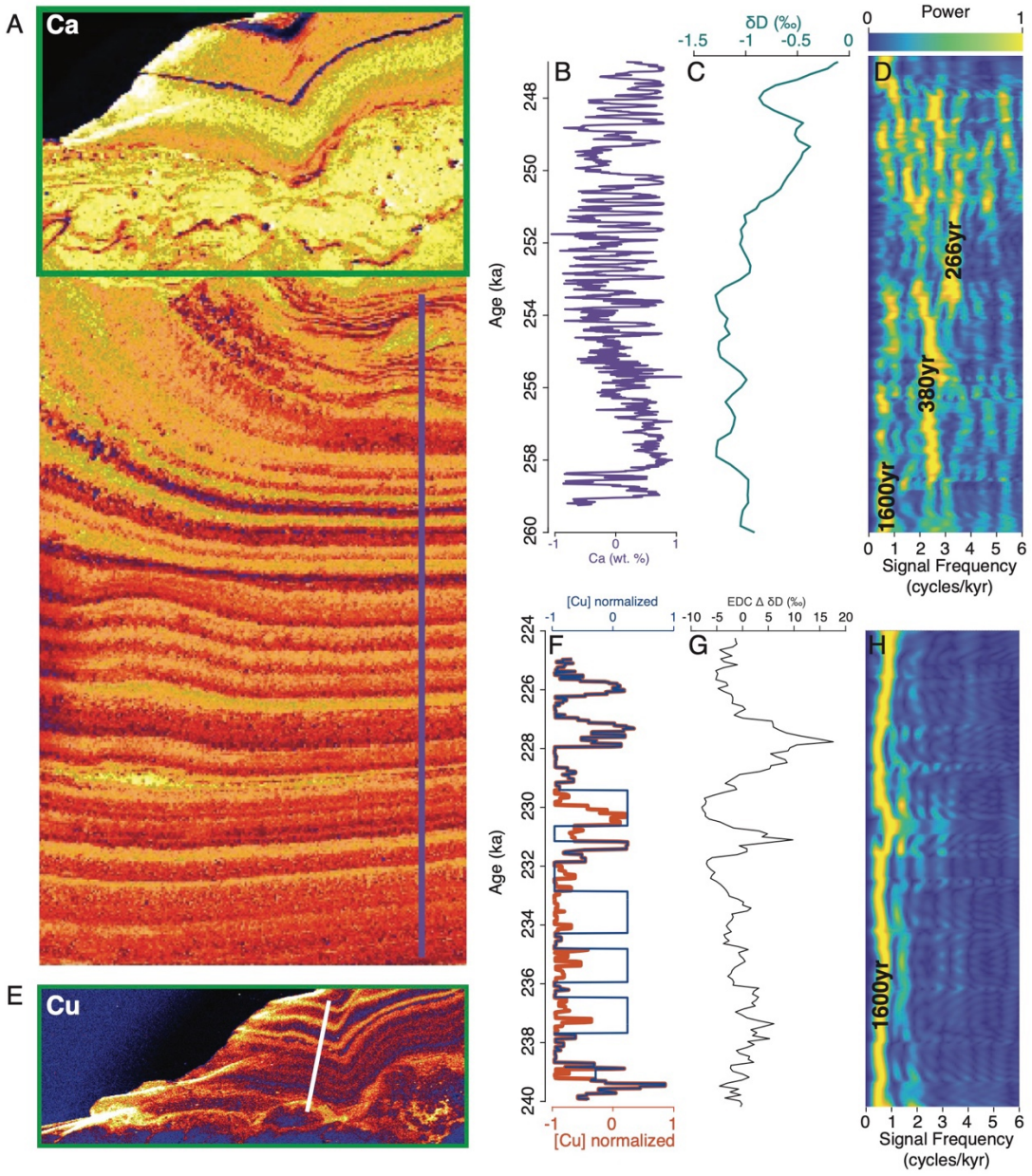

Fig. S2. Frequency analysis of PRR50504 opal-calcite layer deposition. (A) XRF element map of Ca in PRR50504. (B) Ca concentration (wt. %) measured across purple line in A. (C) EPICA Dome C δD record. (D) Signal frequency analysis across B. (E) XRF element map of Cu in upper portion of PRR50504. (F) Cu concentration (wt. %) measured across white line in E. (G) EPICA Dome C δD record. (H) Signal frequency analysis across G.

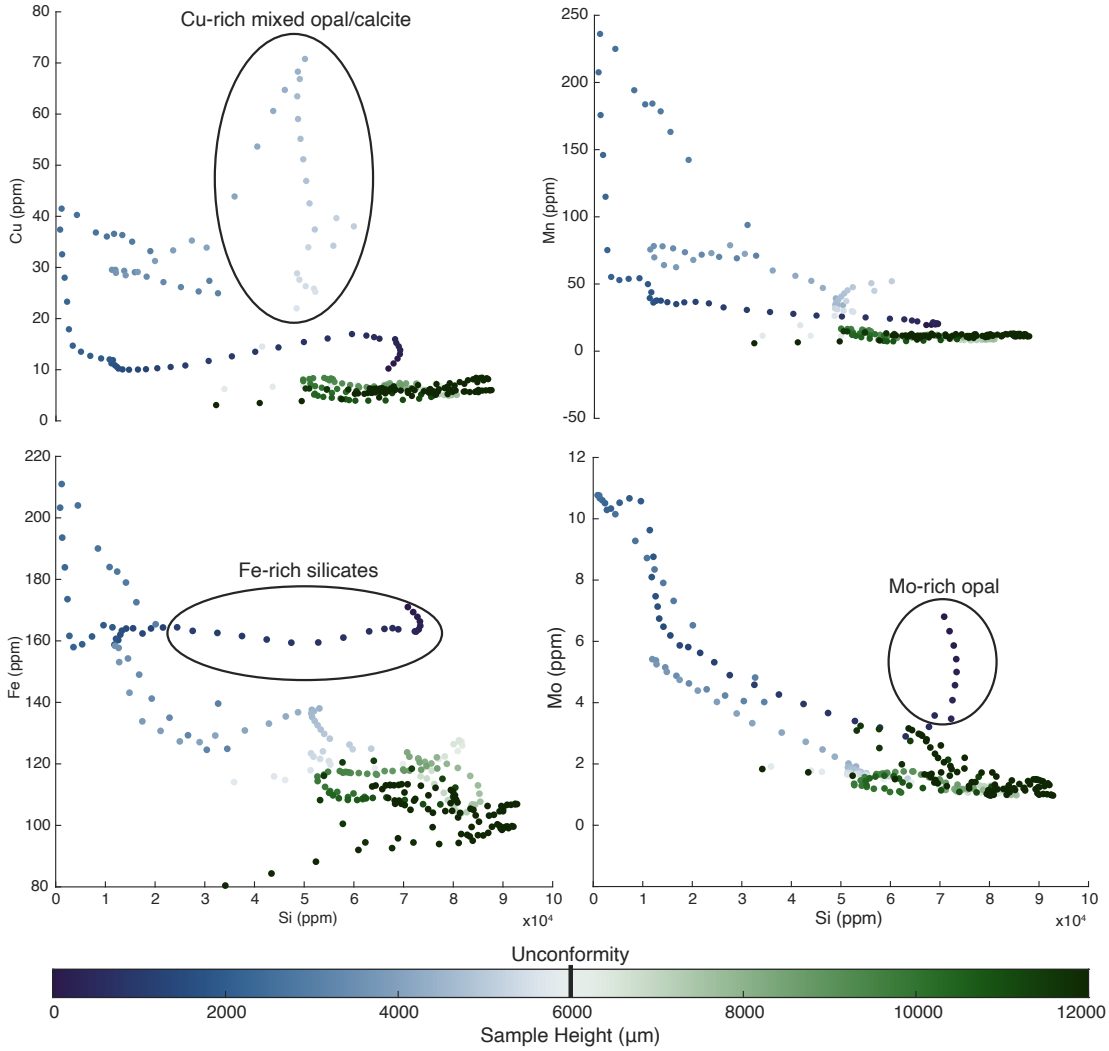

Fig. S3. PRR50504 trace metal versus silicon concentration. Markers colored by sample height.

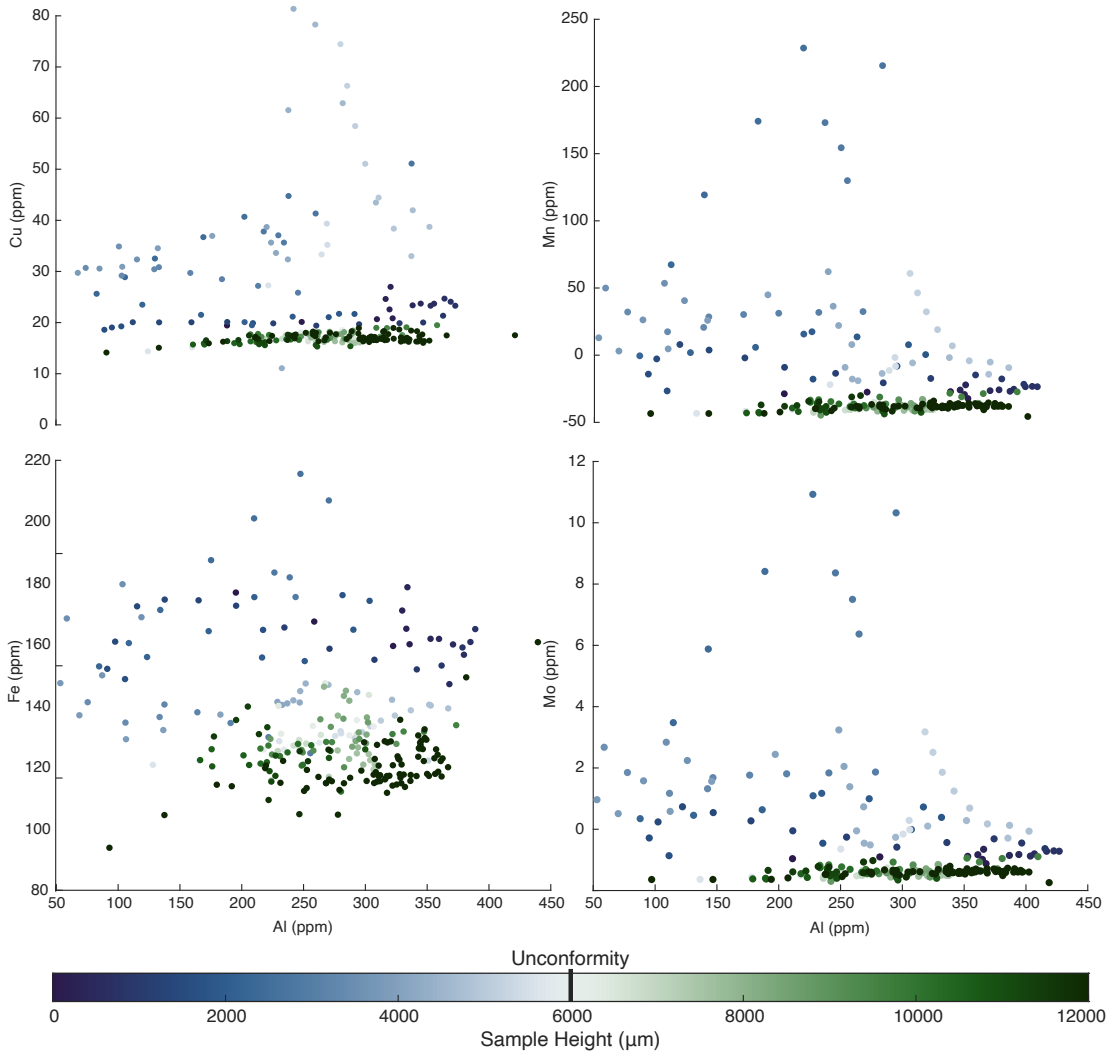

Fig. S4. PRR50504 trace metal versus aluminum concentration. Markers colored by sample height.

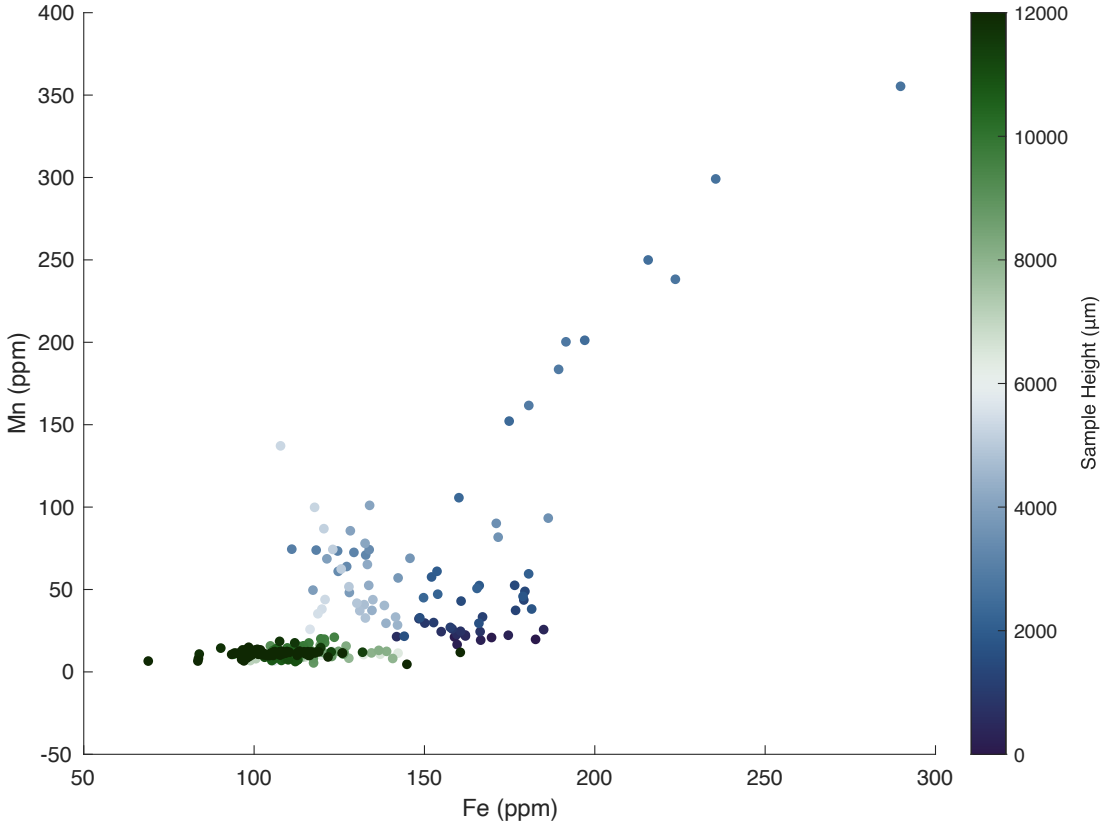

Fig. S5. PRR50504 iron versus manganese concentration. Markers colored by sample height.

References

1. Oppenheimer, M. *et al.* Sea Level Rise and Implications for Low-Lying Islands, Coasts and Communities. in *IPCC Special Report on the Ocean and Cryosphere in a Changing Climate* 321–445 (2019). doi:10.1126/science.aam6284

2. Rignot, E. *et al.* Four decades of Antarctic ice sheet mass balance from 1979–2017. *Proc. Natl. Acad. Sci.* **116**, 1095–1103 (2019).

3. Shen, Q. *et al.* Recent high-resolution Antarctic ice velocity maps reveal increased mass loss in Wilkes Land, East Antarctica. *Sci. Rep.* **8**, 1–8 (2018).

4. Miles, B., Stokes, C. & Jamieson, S. Velocity increases at Cook Glacier, East Antarctica, linked to ice shelf loss and a subglacial flood event. *Cryosphere* **12**, 3123–3136 (2018).

5. Noble, T. L. *et al.* The sensitivity of the Antarctic Ice Sheet to a changing climate: Past, present and future. *Rev. Geophys.* 1–89 (2020). doi:10.1029/2019rg000663

6. Fricker, H. A., Siegfried, M. R., Carter, S. P. & Scambos, T. A. A decade of progress in observing and modeling Antarctic subglacial water systems. *Philos. Trans. R. Soc. A Math. Phys. Eng. Sci.* **374**, (2016).

7. Siegfried, M. R., Fricker, H. A., Carter, S. P. & Tulaczyk, S. Episodic ice velocity fluctuations triggered by a subglacial flood in West Antarctica. *Geophys. Res. Lett.* **43**, 2640–2648 (2016).

8. Bell, R. E., Studinger, M., Shuman, C. A., Fahnestock, M. A. & Joughin, I. Large subglacial lakes in East Antarctica at the onset of fast-flowing ice streams. *Nature* **445**, 904–907 (2007).

9. Dow, C. F., Ross, N., Jeofry, H., Siu, K. & Siegert, M. J. Antarctic basal environment shaped by high-pressure flow through a subglacial river system. *Nat. Geosci.* (2022). doi:10.1038/s41561-022-01059-1

10. Wadham, J. L. *et al.* The potential role of the Antarctic Ice Sheet in global biogeochemical cycles. *Earth Environ. Sci. Trans. R. Soc. Edinburgh* **104**, 55–67 (2013).

11. Christner, B. C. *et al.* A microbial ecosystem beneath the West Antarctic ice sheet. *Nature* **512**, 310–313 (2014).

12. Hawkings, J. R. *et al.* Enhanced trace element mobilization by Earth's ice sheets. *Proc. Natl. Acad. Sci.* 1–12 (2020). doi:10.1073/pnas.2014378117

13. Vick-Majors, T. J. *et al.* Biogeochemical Connectivity Between Freshwater Ecosystems beneath the West Antarctic Ice Sheet and the Sub-Ice Marine Environment. *Global Biogeochem. Cycles* **34**, (2020).

14. Death, R. *et al.* Antarctic ice sheet fertilises the Southern Ocean. *Biogeosciences* **11**, 2635–2643 (2014).

15. Bader, N. A., Licht, K. J., Kaplan, M. R., Kassab, C. & Winckler, G. East Antarctic ice sheet stability recorded in a high-elevation ice-cored moraine. *Quat. Sci. Rev.* **159**, 88–102 (2017).

16. Dutton, A. *et al.* Sea-level rise due to polar ice-sheet mass loss during past warm periods. *Science (80-.).* **349**, 153- (2015).

17. Li, X., Rignot, E., Morlighem, M., Mouginot, J. & Scheuchl, B. Grounding line retreat of Totten Glacier, East Antarctica, 1996 to 2013. *Geophys. Res. Lett.* **42**, 8049–8056 (2015).

18. Rignot, E., Mouginot, J., Morlighem, M., Seroussi, H. & Scheuchl, B. Widespread, rapid grounding line retreat of Pine Island, Thwaites, Smith, and Kohler glaciers, West Antarctica, from 1992 to 2011. *Geophys. Res. Lett.* **41**, 3502–3509 (2014).

19. Joughin, I., Alley, R. B. & Holland, D. M. Ice-Sheet Response to Oceanic Forcing. *Science (80-.).* **338**, 1172–6 (2013).

20. Pollard, D., Chang, W., Haran, M., Applegate, P. & DeConto, R. Large ensemble modeling of the last deglacial retreat of the West Antarctic Ice Sheet: Comparison of simple and advanced statistical techniques. *Geosci. Model Dev.* **9**, 1697–1723 (2016).

21. Mengel, M. & Levermann, A. Ice plug prevents irreversible discharge from east Antarctica. *Nat. Clim. Chang.* **4**, 451–455 (2014).

22. Reese, R., Gudmundsson, G. H., Levermann, A. & Winkelmann, R. The far reach of ice-shelf thinning in Antarctica. *Nat. Clim. Chang.* **8**, 53–57 (2018).

23. Golledge, N. R. *et al.* Antarctic contribution to meltwater pulse 1A from reduced Southern Ocean overturning. *Nat. Commun.* **5**, 1–8 (2014).

24. Blasco, J., Tabone, I., Alvarez-Solas, J., Robinson, A. & Montoya, M. The Antarctic Ice Sheet response to glacial millennial-scale variability. *Clim. Past* **15**, 121–133 (2019).

25. Crowley, T. J. North Atlantic Deep Water Cools the Southern Hemisphere. *Paleoceanography* **7**, 489–497 (1992).

26. Pedro, J. B. *et al.* Beyond the bipolar seesaw: Toward a process understanding of interhemispheric coupling. *Quat. Sci. Rev.* **192**, 27–46 (2018).

27. Lu, J., Chen, G. & Frierson, D. M. W. The position of the midlatitude storm track and eddy-driven westerlies in aquaplanet AGCMs. *J. Atmos. Sci.* **67**, 3984–4000 (2010).

28. Schneider, T., Bischoff, T. & Haug, G. H. Migrations and dynamics of the intertropical convergence zone. *Nature* **513**, 45–53 (2014).

29. Lee, S. Y., Chiang, J. C. H., Matsumoto, K. & Tokos, K. S. Southern Ocean wind response to North Atlantic cooling and the rise in atmospheric CO2: Modeling perspective and paleoceanographic implications. *Paleoceanography* **26**, 1–16 (2011).

30. Marshall, J. & Speer, K. Closure of the meridional overturning circulation through Southern Ocean upwelling. *Nat. Geosci.* **5**, 171–180 (2012).

31. Fretwell, P. *et al.* Bedmap2: Improved ice bed, surface and thickness datasets for Antarctica. *Cryosphere* **7**, 375–393 (2013).

32. Zhang, X., Knorr, G., Lohmann, G. & Barker, S. Abrupt North Atlantic circulation changes in response to gradual CO 2 forcing in a glacial climate state. *Nat. Geosci.* **10**, 518–523 (2017).

33. Galbraith, E. & de Lavergne, C. Response of a comprehensive climate model to a broad range of external forcings: relevance for deep ocean ventilation and the development of late Cenozoic ice ages. *Clim. Dyn.* **52**, 653–679 (2019).

34. Klockmann, M., Mikolajewicz, U. & Marotzke, J. Two AMOC states in response to decreasing greenhouse gas concentrations in the coupled climate model MPI-ESM. *J. Clim.* **31**, 7969–7984 (2018).

35. Barker, S. & Knorr, G. Millennial scale feedbacks determine the shape and rapidity of glacial termination. *Nat. Commun.* **12**, (2021).

36. Weber, M. E. *et al.* Millennial-scale variability in Antarctic ice-sheet discharge

during the last deglaciation. *Nature* **510**, 134–138 (2014).

37. Fogwill, C. J., Turney, C. S. M., Golledge, N. R., Etheridge, D. M. & Rubino, M. Antarctic ice sheet discharge driven by atmosphere-ocean feedbacks at the Last Glacial Termination. *Sci. Rep.* 1–10 (2017). doi:10.1038/srep39979

38. Turney, C. S. M. *et al.* Early Last Interglacial ocean warming drove substantial ice mass loss from Antarctica. *Proc. Natl. Acad. Sci.* **117**, 3996–4006 (2020).

39. Kassab, C. M. *et al.* Formation and evolution of an extensive blue ice moraine in central Transantarctic Mountains, Antarctica. *J. Glaciol.* **66**, 49–60 (2019).

40. Faure, G. Physical Description of the Elephant and Reckline Moraines. in *Workshop on Antarctic Meteorite Standing Surfaces* 24–25 (1990).

41. Cassidy, W., Harvey, R., Schutt, J., Delise, G. & Yanai, K. The meteorite collection of Antarctica. *Meteorites* **27**, 490–525 (1992).

42. Faure, G. & Mensing, T. M. *The Transantarctic Mountains*. *The Transantarctic Mountains* (2011). doi:10.1007/978-90-481-9390-5

43. Hallet, B. Deposits Formed by Subglacial Precipitation of CaCO3. *Geol. Soc. Am. Bull.* **87**, 1003–1015 (1976).

44. Blackburn, T. *et al.* Composition and formation age of amorphous silica coating glacially polished surfaces. *Geology* **47**, 347–350 (2019).

45. Refsnider, K. A. *et al.* Subglacially precipitated carbonates record geochemical interactions and pollen preservation at the base of the Laurentide Ice Sheet on central Baffin Island, eastern Canadian Arctic. *Quat. Res.* **81**, 94–105 (2014).

46. Keller, B. A Bayesian framework for integrated eruption age and age-depth modelling. (2018). doi:10.17605/OSF.IO/TQX3F

47. Aharon, P. Oxygen, carbon and U-series isotopes of aragonites from Vestfold Hills, Antarctica: Clues to geochemical processes in subglacial environments. *Geochim. Cosmochim. Acta* **52**, 2321–2331 (1988).

48. Graly, J. A., Licht, K. J., Kassab, C. M., Bird, B. W. & Kaplan, M. R. Warm-based basal sediment entrainment and far-field Pleistocene origin evidenced in central Transantarctic blue ice through stable isotopes and internal structures. *J. Glaciol.* **64**, 185–196 (2018).

49. Souchez, R. a. & Tison, J.-L. Basal Freezing of Squeezed Water: Its Influence

on Glacier Erosion. *Ann. Glaciol.* **2**, 63–66 (1981).

50. Masson-Delmotte, V. *et al.* A review of antarctic surface snow isotopic composition: Observations, atmospheric circulation, and isotopic modeling. *J. Clim.* **21**, 3359–3387 (2008).

51. German, C. R. & Elderfield, H. Application of the Ce anomaly as a paleoredox indicator: The ground rules. *Paleoceanography* **5**, 823–833 (1990).

52. Yan, Y. *et al.* Two-million-year-old snapshots of atmospheric gases from Antarctic ice. *Nature* **574**, (2019).

53. Montross, S. *et al.* Debris-Rich Basal Ice as a Microbial Habitat, Taylor Glacier, Antarctica. *Geomicrobiol. J.* **31**, 76–81 (2014).

54. Clark, I. D. & Fritz, P. *Environmental Isotopes in Hydrogeology*. (CRC Press, 1997). doi:10.1201/9781482242911

55. Barth, J. A. C., Cronin, A. A., Dunlop, J. & Kalin, R. M. Influence of carbonates on the riverine carbon cycle in an anthropogenically dominated catchment basin: Evidence from major elements and stable carbon isotopes in the Lagan River (N. Ireland). *Chem. Geol.* **200**, 203–216 (2003).

56. Doran, P. T., Kenig, F., Knoepfle, J. L., Mikucki, J. A. & Berry Lyons, W. Radiocarbon distribution and the effect of legacy in lakes of the McMurdo Dry Valleys, Antarctica. *Limnol. Oceanogr.* **59**, 811–826 (2014).

57. McNutt, R. H., Frape, S. K., Fritz, P., Jones, M. G. & MacDonald, I. M. The 87Sr86Sr values of Canadian Shield brines and fracture minerals with applications to groundwater mixing, fracture history, and geochronology. *Geochim. Cosmochim. Acta* **54**, 205–215 (1990).

58. Toner, J. D. & Sletten, R. S. The formation of Ca-Cl-rich groundwaters in the Dry Valleys of Antarctica : Field measurements and modeling of reactive transport. *Geochim. Cosmochim. Acta* **110**, 84–105 (2013).

59. Lyons, W. B. *et al.* The Geochemistry of Englacial Brine From Taylor Glacier, Antarctica. *J. Geophys. Res. Biogeosciences* **124**, 633–648 (2019).

60. Goodwin, I. D. The nature and origin of a jokulhlaup near Casey Station, Antarctica. *J. Glaciol.* **34**, 95–101 (1988).

61. Goodwin, I. D. *et al.* Modern to Glacial age subglacial meltwater drainage at Law Dome, coastal East Antarctica from topography, sediments and

jökulhlaup observations. *Geol. Soc. Spec. Publ.* **461**, 215–230 (2018).

62. Parkhurst, D. L. & Appelo, C. a. J. Description of Input and Examples for PHREEQC Version 3 — A Computer Program for Speciation , Batch-Reaction , One-Dimensional Transport , and Inverse Geochemical Calculations. U.S. Geological Survey Techniques and Methods, book 6, chapter A43, 497 p. *U.S. Geol. Surv. Tech. Methods, B. 6, chapter A43* 6-43A (2013).

63. Hallet, B. Deposits formed by subglacial precipitation of CaCO 3. *Bull. Geol. Soc. Am.* **87**, 1003–1015 (1976).

64. Siegert, M. J., Kwok, R., Mayer, C. & Hubbard, B. Water exchange between the subglacial Lake Vestok and the overlying ice sheet. *Nature* **403**, 643–646 (2000).

65. Ritz, C. Time dependent boundary conditions for calculation of temperature fields in ice sheets. *Int. Assoc. Hydrol. Sci.* **170**, 207–216 (1987).

66. Morse, D. L., Waddington, E. D. & Rasmussen, L. A. Ice deformation in the vicinity of the ice-core site at Taylor Dome, Antarctica, and a derived accumulation rate history. *J. Glaciol.* **53**, 449–460 (2007).

67. Wolff, E. W. *et al.* Changes in environment over the last 800,000 years from chemical analysis of the EPICA Dome C ice core. *Quat. Sci. Rev.* **29**, 285–295 (2010).

68. Buiron, D. *et al.* TALDICE-1 age scale of the Talos Dome deep ice core, East Antarctica. *Clim. Past* **7**, 1–16 (2011).

69. Kahle, E. C. *et al.* Reconstruction of Temperature, Accumulation Rate, and Layer Thinning From an Ice Core at South Pole, Using a Statistical Inverse Method. *J. Geophys. Res. Atmos.* **126**, 1–20 (2021).

70. Baggenstos, D. *et al.* A Horizontal Ice Core From Taylor Glacier, Its Implications for Antarctic Climate History, and an Improved Taylor Dome Ice Core Time Scale. *Paleoceanogr. Paleoclimatology* **33**, 778–794 (2018).

71. Fudge, T. J. *et al.* Variable relationship between accumulation and temperature in West Antarctica for the past 31,000 years. *Geophys. Res. Lett.* **43**, 3795–3803 (2016).

72. Buizert, C. *et al.* Abrupt ice-age shifts in southern westerly winds and Antarctic climate forced from the north. *Nature* **563**, 681–684 (2018).

73. Bahr, D. B., Pfeffer, W. T. & Kasar, G. A review of volume-area scaling of glaciers. *Rev. Geophys.* **53**, 95–140 (2014).

74. Wilson, D. J. *et al.* Ice loss from the East Antarctic Ice Sheet during late Pleistocene interglacials. *Nature* **561**, 383–386 (2018).

75. Spector, P. *et al.* Rapid early-Holocene deglaciation in the Ross Sea, Antarctica. *Geophys. Res. Lett.* **44**, 7817–7825 (2017).

76. Stutz, J. *et al.* Mid-Holocene thinning of David Glacier, Antarctica: Chronology and controls. *Cryosphere* **15**, 5447–5471 (2021).

77. Rhee, H. H. *et al.* Quaternary ice thinning of David Glacier in the Terra Nova Bay region, Antarctica. *Quat. Geochronol.* **67**, 101233 (2022).

78. Golledge, N. R., Levy, R. H., McKay, R. M. & Naish, T. R. East Antarctic ice sheet most vulnerable to Weddell Sea warming. *Geophys. Res. Lett.* **44**, 2343–2351 (2017).

79. Pattyn, F. Antarctic subglacial conditions inferred from a hybrid ice sheet / ice stream model. *Earth Planet. Sci. Lett.* **295**, 451–461 (2010).

80. Van Liefferinge, B. & Pattyn, F. Using ice-flow models to evaluate potential sites of million year-old ice in Antarctica. *Clim. Past* **9**, 2335–2345 (2013).

81. Schoof, C. Ice sheet grounding line dynamics: Steady states, stability, and hysteresis. *J. Geophys. Res. Earth Surf.* **112**, 1–19 (2007).

82. Anderson, H. J., Pedro, J. B., Bostock, H. C., Chase, Z. & Noble, T. L. Compiled Southern Ocean sea surface temperatures correlate with Antarctic Isotope Maxima. *Quat. Sci. Rev.* **255**, 106821 (2021).

83. Ai, X. E. *et al.* Southern Ocean upwelling, Earth's obliquity, and glacial-interglacial atmospheric CO 2 change. *Science (80-.).* **370**, 1348–1352 (2020).

84. Grant, K. M. *et al.* Sea-level variability over five glacial cycles. *Nat. Commun.* **5**, (2014).

85. Golledge, N. R., Marsh, O. J., Rack, W., Braaten, D. & Jones, R. S. Basal conditions of two Transantarctic Mountains outlet glaciers from observation-constrained diagnostic modelling. *J. Glaciol.* **60**, 855–866 (2014).

86. Buizert, C. *et al.* The WAIS Divide deep ice core WD2014 chronology – Part 1: Methane synchronization (68-31 ka BP) and the gas age-ice

age difference. *Clim. Past* **11**, 153–173 (2015).

87. Coplen, T. B. *et al.* New Guidelines for δ13C Measurements. *Anal. Chem.* **78**, 2439–2441 (2006).

88. Ostermann, D. R. & Curry, W. B. Calibration of stable isotopic data: An enriched δ18O standard used for source gas mixing detection and correction. *Paleoceanography* **15**, 353–360 (2000).

89. Clayton, R. N. & Mayeda, T. K. The use of bromine pentafluoride in the extraction of oxygen from oxides and silicates for isotopic analysis. *Geochim. Cosmochim. Acta* **27**, 43–52 (1963).

90. Wostbrock, J. A. G. *et al.* Calibration and application of silica-water triple oxygen isotope thermometry to geothermal systems in Iceland and Chile. *Geochim. Cosmochim. Acta* **234**, 84–97 (2018).

91. Chamberlain, C. P. *et al.* Triple oxygen isotopes of meteoric hydrothermal systems - implications for palaeoaltimetry. *Geochemical Perspect. Lett.* **15**, 6–9 (2020).

92. Ibarra, D. E., Kukla, T., Methner, K. A., Mulch, A. & Chamberlain, C. P. Reconstructing Past Elevations From Triple Oxygen Isotopes of Lacustrine Chert: Application to the Eocene Nevadaplano, Elko Basin, Nevada, United States. *Front. Earth Sci.* **9**, 1–19 (2021).

93. Sharp, Z. D. & Wostbrock, J. A. G. Standardization for the Triple Oxygen Isotope System: Waters, Silicates, Carbonates, Air, and Sulfates. *Rev. Mineral. Geochemistry* **86**, 179–196 (2021).

94. Menicucci, A. J., Matthews, J. A. & Spero, H. J. Oxygen isotope analyses of biogenic opal and quartz using a novel microfluorination technique. *Rapid Commun. Mass Spectrom.* **27**, 1873–1881 (2013).

95. Chapligin, B. *et al.* Inter-laboratory comparison of oxygen isotope compositions from biogenic silica. *Geochim. Cosmochim. Acta* **75**, 7242–7256 (2011).

96. Paton, C., Hellstrom, J., Paul, B., Woodhead, J. & Hergtb, J. Iolite : Freeware for the visualisation and processing of mass spectrometric data. *J. Anal. At. Spectrom.* **26**, 2508–2518 (2011).

97. Marion, G. M., Mironenko, M. V. & Roberts, M. W. FREZCHEM: A geochemical model for cold aqueous solutions. *Comput. Geosci.* **36**, 10–15

(2010).

98. Iler, R. K. *The Chemistry of Silica: Solubility, Polymerization, Colloid and Surface Properties, and Biochemistry*. *John Wiley and Sons Ltd., New York.* (1979).

99. Green, W. J. & Canfield, D. E. Geochemistry of the Onyx River (Wright Valley, Antarctica) and its role in the chemical evolution of Lake Vanda. *Geochim. Cosmochim. Acta* **48**, 2457–2467 (1984).

100. Tréguer, P. *et al.* The silica balance in the world ocean: A reestimate. *Science (80-.).* **268**, 375–379 (1995).

101. Frape, S. K., Fritz, P. & McNutt, R. H. Water-rock interaction and chemistry of groundwaters from the Canadian Shield. *Geochim. Cosmochim. Acta* **48**, 1617–1627 (1984).

102. Bell, R. E. *et al.* Widespread Persistent Thickening of the East Antarctic Ice Sheet by Freezing from the Base. *Science (80-.).* **331**, 1592–1596 (2011).

103. Killawee, J. A., Fairchild, I. J., Tison, J. L., Janssens, L. & Lorrain, R. Segregation of solutes and gases in experimental freezing of dilute solutions: Implications for natural glacial systems. *Geochim. Cosmochim. Acta* **62**, 3637–3655 (1998).

104. Wilson, A. T. Geochemical problems of the Antarctic dry areas. *Nature* **280**, 205–208 (1979).

105. Webster, J. G., Goguel, R. L. & Pond, D. J. Anions and alkali metals in Lake Vanda , Don Juan Pond , and the Onyx River : Further indications of brine origin. 154–156 (1988).

106. Cartwright, K. & Harris, H. J. H. Hydrogeology of the Dry Valley region, Antarctica. *Am. Geophys. Union, Antarct. Res. Ser.* **33**, 193–214 (1981).

107. Levy, J. S., Fountain, A. G., Welch, K. A. & Lyons, W. B. Hypersaline 'wet patches' in Taylor Valley, Antarctica. *Geophys. Res. Lett.* **39**, 1–5 (2012).

108. Harris, H. J. H. & Cartwright, K. Hydrology of the Don Juan Basin, Wright Valley, Antarctica. *Antarct. Res. Ser.* **33**, 162–184 (1981).

109. Angino, E. E. & Armitage, K. B. A Geochemical Study of Lakes Bonney and Vanda, Victoria Land, Antarctica. *J. Geol.* **71**, 89–95 (1963).

110. Healy, M., Webster-Brown, J. G., Brown, K. L. & Lane, V. Chemistry and stratification of Antarctic meltwater ponds II: Inland ponds in the McMurdo Dry Valleys, Victoria Land. *Antarct. Sci.* **18**, 525–533 (2006).

111. Lyons, W. B. *et al.* The geochemistry of upland ponds, Taylor Valley, Antarctica. *Antarct. Sci.* **24**, 3–14 (2012).

112. Carlson, C. A., Phillips, F. M., Elmore, D. & Bentley, H. W. Chlorine-36 tracing of salinity sources in the Dry Valleys of Victria Land, Antarctica. *Geochim. Cosmochim. Acta* **54**, 311–318 (1990).

113. Dickson, J. L., Head, J. W., Levy, J. S. & Marchant, D. R. Don Juan Pond, Antarctica: Near-surface CaCl 2-brine feeding Earth's most saline lake and implications for Mars. *Sci. Rep.* **3**, 1–8 (2013).

114. Toner, J. D., Catling, D. C. & Sletten, R. S. The geochemistry of Don Juan Pond: Evidence for a deep groundwater flow system in Wright Valley, Antarctica. *Earth Planet. Sci. Lett.* **474**, 190–197 (2017).

115. Nurmi, P. A., Kukkonen, I. T. & Lahermo, P. W. Geochemistry and origin of saline groundwaters in the Fennoscandian Shield. *Appl. Geochemistry* **3**, 185–203 (1988).

116. Kim, S. T. & O'Neil, J. R. Equilibrium and nonequilibrium oxygen isotope effects in synthetic carbonates. *Geochim. Cosmochim. Acta* **61**, 3461–3475 (1997).

117. Sharp, Z. D. *et al.* A calibration of the triple oxygen isotope fractionation in the SiO2-H2O system and applications to natural samples. *Geochim. Cosmochim. Acta* **186**, 105–119 (2016).

118. Fitzpatrick, J. J., Muhs, D. R. & Jull, A. J. T. Saline Minerals in the Lewis Cliff Ice Tongue, Buckley Island Quadrangle, Antarctica. *Contrib. to Antarct. Res. I* **50**, 57–69 (1990).

119. Members, W. D. P. Precise interpolar phasing of abrupt climate change during the last ice age. *Nature* **520**, 661–665 (2015).

120. Andersen, K. K. *et al.* High-resolution record of Northern Hemisphere climate extending into the last interglacial period. *Nature* **431**, 147–151 (2004).

121. Jouzel, J. *et al.* Orbital and millennial antarctic climate variability over the past 800,000 years. *Science (80-.).* **317**, 793–796 (2007).

122. Veres, D. *et al.* The Antarctic ice core chronology (AICC2012): An optimized multi-parameter and multi-site dating approach for the last 120 thousand years. *Clim. Past* **9**, 1733–1748 (2013).

123. Phillips, D. L. & Koch, P. L. Incorporating concentration dependence in stable isotope mixing models. *Oecologia* **130**, 114–125 (2002).

124. Ritz, C. *et al.* Potential sea-level rise from Antarctic ice-sheet instability constrained by observations. *Nature* **528**, 115–118 (2015).

125. Nye, J. F. The response of glaciers and ice-sheets to seasonal and climatic changes. *Proc. R. Soc. London. Ser. A. Math. Phys. Sci.* **256**, 559–584 (1960).

126. Bamber, J. L., Vaughan, D. G. & Joughin, I. Widespread complex flow in the interior of the antarctic ice sheet. *Science (80-.).* **287**, 1248–1250 (2000).

127. Huybrechts, P. & De Wolde, J. The dynamic response of the Greenland and Antarctic ice sheets to multiple-century climatic warming. *J. Clim.* **12**, 2169–2188 (1999).

128. Alley, R. B., Clark, P. U., Huybrechts, P. & Joughin, I. Ice-Sheet and Sea-Level Changes. *Science (80-.).* **310**, 456–461 (2005).

129. Gustafson, C. D. *et al.* A dynamic saline groundwater system mapped beneath an Antarctic ice stream. *Science (80-.).* 640–644 (2022).

130. Livingstone, S. J. *et al.* Subglacial lakes and their changing role in a warming climate. *Nat. Rev. Earth Environ.* **3**, 106–124 (2022).

131. Horgan, H. J. *et al.* Estuaries beneath ice sheets. *Geology* **41**, 1159–1162 (2013).

132. Wright, A. P. *et al.* Evidence of a hydrological connection between the ice divide and ice sheet margin in the Aurora Subglacial Basin, East Antarctica. *J. Geophys. Res. Earth Surf.* **117**, 1–15 (2012).

133. Wingham, D. J., Siegert, M. J., Shepherd, A. & Muir, A. S. Rapid discharge connects Antarctic subglacial lakes. *Nature* **440**, 1033–1036 (2006).

134. Fricker, H. A., Scambos, T., Bindschadler, R. & Padman, L. An active subglacial water system in West Antarctica mapped from space. *Science (80-.).* **315**, 1544–1548 (2007).

135. Siegfried, M. R. & Fricker, H. A. Thirteen years of subglacial lake activity in

Antarctica from multi-mission satellite altimetry. *Ann. Glaciol.* **59**, 42–55 (2018).

136. Pattyn, F. Investigating the stability of subglacial lakes with a full Stokes ice-sheet model. *J. Glaciol.* **54**, 353–361 (2008).

137. Scambos, T. A., Berthier, E. & Shuman, C. A. The triggering of subglacial lake drainage during rapid glacier drawdown: Crane Glacier, Antarctic Peninsula. *Ann. Glaciol.* **52**, 74–82 (2011).

138. Weber, M. E., Golledge, N. R., Fogwill, C. J., Turney, C. S. M. & Thomas, Z. A. Decadal-scale onset and termination of Antarctic ice-mass loss during the last deglaciation. *Nat. Commun.* **12**, (2021).

139. Piccione, G. *et al.* Subglacial Precipitates Record East Antarctic Ice Sheet Response To Pleistocene Climate Cycles. *Nat. Commun.* **13**, 1–14 (2022).

140. Iverson, N. R. Coupling between a glacier and a soft bed: II. Model results. *J. Glaciol.* **45**, 41–53 (1999).

141. Stearns, L. A., Smith, B. E. & Hamilton, G. S. Increased flow speed on a large east antarctic outlet glacier caused by subglacial floods. *Nat. Geosci.* **1**, 827–831 (2008).

142. Gourmelen, N. *et al.* Channelized Melting Drives Thinning Under a Rapidly Melting Antarctic Ice Shelf. *Geophys. Res. Lett.* **44**, 9796–9804 (2017).

143. Wei, W. *et al.* Getz Ice Shelf melt enhanced by freshwater discharge from beneath the West Antarctic Ice Sheet. *Cryosphere* **14**, 1399–1408 (2020).

144. Wright, A. & Siegert, M. A fourth inventory of Antarctic subglacial lakes. *Antarct. Sci.* **24**, 659–664 (2012).

145. Sürmelihindi, G. *et al.* Laminated carbonate deposits in Roman aqueducts: Origin, processes and implications. *Sedimentology* **60**, 961–982 (2013).

146. Wróblewski, W., Gradziński, M., Motyka, J. & Stankovič, J. Recently growing subaqueous flowstones: Occurrence, petrography, and growth conditions. *Quat. Int.* **437**, 84–97 (2017).

147. Siegfried, M. R. *et al.* The life and death of a subglacial lake in West Antarctica. *Geology* **XX**, 1–5 (2023).

148. Blackburn, T. *et al.* Ice retreat in Wilkes Basin of East Antarctica during a

warm interglacial. *Nature* **583**, 554–559 (2020).

149. Grootes, P. M. *et al.* The Taylor Dome Antarctic 18 O Record and Globally Synchronous Changes in Climate. *Quat. Res.* **56**, 289–298 (2001).

150. Werner, M., Jouzel, J., Masson-Delmotte, V. & Lohmann, G. Reconciling glacial Antarctic water stable isotopes with ice sheet topography and the isotopic paleothermometer. *Nat. Commun.* **9**, 1–10 (2018).

151. Grousset, F. E. *et al.* Antarctic (Dome C) ice-core dust at 18 k.y. B.P.: Isotopic constraints on origins. *Earth Planet. Sci. Lett.* **111**, 175–182 (1992).

152. Burton, G. R., Morgan, V. I., Boutron, C. F. & Rosman, K. J. R. High-sensitivity measurements of strontium isotopes in polar ice. *Anal. Chim. Acta* **469**, 225–233 (2002).

153. Miller, E. K., Blum, J. D. & Friedland, A. J. Determination of soil exchangable-cation loss and weathering rates using Sr isotopes. *Nature* **362**, 3–6 (1993).

154. Aciego, S., Bourdon, B., Schwander, J., Baur, H. & Forieri, A. Toward a radiometric ice clock: Uranium ages of the Dome C ice core. *Quat. Sci. Rev.* **30**, 2389–2397 (2011).

155. Andersen, M. B., Erel, Y. & Bourdon, B. Experimental evidence for 234U-238U fractionation during granite weathering with implications for 234U/238U in natural waters. *Geochim. Cosmochim. Acta* **73**, 4124–4141 (2009).

156. Chen, S. *et al.* Strong coupling of Asian Monsoon and Antarctic climates on sub-orbital timescales. *Sci. Rep.* **6**, 1–7 (2016).

157. Graly, J. A., Drever, J. I. & Humphrey, N. F. Calculating the balance between atmospheric CO2 drawdown and organic carbon oxidation in subglacial hydrochemical systems. *Global Biogeochem. Cycles* **31**, 709–727 (2017).

158. Li, M., Hinnov, L. & Kump, L. Acycle: Time-series analysis software for paleoclimate research and education. *Comput. Geosci.* **127**, 12–22 (2019).

159. Le Brocq, A. M. *et al.* Evidence from ice shelves for channelized meltwater flow beneath the Antarctic Ice Sheet. *Nat. Geosci.* **6**, 945–948 (2013).

160. Mouginot, J. ., Scheuchl, B. & Rignot, E. MEaSUREs Antarctic Boundaries for IPY 2007-2009 from Satellite Radar, Version 2 [Data Set]. (2017).

161. Lisiecki, L. E. & Raymo, M. E. A Pliocene-Pleistocene stack of 57 globally distributed benthic δ 18O records. *Paleoceanography* **20**, 1–17 (2005).

162. Ashmore, D. W. & Bingham, R. G. Antarctic subglacial hydrology: Current knowledge and future challenges. *Antarct. Sci.* **26**, 758–773 (2014).

163. Wadham, J. L. *et al.* Potential methane reservoirs beneath Antarctica. *Nature* **488**, 633–637 (2012).

164. Tulaczyk, S. *et al.* WISSARD at Subglacial Lake Whillans, West Antarctica: Scientific operations and initial observations. *Ann. Glaciol.* **55**, 51–58 (2014).

165. Priscu, J. C. *et al.* Scientific access into Mercer Subglacial Lake: Scientific objectives, drilling operations and initial observations. *Ann. Glaciol.* (2021). doi:10.1017/aog.2021.10

166. Mikucki, J. A. *et al.* A Contemporary Microbially Maintained Subglacial Ferrous "Ocean". *Science (80-.).* **663**, 397–401 (2009).

167. Skidmore, M., Tranter, M., Tulaczyk, S. & Lanoil, B. Hydrochemistry of ice steams beds- evaporitic or microbial effects? *Hydrol. Process.* **24**, 517–523 (2010).

168. Michaud, A. B. *et al.* Solute sources and geochemical processes in Subglacial Lake. *Geology* **44**, 347–350 (2016).

169. Wadham, J. L. *et al.* Ice sheets matter for the global carbon cycle. *Nat. Commun.* **10**, (2019).

170. Anderson, S. P. Glaciers show direct linkage between erosion rate and chemical weathering fluxes. *Geomorphology* **67**, 147–157 (2005).

171. Jamieson, S. S. R., Sugden, D. E. & Hulton, N. R. J. The evolution of the subglacial landscape of Antarctica. *Earth Planet. Sci. Lett.* **293**, 1–27 (2010).

172. McKay, C. P., Andersen, D. & Davila, A. Antarctic environments as models of planetary habitats: University Valley as a model for modern Mars and Lake Untersee as a model for Enceladus and ancient Mars. *Polar J.* **7**, 303–318 (2017).

173. Corsetti, F. A., Olcott, A. N. & Bakermans, C. The biotic response to Neoproterozoic snowball earth. *Palaeogeogr. Palaeoclimatol. Palaeoecol.* **232**, 114–130 (2006).

174. Michaud, A. B. *et al.* Solute sources and geochemical processes in Subglacial Lake Whillans, West Antarctica. *Geology* **44**, 347–350 (2016).

175. Karr, E. A. *et al.* Diversity and distribution of sulfate-reducing bacteria in permanently frozen Lake Fryxell, McMurdo Dry Valleys, Antarctica. *Appl. Environ. Microbiol.* **71**, 6353–6359 (2005).

176. Wadham, J. L. *et al.* Biogeochemical weathering under ice: Size matters. *Global Biogeochem. Cycles* **24**, (2010).

177. Materials and methods are available as supplementary materials.
178. Tuckett, P. A. *et al.* Rapid accelerations of Antarctic Peninsula outlet glaciers driven by surface melt. *Nat. Commun.* **10**, 1–8 (2019).

179. Lamb, A. L., Wilson, G. P. & Leng, M. J. A review of coastal palaeoclimate and relative sea-level reconstructions using δ13C and C/N ratios in organic material. *Earth-Science Rev.* **75**, 29–57 (2006).

180. Raven, J. A. *et al.* Mechanistic interpretation of carbon isotope discrimination by marine macroalgae and seagrasses. *Funct. Plant Biol.* **29**, 355 (2002).

181. Hanshaw, B. B. & Hallet, B. Oxygen Isotope Composition of Subglacially Precipitated Calcite: Possible Paleoclimatic Implications. *Science (80-.).* **200**, 1267–1270 (1978).

182. Sharp, M., Tison, J.-L. & Fierens, G. Geochemistry of Subglacial Calcites: Implications for the Hydrology of the Basal Water Film. *Arct. Alp. Res.* **22**, 141 (1990).

183. Lipar, M. *et al.* Subglacial carbonate deposits as a potential proxy for a glacier's former presence. *Cryosphere* **15**, 17–30 (2021).

184. Lemmens, M., Lorrain, R. & Haren, J. Isotopic Composition of Ice and Subglacially Precipitated Calcite in an Alpine Area. *Zeitschrift für Gletscherkd. und Glazialgeol.* **18**, 151–159 (1983).

185. Thomazo, C. *et al.* Geochemical processes leading to the precipitation of subglacial carbonate crusts at bossons glacier, mont blanc massif (French alps). *Front. Earth Sci.* **5**, 1–16 (2017).

186. Edwards, G. H. *et al.* Terrestrial evidence for ocean forcing of Heinrich events and subglacial hydrologic connectivity of the Laurentide Ice Sheet. *Sci. Adv.* **8**, 1–13 (2022).

187. Hillaire-Marcel, C. & Causse, C. The late pleistocene Laurentide glacier: Th U dating of its major fluctuations and δ18O range of the ice. *Quat. Res.* **32**, 125–138 (1989).

188. Hillaire-Marcel, C., Soucy, J.-M. & Cailleux, A. Analyse isotopique de concrétions sous-glaciaires de l'inlandsis laurentidien et teneur en oxygène 18 de la glace. *Can. J. Earth Sci.* **16**, 1494–1498 (1979).

189. Tullborg, E. L. & Larson, S. Å. δ18O and δ13C for limestones, calcite fissure infillings and calcite precipitates from Sweden. *Gff* **106**, 127–130 (1984).

190. Graly, J. A., Humphrey, N. F., Landowski, C. M. & Harper, J. T. Chemical weathering under the Greenland ice sheet. *Geology* **42**, 551–554 (2014).

191. Michaud, A. B. *et al.* Microbial oxidation as a methane sink beneath the West Antarctic Ice Sheet. *Nat. Geosci.* **10**, 582–586 (2017).

192. Ingalls, M. *et al.* P/Ca in Carbonates as a Proxy for Alkalinity and Phosphate Levels. *Geophys. Res. Lett.* **47**, 1–11 (2020).

193. Cook, C. P. *et al.* Glacial erosion of East Antarctica in the Pliocene: A comparative study of multiple marine sediment provenance tracers. *Chem. Geol.* **466**, 199–218 (2017).

194. Lechte, M. A. *et al.* Subglacial meltwater supported aerobic marine habitats during Snowball Earth. *Proc. Natl. Acad. Sci. U. S. A.* **116**, 25478–25483 (2019).

195. Hamelin, B., Bard, E., Zindler, A. & Fairbanks, R. G. 234U238U mass spectrometry of corals: How accurate is the UTh age of the last interglacial period? *Earth Planet. Sci. Lett.* **106**, 169–180 (1991).

196. Frisia, S. *et al.* The influence of Antarctic subglacial volcanism Maximum. *Nat. Commun.* **8**, 1–9 (2017).

197. Cheng, H. *et al.* The half-lives of uranium-234 and thorium-230. *Chem. Geol.* **169**, 17–33 (2000).

198. T.E.Krogh. A low-contamination method for hydrothermal decomposition of zircon and extraction of U and Pb for isotopic age determinations. *Geochim. Cosmochim. Acta* **87**, 485–494 (1973).

199. McLean, N. M., Bowring, J. F. & Bowring, S. A. An algorithm for U-Pb isotope dilution data reduction and uncertainty propagation. *Geochemistry,*

Geophys. Geosystems **12**, n/a-n/a (2011).

200. Northrup, P. The TES beamline (8-BM) at NSLS-II : tender-energy spatially resolved X-ray absorption spectroscopy and X-ray fluorescence imaging. *J. Synchrotron Radiat.* 1–11 (2019). doi:10.1107/S1600577519012761

201. Einsiedl, F., Schäfer, T. & Northrup, P. Combined sulfur K-edge XANES spectroscopy and stable isotope analyses of fulvic acids and groundwater sulfate identify sulfur cycling in a karstic catchment area. *Chem. Geol.* **238**, 268–276 (2007).

202. Xia, K. *et al.* XANES Studies of Oxidation States of Sulfur in Aquatic and Soil Humic Substances. *Soil Sci. Soc. Am. J.* **62**, 1240–1246 (1998).

203. Huffman, G. P. *et al.* Quantitative analysis of all major forms of sulfur in coal by x-ray absorption fine structure spectroscopy. *Energy & Fuels* **5**, 574–581 (1991).

204. Sigman, D. M., Hain, M. P. & Haug, G. H. The polar ocean and glacial cycles in atmospheric CO2 concentration. *Nature* **466**, 47–55 (2010).

205. Sabine, C. L. *et al.* The Oceanic Sink for Anthropogenic CO 2. *Science (80-.).* **305**, 367–371 (2004).

206. Landschützer, P. *et al.* The reinvigoration of the Southern Ocean carbon sink. *Science (80-.).* **349**, 1221–1224 (2015).

207. Martin, J. H. Glacial-interglacial CO 2 change: The Iron Hypothesis. *Paleoceanography* **5**, 1–13 (1990).

208. Balaguer, J., Koch, F., Hassler, C. & Trimborn, S. Iron and manganese co-limit the growth of two phytoplankton groups dominant at two locations of the Drake Passage. *Commun. Biol.* **5**, 1–12 (2022).

209. Browning, T. J., Achterberg, E. P., Engel, A. & Mawji, E. Manganese co-limitation of phytoplankton growth and major nutrient drawdown in the Southern Ocean. *Nat. Commun.* **12**, 1–9 (2021).

210. Martínez-García, A. *et al.* Iron fertilization of the subantarctic ocean during the last ice age. *Science (80-.).* **343**, 1347–1350 (2014).

211. Jaccard, S. L., Galbraith, E. D., Martínez-Garciá, A. & Anderson, R. F. Covariation of deep Southern Ocean oxygenation and atmospheric CO2 through the last ice age. *Nature* **530**, 207–210 (2016).

212. Martínez-Garcia, A. *et al.* Southern Ocean dust-climate coupling over the past four million years. *Nature* **476**, 312–315 (2011).

213. Shoenfelt, E. M., Winckler, G., Lamy, F., Anderson, R. F. & Bostick, B. C. Highly bioavailable dust-borne iron delivered to the Southern Ocean during glacial periods. *Proc. Natl. Acad. Sci.* **115**, 11180–11185 (2018).

214. Herraiz-Borreguero, L., Lannuzel, D., van der Merwe, P., Treverrow, A. & Pedro, J. B. Large flux of iron from the Amery Ice Shelf marine ice to Prydz Bay, East Antarctica. *J. Geophys. Res. Ocean.* **121**, 6009–6020 (2016).

215. Gerringa, L. J. A. *et al.* Iron from melting glaciers fuels the phytoplankton blooms in Amundsen Sea (Southern Ocean): Iron biogeochemistry. *Deep. Res. Part II Top. Stud. Oceanogr.* **71**–**76**, 16–31 (2012).

216. Alderkamp, A. C. *et al.* Iron from melting glaciers fuels phytoplankton blooms in the Amundsen Sea (Southern Ocean): Phytoplankton characteristics and productivity. *Deep. Res. Part II Top. Stud. Oceanogr.* **71**–**76**, 32–48 (2012).

217. Annett, A. L. *et al.* Comparative roles of upwelling and glacial iron sources in Ryder Bay, coastal western Antarctic Peninsula. *Mar. Chem.* **176**, 21–33 (2015).

218. Monien, D. *et al.* Meltwater as a source of potentially bioavailable iron to Antarctica waters. *Antarct. Sci.* **29**, 277–291 (2017).

219. Forsch, K. O. *et al.* Seasonal dispersal of fjord meltwaters as an important source of iron and manganese to coastal Antarctic phytoplankton. *Biogeosciences* **18**, 6349–6375 (2021).

220. Raiswell, R., Benning, L. G., Tranter, M. & Tulaczyk, S. Bioavailable iron in the Southern Ocean: The significance of the iceberg conveyor belt. *Geochem. Trans.* **9**, 1–9 (2008).

221. Raiswell, R. *et al.* Potentially bioavailable iron delivery by iceberg-hosted sediments and atmospheric dust to the polar oceans. *Biogeosciences* **13**, 3887–3900 (2016).

222. Hawkings, J. R. *et al.* Ice sheets as a significant source of highly reactive nanoparticulate iron to the oceans. *Nat. Commun.* **5**, 3929 (2014).

223. Piccione, G., Blackburn, T., Hain, M., Tulaczyk, S. & Carney, C. Microbes drive subglacial CO2 production and silicate weathering throughout

Antarctica. *Rev.*

224. Piccione, G., Pinter, S., Blackburn, T. & Tulaczyk, S. Accelerated Antarctic ice loss through ocean forced changes in subglacial hydrology. *Rev.*

225. Bazin, L. *et al.* An optimized multi-proxy, multi-site Antarctic ice and gas orbital chronology (AICC2012): 120-800 ka. *Clim. Past* **9**, 1715–1731 (2013).

226. Katz, J. L., Reick, M. R., Herzog, R. E. & Parsiegla, K. I. Calcite growth inhibition by iron. *Langmuir* **9**, 1423–1430 (1993).

227. Calvert, S. E. & Pedersen, T. F. Geochemistry of Recent oxic and anoxic marine sediments: Implications for the geological record. *Mar. Geol.* **113**, 67–88 (1993).

228. Hawkings, J. R. *et al.* Biolabile ferrous iron bearing nanoparticles in glacial sediments. *Earth Planet. Sci. Lett.* **493**, 92–101 (2018).

229. Scott, C. & Lyons, T. W. Contrasting molybdenum cycling and isotopic properties in euxinic versus non-euxinic sediments and sedimentary rocks: Refining the paleoproxies. *Chem. Geol.* **324–325**, 19–27 (2012).

230. Tribovillard, N., Algeo, T. J., Lyons, T. & Riboulleau, A. Trace metals as paleoredox and paleoproductivity proxies: An update. *Chem. Geol.* **232**, 12–32 (2006).

231. Mikucki, J. A. *et al.* Deep groundwater and potential subsurface habitats beneath an Antarctic dry valley. *Nat. Commun.* **6**, (2015).

232. Bhatia, M. P. *et al.* Greenland meltwater as a significant and potentially bioavailable source of iron to the ocean. *Nat. Geosci.* **6**, 274–278 (2013).

233. Statham, P. J., Skidmore, M. & Tranter, M. Inputs of glacially derived dissolved and colloidal iron to the coastal ocean and implications for primary productivity. *Global Biogeochem. Cycles* **22**, 1–11 (2008).

234. Krause, J. *et al.* Trace Element (Fe, Co, Ni and Cu) Dynamics Across the Salinity Gradient in Arctic and Antarctic Glacier Fjords. *Front. Earth Sci.* **9**, 1–20 (2021).

235. Ravel, B. & Newville, M. ATHENA , ARTEMIS , HEPHAESTUS : data analysis for X-ray absorption spectroscopy using IFEFFIT. *J. Synchrotron Radiat.* **12**, 537–541 (2005).

236. Lee, Y. J., Reeder, R. J., Wenskus, R. W. & Elzinga, E. J. Structural relaxation in the MnCO3-CaCo3 solid solution: A Mn K-edge EXAFS study. *Phys. Chem. Miner.* **29**, 585–594 (2002).

237. Condon, D. J., McLean, N., Noble, S. R. & Bowring, S. A. Isotopic composition (238U/235U) of some commonly used uranium reference materials. *Geochim. Cosmochim. Acta* **74**, 7127–7143 (2010).

238. Bintanja, R. On the Glaciological, Meteorological, and Significance. *Rev. Geophys.* **37**, 337–359 (1999).

239. Faure, G. & Harwood, D. M. Marine microfossils in till clasts of the Elephant Moraine on the east antarctic ice sheet. in *Antarctic Journal of the United States* 23–25 (1990).

240. Matsuoka, K. *et al.* Quantarctica, an integrated mapping environment for Antarctica, the Southern Ocean, and sub-Antarctic islands. *Environ. Model. Softw.* **140**, (2021).

241. Nishiizumi, K. Subaerial exposure ages of bedrock near meteorite stranding surfaces. in *Antarctic Meteorite Stranding Surfaces* 60–64 (1990).

242. Jull, A. J. T. Terrestrial ages of meteorites. in *Accretion of extraterrestrial matter throughout Earth's history* 241–266 (2001). doi:10.1038/293433a0

243. Coren, F., Delisle, G. & Sterzai, P. Ice dynamics of the Allan Hills meteorite concentration sites revealed by satellite aperture radar interferometry. *Meteorit. Planet. Sci.* **38**, 1319–1330 (2003).

244. Rignot, E., Mouginot, J. & Scheuchl, B. Ice flow of the antarctic ice sheet. *Science (80-.).* **333**, 1427–1430 (2011).

245. Mouginot, J., Scheuch, B. & Rignot, E. Mapping of ice motion in antarctica using synthetic-aperture radar data. *Remote Sens.* **4**, 2753–2767 (2012).

246. Souchez, R., Lemmens, M. & Chappellaz, J. Flow-induced mixing in the GRIP basal ice deduced from the CO2 and CH4 records. *Geophys. Res. Lett.* **22**, 41–44 (1995).

247. Steig, E. J. *et al.* Continuous-Flow Analysis of δ 17O, δ 18O, and δD of H2O on an Ice Core from the South Pole. *Front. Earth Sci.* **9**, 1–14 (2021).

248. Jouzel, Jean and Souchez, R. A. Melting-Refreezing At the Glacier Sole and the Isotopic Composition of Ice. *J. Glaciol.* **28**, 35–42 (1982).

249. Faure, G., Hoefs, J., Jones, L. M., Curtis, J. B. & Pride, D. E. Extreme 18O depletion in calcite and chert clasts from the Elephant Moraine on the East Antarctic ice sheet. *Nature* **332**, 352–354 (1988).

250. Marsh, N. B. *et al.* Sources of solutes and carbon cycling in perennially ice-covered Lake Untersee, Antarctica. *Sci. Rep.* **10**, 1–12 (2020).

251. Diaz, M. A. *et al.* Stable Isotopes of Nitrate, Sulfate, and Carbonate in Soils From the Transantarctic Mountains, Antarctica: A Record of Atmospheric Deposition and Chemical Weathering. *Front. Earth Sci.* **8**, 1–19 (2020).

252. Lorius, C., Merlivat, L., Jouzel, J. & Pourchet, M. A 30,000-yr isotope climatic record from Antarctic ice. *Nature* **280**, 644–648 (1979).

253. Kigoshi, K. Alpha-Recoil Thorium-234 : Dissolution into Water and the Uranium-234 / Uranium-238 Disequilibrium in Nature. *Science (80-.).* **173**, 47–48 (1971).

254. Henderson, G. M., Hall, B. L., Smith, A. & Robinson, L. F. Control on (234U/238U) in lake water: A study in the Dry Valleys of Antarctica. *Chem. Geol.* **226**, 298–308 (2006).

255. MacAyeal, D. R. Binge/purge oscillations of the Laurentide Ice Sheet as a cause of the North Atlantic's Heinrich events. *Paleoceanography* **8**, 775–784 (1993).

256. Favier, V. *et al.* An updated and quality controlled surface mass balance dataset for Antarctica. *Cryosphere* **7**, 583–597 (2013).

257. Hulbe, C. & Fahnestock, M. Century-scale discharge stagnation and reactivation of the Ross ice streams, West Antarctica. *J. Geophys. Res. Earth Surf.* **112**, 1–11 (2007).

258. Tulaczyk, S., Kamb, W. B. & Engelhardt, H. F. Basal mechanics of Ice Stream B, West Antarctica 2. Undrained plastic bed model. *J. Geophys. Res. Solid Earth* **105**, 483–494 (2000).

259. Goodge, J. W. Crustal heat production and estimate of terrestrial heat flow in central East Antarctica, with implications for thermal input to the East Antarctic ice sheet. *Cryosphere* **12**, 491–504 (2018).

260. Barbante, C. *et al.* One-to-one coupling of glacial climate variability in Greenland and Antarctica. *Nature* **444**, 195–198 (2006).

261. Begeman, C. B., Tulaczyk, S. M. & Fisher, A. T. Spatially Variable Geothermal Heat Flux in West Antarctica: Evidence and Implications. *Geophys. Res. Lett.* **44**, 9823–9832 (2017).

262. Cauquoin, A. *et al.* Comparing past accumulation rate reconstructions in East Antarctic ice cores using 10Be, water isotopes and CMIP5-PMIP3 models. *Clim. Past* **11**, 355–367 (2015).

263. Bintanja, R. On the Glaciological, Meteorological, and Climatological Significance of Antarctic Blue Ice Areas. *Rev. Geophys.* **37**, 337–359 (1999).

264. Cuffey, K. M. & Paterson, W. S. . B. *Physics of Glaciers, Fourth Edition*. *The Physics of Glaciers* (2010).

265. Goehring, B. M., Balco, G., Todd, C., Moening-Swanson, I. & Nichols, K. Late-glacial grounding line retreat in the northern Ross Sea, Antarctica. *Geology* **47**, 291–294 (2019).

266. Neuhaus, S. *et al.* Did Holocene climate changes drive West Antarctic grounding line retreat and re-advance? *Cryosph. Discuss.* 1–30 (2021). doi:10.5194/tc-2020-308

267. Cuffey, K. M. & Paterson, W. S. B. *The physics of glaciers*. (2010).

268. Siddall, M., Rohling, E. J., Thompson, W. G. & Waellbroeck, C. Marine isotope stage 3 sea level fluctuations: Data synthesis and new outlook. *Rev. Geophys.* **46**, 1–29 (2008).

269. Anderson, J. B. *et al.* Ross Sea paleo-ice sheet drainage and deglacial history during and since the LGM. *Quat. Sci. Rev.* **100**, 31–54 (2014).

270. Martin, J. E., Patrick, D., Kihm, A. J., Foit, F. F. & Grandstaff, D. E. Lithostratigraphy, tephrochronology, and rare earth element geochemistry of fossils at the classical pleistocene Fossil Lake area, south central Oregon. *J. Geol.* **113**, 139–155 (2005).

271. De Carlo, E. H. & Green, W. J. Rare earth elements in the water column of Lake Vanda, McMurdo Dry Valleys, Antarctica. *Geochim. Cosmochim. Acta* **66**, 1323–1333 (2002).

272. Dreybrodt, W., Buhmann, D., Michaelis, J. & Usdowski, E. Geochemically controlled calcite precipitation by CO2 outgassing: Field measurements of precipitation rates in comparison to theoretical predictions. *Chem. Geol.* **97**, 285–294 (1992).

273. Dandurand, J. L. *et al.* Kinetically controlled variations of major components and carbon and oxygen isotopes in a calcite-precipitating spring. *Chem. Geol.* **36**, 299–315 (1982).

274. Greene, C. A., Gwyther, D. E. & Blankenship, D. D. Antarctic Mapping Tools for MATLAB. *Comput. Geosci.* **104**, 151–157 (2017).

275. Zeebe, R. & Wolf-Gladrow, D. *CO2 in Seawater: Equilibrium, Kinetics, Isotopes*. (2001).

276. Davis, C. L. *et al.* Biogeochemical and historical drivers of microbial community composition and structure in sediments from Mercer Subglacial Lake, West Antarctica. *ISME Commun.* **3**, 8 (2023).

277. Lamarche-Gagnon, G. *et al.* Greenland melt drives continuous export of methane from the ice-sheet bed. *Nature* **565**, 73–77 (2019).